UNIVERSITY OF CALIFORNIA
RIVERSIDE

Nanomaterials for Electrical and Electrochemical Sensors

A Dissertation submitted in partial satisfaction
of the requirements for the degree of

Doctor of Philosophy

in

Materials Science and Engineering

by

Mohammed Sedki Abuelhassan

March 2022

Dissertation Committee:
Dr. Ashok Mulchandani, Chairperson
Dr. Ruoxue Yan
Dr. Mahesh Neupane

The Dissertation of Mohammed Sedki Abuelhassan is approved:

_____

_____

_____

Committee Chairperson

University of California, Riverside

ACKNOWLEGMENTS

I would like to thank my advisor, Prof. Ashok Mulchandani, for his guidance and support throughout this whole PhD journey. He has been always there whenever needed, not only on the academic and technical level, but also on the personal side. He has been open for trying new ideas, which helped fuel my passion and eagerness for research.

I sincerely appreciate the help and support from my dissertation committee members, Prof. Ruoxue Yan and Prof. Mahesh Neupane. I also thank Prof. Jianlin Liu and Prof. Huinan Liu for their help and guidance.

I would like also to thank my current and former lab mates: Thien-Toan Tran, Tung Pham, Yu Shen, Mika Hattada, and Guo Zhao. I thank my intern students who did a great job during their work with me, Xingyu Chen, Kenta Nakama, and Adam Koziol. A special thanks to my former colleague Claudia Chaves, and my current sincere lab mate, Ying Chen. You all have contributed in a way or another into achieving this goal.

I want to express my deepest and sincerest appreciation to my educational institutes starting from Bourns College of engineering at the University of California, Riverside, and my Egyptian institutes, where I built most of the knowledge I utilized in this PhD work, starting from the Chemistry department at Sohag University, the Center for Nanotechnology at Nile University, and finally the Nanomedicine Lab at the department of Materials Science at Zewail City of Science and Technology.

I am very grateful to my previous advisors: Prof. Mohamed Abdel-Mottaleb, Prof. Mona Bakr, Prof. Manal Fawzy, and Prof. Ibrahim El-sherbiny. I express my gratitude to Prof. Rabeay Hassan and Prof. Islam Khalil for their very sincere recommendations, technical support, and guidance whenever needed. Prof. Hassan was always caring for my academic progress and personal development; he was also the one who connected me with Prof. Mulchandani.

Last but not least, I would love to thank the very kind and wonderful person who left our life to a better place, Prof. Nahla Elkady who helped me a lot at the very beginning of my academic career, when I really needed such help and guidance.

The text of this dissertation in part is a reprint of the materials as it appears in: "Nano-FET-enabled biosensors: Materials perspective and recent advances in North America. *Biosensors and Bioelectronics* 176 (2021): 112941; Non-lytic M13 phage-based highly sensitive impedimetric cytosensor for detection of coliforms. *Biosensors and Bioelectronics* 148 (2020): 111794; Linker-Free Magnetite-Decorated Gold Nanoparticles (Fe3O4-Au): Synthesis, Characterization, and Application for Electrochemical Detection of Arsenic (III). *Sensors* 21, no. 3 (2021): 883; Label-free chemiresistor biosensor based on reduced graphene oxide and M13 bacteriophage for detection of coliforms." *Analytica Chimica Acta* 1150 (2021): 338232; Synthesis of pristine graphene-like behaving rGO thin film: Insights into what really matters." *Carbon* 186 (2022): 437-451". The co-author Dr. Ashok Mulchandani listed in all of these publications directed and supervised the research which forms the basis for this dissertation.

DEDICATION

To my parents, wife, and Sedki’s family

ABSTRACT OF THE DISSERTATION

Nanomaterials for Electrical and Electrochemical Sensors

by

Mohammed Sedki Abuelhassan

Doctor of Philosophy, Graduate Program in Materials Science and Engineering
University of California, Riverside, March 2022
Professor Ashok Mulchandani, Chairperson

The increasing environmental contamination, especially from heavy metals, toxic gases, radioactive materials, pesticides, and pathogens, is a global concern. In this regard, electrical and electrochemical sensors attracted a huge attention. The efficiency and sensitivity of any sensor system is highly dependent on its sensing material interface. This work is focused on synthesis, characterization, and optimization of different nanomaterials (0D, 1D, and 2D) for the sensitive detection of three environmental contaminants, i.e. bacteria, heavy metals (Arsenic), and toxic gases (NO_2). Tuning the material properties to harvest the highest efficiency, for bio/chemical sensors, is a main challenge in every project.

A linker-free gold magnetite nanocomposite (Fe_3O_4-Au) was synthesized using a novel approach that provided very tiny magnetite (~ 10 nm) nanoparticles (NPs) with a high surface area, and synergistic electrocatalytic effects of the two nanomaterials due to the

zero spacing between them. Fe_3O_4-Au NPs-ionic liquid was modified on glassy carbon electrode (GCE) and achieved a trace level detection of As(III) in water using anodic stripping voltammetry.

Non-lytic M13 phage was chemically loaded to AuNPs-GCE and used for the first time for the highly sensitive, selective, and stable (thermally and chemically) impedimetric detection of E. coli in water.

A detailed experimental study of what really matters for getting pristine graphene-like rGO thin film, supported by DFT calculations, was conducted. The rGO thin film was then integrated into microfabricated interdigitated and single gap devices with back gating for field-effect transistor (FET) measurements and applications. The material's electronic properties of bandgap and charge carrier mobility were monitored and correlated with the material quality. The resulting high quality rGO thin film served as a semiconductor channel in FET-based electrical sensors for detection of bacteria and heavy metals. Lastly, $MoSe_2$, and ternary $MoSe_{2(2-x)}Te_{2x}$ alloys were synthesized using chemical vapor deposition (CVD), with a gradient variation in (x) to tune the band gap and carrier mobility of the corresponding alloys for near-infrared (NIR) optoelectronic applications. Orders of magnitude enhancement in the device output was observed by Te doping. By a precise control of the epitaxial growth factors, Janus $MoSe_{2(2-y)}Te_{2y}/MoSe_{2(2-x)}Te_{2x}$ heterostructure with defect-free interface was synthesized, and an antiambipolar transistor was recorded for the first time.

Contents

List of Figures

CHAPTER 1

1.1. Introduction

1.1.1. Overview

A chem/biosensor is an analytical tool that transforms chem/biological events into a measurable output signal. A biosensor consists of three main parts, a biological recognition element or simply a bioreceptor, a transducer, and the associated electronics or signal processor [1]. The material interface is a crucial part of the transduction process. For chemical sensors, it is the same structure as biosensor, but adding a recognition element or not is based on the application. Based on the type of transducer, sensors can be stratified into mechanical, optical, electrochemical, electrical, etc [2–4]. Mechanical sensors detect events in the form of changes in mechanical properties such as stress or strain on cantilever (e.g. cantilever sensors) or changes in mechanical waves in a piezoelectric material (e.g. acoustic wave sensors) [5]. Optical sensors depend on the change in optical signal utilizing many techniques, including surface plasmon resonance, Raman scattering, fluorescence, and colorimetry [6]. Electrochemical sensors are a group of sensors that measure the change in current (amperometric), impedance (impedimetric), potential (potentiometric), or conductivity (conductometric) as a response to a change in analyte's concentration [7,8]. On the other hand, electrical sensors rely on detecting the change in electrical signal associated with variation in analyte's concentration and can be classified into field-effect transistors (FET), chemiresistors, chemical diodes, etc [9]. For each type of these sensors there are strengths and weaknesses, and it all depends on researchers'/users' preferences based on the requirements of each application, available resources and other contributing factors.

1.1.2. Scope of this research

This work is focused on electrical (FET) and electrochemical (Electrochemical Impedance spectroscopy, EIS) environmental sensors. For each project of this dissertation work, we do synthesis and properties tuning of different nanomaterials, characterize them using all possible types of characterizations (e.g. microscopic, spectroscopic, electrochemical, electrical, etc.), and implement them into micro/nanodevices, and finally apply them for the detection of bacteria, heavy metals, and toxic gases (NO2). From materials aspect of chem/biosensors, we focus on the relationship between processing, structure, properties, and performance of nanomaterials. There are four main projects or goals that form this dissertation:

- **Project 1:** Synthesis of linker-free Fe_3O_4-Au nanocomposite for electrochemical detection of As (III) in water
- **Project 2:** Evaluation of *M13* phage nanofibers for EIS bacterial biosensor
- **Project 3:** Synthesis of pristine graphene-like behaving rGO thin film: insights into what really matters
- **Project 4:** CVD synthesis of $MoSe_2$ and $MoSe_{2(2-x)}Te_{2x}$ ternary alloys and Janus defect-free interface $MoSe_{2(2-y)}Te_{2y}/MoSe_{2(2-x)}Te_{2x}$ heterostructures for FET optoelectronics

In the first project, a new facile method was introduced for the in-situ synthesis of linker-free Fe_3O_4-Au nanocomposite for electrochemical detection of As (III) in water. The linker-free synthesis approach allowed for synergistic electrocatalytic performance between Au and Fe_3O_4 nanoparticles. In the second project, *M13* bacteriophage is

harvested and chemically loaded to glassy carbon electrode-gold nanoparticles (GCE/AuNPs) using covalent bonding through a short carbon chain linker and EDC/NHS chemistry. Faradaic EIS as a very sensitive electrochemical technique was used as the transduction system. The fabricated *M13*-EIS biosensor was implemented for the first time in early detection of coliforms (e.g. *E. coli*) in water at a super low limit of detection of 14 cell/mL, with a high stability against elevated temperatures and pH changes for more than a weak. In a continuation of this project, M13 was replaced with antibody for the early detection of *Bacteroides Thetaiotaomicron,* which is a very promising bioindicator of water contamination with feces. In the third project, a detailed mechanistic was introduced to study the effet of lateral sheet size on the quality of reduced graphene oxide (rGO) thin films, with more experimental and theoretical insights into what really matters to get pristine graphene-like behaving rGO thin film. In addition, the effect of low-temperature thermal reduction on rGO thin nanosheets' properties was studied. The optimized rGO thin film was implemented in micro-fabricated FET devices and the electronic properties of rGO were extracted. The optimized thin film showed a very low band gap of 0.4 eV, and a very high carrier mobility. In a continuation of this project, we have loaded M13 bacteriophage into the fabricated device, forming M13-rGO-FET biosensor and applied it into the detection of *E. coli* in water. In the last project, a large area and high quality $MoSe_2$ nanosheets were synthesized using chemical vapor deposition, characterized, and implemented for the first time as a near-infrared (NIR) optoelectronic device for the detection of NO_2 gas. Further, we studied the doping of $MoSe_2$ crystal with Te, to form ternary $MoSe_{2(2-x)}Te_{2x}$ alloys. In addition, we synthesized

Janus in-situ prepared $MoSe_{2(2-y)}Te_{2y}/MoSe_{2(2-x)}Te_{2x}$ defect-free interface heterostructures, where $y \neq x$, and $y \geq 0$.

1.2. References

[1] K. Baryeh, S. Takalkar, M. Lund, G. Liu, Introduction to medical biosensors for point of care applications, in: Med. Biosens. Point Care Appl., Elsevier, 2017: pp. 3–25.

[2] E.O. Blair, D.K. Corrigan, A review of microfabricated electrochemical biosensors for DNA detection, Biosens. Bioelectron. 134 (2019) 57–67.

[3] J. Kim, A.S. Campbell, B.E.-F. de Ávila, J. Wang, Wearable biosensors for healthcare monitoring, Nat. Biotechnol. 37 (2019) 389–406.

[4] Z. Liao, Y. Zhang, Y. Li, Y. Miao, S. Gao, F. Lin, Y. Deng, L. Geng, Microfluidic chip coupled with optical biosensors for simultaneous detection of multiple analytes: A review, Biosens. Bioelectron. 126 (2019) 697–706.

[5] J.X.J. Zhang, K. Hoshino, Chapter 6-Mechanical transducers: Cantilevers, acoustic wave sensors, and thermal sensors, Mol. Sensors Nanodevices Princ. Des. Appl. Biomed. Eng. (2014) 321–414.

[6] L. Xu, N. Shoaei, F. Jahanpeyma, J. Zhao, M. Azimzadeh, K.T. Al, Optical, electrochemical and electrical (nano) biosensors for detection of exosomes: A comprehensive overview, Biosens. Bioelectron. (2020) 112222.

[7] A.C. Peixoto, A.F. Silva, Smart devices: Micro-and nanosensors, in: Bioinspired Mater. Med. Appl., Elsevier, 2017: pp. 297–329.

[8] C.M. Hussain, R. Keçili, Electrochemical techniques for environmental analysis, Mod. Environ. Anal. Tech. Pollut. (2020) 199–222.

[9] M.-S. Yao, W.-H. Li, G. Xu, Metal–organic frameworks and their derivatives for electrically-transduced gas sensors, Coord. Chem. Rev. 426 (2021) 213479. https://doi.org/https://doi.org/10.1016/j.ccr.2020.213479.

CHAPTER 2

Linker-Free Magnetite-Decorated Gold Nanoparticles (Fe_3O_4-Au): Synthesis, Characterization, and Application for Electrochemical Detection of Arsenic (III)

Abstract: Linker-free magnetite nanoparticles (Fe_3O_4NPs)-decorated gold nanoparticles (AuNPs) were grown using a new protocol that can be used as a new platform for synthesis of other intact metal–metal oxide nanocomposites without the need for linkers. This minimizes the distance between the metal and metal oxide nanoparticles and ensures the optimum combined effects between the two material interfaces. X-ray diffraction (XRD) and Fourier transform infrared (FTIR) spectroscopy confirmed the successful synthesis of the Fe_3O_4-Au nanocomposite, without any change in the magnetite phase. Characterization, using transmission electron microscopy (TEM), scanning electron microscopy (SEM) and energy dispersive X-ray (EDX) spectroscopy, revealed the composite to consist of AuNPs of 70±10 nm diameter decorated with tiny 10±3 nm diameter Fe_3O_4NPs in Au:Fe mass ratio of 5:1. The prepared Fe_3O_4-Au nanocomposite was embedded in ionic liquid (IL) and applied for the modification of glassy carbon electrode (GCE) for the electrochemical detection of As(III) in water. By combining the excellent catalytic properties of the AuNPs with the high adsorption capacity of the tiny Fe_3O_4NPs towards As(III), as well as the good conductivity of IL, the Fe_3O_4-Au-IL nanocomposite showed excellent performance in the square wave anodic stripping voltammetry detection of As(III). Under the optimized conditions, a linear range of 1 to 100 µg/L was achieved with a detection limit of 0.22 µg/L (S/N = 3), and no interference from 100-fold higher concentrations of a wide variety of cations and anions found in water. A very low residual standard deviation of 1.16%

confirmed the high precision/reproducibility of As(III) analysis and the reliability of the Fe_3O_4-Au-IL sensing interface. Finally, this proposed sensing interface was successfully applied to analyzing synthetic river and wastewater samples with a 95-101% recovery, demonstrating excellent accuracy, even in complex synthetic river and wastewater samples containing high concentrations of humic acid without any sample pretreatments.

2.1. Introduction

The contamination of arsenic in water is a significant concern to human health [1–3], as exposure can lead to a range of acute and chronic diseases, such as dysphasia, facial edema, dehydration, jaundice, and cancer [4–10]. Inorganic arsenic compounds, arsenite (As(III)) and arsenate (As(V)) commonly exist in the environment either due to geochemical enrichment or industrial processes. Arsenite and arsenate are more toxic than the organic forms. Arsenite, which is the most toxic, is a mobile and soluble form of arsenic [11]. Usually, the content of As(III) in water is a serious problem, because even though its concentration is very low, it is highly toxic even at trace levels and can enter the human body in different ways, causing serious health problems. The World Health Organization (WHO) has recommended an upper limit of 10 ppb for total arsenic in drinking water [11].

Different analytical strategies based on spectrometry, such as atomic fluorescence spectrometry [12], inductively coupled plasma mass spectrometry (ICP-MS) [13] and graphite furnace atomic absorption spectrometry [14] are frequently used to determine As(III) at trace levels in a variety of samples. While these techniques have high sensitivity for As(III) detection, they have limitations of high operating cost, expensive instruments,

requirement of professional operators and bulky instrumentation, which make them unsuitable for on-site routine analysis.

In contrast to these methods, electrochemical analyses, and in particular, anodic stripping voltammetry (ASV), is a low cost, low limit of detection (LOD) sensing method that has the benefit of convenient operation, high sensitivity, and the ability to perform real-time analysis [15,16]. Usually, the fabrication of an electrochemical sensor based on electrode modification can be divided into the following steps [15–18]: 1. nanocomposites synthesis and characterization; 2. electrode fabrication and pretreatment; 3. electrode modification using the synthesized nanocomposites. Electrodes of various nano-materials/particles, such as carbon nanotubes, metal oxides, noble metals (Au, Ag and Pt), and graphene, have been used for As(III) determination [15–18]. Previous reports demonstrated that AuNPs-modified electrodes could enhance the anodic current response toward As(III) more effectively than other materials relying on chemical reduction by electrogenerated H_2 [19–25]. However, these methods need strong acidic conditions to guarantee enough electrogenerated H_2 availability for electrochemical reduction of As(III) to As(0) during the electrochemical reduction/deposition step. This limits the application of Au-based materials for the detection of As(III) by non-professionals and in the field.

Recently, a number of Fe_3O_4-based materials have been synthesized for arsenic removal because of the excellent arsenic adsorption ability of Fe_3O_4 [26,27]. In addition, some studies have been performed utilizing Fe_3O_4-based materials to analyze the concentration of As(III) [28,29]. However, the poor conductivity of Fe_3O_4 has limited its sensitivity for electrochemical detection. To improve the electrode conductivity and electrocatalytic

activity, electrodes modified with Au-Fe_3O_4 nanocomposite were reported [30,31]. However, the synthesis procedures used linkers such as oleic acid, oleyl amine, or aminopropyl trimethoxy silane to attach/decorate Au nanoparticles on Fe_3O_4, required a high temperature and high-pressure autoclave for Fe_3O_4 synthesis, and were time-consuming (~24 h). The linker introduces separation between the adsorbed As(III) on magnetite and the Au nanoparticle catalyst that could potentially reduce electron transfer rate/efficiency [32]. Moreover, a large fraction of the adsorbing material surface area was covered/blocked by Au NPs.

Here, we report linker-free grown AuNPs decorated with Fe_3O_4NPs (Fe_3O_4-Au) nanocomposite using a facile, faster and green chemistry synthesis route for application in chemically modified electrode ASV detection of As (III) in water. The important differences in the nanocomposite material between this work and the literature include the morphology/architecture and synthesis method as follows. 1) There is no linker between Fe_3O_4 and Au, which minimizes the distance between the metal and metal oxide nanoparticles and ensures the optimum combined effects between the two material interfaces. 2) Nanocomposite consists of AuNPs (70 nm average diameter) decorated with very tiny (10 nm average diameter) Fe_3O_4NPs which provide a higher surface area of the adsorbent for As(III). 3) The synthesis uses a co-precipitation method that is performed at low temperature (80 ^oC) and atmospheric pressure and does not require harsh organic solvents to synthesize Fe_3O_4NPs.

The introduced material was used to modify the surface of a glassy carbon electrode (Fe_3O_4-Au-IL/GCE) and applied as a working electrode in the ASV detection of As(III).

The results exhibited a comparable or higher sensitivity than the modified electrodes reported in the literature. The combination of AuNPs, Fe_3O_4 NPs, and IL resulted in many intriguing combined effects and catalytic abilities, such as an excellent ability to adsorb As(III), high electrical conductivity and good stability. In addition, the synthesis method introduced in this work can be used as a new platform for synthesis of intact metal-Fe_3O_4 nanocomposites without the need for any linkers to achieve the optimum combined effects between the materials. Moreover, the electrode materials were characterized using different techniques (CV, SEM, EDS, XRD, TEM and EIS). Furthermore, a dual-catalysis system has been proposed for the first time to investigate and explain the catalytic mechanism behind the phenomenon. Finally, the analytical application of Fe_3O_4-Au-IL/GCE was tested for the measurement of As(III) in synthetic river water and wastewater samples.

2.2. Materials and Methods

2.2.1. Materials and Instruments

Ferrous chloride ($FeCl_2 \cdot 4H_2O$), ferric chloride ($FeCl_3 \cdot 6H_2O$), ethylene glycol (EG), ammonium hydroxide (NH_4OH, 25%), sodium citrate, sodium hydroxide (NaOH), hydrogen tetrachloroaurate ($HAuCl_4 \cdot 3H_2O$), polyvinyl alcohol (PVA), sodium acetate (CH_3COONa), ammonium acetate (CH_3COONH_4), monopotassium phosphate (KH_2PO_4), sodium bicarbonate ($NaHCO_3$), manganese sulfate ($MnSO_4$), zinc sulfate ($ZnSO_4$), magnesium sulfate ($MgSO_4$), and calcium chloride ($CaCl_2$) were purchased from Fisher Scientific (USA). Humic acid sodium salt (Technical grade) was purchased from Sigma-Aldrich. Ionic liquid ([C4dmim][NTf_2]) was obtained from IoLiTec Ionic Liquids Technologies, INC. (USA). Arsenic trioxide (As_2O_3) was purchased from Strem

Chemicals, INC. (USA). An As(III) stock solution (1 mg/mL) was prepared by dissolving As_2O_3 in the 1.0 M aqueous NaOH. Sodium acetate trihydrate was obtained from Fisher Scientific (USA) and prepared as acetate buffer solution (0.2 M) with acetic acid for the electroanalysis of As(III).

The prepared Fe_3O_4NPs (magnetite), AuNPs, and Fe_3O_4-Au were characterized by scanning electron microscopy (SEM, Zeiss 1540 XB Crossbeam scanning electron microscope.), transmission electron microscopy (TEM, FEI Tecnai12), energy dispersive X-ray spectroscopy (EDX), X-ray diffraction (XRD, PANalytical Empyrean Series 2), and Fourier transform infra-red (FTIR, Thermo Nicolet 6700) spectroscopy. Electrochemical analysis, i.e., cyclic voltammetry (CV), square wave anodic stripping voltammetry (SWASV), and electrochemical impedance spectroscopy (EIS) were performed on a CH Instrument 760Celectrochemical workstation. A three-electrode system and a 20 mL cell were used for all measurements, in which Fe_3O_4-Au-IL/GCE, Pt wire, and Ag/AgCl electrode were used as working, counter, and reference electrodes, respectively. During the deposition step, the test solution was stirred using a magnetic stir bar. The As(III) in synthetic wastewater detected by ICP-MS (PerkinElmer NexION 2000) was used to confirm the robustness of our synthesis method in complex water streams.

2.2.2. Synthesis and Modification of Fe3O4-Au-IL Nanocomposite

In this procedure, Fe_3O_4NPs were prepared using the co-precipitation method, as reported earlier [33], with some modifications. The de-ionized (DI) water and reagents used in this procedure were all de-oxygenated before use. In brief, a mixture of $FeCl_2 \cdot 4H_2O$ and $FeCl_3 \cdot 6H_2O$ (20 mg and 32 mg, respectively) was added to the solution consisting of 20

mL of DI water and 20 mL of EG. The mixed solution was heated to 60 ℃ with stirring under nitrogen purging. Ammonia solution (5%) was added dropwise to the above solution until reaching the pH of 10, and then the reaction mixture was agitated for half an hour. The obtained mixture was washed a few times with DI water by means of an external magnet to remove the excess ammonia solution and surfactant. Quantities of 10 mL of $HAuCl_4 \cdot 3H_2O$ (20 mg/mL) and 10 mL of EG were added to the obtained Fe_3O_4NPs and stirred for 2 min at 80 ℃. Then, 5 mL of sodium citrate (0.3%) was added to the Fe_3O_4-Au^{3+} solution and stirred at 80 ℃ for half an hour to obtain the Fe_3O_4-Au nanocomposite. The prepared suspension was washed with DI water by means of an external magnet to remove the excess surfactants and the free AuNPs that were not bonded to magnetite, if any. A quantity of 4 mL of Fe_3O_4-Au nanocomposite solution (1 mg/mL) was mixed with 300 μL of 0.5% ionic liquid (IL) in ethanol to obtain the Fe_3O_4-Au-IL hybrid structure. The surface of GCE was polished by 0.05 mm alumina powder before modification, and was then immersed in 1:1 HNO_3, absolute ethanol and water for sonication, separately. Subsequently, 8 μL of the Fe_3O_4-Au-IL suspension was drop-casted onto the surface of GCE and dried in oven at 60 ℃. Other electrodes were prepared the same way as described above.

2.2.3. Stripping Voltammetry Analysis of As(III)

The electrochemical measurements of SWASV were performed in a 0.2 M acetate buffer solution (pH 5.0) containing different concentrations of As(III). Unless stated otherwise, −0.9 V was used as a deposition/reduction potential for the pre-deposition of As(III) under stirring for 200 s. The stirring was stopped once the deposition step was completed. An

anodic stripping voltammogram was obtained from −0.4 to 0.3 V after an equilibration period of 10 s. The frequency, amplitude and potential step were 25 Hz, 25 mV and 5 mV, respectively. To regenerate the modified electrode before the next measurement at the end of stripping, an oxidation potential of 0.6 V was applied to the working electrode for 120 s to remove any As(0) residuals which may not be completely stripped from the electrode surface.

2.2.4. *Preparation of Water Samples*

DI water containing 150 ppm magnesium nitrate, 60 ppm ammonia chloride, 500 ppm calcium chloride, 50 ppm sodium citrate and 500 ppm potassium calcium chloride (1260 ppm total dissolved solids), simulating the chemical composition of Yamuna River in Northern India, was spiked with As(III) and tested with the developed sensor to evaluate sensor performance. To further validate the robustness of our electrode, the electrode was used to measure As(III) in synthetic wastewater, the recipe of which was modified from the literature [34] and listed in Appendix A, **Table A1**. In these experiments, a 10 mL water sample test solution composed of 9 mL simulated water and 1 mL 2 M acetate buffer (pH 5.0) was used for each measurement to ensure the pH 5.0 buffer condition with 0.2 M acetate.

2.3. Results and Discussion

In this work, we employ the concept of adsorbent-assisted stripping voltammetry analysis for sensitive detection of As(III) based on a sensing interface of AuNPs decorated with Fe_3O_4NPs (Fe_3O_4-Au). AuNPs have excellent catalytic properties and the Fe_3O_4NPs are

highly adsorptive to As (III), which makes Fe_3O_4-Au a very promising material for the stripping voltammetry analysis of As(III). Additionally, ionic liquids (IL) have high adhesiveness, conductivity, work across a wide potential window, and have been widely used in the modification of electrodes [35–40]. Incorporating IL into the nanocomposite should further enhance the sensitivity and stability of the sensing interface on the electrode surface.

The synthesis method introduced in this work can be used as a new platform for synthesis of intact metal-Fe_3O_4 nanocomposites without the need for any linkers, which minimizes the distance between the metal and metal oxide nanoparticles and ensures the optimum combined effects between the materials. In this method, EG could provide magnetite with hydroxyl groups that facilitate the chelation of Au^{3+} ions (Fe_3O_4-Au^{3+}), as illustrated in the schematic diagram of **Fig. 2.1**. In this novel platform method, sodium citrate is a mild reducing and capping agent that can reduce gold ions slowly into AuNPs [41,42], while it will not reduce $Fe^{3+/2+}$ in magnetite and hence it enables the synthesis of the Fe_3O_4-Au nanocomposite in situ without any linkers.

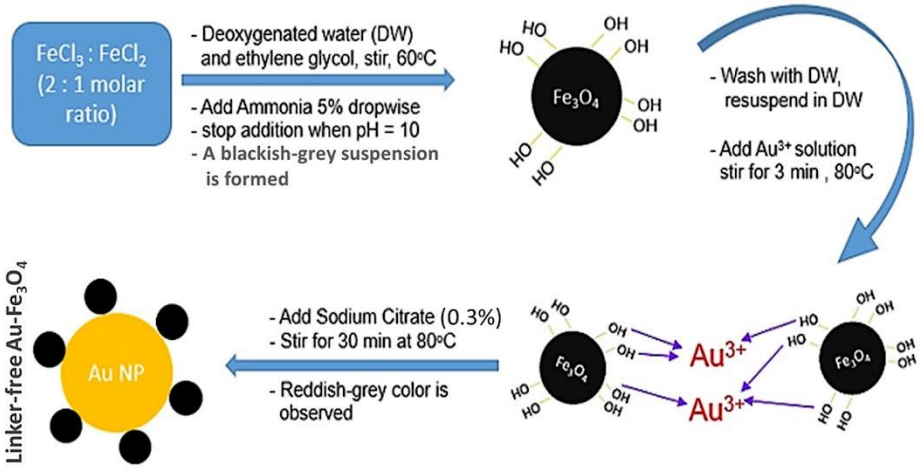

Figure 2.1. Schematic of Fe_3O_4-Au nanoparticle preparation and the suggested mechanism of its formation.

2.3.1. Physicochemical Characterization of Fe3O4-Au Nanocomposite

The introduced synthesis method is time saving (1–2 h), as the synthesis of magnetite NPs was conducted using the co-precipitation method. It is also linker-free with no barrier between gold and magnetite, which improves the electron transfer between them and enhances their combined effects. This procedure uses simple chemicals that are mostly ecofriendly, and very easy to wash using deionized water, if any excess is present. In addition, magnetite nanoparticles were prepared to be very tiny (≈10 nm) to allow for higher surface area and higher adsorption of As(III). The morphology and sizes of the prepared particles were assessed using SEM and TEM imaging as illustrated in **Fig. 2.2**. The synthesized Fe_3O_4-Au suspension was drop-casted as a thin film on a piece of silicon wafer, at the same concentration and volume used in preparing the electrode materials, and sputtered with Pd/Pt to reduce surface charging, and then imaged by SEM. The SEM image in **Fig. 2.2a** illustrates that AuNPs (the bigger and brighter particles) are surrounded by much smaller Fe_3O_4NPs. However, the Fe_3O_4NPs were not well resolved. Further imaging

of Fe_3O_4-Au by TEM (**Fig. 2.2b**) shows a 70 nm spherical core AuNP decorated with Fe_3O_4NPs, which agrees with the SEM image. The TEM image of Fe_3O_4NPs showed the particles are spherical with an average size of 10±3 nm (**Fig. 2.2 (c&d)**). The TEM images confirm the success of the proposed platform, as the AuNPs and Fe_3O_4NPs are directly bound to each other without separation between them. Furthermore, EDX spectroscopy was implemented to calculate the actual weight ratio between Au and Fe in the prepared nanocomposite. The results in Appendix A (**Fig. A1**)**,** determined that the weight ratio is approximately 5:1 (Au:Fe).

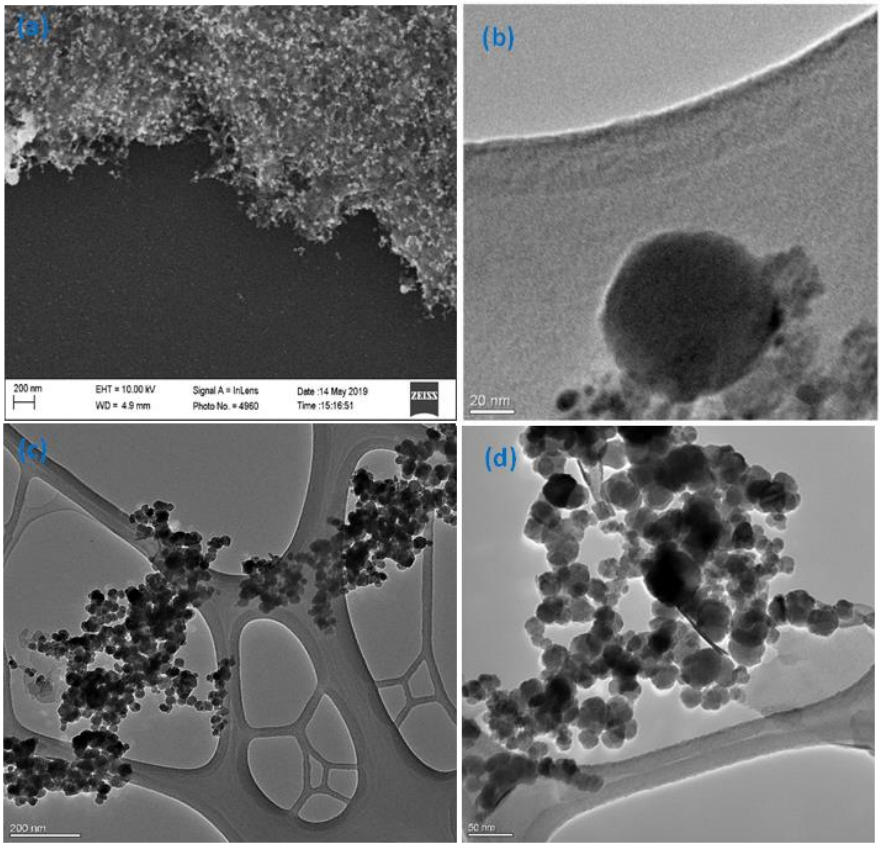

Figure 2.2. Electron microscopy images. (a) SEM image of a thin film of Fe_3O_4-Au nanocomposite on a silicon wafer sputtered with Pd/Pt, (b) a higher resolution TEM image of the prepared nanocomposite, and (c&d) TEM images of the Fe_3O_4NPs.

The results of the XRD analysis of magnetite (Fe_3O_4) NPs in **Fig. 2.3** show diffraction peaks at 30.17°, 35.53°, 43.27°, 56.96°, 62.69°, which can be assigned to the (220), (311), (400), (511), and (440) planes of the cubic inverse spinel-type structure of magnetite (PDF#85-1436) [43,44]. Moreover, the diffraction pattern of Fe_3O_4-Au has the same peaks of magnetite addressed above in addition to the characteristic peaks of the face-centered cubic (FCC) AuNPs at 38.23°, 44.54°, 64.71°, 77.69°, which can be assigned to the (111), (200), (220), and (311) planes, (Pattern 4-784) [45]. Hence, the XRD data confirm the successful synthesis of the Fe_3O_4-Au nanocomposite, without any change in the magnetite phase. Moreover, the intensity of AuNPs peaks is higher because they are in a higher concentration, which agrees with the EDS data, in which the weight ratio is around 5:1 (Au:Fe) (**Fig. A1**). FTIR spectrum analysis (**Fig. 2.4**) of Fe_3O_4NPs shows a broad peak centering at 3380 cm^{-1} and two peaks at 2900 and 2915 cm^{-1}, which are attributed to the stretching vibrations of O-H and C-H groups from EG, respectively. In addition, Fe-O vibrations show two peaks at 1380 and 565 cm^{-1}. Vibrational peaks of Fe_3O_4NPs are in a good agreement with published work [46]. On the other hand, the spectrum of AuNPs shows stretching vibrations of O-H groups of PVA at 3320 cm^{-1}, vibrations of C=O groups of sodium citrate at 1730 cm^{-1} and stretching vibrations of C-H groups at 2900 and 2915 cm^{-1}. The FTIR spectrum of Fe_3O_4-Au contains all the peaks from both spectra of Au and Fe_3O_4, which confirms the successful synthesis of this nanocomposite.

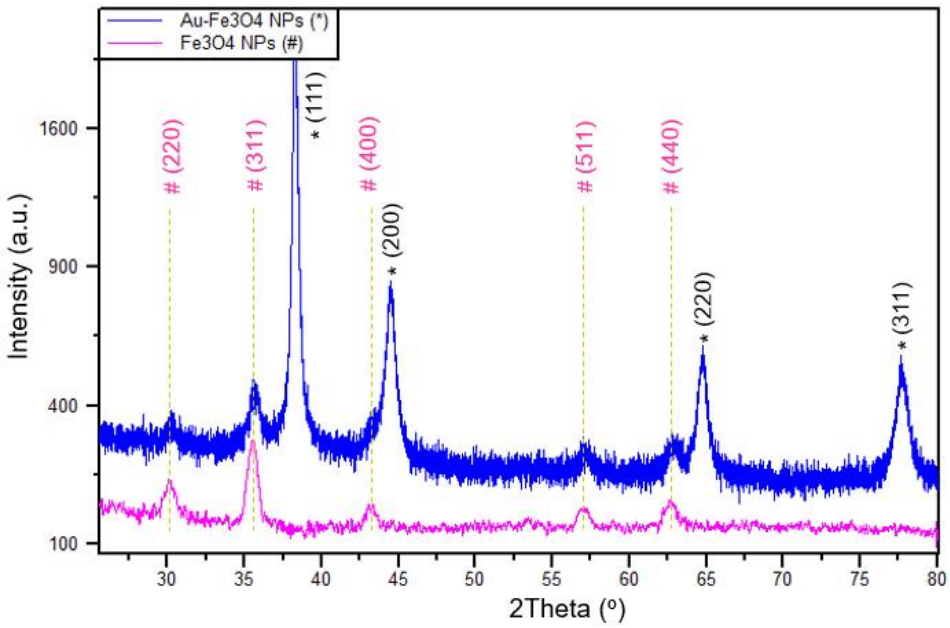

Figure 2.3. XRD patterns of Fe_3O_4NPs and Fe_3O_4-Au.

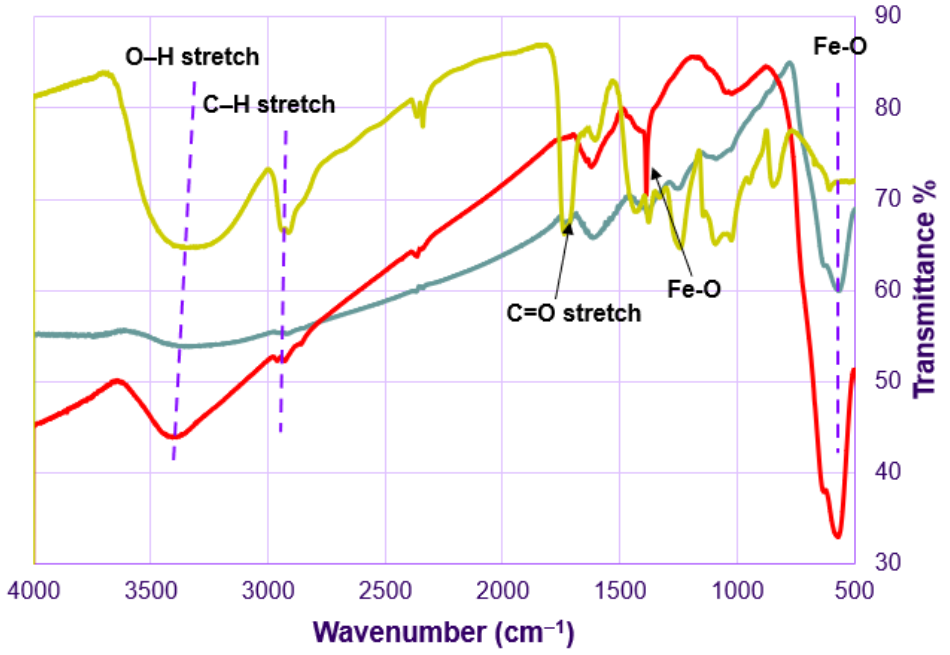

Figure 2.4. FTIR spectra of Fe_3O_4 (red), Au (yellow), and Fe_3O_4-Au (blue).

2.3.2. Electrochemical Characterizations of Modified Electrodes

The electrochemical characteristics of bare GCE and different modified GCEs, i.e., Fe_3O_4NPs/GCE, Fe_3O_4-Au/GCE, and Fe_3O_4-Au-IL/GCE were investigated using CV based on a ferri/ferrocyanide $[Fe(CN)_6]^{3-/4-}$ redox probe (Appendix A, **Fig. A2a**). On the bare GCE, two well-defined redox peaks of $[Fe(CN)_6]^{3-/4-}$ were found in curve a. When compared to the bare GCE, Fe_3O_4NPs/GCE showed a decreased redox current of $[Fe(CN)_6]^{3-/4-}$, because of the poor conductivity of Fe_3O_4. However, stronger redox peaks were found with the Fe_3O_4-Au/GCE (curve c) compared to the Fe_3O_4NPs/GCE, due to the excellent electrical conductivity of the AuNPs. Furthermore, the addition of IL to the nanocomposite, i.e., Fe_3O_4-Au-IL/GCE, increased its conductivity and resulted in stronger redox peaks.

EIS was used to explore the material/electrode interface properties and changes based on the impedance changes (Appendix A, **Fig. A2b**). The EIS results show different semicircles, each with a diameter equivalent to the charge transfer resistance (R_{ct}), which corresponds to the process of electron transfer limitation [47–49]. Based on the value of semicircle diameter, the order of the R_{ct} of different modified electrodes was as follows: Fe_3O_4/GCE (curve b) > Fe_3O_4-Au/GCE (curve c) > Fe_3O_4-Au-IL/GCE > bare GCE (curve a). The EIS results are consistent with those of CV.

2.3.3. Optimization of Analysis Parameters

Deposition potential and deposition time play a key role in the SWASV sensitivity (stripping peak current/concentration) of heavy metals detection. Additionally, Fe_3O_4NPs and AuNPs play a unique role in the dual-catalytic system for the SWASV detection of

As(III). Therefore, in this study, responses of Fe_3O_4-Au-IL/GCE toward As(III) were investigated to find optimal values of deposition potential, deposition time and the mass ratio of Fe_3O_4 to AuNPs. **Fig. 2.5a** shows the influence of deposition potential on the stripping peak current of 20 ppb As(III) for 200 s deposition time and Fe:Au of 1:5. As shown in the figure, the stripping peak current increased with an increase of deposition potential reaching a maximum at -0.9 V followed by a small decrease at deposition potential above -0.9 V. The lower currents at potentials below -0.9 V are ascribed to incomplete reduction of As(III). On the other hand, the small decrease in current at deposition potentials above -0.9 V are the result of hydrogen evolution. Thus, the deposition potential of -0.9 V was chosen for As(III) preconcentration.

The effect of deposition time on the peak current of 20 ppb As(III) at -0.9 V deposition potential and Fe:Au of 1:5 is shown in the **Fig. 2.5b**. The results show a monotonic increase in peak current as a function of deposition time. The direct relation between the current and deposition time suggests a lower LOD could be expected by increasing the deposition time. However, as a longer deposition time implies a longer analysis time, we selected a 200 s deposition period.

Different mass ratios of AuNPs to Fe_3O_4NPs in Fe_3O_4-Au composite on the stripping peak current of 50 ppb As(III) at -0.9 V deposition potential and 200 s deposition time were examined (**Fig. 2.5c**). The results show an increase in the stripping peak current from 1.8 μA to ~6.6 μA when the Fe_3O_4-Au composite contained 10 to 16.3% (by mass) of Fe followed by a rapid drop to ~0.3 μA for 100% Fe (i.e., Fe_3O_4NPs only). This indicates a clear complementarity relationship between the two components of the nanocomposite in

enhancing the sensitivity of the sensor for As(III) detection. It is interesting that although Fe_3O_4NPs have a strong adsorption capacity for the As(III), the response on Fe_3O_4NPs/GCE was the smallest. That may be ascribed to the poor conductivity of Fe_3O_4NPs, which affects both reduction of As(III) to As(0) and the oxidation of As(0) to As(III) on the electrode surface. Additionally, while the stripping response on AuNPs/GCE was higher than Fe_3O_4NPs/GCE, it was lower than Fe_3O_4-Au/GCE at different Fe mass ratios. This may be attributed to the combined effect of the strong adsorption capacity of Fe_3O_4 and good conductivity and catalytic ability of AuNPs. Based on cost and maximum sensitivity, Fe_3O_4-Au nanocomposite containing 16.3% (by mass) Fe was selected as the optimum composition.

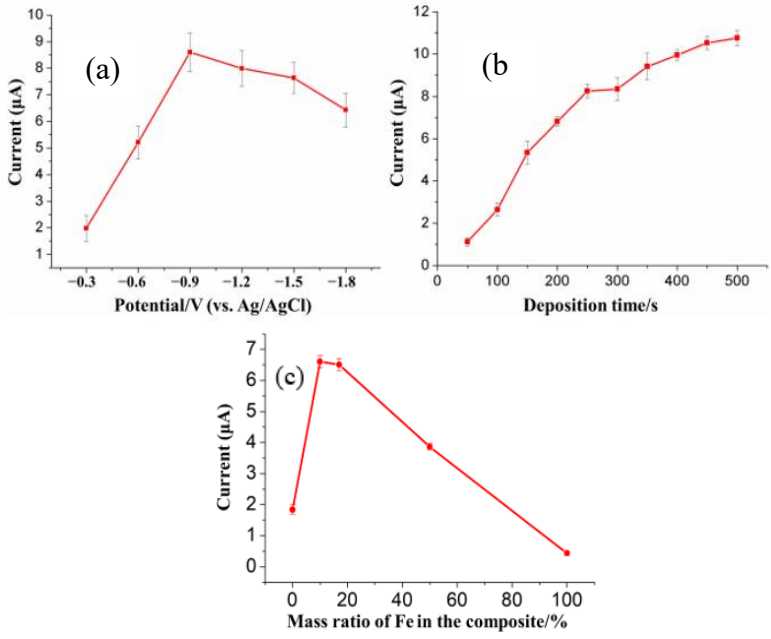

Figure 2.5. (a) Effect of the deposition potential, (b) deposition time and (c) weight ratio between Fe and Au on stripping current for 20 ppb (a and b) and 50 ppb (c) of As(III) in 0.2 M pH 5.5 acetate buffer at Fe_3O_4-Au-IL/GCE. Each data point is an average of 5 measurements from 3 electrodes and error bars represent ±1 standard deviation.

2.3.4. Analytical Characteristics of Fe3O4-Au-IL/GCE for As(III)

The stripping responses of 50 μg/L As(III) on bare GCE and different modified electrodes are shown in **Fig. 2.6**. As shown in **Fig. 2.6a**, almost no stripping response was obtained on the bare GCE. The stripping response of As(III) on Fe_3O_4NPs/GCE was not significant either, due to the poor conductivity of Fe_3O_4NPs. In contrast, at the Fe_3O_4-Au/GCE, a higher stripping peak signal was obtained due to the combined effect of Fe_3O_4NPs and AuNPs, which can be ascribed to the dual-catalysis system (**Fig. 2.6b**). H_2 was electrogenerated on the AuNP decorated with Fe_3O_4NPs at the applied negative potential during the electrodeposition step. The generated H_2 then donates electrons in the reduction of As(III) to As(0), and forms H^+ ions. Due to the strong adsorption capacity of Fe_3O_4NPs, As(III) concentration near the electrode surface gradually increased, which enhanced the catalytic efficiency of H_2 on the As(III) adsorbed to Fe_3O_4NPs even at a high pH condition (the first catalytic system). Furthermore, the surface-activated Fe(II) can also donate an electron to form Fe(III), which helps reduce As(III). The produced Fe(III) will then acquire an electron, to revert to Fe(II), from either the electrode or the oxidation of As(0) to As(III) during the stripping process of SWASV. The procedure described above is a complete Fe(II)/Fe(III) cycle. During this process, the electron transfer between electrode and As(III) was mediated by Fe(II), which was used as an electrocatalyst (the second catalytic system). This mediation of the Fe(II)/Fe(III) cycle together with the catalysis of AuNPs will efficiently promote the deposition of As(III) and further enhance the sensitivity toward the electrochemical detection of As(III) [23,50]. Additionally, the stripping peak current was

further improved with Fe_3O_4-Au-IL/GCE due to the good conductivity and adhesiveness of IL.

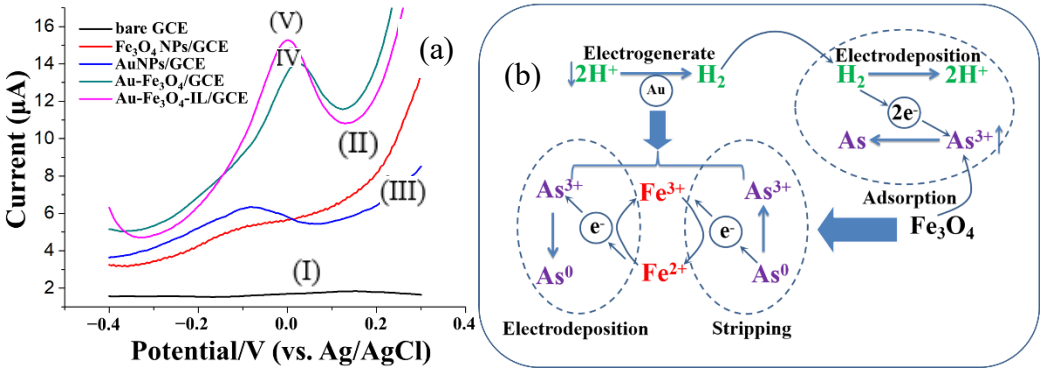

Figure 2.6. (a) The SWASV responses of 50 µg/L As(III) on different modified electrodes; (I) bare GCE, (II) Fe_3O_4NPs/GCE, (III) AuNPs/GCE, (IV) Fe_3O_4-Au/GCE and (V) Fe_3O_4-Au-IL/GCE. (b) The catalytic mechanism of Fe_3O_4-Au in the electroanalysis of As(III). Glassy carbon electrode (GCE); ionic liquid (IL).

2.3.4.1. Sensitivity, Limit of Detection, and Reproducibility

The Fe_3O_4-Au-IL/GCE operating at optimal Fe:Au mass ratio, deposition potential, and deposition time determined above, was applied to analyze 0 to 100 ppb of As (III) in 0.2 M pH 5 acetate buffer (**Fig. 2.7**). The results show well-defined Gaussian shaped response with peak current around 0 V which increased with increasing As(III) concentration (**Fig. 2.7a**). As illustrated in **Fig. 2.7b**, the peak stripping current, i.e., response, was linearly related to As(III) concentration over the complete concentration range of 0 to 100 ppb. The sensitivity (the slope of the calibration plot) was 0.122 mA/ppb As(III) and the LOD (calculated based on S/N = 3) was 0.22 ppb. The high sensitivity and low LOD is credited to the combined effects of excellent absorption ability for As(III), high electrical

conductivity and good stability of AuNPs, Fe_3O_4 NPs and IL. Appendix A, **Table A2** shows a comparison of this work to the previous literature in terms of electrode material, technique, linear range, and limit of detection.

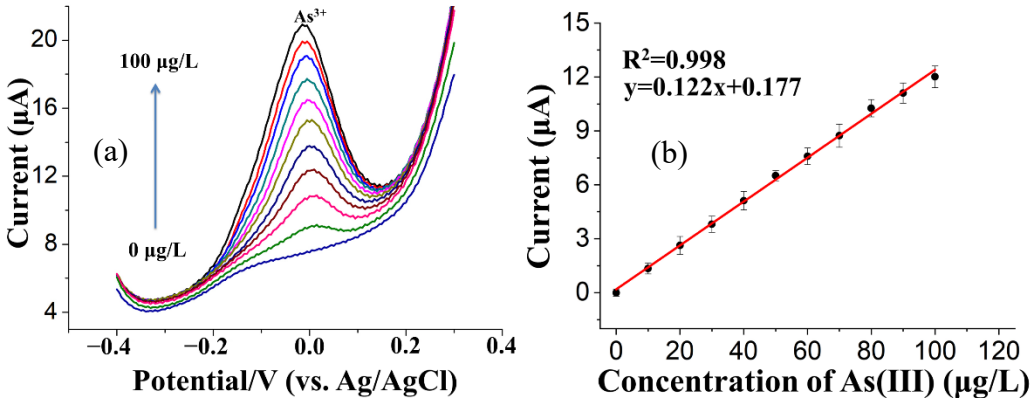

Figure 2.7. (a) SWAS voltammograms for additions of 0, 10, 20, 30, 40, 50, 60, 70, 80, 90 and 100 µg/L As(III). (b) The corresponding calibration curve of As(III).

Furthermore, the developed sensor demonstrated excellent reproducibility as evidenced by a very low (1.16%) relative standard deviation (RSD) for five repetitive measurements of 60 ppb As(III) (Appendix A, **Fig. A3**).

2.3.4.2. Selectivity

Water sources contain a plethora of anions and cations that can potentially have a negative influence on the SWASV detection accuracy of As(III). We investigated the selectivity of the proposed sensor based on the analysis of 50 ppb of As(III) from 100-fold higher concentrations of Na^+, K^+, Ca^{2+}, Zn^{2+}, Mg^{2+}, Mn^{2+} and Fe^{2+}, and a 150-fold higher concentrations of Cl^-, NO_3^-, SO_4^{2-}, CO_3^{2-}, F^- and PO_4^{2-}. As shown in **Fig. 2.8**, there were

no measurable changes in the peak current signals (current variation < ± 10%) in the presence of all the tested ions, confirming the proposed Fe_3O_4-Au-IL/GCE is efficient in the detection of As(III) in the presence of non-target species in water.

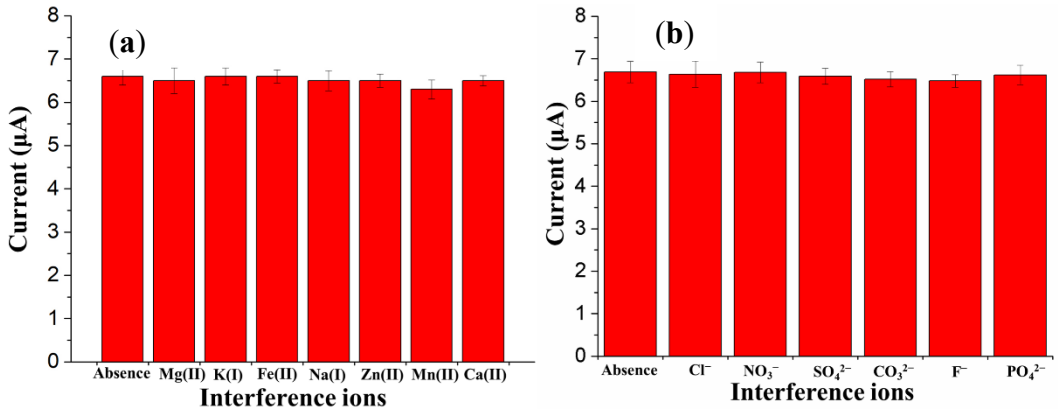

Figure 2.8. The selectivity of the proposed sensor in the presence of high concentrations of different ions (a: Cation; b: Anion) on the stripping peak current of 50 μg/L As(III) at Fe_3O_4-Au-IL/GCE in 0.2 M acetate buffer (pH 5.0). Each data point is an average of 5 measurements from 3 electrodes and error bars represent ±1 standard deviation.

2.3.5. Analysis of Simulated Water Samples

To evaluate the applicability of Fe_3O_4-Au-IL/GCE for practical application, the sensor was applied to detect 5, 10 and 15 ppb of As(III) spiked in simulated river water representing the chemical composition of Yamuna River water in Northern India. Yamuna River is one of the most polluted rivers in India, and perhaps the world, with a complex matrix of pollutants [51,52]. As shown in **Table 2.1**, the recoveries (i.e., agreement) ranged from 97.2% to 101.3% (average of 99.06%) and the RSD ranged from 3.3% to 4.8% (average 3.9%). The excellent recoveries and low RSD demonstrate the promise of the developed sensor for monitoring As(III) in real environmental samples. To further validate Fe_3O_4-Au-IL/GCE's robustness in complex wastewater streams, we used the sensor to detect As(III) in synthetic wastewater samples containing high concentrations of humic acid (50 mg/L),

and compared it with values measured using ICP-MS. The Fe_3O_4-Au-IL/GCE sensor successfully determined As(III) concentrations, which were comparable to the results generated by ICP-MS (i.e., 95.4% ±4.7%) indicating that Fe_3O_4-Au-IL/GCE is a robust electrode for detecting As(III) in complex water streams.

Table 2.1. Detection of As(III) in simulated river water.

Sample no.	Found[a] (µg/L)	Added (µg/L)	Detected after adding[a] (µg/L)	Mean recovery (%)	RSD (%)
1	3.12±1.08	5	7.98±1.23	97.2	4.8
2	4.89±0.89	10	15.02±1.15	101.3	3.3
3	9.95±0.96	15	24.75±0.90	98.67	3.6

[a] Mean value ± Standard Deviation. Each data point is an average ±1 standard deviation from 3 measurements using 3 electrodes.

2.4. Conclusions

In this work, an effective sensitive interface was designed using AuNPs decorated with Fe_3O_4NPs embedded in IL for the determination of As(III) at a trace level based on adsorbent-assisted in-situ electrocatalysis. The procedure for Fe_3O_4-Au synthesis introduced in this work 1) produced very tiny (≈10 nm) Fe_3O_4NPs enhancing the surface area for As(III) adsorption, 2) did not use a linker between gold and magnetite, which enhanced their combined effects, 3) is a green chemistry approach and 4) greatly reduced synthesis time (1–2 h). The proposed Fe_3O_4-Au-IL/GCE significantly enhanced the stripping response of As(III) as compared with the Fe_3O_4/GCE and AuNPs/GCE, as it

provided a specific interface for As(III) to transfer electrons. Additionally, a Fe(II)/Fe(III) cycle and electrogenerated H_2 were activated to catalyze the reduction/stripping of the As(III)/As(0), which enabled a high sensitivity. The presence of IL in the composite contributed to better sensitivity and stability. The analytical, spectroscopic and microscopic features of the proposed Fe_3O_4-Au-IL/GCE characterization by XRD, EDX, TEM, SEM, EIS SWASV, and CV showed that the combined effect of AuNPs, Fe_3O_4 and IL resulted in a much better electrical conductivity, larger specific surface area and higher catalytic ability than the bare electrode. Moreover, several synthetic water samples were tested to further verify the practicability of the proposed platform. The results showed that Fe_3O_4-Au-IL/GCE can be successfully applied to the analysis of As(III) in synthetic river and wastewater samples without any sample pretreatment procedures, which suggested that it could be further applied to heavy metal analysis in real samples.

2.5. References

1. Rodríguez-Lado, L.; Sun, G.; Berg, M.; Zhang, Q.; Xue, H.; Zheng, Q.; Johnson, C.A. Groundwater arsenic contamination throughout China. *Science* **2013**, *341*, 866–868.

2. Smith, A.; Lopipero, P.; Chung, J.; Haque, R.; Hernandez, A.; Moore, L.; Steinmaus, C. Arsenic in drinking water and cancer risks estimated from epidemiological studies in Argentina, Chile, Taiwan and Japan. *Epidemiology* **2000**, *11*, S93.

3. Ning, Z.; Lobdell, D.T.; Kwok, R.K.; Liu, Z.; Zhang, S.; Ma, C.; Riediker, M.; Mumford, J.L. Residential exposure to drinking water arsenic in Inner Mongolia, China. *Toxicol. Appl. Pharmacol.* **2007**, *222*, 351–356.

4. Feeney, R.; Kounaves, S.P. On-site analysis of arsenic in groundwater using a microfabricated gold ultramicroelectrode array. *Anal. Chem.* **2000**, *72*, 2222–2228.

5. Tchounwou, P.B.; Patlolla, A.K.; Centeno, J.A. Invited reviews: Carcinogenic and systemic health effects associated with arsenic exposure—A critical review. *Toxicol. Pathol.* **2003**, *31*, 575–588.

6. Shi, H.; Shi, X.; Liu, K.J. Oxidative mechanism of arsenic toxicity and carcinogenesis. *Mol. Cell. Biochem.* **2004**, *255*, 67–78.

7. Melamed, D. Monitoring arsenic in the environment: A review of science and technologies with the potential for field measurements. *Anal. Chim. Acta* **2005**, *532*, 1–13.

8. Rahman, M.R.; Okajima, T.; Ohsaka, T. Selective detection of As (III) at the Au (111)-like polycrystalline gold electrode. *Anal. Chem.* **2010**, *82*, 9169–9176.

9. Mays, D.E.; Hussam, A. Voltammetric methods for determination and speciation of inorganic arsenic in the environment—A review. *Anal. Chim. Acta* **2009**, *646*, 6–16.

10. Sengupta, M.K.; Sawalha, M.F.; Ohira, S.-I.; Idowu, A.D.; Dasgupta, P.K. Green analyzer for the measurement of total arsenic in drinking water: Electrochemical reduction of arsenate to arsine and gas phase chemiluminescence with ozone. *Anal. Chem.* **2010**, *82*, 3467–3473.

11. Zaib, M.; Athar, M.M.; Saeed, A.; Farooq, U. Electrochemical determination of inorganic mercury and arsenic—A review. *Biosens. Bioelectron.* **2015**, *74*, 895–908.

12. Cai, Y. Speciation and analysis of mercury, arsenic, and selenium by atomic fluorescence spectrometry. *TrAC Trends Anal. Chem.* **2000**, *19*, 62–66.

13. Álvarez-Llamas, G.; del Rosario Fernández de laCampa, M.; Sanz-Medel, A. ICP-MS for specific detection in capillary electrophoresis. *TrAC Trends Anal. Chem.* **2005**, *24*, 28–36.

14. Zhang, N.; Fu, N.; Fang, Z.; Feng, Y.; Ke, L. Simultaneous multi-channel hydride generation atomic fluorescence spectrometry determination of arsenic, bismuth, tellurium and selenium in tea leaves. *Food Chem.* **2011**, *124*, 1185–1188.

15. Barek, J.; Peckova, K.; Vyskocil, V. Adsorptive stripping voltammetry of environmental carcinogens. *Curr. Anal. Chem.* **2008**, *4*, 242–249.

16. Alves, G.M.S.; Magalhães, J.M.C.S.; Salaün, P.; Van den Berg, C.M.G.; Soares, H.M.V.M. Simultaneous electrochemical determination of arsenic, copper, lead and mercury in unpolluted fresh waters using a vibrating gold microwire electrode. *Anal. Chim. Acta* **2011**, *703*, 1–7.

17. Castaneda, M.T.; Merkoçi, A.; Pumera, M.; Alegret, S. Electrochemical genosensors for biomedical applications based on gold nanoparticles. *Biosens. Bioelectron.* **2007**, *22*, 1961–1967.

18. Martínez-Paredes, G.; González-García, M.B.; Costa-García, A. Lead sensor using gold nanostructured screen-printed carbon electrodes as transducers. *Electroanal. Int. J. Devoted Fundam. Pract. Asp. Electroanal.* **2009**, *21*, 925–930.

19. Anker, J.N.; Hall, W.P.; Lyandres, O.; Shah, N.C.; Zhao, J.; Van Duyne, R.P. Biosensing with plasmonic nanosensors. Nanoscience and technology: A collection of reviews from nature journals. *World Sci.* **2010**, 308–319.

20. Huang, J.; Chen, H. Heat-assisted electrodissolution of platinum in an ionic liquid. *Angew. Chem.* **2012**, *124*, 1716–1720.

21. Sasaki, K.; Naohara, H.; Cai, Y.; Choi, Y.M.; Liu, P.; Vukmirovic, M.B.; Wang, J.X.; Adzic, R.R. Core-protected platinum monolayer shell high-stability electrocatalysts for fuel-cell cathodes. *Angew. Chem.* **2010**, *122*, 8784–8789.

22. Guo, S.; Wang, E. Noble metal nanomaterials: Controllable synthesis and application in fuel cells and analytical sensors. *Nano Today* **2011**, *6*, 240–264.

23. Bu, L.; Gu, T.; Ma, Y.; Chen, C.; Tan, Y.; Xie, Q.; Yao, S. Enhanced cathodic preconcentration of As (0) at Au and Pt electrodes for anodic stripping voltammetry analysis of As (III) and As (V). *J. Phys. Chem. C* **2015**, *119*, 11400–11409.

24. Majid, E.; Hrapovic, S.; Liu, Y.; Male, K.B.; Luong, J.H.T. Electrochemical determination of arsenite using a gold nanoparticle modified glassy carbon electrode and flow analysis. *Anal. Chem.* **2006**, *78*, 762–769.

25. Pungjunun, K.; Chaiyo, S.; Jantrahong, I.; Nantaphol, S.; Siangproh, W.; Chailapakul, O. Anodic stripping voltammetric determination of total arsenic using a gold nanoparticle-modified boron-doped diamond electrode on a paper-based device. *Microchim. Acta* **2018**, *185*, 324.

26. Hokkanen, S.; Repo, E.; Lou, S.; Sillanpää, M. Removal of arsenic (V) by magnetic nanoparticle activated microfibrillated cellulose. *Chem. Eng. J.* **2015**, *260*, 886–894.

27. Chandra, V.; Park, J.; Chun, Y.; Lee, J.W.; Hwang, I.-C.; Kim, K.S. Water-dispersible magnetite-reduced graphene oxide composites for arsenic removal. *ACS Nano* **2010**, *4*, 3979–3986.

28. Xie, Z.; Xu, J.; Xie, F.; Xiong, S. Electrochemical detection of As (III) by a rGO/Fe_3O_4-modified screen-printed carbon electrode. *Anal. Sci.* **2016**, *32*, 1053–1058.

29. Devi, P.; Sharma, C.; Kumar, P.; Kumar, M.; Bansod, B.K.S.; Nayak, M.K.; Singla, M.L. Selective electrochemical sensing for arsenite using rGO/Fe_3O_4 nanocomposites. *J. Hazard. Mater.* **2017**, *322*, 85–94.

30. Wei, J.; Li, S.-S.; Guo, Z.; Chen, X.; Liu, J.-H.; Huang, X.-J. Adsorbent assisted in situ electrocatalysis: An ultra-sensitive detection of As (III) in water at Fe_3O_4 nanosphere densely decorated with Au nanoparticles. *Anal. Chem.* **2016**, *88*, 1154–1161.

31. Li, S.-S.; Zhou, W.-Y.; Jiang, M.; Guo, Z.; Liu, J.-H.; Zhang, L.; Huang, X.-J. Surface Fe (II)/Fe (III) cycle promoted ultra-highly sensitive electrochemical sensing of arsenic (III) with dumbbell-like Au/Fe_3O_4 nanoparticles. *Anal. Chem.* **2018**, *90*, 4569–4577.

32. Hassan, Y.; Chuang, C.-H.; Kobayashi, Y.; Coombs, N.; Gorantla, S.; Botton, G.A.; Winnik, M.A.; Burda, C.; Scholes, G.D. Synthesis and optical properties of linker-free TiO_2/CdSe nanorods. *J. Phys. Chem. C* **2014**, *118*, 3347–3358.

33. Sedki, M.; Khalil, I.A.; El-Sherbiny, I.M. Hybrid nanocarrier system for guiding and augmenting simvastatin cytotoxic activity against prostate cancer. *Artif. Cells Nanomed. Biotechnol.* **2018**, *46*, S641–S650.

34. Yoo, H.; Ahn, K.-H.; Lee, H.-J.; Lee, K.-H.; Kwak, Y.-J.; Song, K.-G. Nitrogen removal from synthetic wastewater by simultaneous nitrification and denitrification (SND) via nitrite in an intermittently-aerated reactor. *Water Res.* **1999**, *33*, 145–154.

35. Wei, D.; Ivaska, A. Applications of ionic liquids in electrochemical sensors. *Anal. Chim. Acta* **2008**, *607*, 126–135.

36. Pandey, S. Analytical applications of room-temperature ionic liquids: A review of recent efforts. *Anal. Chim. Acta* **2006**, *556*, 38–45.

37. Rozniecka, E.; Shul, G.; Sirieix-Plenet, J.; Gaillon, L.; Opallo, M. Electroactive ceramic carbon electrode modified with ionic liquid. *Electrochem. Commun.* **2005**, *7*, 299–304.

38. Khani, H.; Rofouei, M.K.; Arab, P.; Gupta, V.K.; Vafaei, Z. Multi-walled carbon nanotubes-ionic liquid-carbon paste electrode as a super selectivity sensor: Application to potentiometric monitoring of mercury ion (II). *J. Hazard. Mater.* **2010**, *183*, 402–409.

39. Xiong, S.-Q.; Wei, Y.; Guo, Z.; Chen, X.; Wang, J.; Liu, J.-H.; Huang, X.-J. Toward membrane-free amperometric gas sensors: An ionic liquid–nanoparticle composite approach. *J. Phys. Chem. C* **2011**, *115*, 17471–17478.

40. Huang, X.-J.; Aldous, L.; O'Mahony, A.M.; del Campo, F.J.; Compton, R.G. Toward membrane-free amperometric gas sensors: A microelectrode array approach. *Anal. Chem.* **2010**, *82*, 5238–5245.

41. Das, R.S.; Singh, B.; Mukhopadhyay, S.; Banerjee, R. Gold nano particles catalyzed oxidation of hydrazine by a metallo-superoxide complex: Experimental evidences for surface activity of gold nano particles. *Dalt. Trans.* **2012**, *41*, 4641–4648.

42. Olesiak-Banska, J.; Gordel, M.; Kolkowski, R.; Matczyszyn, K.; Samoc, M. Third-order nonlinear optical properties of colloidal gold nanorods. *J. Phys. Chem. C* **2012**, *116*, 13731–13737.

43. Li, Y.; Yang, S.; Lu, X.; Duan, W.; Moriga, T. Synthesis and evaluation of the SERS effect of Fe_3O_4–Ag Janus composite materials for separable, highly sensitive substrates. *RSC Adv.* **2019**, *9*, 2877–2884.

44. Márquez, F.; Herrera, G.M.; Campo, T.; Cotto, M.; Ducongé, J.; Sanz, J.M.; Elizalde, E.; Perales, Ó.; Morant, C. Preparation of hollow magnetite microspheres and their applications as drugs carriers. *Nanoscale Res. Lett.* **2012**, *7*, 210.

45. Krishnamurthy, S.; Esterle, A.; Sharma, N.C.; Sahi, S. V Yucca-derived synthesis of gold nanomaterial and their catalytic potential. *Nanoscale Res. Lett.* **2014**, *9*, 627.

46. Quy, D. Van; Hieu, N.M.; Tra, P.T.; Nam, N.H.; Hai, N.H.; Thai Son, N.; Nghia, P.T.; Anh, N.T. Van; Hong, T.T.; Luong, N.H. Synthesis of silica-coated magnetic nanoparticles and application in the detection of pathogenic viruses. *J. Nanomater.* **2013**, *2013*, doi:10.1155/2013/603940.

47. Adams, D.M.; Brus, L.; Chidsey, C.E.D.; Creager, S.; Creutz, C.; Kagan, C.R.; Kamat, P.V.; Lieberman, M.; Lindsay, S.; Marcus, R.A. Charge transfer on the nanoscale: Current status. *J. Phys. Chem. B* **2003**, *107*, 6668–6697.

48. Sedki, M.; Chen, X.; Chen, C.; Ge, X.; Mulchandani, A. Non-lytic M13 phage-based highly sensitive impedimetric cytosensor for detection of coliforms. *Biosens. Bioelectron.* **2020**, *148*, 111794.

49. Zhao, G.; Sedki, M.; Ma, S.; Villarreal, C.; Mulchandani, A.; Jassby, D. Bismuth subcarbonate decorated reduced graphene oxide nanocomposite for the sensitive stripping voltammetry analysis of Pb(II) and Cd(II) in water. *Sensors* **2020**, *20*, 6085.

50. Renock, D.; Voorhis, J. Electrochemical investigation of arsenic redox processes on pyrite. *Environ. Sci. Technol.* **2017**, *51*, 3733–3741.

51. Misra, A.K. A river about to die: Yamuna. *J. Water Resour. Prot.* **2010**, *2*, 489.

52. Malik, D.; Singh, S.; Thakur, J.; Singh, R.K.; Kaur, A.; Nijhawan, S. Heavy metal pollution of the Yamuna River: An introspection. *Int. J. Curr. Microbiol. Appl. Sci.* **2014**, *3*, 856–863.

CHAPTER 3

Non-lytic M13 Phage-Based Highly Sensitive Impedimetric Cytosensor for Detection of Coliforms

Abstract: A highly sensitive and selective non-lytic *M13* phage-based electrochemical impedance spectroscopy (EIS) cytosensor for early detection of coliforms is introduced for the first time. AuNPs were electrochemically deposited on the surface of glassy carbon electrode, and the M13 phage particles were immobilized on them using 3-mercaptopropanoic acid linker and zero-length crosslinkers (EDC/NHS). Next, the sensor surface was blocked to avoid non-specific binding. The M13-EIS cytosensor was tested for detection of F^+ pili *Escherichia coli species*, using *XL1-Blue* and *K12* strains, as examples of coliforms. The selectivity against non-host strains was demonstrated using *Pseudomonas Chlororaphis*. The binding of *E. coli* to the *M13* phage on the cytosensor surface increased the charge transfer resistance, enabling detection of coliforms. The biosensor achieved a limit of detection (LOD) of 14 CFU/mL, the lowest reported to-date using EIS-phage sensors and exhibited a high selectivity towards the tested coliforms. The SEM micrographs confirmed the successful capturing of *E. coli* on the M13-based EIS cytosensor. Moreover, the sensor showed almost the same sensitivity in the simulated river water samples as in phosphate buffer, reflecting its applicability to real samples. On the other hand, this sensor system exhibited high stability at harsh environmental conditions of pH (3.0-10.0) and temperature as high as 45 ^oC for up to two weeks. Overall, this sensor system has excellent potential for real field detection of fecal coliforms.

3.1. Introduction

Bacterial infectious diseases remain one of the main causes of morbidity and mortality worldwide. Around 250 million people, per year, are affected by pathogenic infections, of which around 8% are mortal [53]. Although there is a progress in declining the number of deaths caused by bacterial infections, it is only by 1%. Fecal coliform contamination in aquatic environments is a serious problem, caused mainly by the presence of human or animal fecal material in water [54]. Fecal coliforms cause diarrhea, but they are not highly pathogenic by their nature. However, large number of fecal coliforms in water indicate the higher risk of the presence of other pathogens in water, causing severe infections, including dysentery, typhoid fever, ear infections, hepatitis A, etc. *Escherichia coli* is considered the main indicator of fecal contaminations used in the water quality testing [55–57].

The currently available diagnostic tools for coliform use complex and time-consuming microbiological assays such as selective growth, cell counting, microscopic examination, etc. (Spiegelman et al., 2005; Keer and Birch, 2003). Moreover, the results from these techniques are also hard to interpret and need expertise. Other contemporary techniques such ELISA [60] and PCR [61] are used with high sensitivity for detection of microbes. However, they are also expensive and time-consuming [62,63].

Recently, microbial electrochemical sensors (MESs) were introduced as accurate, real-time and highly sensitive systems for early detection of microbes, assessment of cell viability, and understanding the biochemical pathways and mechanisms [64–67]. Electrochemical biosensors attract great deal of attention because they are fast and highly sensitive [68–71]. Electrochemical impedance spectroscopy (EIS) is an effective tool to rapidly and

sensitively monitor the minute changes at the electrode interface. Moreover, EIS is a nondestructive technique due to the small amplitude perturbation [72]. Therefore, the label-free electrochemical impedance cytosensors have been increasingly explored for clinical diagnosis.

The specificity of a biosensor for a specific detection of a target bacteria/microorganism greatly depends on the type of the biorecognition element. In this regard, aptamers, peptides, and antibodies possess high selectivity. However, they are highly sensitive to the environmental conditions and susceptible to damage or loss of binding activity in harsh conditions (Zhou et al., 2017). On the other hand, bacteriophages, or shortly phages, are viruses that bind very strongly and specifically to target bacteria (Chen et al., 2015b; Soper et al., 2002; Zhou et al., 2017). Phages have many advantages that entitle them to be heavily used as biorecognition elements [77]. Phages are inexpensive and easy to prepare and purify, stable against harsh conditions of organic solvents and high temperature [77–81]. Moreover, phages are easy to immobilize on sensor surface due to their functional groups [78].

The phage recognizes its host bacterium through binding to specific receptors on the bacterial surface. Upon attachment, the phage penetrates the bacterial cell membrane, injects its genetic material (DNA/RNA) that initiates protein synthesis, replication and phage assembly inside the bacterium [82]. The phages then exit bacterial cell by different mechanisms depending on the type of the phage; either by cell lysis (lytic phages), such as T4 & T7 phages, or by extrusion without killing the host cell (non-lytic phage), for example M13 phage [83].

Zhou et al. used T2 bacteriophage-based biosensor for electrochemical detection of *E. coli* B, with a limit of detection of 10^3 CFU/mL (Zhou et al., 2017). The sensor's first response was an increase in impedance due to the attachment of the insulating layer of bacteria, followed by a sudden decrease due to the release of molecules on cell lysis. This makes the biosensor less reliable, if more bacteria were still getting immobilized while others are being ruptured, producing opposite responses. Other studies used the lytic phages (λ, T4 & T7) for cell lysis to release some molecules, such as β-galactosidase, which were used indirectly in the qualitative and quantitative detection of bacteria [85–87]. Although the low detection limit of a few CFU was achieved by detecting the released molecules, the detection required a very long time (6 h).

In this work, we present for the first time, a non-lytic filamentous M13 phage-modified impedimetric microbial biosensor for an early detection of the fecal coliform bacteria, *E. coli*. When compared to reported cytosensors using lytic phages where the sensor response initially increased due to bacteria attachment and then decreased due to release of conductive cellular contents upon cell lysis, the response of our sensor only increased with increasing concentration/binding of *E. coli* to non-lytic *M13* phage. This we believe is an advantage. The *M13* phage is immobilized on the electrodeposited gold nanoparticles (AuNPs) on glassy carbon electrode (GCE) by means of covalent bonding using 3-mercatopropanoic acid as a linker between AuNPs and M13. The limit of detection of the biosensor is very promising, reaching the LOD of 14 CFU/mL, and the sensor has excellent stability over a wide range of pH (3.0 – 10.0) and temperatures (25 and 45 ^{o}C).

3.2. Materials and methods

3.2.1. Materials

Gold chloride hydrate, potassium ferricyanide, 3-mercaptopropanoic acid (MPA), 2-(N-morpholino) ethane sulfonic acid (MES), 1-Ethyl-3-(3-dimethylaminopropyl) carbodiimide (EDC), N-Hydroxysuccinimide (NHS), and Bovine albumin (BSA) were purchased from Sigma-Aldrich (St. Louis, USA). Ethanol amine (EA) was purchased from Acros Organic-Fisher Scientific. All solutions were prepared with Milli-Q water.

3.2.2. Cell culture and bacteriophage preparation

Single colony of XL1-blue (*Escherichia coli* K12) was inoculated to LB media supplemented with 10 μg/mL tetracycline and incubated at 37 ^{o}C with 250 rpm shaking. After overnight culture, cells were harvested by centrifugation at 5,000×g for 5 min. Collected cells were washed three times with PB buffer and ready for assays. Similarly, *Pseudomonas chlororaphis* was cultured in LB media.

For bacteriophage preparation, overnight culture of XL1-blue was 1:100 inoculated to 50 mL 2×YT/Tet media and cultured at 37 °C with shaking. When OD_{600} reached 0.3, 100 μL stock of bacteriophage M13KO7 (~10^{13} pfu/mL) was added to cell culture and incubated at 37 °C without shaking for 30 min. Kanamycin was then added to media to give a final concentration of 35 μg/mL. Cells were overnight cultured at 30 °C, 250 rpm, and centrifuged at 7,000 ×g for 30 min. The supernatant was collected and mixed with 12.5 mL ice-hold 20% w/v PEG6000 / 2.5 M NaCl solution. After incubation for 2 hours at 4 °C,

the mixture was centrifuged at 11,000 ×g for 30 min and the pellets were resuspended in 10 mL TE (10 mM Tris / 1mM EDTA). The resuspended solution was centrifuged at 18,000 ×g for 15 min and the supernatant was filtrated by using 0.22 μm filters. The titer of prepared phage was determined by serial dilution of infected XL1-blue cells on Tet/Kan agar plates.

3.2.3. Electrodeposition of AuNPs

Before electrodeposition of AuNPs on its surface, GCE (3 mm in diameter) was polished with 0.2 μm alumina slurry on microcloth pad, rinsed and washed ultrasonically with deionized water. AuNPs were electrochemically deposited on the cleaned GCE by 15 cycles of cyclic voltammetry (CV) in 10 mM gold chloride solution by scanning the potential from -0.7 to -1.2 V at a scan rate of 0.05 V/s [88]. Pt mesh worked as the counter electrode, while Ag/AgCl was used as the reference electrode. The prepared AuNPs were characterized by SEM imaging, EDX spectroscopy, CV and EIS measurements. The SEM FEI NNS450 was used in all SEM characterizations in this work.

3.2.4. Surface modification with M13 phage

Fig. 3.1 shows a schematic of the surface modification steps, including electrodeposition of AuNPs, for sensor fabrication. GCE with electrodeposited AuNPs was immersed in 0.1 M solution of 3-mercaptopropanoic acid (MPA) in ethanol for 1 h to form a self-assembled monolayer on gold surface, followed by washing with ethanol to remove any physically adsorbed MPA molecules. The carboxyl group of MPA was then activated using

EDC/NHS chemistry. Briefly, the Au-MPA electrode was immersed in 0.1 M MES buffer (pH 5.5) containing 0.15 M EDC for 20 min. then removed from EDC solution and immersed in 0.15 M NHS for other 20 min. The electrode was washed using MES buffer to remove unreacted EDC/NHS molecules. The modified and activated electrode was incubated with M13 solution (10^{11} PFU/mL) at 4 °C for 3-4 h, followed by rinsing with PB buffer to remove unbound phages. Subsequently, the electrode was immersed in 0.1 M ethanolamine solution for 30 min to passivate unreacted -NHS groups, followed by incubation with 0.2 % BSA solution for 30 min to block unfunctionalized Au. The electrode was washed thoroughly with PB solution. In this work, EA+BSA are labeled as "blocker" on graphs and schemes. All the modifications steps during the electrode fabrication were monitored and characterized using CV and EIS in ferricyanide solution.

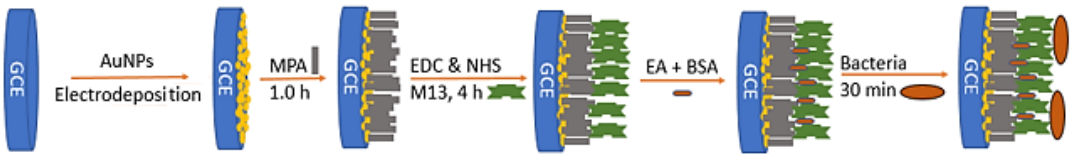

Figure 3.1. Schematic diagram of the EIS cytosensor fabrication process.

3.2.5. Instruments and measurements

All electrochemical (CV and EIS) measurements were performed in potassium ferricyanide $K_3Fe(CN)_6$, as redox probe. The 10 mM ferricyanide solution was prepared in 0.1 M KCl and phosphate buffer (pH 7.4). The electrochemical measurements were done using CHI 6005E with Pt mesh as auxiliary electrode and Ag/AgCl as reference electrode. All EIS

measurements were conducted at the Faradaic potential of 0.15 V, which was determined from CV ($E_{1/2}$ = 0.15 V), and at the frequency range of 1-10^4 Hz. For detection of microbial cells, the modified and washed electrodes were immersed in bacterial cells suspension in PB at pH 7.4 for 30 min, washed to remove any non-specifically adsorbed bacterial cells, followed by EIS measurement. The charge transfer resistance value, R_{ct} (Ohms) was extracted by computer simulation and fitting of the data using the CHI 6005E software.

Charge transfer resistance change (ΔR_{ct}) is calculated from the equation $\Delta R_{ct} = R_{ctf} - R_{cti}$, where R_{ctf} is the equilibrated R_{ct} after incubation with bacteria in PB or simulated river water followed by washing with PB, and R_{cti} is the recorded R_{ct} of the sensor after M13 immobilization and blocking, washing and incubation in PB or simulated river water followed by washing with PB. The sensors were stored in refrigerator in PB, except for studies of temperature stability when they were stored at room temperature or 45 ^oC.

3.2.6. SEM imaging

The imaging was pursued on gold film instead of gold nanoparticles to avoid any feature overlap. The thin film of gold was functionalized with MPA and them modified with M13 phage and incubated with *E. coli XL1-Blue*. After 30 min incubation with *E. coli XL1-Blue*, the phage-modified electrode was rinsed with PB solution and left to dry for 2 h, and then coated with a thin film of Pt/Pd sputtering to enhance the conductivity of samples and avoid surface charging, as all phages, bacteria, EA and BSA are non-conductive.

3.2.7. Preparation of artificial water samples

The composition of the artificial river water was prepared to simulate the chemical/biological composition of Yamuna River in northern India. The samples were prepared by dissolving 50 mg/L sodium citrate, 60 mg/L ammonium chloride, 500 mg/L potassium chloride, 500 mg/L calcium chloride, 150 mg/L magnesium nitrate in de-ionized water. The pH was adjusted to pH 7.5 and kept at 4^{o}C for future use. *E. coli XL1-blue* bacteria were spiked into an aliquot of the simulated river water samples and serially diluted to the required concentration range (10^2 – 10^5 CFU/mL).

3.3. Results and Discussion

As discussed in the introduction, the usage of bacteriophages as biorecognition elements in microbial biosensors is highly promising and preferred due to their higher stability compared to antibodies [77]. In addition, they are selective to their strain based on the receptors on the bacteria cell wall. The infection/binding process of M13 phage to *E. coli* involves the binding of the minor coat gene 3 protein (g3p) of the phage to the F pili (primary receptor) of bacteria, followed by the binding to the inner membrane protein TolA as a coreceptor [89–91]. Hence, it binds to *E. coli* strains with F^+, such as *XL1-Blue* and *K12*, while it doesn't bind to the non-*E. coli* strains. In this study, AuNPs were electrochemically deposited on the GCE to increase the available surface area and enhance the electron transfer at the electrodes surface. *E. coli XL1-Blue* and *K12* were used as the host/positive cells, while *P. chlororaphis* was implemented as the non-host/negative cells to test the EIS cytosensor selectivity. To eliminate potential false positive reading, the same measurements were carried out using a similar sensor structure but without modifying the

sensor surface with M13 phage, as a negative control. To determine the efficiency of the EIS cytosensor, the sensitivity and LOD were determined using *XL1-Blue* as the host strain.

3.3.1. Cytosensor fabrication

3.3.1.1. Electrodeposition and characterization of AuNPs

As a clean, reproducible, and well dispersed particles-production method, electrochemical deposition was implemented to deposit a film of well-dispersed AuNPs on the surface of GCE.

As mentioned in methods, the deposition was carried out using 15 cycles of CV in the potential range of -0.7 to -1.2 V, with a scan rate of 0.05 V/s [88]. The CV of the GCE-AuNPs shows stronger redox peaks of ferricyanide compared to bare-GCE (**Fig. 3.2a**) which can be attributed to the higher surface area of AuNPs and their strong electrocatalytic activity [92]. The EIS measurements were consistent with the CV measurement as there is a clear decrease in the faradaic impedance response by introducing AuNPs (**Fig. 3.2b)**. Moreover, SEM images showed good coverage of the GCE with well-dispersed and semi-spherical AuNPs (**Fig. 3.2c)**. The average particle size was 51.64±2.36 nm. EDX spectroscopy confirmed the successful formation of AuNPs, and the EDX mapping confirmed the NPs on the surface were AuNPs (**Fig. 3.2 (d-f))**.

3.3.1.2. Bioreceptor functionalization and blocking

A robust and reproducible functionalization of electrode surface with bioreceptor and blockers is critical for a highly efficient biosensor. The success of each modification step

in the cytosensor fabrication process was assessed by electrochemical techniques of CV and EIS using $[Fe(CN)_6]^{3-}$, as a redox probe. CV is a facile yet efficient technique for investigating modified electrode surface features. The deviations in peak current and peak potentials separation of redox probe are related to electron transfer rate constant. **Fig. 3.3a** illustrates the cyclic voltammograms post each functionalization/modification steps involved in the final sensor fabrication. As shown in the figure, there was a gradual decrease of the CV peak currents and correspondingly very small increase in the peak-to-peak redox potential after each modification. These changes are attributed to the repulsion of negatively charged $[Fe(CN)_6]^{3-}$ by -COOH groups of MPA and reduced conductivity of the electrode due to immobilization of non-conductive M13 phages and blocking with insulating BSA protein of GCE-AuNPs electrode.

EIS, another facile electrochemical technique which measures the electron transfer process at electrode-solution interface, was used to corroborate the above CV findings. The EIS measurements and corresponding Nyquist plots, shown in **Fig. 3.3b**, were fitted to Randles equivalent circuit, **Fig. 3.3b (inset)**, to calculate the charge transfer resistance (R_{ct}) after each modification step [93]. Randles circuit is composed of the solution resistance (R_s), charge transfer resistance (R_{ct}) which is given by the diameter of the half-circle in the Nyquist plot, double layer capacitance (C_{dl}), and Warburg element (W). As anticipated and in agreement with CV results, R_{ct} increased after each modification confirming successful functionalization of the electrode surface with bioreceptor and blockers.

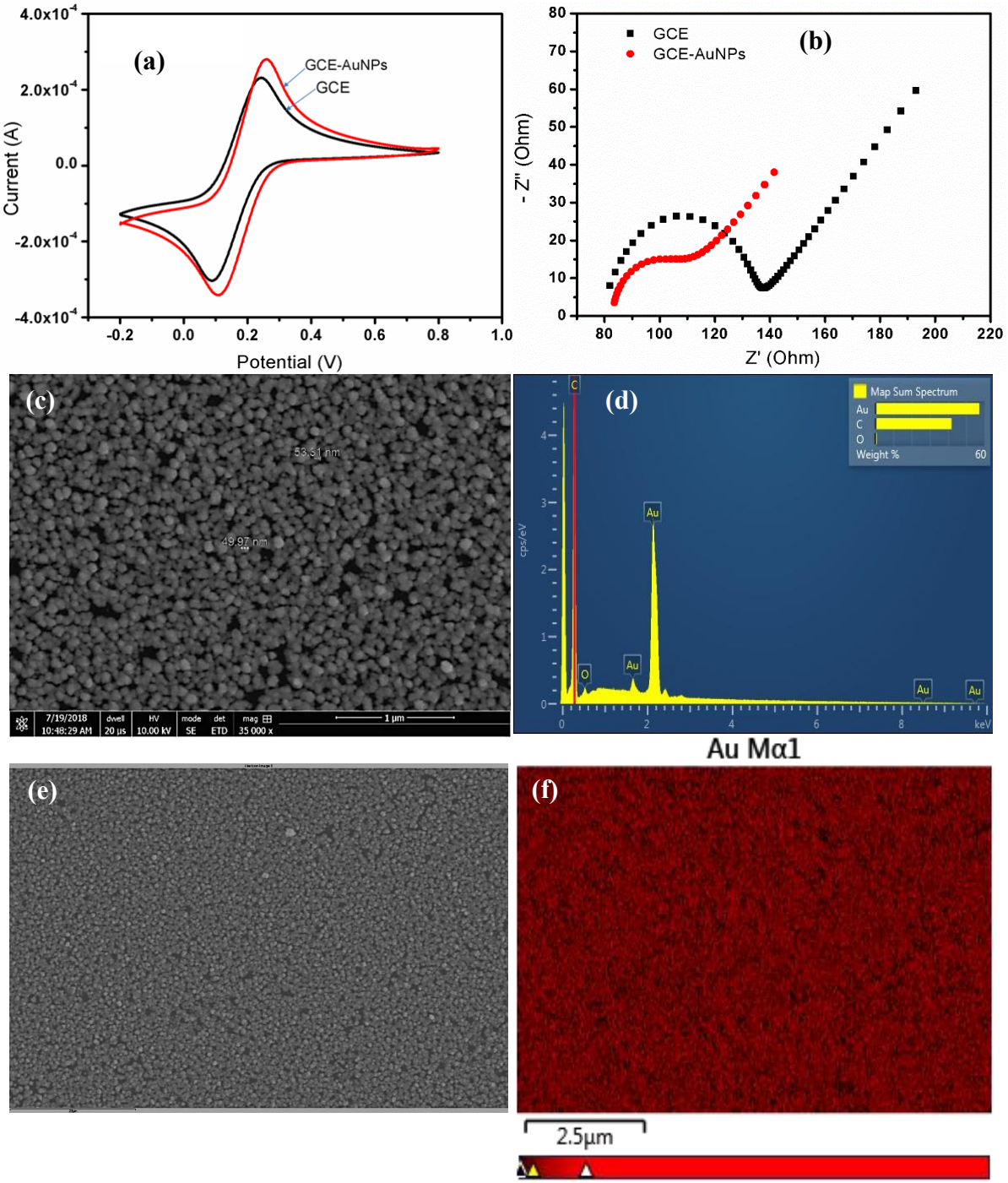

Figure 3.2. Cyclic voltammograms (a) and Nyquist plots of EIS signal (b) of GCE and GCE-AuNP electrodes. SEM image (c), EDX (d) and EDX mapping (e and f) of electrodeposited AuNPs on GCE electrode.

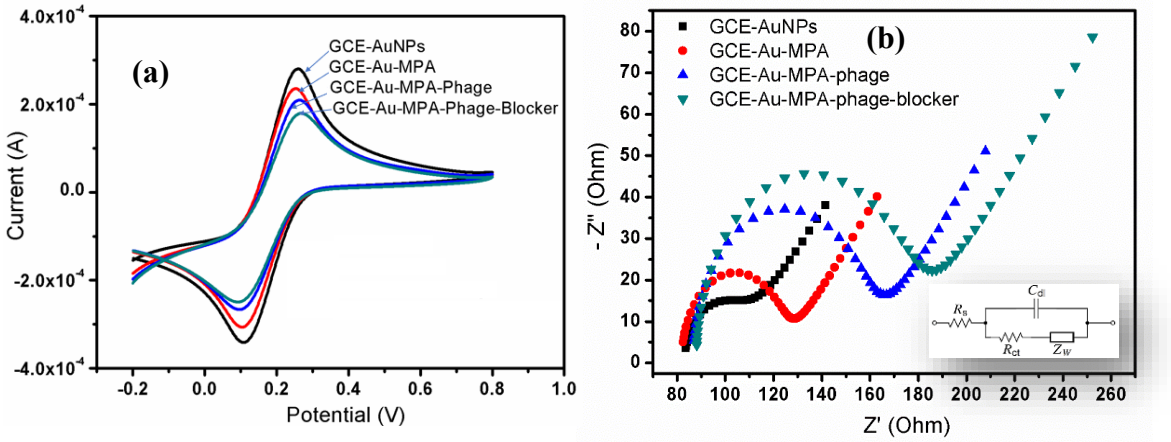

Figure 3.3. Cyclic voltammograms (a) and Nyquist plots of the EIS responses (b) of GCE-AuNPs, GCE-Au-MPA, GCE-Au-MPA-phage and GCE-Au-MPA-phage-blocker electrodes. The inset is Randles equivalent circuit.

3.3.2. Optimization of incubation times of phages and target pathogens

To ensure highest loading efficiency of M13 phages on GCE-Au electrode, the electrode (GCE-Au-MPA-NHS) was incubated with 10^{11} PFU/mL of M13 for different time intervals (1, 2, 3, 4 & 8 h) and the corresponding ΔR_{ct} values were recorded. As illustrated in **Fig. 3.4a**, ΔR_{ct} gradually increased due to increased binding of M13 phages up to 3 h and then plateaued. In the same context, to determine the optimum incubation time of the analyte with the GCE-Au-MPA-NHS-M13-blocker electrode, 10^5 CFU/mL of *E. coli XL1-Blue* cells were incubated for 10, 20, 30 and 40 min. The results, **Fig. 3.4b**, showed an initial rapid increase in impedance due to the binding of a large number of *E. coli* cells followed by a slow increase and plateauing at 30 min. Based on these results, a 3-4 h incubation time was used for phage immobilization and 30 min incubation of the phage-modified cytosensor with the analyte sample were employed in subsequent experiments.

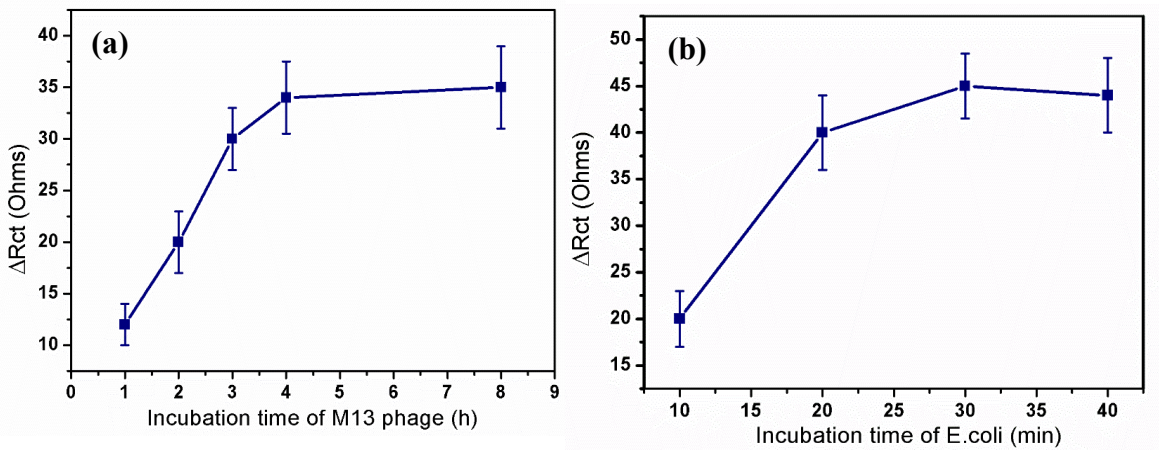

Figure 3.4. Optimization of the incubation times of (a) M13 phages with GCE-AuNP-NHS and (b) E. coli XL1-Blue (10^5 CFU/mL) cells with the GCE-Au-MPA-phage-blocker electrodes. Each data point is an average of responses from 1 electrode, measured 3 times and error bars represent ± 1 standard deviation.

3.3.3. Detection of E. coli XL1-Blue and E. coli K12

As mentioned above, detection of bacterial cells using M13 bacteriophage as a bioreceptor starts with the binding of the minor coat gene 3 protein (g3p) of M13 phage to the F pili (primary receptor) of bacteria, followed by binding to the inner membrane protein TolA as a coreceptor [89–91]. SEM imaging was performed to investigate the interaction between the bioreceptor M13 phage and its target *E. coli*. The SEM image in **Fig. 3.5a** shows nicely distributed clusters of the liquid crystal M13 phages on the gold surface with several captured *E. coli* cells (identified by red arrows). A zoomed-in image (**Fig. 3.5b**) of the captured bacteria shows phages surrounding the bacteria and immobilizing it to the electrode surface. A slightly enlarged/enveloped appearance of M13 phages may be attributed to the coating of PEG/NaCl, from the phage amplification process (please see

methods) and/or a contribution from the blocker (0.2% BSA) as previously reported [83,94].

It is worth briefly discussing the possible shapes and phases of M13 phages under different incubation/concentration conditions. M13 phages are liquid crystals of different phases. According to Dogic et al. (2016), at low concentrations, the phages are disordered and point in random directions in the isotropic phase. As the concentration increases, the phages start to be more oriented and aligned along one particular axis in the nematic phase that transitions to more ordered phases, particularly the smectic phase. Interestingly, phage molecules in the smectic phase organize into one-rod-length thick layers that are liquid-like aligned rods stacked on top of each other (Dogic et al., 2016). Moreover, *M13* phage can have different shapes. It can be filamentous in the normal case, or spheroid in the hydrophobic-hydrophilic interfaces, or I-form particles at low temperatures (around 2^{o} C) [96,97].

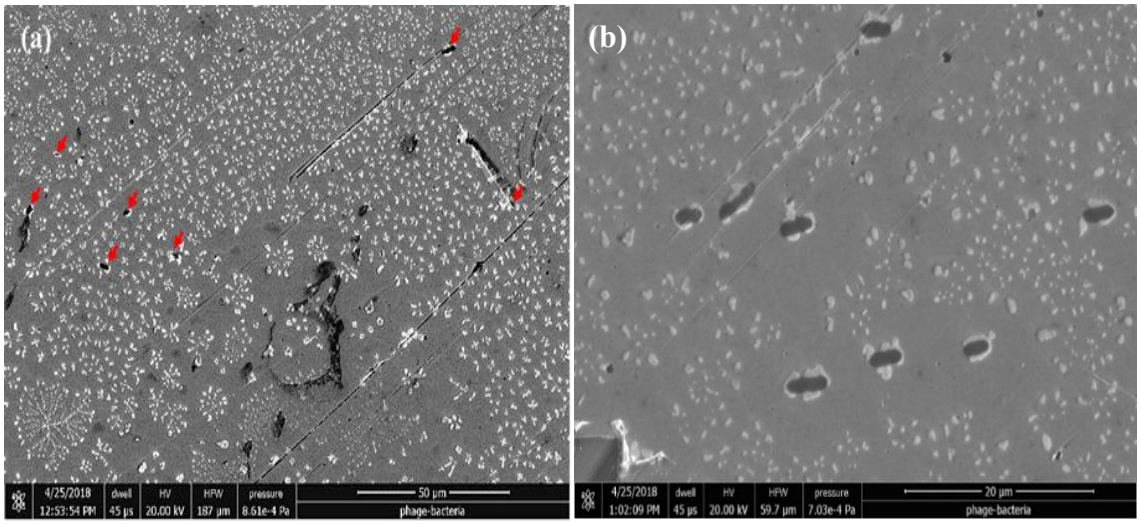

Figure 3.5. (a) SEM micrograph of the M13 phages immobilized on Au electrode and captured E. coli XL1-Blue cells (pointed at by red arrows). (b) Higher magnification SEM image of E. coli bacteria captured by M13 phages.

3.3.4. Analytical characteristics of the cytosensor

We evaluated the performance of the cyctosensor in terms of sensitivity, limit of detection, reproducibility and selectivity. **Fig. 3.6** shows the sensor response (ΔR_{ct}) as a function of *E. coli XL1-Blue* concentration. The results showed that the cytosensor response (ΔR_{ct}) increased, i.e. R_{ct} increased, as a function of *E. coli XL1-Blue* concentration over a broad dynamic range from 10^1 to 10^7 CFU/mL (Appendix B, **Fig. B1**). The calibration plot in **Fig. 3.6** is an average of responses of three separate cytosensors with each sensor exposed to 10-fold increasing concentrations of the target bacteria covering the 10^1 to 10^7 CFU/mL range. Each analyte sample was incubated with the cytosensor for 30 min, washed with PB followed by EIS measurement in between the samples. The increase in charge transfer resistance can be attributed to the insulating effect of the bacterial cells, and the possibility that they prevent redox probe molecules from reaching the electrode surface [98,99].

The positive control experiment, in which the sensor without M13 phage was exposed to 10^3, 10^4 and 10^5 CFU/mL of *E. coli XL1-Blue* had a minimal response when compared to a sensor with bioreceptor M13 phage (Appendix B, **Fig. B2**). Additionally, negative control experiment in which a cytosensor with M13 phage was exposed to blank PB, i.e. no *E. coli XL1-Blue*, repeatedly had a response of ΔR_{ct} = 4.00 ± 3.51 (n= 3). The above results confirmed the high quality of biofunctionalization protocol and the corresponding cytosensors prepared in this study.

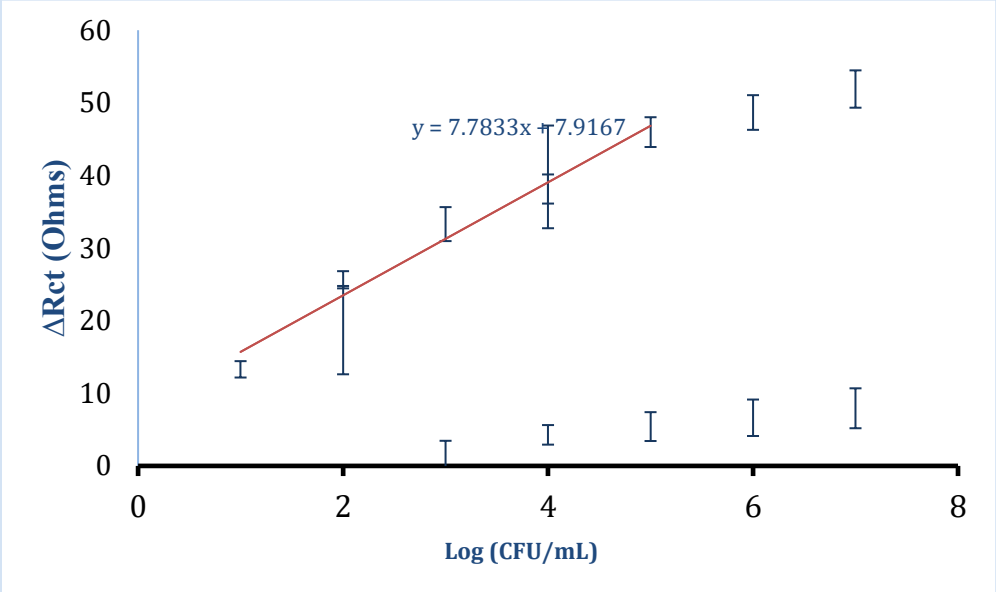

Figure 3.6. Response (ΔR_{ct}) of the cytosenor to increasing concentrations of E. coli XL1-Blue (circles); E. coli K-12 (triangles) and P. chlororaphis (squares). Each data point is an average of responses from 3 different M13-modified electrodes and error bars represent ± 1 standard deviation.

3.3.4.1. Sensitivity and limit of detection

As shown in **Fig. 3.6**, the cytosensor response was linearly related to the log of *E. coli XL1-Blue* concentration between 10^1 to 10^5 CFU/mL with a sensitivity (the slope of the calibration plot, d(ΔRct)/dlog(CFU/mL)) of 7.78 Ohms per Log (CFU/mL) or 7.78 Ohms

per 10 (CFU/mL). The limit of detection (LOD) of the cytosensor calculated based on the equation LOD = 3*SD/S, where SD is the standard deviation of blank sample (SD = 3.51 Ohms, n = 3), and S is the sensitivity, was estimated to be 13.53 ≈ 14 CFU/mL. This limit of detection is the lowest in the EIS-phage cytosensors published to-date. This low LOD may be credited to 1) the non-lytic nature of the M13 phages which helped detect bacterial cells as an increase in Rct, without getting countered by the conductive content of cells released from the cells, as in the case of lytic phages-based biosensors and 2) the high surface area of AuNPs and the efficient chemical binding of M13 to the nanoparticles surface. Furthermore, the cytosensors had excellent reproducibility as evident by the low standard deviation (1.12 to 2.57) and relative standard deviation (4.46 to 8.47%; please see **Table B1** in Appendix B) of the data points obtained from 3 independent cytosensors used to generate the calibration plot in **Fig. 3.6**.

3.3.4.2. Selectivity

Similar to *E. coli XL1-Blue*, *E. coli K12* is F pili positive and host for M13 phages. Therefore, an increase in impedance is expected after incubation of the M13-modified sensor with this strain also. As shown in Appendix B, **Fig. B3**, there was an increase in half-circle diameter of Nyquist plot, which represents the charge transfer resistance of cytosensor from the original value when exposed to 10^2 and 10^4 CFU/mL of *E. coli K12*. The ΔR_{ct} values for these concentrations were statistically similar to that for *E. coli XL1-Blue* (**Fig. 3.6**). On-the-other-hand, as shown in **Fig. 3.6**, there was no significant change in the charge transfer resistance with the non-host *P. chlororaphis* bacteria (ΔR_{ct} values

were similar to that for blank/buffer even at 10^7 CFU/mL) compared to the response with the host *E. coli XL1-Blue*. The ability of our sensor to detect multiple strains of *E. coli* while not responding to non-*E. coli* bacteria, is a useful characteristic in the goal of selectively monitoring coliforms.

3.3.4.3. Stability

The M13 phage-based EIS cytosensor was tested for stability at 22 ^oC (room temperature) and 45 ^oC by comparing ΔRct for detection of *E. coli XL-1 blue* at the same concentration (10^3 CFU/mL). Fourteen M13 phage modified cytosensors, were prepared on working electrodes of evaporated gold on Kapton substrate that was modified with M13 phage and blocked with blocking agents using protocol described previously. A pair of sensors were used immediately for the day zero time point reading while six sensors each were kept in PB at 22 ^oC (room temperature) and 45 ^oC until day 16 for future time points. Two electrodes were removed from each storage condition and evaluated for detection efficiency. As shown in Appendix B, **Table B2**, there was no significant difference in the sensing efficiency of the sensors for up to 16 days at these temperatures. The stability at temperature as high as 45 ^oC for an extended period is a beneficial feature of our phage-based sensor over antibodies-based sensors for field applications and variation of temperature that the sensor may encounter during shipping. Additionally, the stability of the M13-based EIS sensor was investigated in a wide range of pH values. Multiple electrodes were prepared the same way as mentioned earlier and incubated in pH 2.0 to 10.0 buffer for an hour followed by evaluating detection of 10^3 CFU/mL *E. coli XL-1 blue*

in PB. As illustrated in Appendix B, **Fig. S4**, the sensor had negligible decrease in sensing response over the pH range of 4.5 – 8.0, that decreased slightly to 80±14% at pH 10 and 75±20% at pH 3 and dropped significantly to 35±10% at pH 2. These results verify the very good to high stability of M13 phage-based sensor on exposure to pH 3 to 10.

3.3.5. Analysis of simulated river water samples

To assess the suitability of M13 phage-based EIS cytosensor for practical application, it was applied to detect *E. coli XL1-Blue* spiked in simulated river water mimicking the chemical/biological composition of Yamuna River in northern India. The sensor response in river water was compared to that in PB for bacteria concentration from 10^2 to10^5 CFU/mL. As shown in **Fig. 3.7**, the response was linearly correlated to the concentration over this concentration range with a slope of 6.685 Ohms per 10 CFU/mL, which was statistically identical ($p > 0.05$) to that in PB (S=6.583 Ohms per 10 CFU/mL) over all the concentrations. A slight consistent off-set/difference of the sensor response between simulated river water and PB can be attributed to the difference in composition of the two water samples. These results demonstrate the promise of the present sensor for the real field applications.

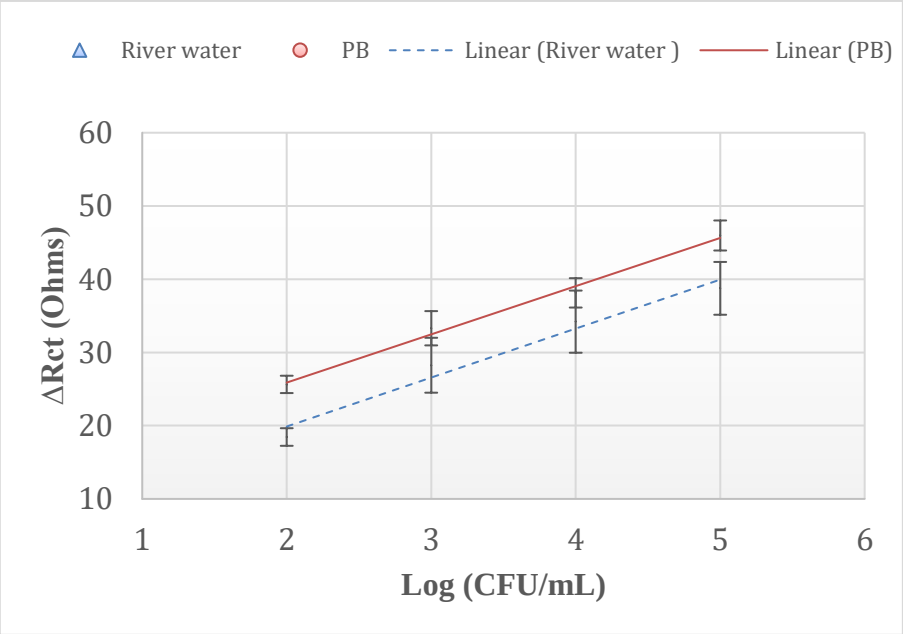

Figure 3.7. Response (ΔR_{ct}) of the cytosenor to increasing concentrations of E. coli XL1-Blue in PB (circle) and simulated river water (square). Each data point is an average of responses from 1 electrode, measured 3 times and error bars represent ± 1 standard deviation.

3.4. Conclusions

To conclude, an easy to fabricate and use EIS cytosensor based on non-lytic bacteriophage M13 for measurement of coliforms was introduced. The sensor exhibited the lowest limit of detection (≈ 14 CFU/mL) reported to-date for phage-based EIS cytosensors for coliforms. This excellent limit of the detection of the cytosensor can be attributed to the non-lytic nature of the M13 phage and the high surface area of AuNPs and the efficient chemical binding of M13 to the surface of well-dispersed nanoparticles. The sensor was selective for F^+ pili *E. coli* species, such as *XL1-Blue and K12*, when compared to non-host *P. chlororaphis* bacteria. Additionally, the sensor demonstrated excellent stability (over 2 weeks at 45 ^oC) and precision. Furthermore, the sensor was successfully applied for the

detection of *E. coli XL1-Blue* in simulated river water. These features make it a potential analytical tool for ideal for monitoring coliform in environmental waters. In terms of its suitability to real field application, the M13 sensor system was tested in simulated river water, where it exhibited good response with neglectable interference with the water composition variation. In addition, the sensor system shows high stability over a wide range of pH and at elevated temperatures. Summing all together, the proposed M13 phage-based cytosensor is highly sensitive, selective, and stable for detection of fecal coliforms in water samples.

3.5. References

[1] L. Rodríguez-Lado, G. Sun, M. Berg, Q. Zhang, H. Xue, Q. Zheng, C.A. Johnson, Groundwater arsenic contamination throughout China, Science (80-.). 341 (2013) 866–868.

[2] A. Smith, P. Lopipero, J. Chung, R. Haque, A. Hernandez, L. Moore, C. Steinmaus, Arsenic in drinking water and cancer risks estimated from epidemiological studies in Argentina, Chile, Taiwan and Japan, in: Epidemiology, LIPPINCOTT WILLIAMS & WILKINS 530 WALNUT ST, PHILADELPHIA, PA 19106-3621 USA, 2000: pp. S93–S93.

[3] Z. Ning, D.T. Lobdell, R.K. Kwok, Z. Liu, S. Zhang, C. Ma, M. Riediker, J.L. Mumford, Residential exposure to drinking water arsenic in Inner Mongolia, China, Toxicol. Appl. Pharmacol. 222 (2007) 351–356.

[4] R. Feeney, S.P. Kounaves, On-site analysis of arsenic in groundwater using a microfabricated gold ultramicroelectrode array, Anal. Chem. 72 (2000) 2222–2228.

[5] P.B. Tchounwou, A.K. Patlolla, J.A. Centeno, Invited reviews: carcinogenic and systemic health effects associated with arsenic exposure—a critical review, Toxicol. Pathol. 31 (2003) 575–588.

[6] H. Shi, X. Shi, K.J. Liu, Oxidative mechanism of arsenic toxicity and carcinogenesis, Mol. Cell. Biochem. 255 (2004) 67–78.

[7] D. Melamed, Monitoring arsenic in the environment: a review of science and technologies with the potential for field measurements, Anal. Chim. Acta. 532 (2005) 1–13.

[8] M.R. Rahman, T. Okajima, T. Ohsaka, Selective detection of As (III) at the Au (111)-like polycrystalline gold electrode, Anal. Chem. 82 (2010) 9169–9176.

[9] D.E. Mays, A. Hussam, Voltammetric methods for determination and speciation of inorganic arsenic in the environment—a review, Anal. Chim. Acta. 646 (2009) 6–16.

[10] M.K. Sengupta, M.F. Sawalha, S.-I. Ohira, A.D. Idowu, P.K. Dasgupta, Green analyzer for the measurement of total arsenic in drinking water: electrochemical reduction of arsenate to arsine and gas phase chemiluminescence with ozone, Anal. Chem. 82 (2010) 3467–3473.

[11] M. Zaib, M.M. Athar, A. Saeed, U. Farooq, Electrochemical determination of inorganic mercury and arsenic—a review, Biosens. Bioelectron. 74 (2015) 895–908.

[12] Y. Cai, Speciation and analysis of mercury, arsenic, and selenium by atomic fluorescence spectrometry, TrAC Trends Anal. Chem. 19 (2000) 62–66.

[13] G. Álvarez-Llamas, M. del Rosario Fernández de laCampa, A. Sanz-Medel, ICP-MS for specific detection in capillary electrophoresis, TrAC Trends Anal. Chem. 24 (2005) 28–36.

[14] N. Zhang, N. Fu, Z. Fang, Y. Feng, L. Ke, Simultaneous multi-channel hydride generation atomic fluorescence spectrometry determination of arsenic, bismuth, tellurium and selenium in tea leaves, Food Chem. 124 (2011) 1185–1188.

[15] J. Barek, K. Peckova, V. Vyskocil, Adsorptive stripping voltammetry of environmental carcinogens, Curr. Anal. Chem. 4 (2008) 242–249.

[16] G.M.S. Alves, J.M.C.S. Magalhães, P. Salaün, C.M.G. Van den Berg, H.M.V.M. Soares, Simultaneous electrochemical determination of arsenic, copper, lead and mercury in unpolluted fresh waters using a vibrating gold microwire electrode, Anal. Chim. Acta. 703 (2011) 1–7.

[17] M.T. Castaneda, A. Merkoçi, M. Pumera, S. Alegret, Electrochemical genosensors for biomedical applications based on gold nanoparticles, Biosens. Bioelectron. 22 (2007) 1961–1967.

[18] G. Martínez-Paredes, M.B. González-García, A. Costa-García, Lead Sensor Using Gold Nanostructured Screen-Printed Carbon Electrodes as Transducers, Electroanal. An Int. J. Devoted to Fundam. Pract. Asp. Electroanal. 21 (2009) 925–930.

[19] J.N. Anker, W.P. Hall, O. Lyandres, N.C. Shah, J. Zhao, R.P. Van Duyne, Biosensing with plasmonic nanosensors. Nanoscience and Technology: A Collection of Reviews from Nature Journals, World Sci. (2010) 308–319.

[20] J. Huang, H. Chen, Heat-Assisted Electrodissolution of Platinum in an Ionic Liquid, Angew. Chemie. 124 (2012) 1716–1720.

[21] K. Sasaki, H. Naohara, Y. Cai, Y.M. Choi, P. Liu, M.B. Vukmirovic, J.X. Wang, R.R. Adzic, Core-protected platinum monolayer shell high-stability electrocatalysts for fuel-cell cathodes, Angew. Chemie. 122 (2010) 8784–8789.

[22] S. Guo, E. Wang, Noble metal nanomaterials: controllable synthesis and application in fuel cells and analytical sensors, Nano Today. 6 (2011) 240–264.

[23] L. Bu, T. Gu, Y. Ma, C. Chen, Y. Tan, Q. Xie, S. Yao, Enhanced cathodic preconcentration of As (0) at Au and Pt electrodes for anodic stripping voltammetry analysis of As (III) and As (V), J. Phys. Chem. C. 119 (2015) 11400–11409.

[24] E. Majid, S. Hrapovic, Y. Liu, K.B. Male, J.H.T. Luong, Electrochemical determination of arsenite using a gold nanoparticle modified glassy carbon electrode and flow analysis, Anal. Chem. 78 (2006) 762–769.

[25] K. Pungjunun, S. Chaiyo, I. Jantrahong, S. Nantaphol, W. Siangproh, O. Chailapakul, Anodic stripping voltammetric determination of total arsenic using a gold nanoparticle-modified boron-doped diamond electrode on a paper-based device, Microchim. Acta. 185 (2018) 324.

[26] S. Hokkanen, E. Repo, S. Lou, M. Sillanpää, Removal of arsenic (V) by magnetic nanoparticle activated microfibrillated cellulose, Chem. Eng. J. 260 (2015) 886–894.

[27] V. Chandra, J. Park, Y. Chun, J.W. Lee, I.-C. Hwang, K.S. Kim, Water-dispersible magnetite-reduced graphene oxide composites for arsenic removal, ACS Nano. 4 (2010) 3979–3986.

[28] Z. Xie, J. Xu, F. Xie, S. Xiong, Electrochemical Detection of As (III) by a rGO/Fe3O4-modified Screen-Printed Carbon Electrode, Anal. Sci. 32 (2016) 1053–1058.

[29] P. Devi, C. Sharma, P. Kumar, M. Kumar, B.K.S. Bansod, M.K. Nayak, M.L. Singla, Selective electrochemical sensing for arsenite using rGO/Fe3O4 nanocomposites, J. Hazard. Mater. 322 (2017) 85–94.

[30] J. Wei, S.-S. Li, Z. Guo, X. Chen, J.-H. Liu, X.-J. Huang, Adsorbent assisted in situ electrocatalysis: An ultra-sensitive detection of As (III) in water at Fe3O4 nanosphere densely decorated with Au nanoparticles, Anal. Chem. 88 (2016) 1154–1161.

[31] S.-S. Li, W.-Y. Zhou, M. Jiang, Z. Guo, J.-H. Liu, L. Zhang, X.-J. Huang, Surface Fe (II)/Fe (III) cycle promoted ultra-highly sensitive electrochemical sensing of arsenic (III) with dumbbell-like Au/Fe3O4 nanoparticles, Anal. Chem. 90 (2018) 4569–4577.

[32] Y. Hassan, C.-H. Chuang, Y. Kobayashi, N. Coombs, S. Gorantla, G.A. Botton, M.A. Winnik, C. Burda, G.D. Scholes, Synthesis and optical properties of linker-free TiO2/CdSe nanorods, J. Phys. Chem. C. 118 (2014) 3347–3358.

[33] M. Sedki, I.A. Khalil, I.M. El-Sherbiny, Hybrid nanocarrier system for guiding and augmenting simvastatin cytotoxic activity against prostate cancer, Artif. Cells, Nanomedicine, Biotechnol. 46 (2018) S641–S650.

[34] H. Yoo, K.-H. Ahn, H.-J. Lee, K.-H. Lee, Y.-J. Kwak, K.-G. Song, Nitrogen removal from synthetic wastewater by simultaneous nitrification and denitrification (SND) via nitrite in an intermittently-aerated reactor, Water Res. 33 (1999) 145–154.

[35] D. Wei, A. Ivaska, Applications of ionic liquids in electrochemical sensors, Anal. Chim. Acta. 607 (2008) 126–135.

[36] S. Pandey, Analytical applications of room-temperature ionic liquids: A review of recent efforts, Anal. Chim. Acta. 556 (2006) 38–45.

[37] E. Rozniecka, G. Shul, J. Sirieix-Plenet, L. Gaillon, M. Opallo, Electroactive ceramic carbon electrode modified with ionic liquid, Electrochem. Commun. 7 (2005) 299–304.

[38] H. Khani, M.K. Rofouei, P. Arab, V.K. Gupta, Z. Vafaei, Multi-walled carbon nanotubes-ionic liquid-carbon paste electrode as a super selectivity sensor: application to potentiometric monitoring of mercury ion (II), J. Hazard. Mater. 183 (2010) 402–409.

[39] S.-Q. Xiong, Y. Wei, Z. Guo, X. Chen, J. Wang, J.-H. Liu, X.-J. Huang, Toward membrane-free amperometric gas sensors: an ionic liquid–nanoparticle composite approach, J. Phys. Chem. C. 115 (2011) 17471–17478.

[40] X.-J. Huang, L. Aldous, A.M. O'Mahony, F.J. del Campo, R.G. Compton, Toward membrane-free amperometric gas sensors: A microelectrode array approach, Anal. Chem. 82 (2010) 5238–5245.

[41] R.S. Das, B. Singh, S. Mukhopadhyay, R. Banerjee, Gold nano particles catalyzed oxidation of hydrazine by a metallo-superoxide complex: experimental evidences for surface activity of gold nano particles, Dalt. Trans. 41 (2012) 4641–4648.

[42] J. Olesiak-Banska, M. Gordel, R. Kolkowski, K. Matczyszyn, M. Samoc, Third-order nonlinear optical properties of colloidal gold nanorods, J. Phys. Chem. C. 116 (2012) 13731–13737.

[43] Y. Li, S. Yang, X. Lu, W. Duan, T. Moriga, Synthesis and evaluation of the SERS effect of Fe 3 O 4–Ag Janus composite materials for separable, highly sensitive substrates, RSC Adv. 9 (2019) 2877–2884.

[44] F. Márquez, G.M. Herrera, T. Campo, M. Cotto, J. Ducongé, J.M. Sanz, E. Elizalde, Ó. Perales, C. Morant, Preparation of hollow magnetite microspheres and their applications as drugs carriers, Nanoscale Res. Lett. 7 (2012) 210.

[45] S. Krishnamurthy, A. Esterle, N.C. Sharma, S. V Sahi, Yucca-derived synthesis of gold nanomaterial and their catalytic potential, Nanoscale Res. Lett. 9 (2014) 627.

[46] D. Van Quy, N.M. Hieu, P.T. Tra, N.H. Nam, N.H. Hai, N. Thai Son, P.T. Nghia, N.T. Van Anh, T.T. Hong, N.H. Luong, Synthesis of silica-coated magnetic nanoparticles and application in the detection of pathogenic viruses, J. Nanomater. 2013 (2013).

[47] D.M. Adams, L. Brus, C.E.D. Chidsey, S. Creager, C. Creutz, C.R. Kagan, P. V Kamat, M. Lieberman, S. Lindsay, R.A. Marcus, Charge transfer on the nanoscale: current status, J. Phys. Chem. B. 107 (2003) 6668–6697.

[48] M. Sedki, X. Chen, C. Chen, X. Ge, A. Mulchandani, Non-lytic M13 phage-based highly sensitive impedimetric cytosensor for detection of coliforms, Biosens. Bioelectron. 148 (2020) 111794.

[49] G. Zhao, M. Sedki, S. Ma, C. Villarreal, A. Mulchandani, D. Jassby, Bismuth subcarbonate decorated reduced graphene oxide nanocomposite for the sensitive stripping voltammetry analysis of Pb(II) and Cd(II) in water, Sensors (Switzerland). 20 (2020). https://doi.org/10.3390/s20216085.

[50] D. Renock, J. Voorhis, Electrochemical investigation of arsenic redox processes on pyrite, Environ. Sci. Technol. 51 (2017) 3733–3741.

[51] A.K. Misra, A river about to die: Yamuna, J. Water Resour. Prot. 2 (2010) 489.

[52] D. Malik, S. Singh, J. Thakur, R.K. Singh, A. Kaur, S. Nijhawan, Heavy metal pollution of the Yamuna River: An introspection, Int. J. Curr. Microbiol. App. Sci. 3 (2014) 856–863.

[53] C. Dye, After 2015: infectious diseases in a new era of health and development, Phil. Trans. R. Soc. B. 369 (2014) 20130426.

[54] K.M. Wibowo, M.Z. Sahdan, N.I. Ramli, A. Muslihati, N. Rosni, V.H. Tsen, H. Saim, S.A. Ahmad, Y. Sari, Z. Mansor, Detection of Escherichia Coli Bacteria in Wastewater by using Graphene as a Sensing Material, in: J. Phys. Conf. Ser., IOP Publishing, 2018: p. 12063.

[55] N.J. Ashbolt, W.O.K. Grabow, M. Snozzi, 13 Indicators of microbial water quality, (2001).

[56] S.T. Odonkor, J.K. Ampofo, Escherichia coli as an indicator of bacteriological quality of water: an overview, Microbiol. Res. (Pavia). 4 (2013) 2.

[57] N. Massad-Ivanir, G. Shtenberg, N. Raz, C. Gazenbeek, D. Budding, M.P. Bos, E. Segal, Porous silicon-based biosensors: Towards real-time optical detection of target bacteria in the food industry, Sci. Rep. 6 (2016) 38099.

[58] D. Spiegelman, G. Whissell, C.W. Greer, A survey of the methods for the characterization of microbial consortia and communities, Can. J. Microbiol. 51 (2005) 355–386.

[59] J.T. Keer, L. Birch, Molecular methods for the assessment of bacterial viability, J. Microbiol. Methods. 53 (2003) 175–183.

[60] B. Byrne, E. Stack, N. Gilmartin, R. O'Kennedy, Antibody-based sensors: principles, problems and potential for detection of pathogens and associated toxins, Sensors. 9 (2009) 4407–4445.

[61] F. v. Wintzingerode, U.B. Göbel, E. Stackebrandt, Determination of microbial diversity in environmental samples: pitfalls of PCR-based rRNA analysis, FEMS Microbiol. Rev. 21 (1997) 213–229.

[62] R.Y.A. Hassan, U. Wollenberger, Mediated bioelectrochemical system for biosensing the cell viability of Staphylococcus aureus, Anal. Bioanal. Chem. 408 (2016) 579–587.

[63] D. V Lim, J.M. Simpson, E.A. Kearns, M.F. Kramer, Current and developing technologies for monitoring agents of bioterrorism and biowarfare, Clin. Microbiol. Rev. 18 (2005) 583–607.

[64] H.M.M. Selim, A.M. Kamal, D.M.M. Ali, R.Y.A. Hassan, Bioelectrochemical systems for measuring microbial cellular functions, Electroanalysis. 29 (2017) 1498–1505.

[65] M. Sedki, R.Y.A. Hassan, A. Hefnawy, I.M. El-Sherbiny, Sensing of bacterial cell viability using nanostructured bioelectrochemical system: rGO-hyperbranched chitosan nanocomposite as a novel microbial sensor platform, Sensors Actuators, B Chem. 252 (2017). https://doi.org/10.1016/j.snb.2017.05.163.

[66] D.C. Wallace, W. Fan, V. Procaccio, Mitochondrial energetics and therapeutics, Annu. Rev. Pathol. Mech. Dis. 5 (2010) 297–348.

[67] F.J. Rawson, A.J. Downard, K.H. Baronian, Electrochemical detection of intracellular and cell membrane redox systems in Saccharomyces cerevisiae, Sci. Rep. 4 (2014) 5216.

[68] D. Ivnitski, I. Abdel-Hamid, P. Atanasov, E. Wilkins, S. Stricker, Application of electrochemical biosensors for detection of food pathogenic bacteria, Electroanal. An Int. J. Devoted to Fundam. Pract. Asp. Electroanal. 12 (2000) 317–325.

[69] E.B. Setterington, E.C. Alocilja, Electrochemical biosensor for rapid and sensitive detection of magnetically extracted bacterial pathogens, Biosensors. 2 (2012) 15–31.

[70] C. Bao, L. Chen, T. Wang, C. Lei, F. Tian, D. Cui, Y. Zhou, One step quick detection of cancer cell surface marker by integrated NiFe-based magnetic biosensing cell

cultural chip, Nano-Micro Lett. 5 (2013) 213–222.

[71] A. Zhang, W. Guo, H. Ke, X. Zhang, H. Zhang, C. Huang, D. Yang, N. Jia, D. Cui, Sandwich-format ECL immunosensor based on Au star@ BSA-Luminol nanocomposites for determination of human chorionic gonadotropin, Biosens. Bioelectron. 101 (2018) 219–226.

[72] X. Guo, A. Kulkarni, A. Doepke, H.B. Halsall, S. Iyer, W.R. Heineman, Carbohydrate-based label-free detection of Escherichia coli ORN 178 using electrochemical impedance spectroscopy, Anal. Chem. 84 (2011) 241–246.

[73] L. Han, P. Liu, V.A. Petrenko, A.H. Liu, A label-free electrochemical impedance cytosensor based on specific peptide-fused phage selected from landscape phage library, Sci. Rep. 6 (2016) 1–10. https://doi.org/10.1038/srep22199.

[74] Y. Zhou, A. Marar, P. Kner, R.P. Ramasamy, Charge-Directed Immobilization of Bacteriophage on Nanostructured Electrode for Whole-Cell Electrochemical Biosensors, Anal. Chem. 89 (2017) 5734–5741. https://doi.org/10.1021/acs.analchem.6b03751.

[75] S.A. Soper, A.C. Henry, B. Vaidya, M. Galloway, M. Wabuyele, R.L. McCarley, Surface modification of polymer-based microfluidic devices, Anal. Chim. Acta. 470 (2002) 87–99.

[76] J. Chen, B. Duncan, Z. Wang, L.S. Wang, V.M. Rotello, S.R. Nugen, Bacteriophage-based nanoprobes for rapid bacteria separation, Nanoscale. 7 (2015) 16230–16236. https://doi.org/10.1039/c5nr03779d.

[77] J. Chen, B. Duncan, Z. Wang, L.-S. Wang, V.M. Rotello, S.R. Nugen, Bacteriophage-based nanoprobes for rapid bacteria separation, Nanoscale. 7 (2015) 16230–16236.

[78] M. Janczuk, J. Niedziółka-Jönsson, K. Szot-Karpińska, Bacteriophages in electrochemistry: A review, J. Electroanal. Chem. 779 (2016) 207–219.

[79] V. Nanduri, I.B. Sorokulova, A.M. Samoylov, A.L. Simonian, V.A. Petrenko, V. Vodyanoy, Phage as a molecular recognition element in biosensors immobilized by physical adsorption, Biosens. Bioelectron. 22 (2007) 986–992.

[80] H. Handa, S. Gurczynski, M.P. Jackson, G. Auner, J. Walker, G. Mao, Recognition of Salmonella typhimurium by immobilized phage P22 monolayers, Surf. Sci. 602 (2008) 1392–1400.

[81] G. Ertürk, R. Lood, Bacteriophages as biorecognition elements in capacitive biosensors: Phage and host bacteria detection, Sensors Actuators B Chem. 258 (2018) 535–

543.

[82] R. Edgar, M. McKinstry, J. Hwang, A.B. Oppenheim, R.A. Fekete, G. Giulian, C. Merril, K. Nagashima, S. Adhya, High-sensitivity bacterial detection using biotin-tagged phage and quantum-dot nanocomplexes, Proc. Natl. Acad. Sci. 103 (2006) 4841–4845.

[83] M. Ploss, A. Kuhn, Kinetics of filamentous phage assembly, Phys. Biol. 7 (2010) 45002.

[84] Y. Zhou, A. Marar, P. Kner, R.P. Ramasamy, Charge-directed immobilization of bacteriophage on nanostructured electrode for whole-cell electrochemical biosensors, Anal. Chem. 89 (2017) 5734–5741.

[85] J. Chen, S.D. Alcaine, Z. Jiang, V.M. Rotello, S.R. Nugen, Detection of Escherichia coli in drinking water using T7 bacteriophage-conjugated magnetic probe, Anal. Chem. 87 (2015) 8977–8984.

[86] T. Neufeld, A. Schwartz-Mittelmann, D. Biran, E.Z. Ron, J. Rishpon, Combined phage typing and amperometric detection of released enzymatic activity for the specific identification and quantification of bacteria, Anal. Chem. 75 (2003) 580–585.

[87] S. Burnham, J. Hu, H. Anany, L. Brovko, F. Deiss, R. Derda, M.W. Griffiths, Towards rapid on-site phage-mediated detection of generic Escherichia coli in water using luminescent and visual readout, Anal. Bioanal. Chem. 406 (2014) 5685–5693.

[88] J. Elias, M. Gizowska, P. Brodard, R. Widmer, T. Graule, J. Michler, L. Philippe, Electrodeposition of gold thin films with controlled morphologies and their applications in electrocatalysis and SERS, Nanotechnology. 23 (2012) 255705.

[89] J. Lubkowski, F. Hennecke, A. Plückthun, A. Wlodawer, Filamentous phage infection: crystal structure of g3p in complex with its coreceptor, the C-terminal domain of TolA, Structure. 7 (1999) 711–722.

[90] N.M. Bardhan, D. Ghosh, A.M. Belcher, M13 virus based detection of bacterial infections in living hosts, J. Biophotonics. 7 (2014) 617–623.

[91] F. Karlsson, C.A.K. Borrebaeck, N. Nilsson, A.-C. Malmborg-Hager, The mechanism of bacterial infection by filamentous phages involves molecular interactions between TolA and phage protein 3 domains, J. Bacteriol. 185 (2003) 2628–2634.

[92] G. Chang, H. Shu, K. Ji, M. Oyama, X. Liu, Y. He, Gold nanoparticles directly modified glassy carbon electrode for non-enzymatic detection of glucose, Appl. Surf. Sci. 288 (2014) 524–529.

[93] F. Lisdat, D. Schäfer, The use of electrochemical impedance spectroscopy for biosensing, Anal. Bioanal. Chem. 391 (2008) 1555.

[94] R.Y. Sweeney, E.Y. Park, B.L. Iverson, G. Georgiou, Assembly of multimeric phage nanostructures through leucine zipper interactions, Biotechnol. Bioeng. 95 (2006) 539–545.

[95] Z. Dogic, Filamentous phages as a model system in soft matter physics, Front. Microbiol. 7 (2016) 1013.

[96] M. Manning, S. Chrysogelos, J. Griffith, Mechanism of coliphage M13 contraction: intermediate structures trapped at low temperatures., J. Virol. 40 (1981) 912–919.

[97] T.-T. Ngo-Duc, M.S. Zaman, C.-H. Moon, E.D. Haberer, Morphology manipulation of M13 bacteriophage template for nanostructure assembly, in: Nanobiosystems Process. Charact. Appl. VII, International Society for Optics and Photonics, 2014: p. 91710X.

[98] K. Bekir, H. Barhoumi, M. Braiek, A. Chrouda, N. Zine, N. Abid, A. Maaref, A. Bakhrouf, H. Ben Ouada, N. Jaffrezic-Renault, Electrochemical impedance immunosensor for rapid detection of stressed pathogenic Staphylococcus aureus bacteria, Environ. Sci. Pollut. Res. 22 (2015) 15796–15803.

[99] C. Tlili, E. Sokullu, M. Safavieh, M. Tolba, M.U. Ahmed, M. Zourob, Bacteria screening, viability, and confirmation assays using bacteriophage-impedimetric/loop-mediated isothermal amplification dual-response biosensors, Anal. Chem. 85 (2013) 4893–4901.

[100] A. Shabani, C.A. Marquette, R. Mandeville, M.F. Lawrence, Carbon microarrays for the direct impedimetric detection of Bacillus anthracis using Gamma phages as probes, Analyst. 138 (2013) 1434–1440.

[101] Y. Li, R. Afrasiabi, F. Fathi, N. Wang, C. Xiang, R. Love, Z. She, H.-B. Kraatz, Impedance based detection of pathogenic E. coli O157: H7 using a ferrocene-antimicrobial peptide modified biosensor, Biosens. Bioelectron. 58 (2014) 193–199.

[102] L. Han, P. Liu, V.A. Petrenko, A. Liu, A label-free electrochemical impedance cytosensor based on specific peptide-fused phage selected from landscape phage library, Sci. Rep. 6 (2016) 22199.

[103] Y. Lan, H. Luo, X. Ren, Y. Wang, Y. Liu, Anodic stripping voltammetric determination of arsenic (III) using a glassy carbon electrode modified with gold-palladium bimetallic nanoparticles, Microchim. Acta. 178 (2012) 153–161.

[104] A. Chowdhury, S. Ferdousi, M.M. Islam, T. Okajima, T. Ohsaka, Arsenic detection by nanogold/conducting-polymer-modified glassy carbon electrodes, J. Appl. Polym. Sci. 104 (2007) 1306–1311.

[105] E. Nunez-Bajo, M.C. Blanco-López, A. Costa-García, M.T. Fernández-Abedul, Electrogeneration of Gold Nanoparticles on Porous-Carbon Paper-Based Electrodes and Application to Inorganic Arsenic Analysis in White Wines by Chronoamperometric Stripping, Anal. Chem. 89 (2017) 6415–6423.

[106] S.-H. Shin, H.-G. Hong, Anodic stripping voltammetric detection of arsenic (III) at platinum-iron (III) nanoparticle modified carbon nanotube on glassy carbon electrode, Bull. Korean Chem. Soc. 31 (2010) 3077–3083.

CHAPTER 4

Impedimetric Immunosensor for Early Detection of *Bacteroides* as Bioindicators of Fecal Contamination of Drinking-Water

Abstract: Fecal contamination forms a major burden on public health, as a source of illness with many diseases including dysenteries, cholera, diarrheal diseases, and enteric fevers. *Bacteroides* were found more accurate bioindicators for drinking-water contamination with feces than coliforms and *E. coli*. However, there are no Bacteroides-based biosensors developed. In this work, an electrochemical (impedimetric) immunosensor is developed for the sensitive and selective detection of *Bacteroides thetaiotaomicron* (*B. theta*). The working electrode (glassy carbon) was modified with electrodeposited gold nanoparticles (AuNPs) and functionalized with ani-B. theta antibody via means of covalent bonding to a linker on AuNPs. The sensor fabrication was monitored using electrochemical analysis and electron microscopy imaging. The introduced impedimetric immunosensor achieved a very low limit of detection of 10 CFU/mL of *B. theta* in phosphate buffer (PB) solution. This sensor showed a high selectivity for *B. theta* over other non-host bacterial strain, *E. coli*. The sensor system showed no remarkable response in control experiments, i.e. in absence of antibody, and host bacteria, which eliminates the possibility of any false positive results. The sensor system was tested for detecting *B. theta* spiked in river and tap water sample, to verify their suitability for real field, and it showed a highly similar response to PB samples. Finally, SEM imaging of the sensor system, after incubation with two different concentrations of *B. theta* and washing with PB, confirmed the successful binding of host cells.

4.1. Introduction

Drinking-water pollution is a serious problem raising a huge global concern. Among the various types of pollutants, fecal contamination is associated many pathogenic infections, including dysenteries, cholera, diarrheal diseases, and enteric fevers [1–3]. Coliforms are not one type of bacteria, but a large group of Gram-negative, facultatively anaerobic bacteria found in vegetation, soil, and mammals' intestine [4]. *E. coli* is one type of coliforms that are only found in mammals gut. Total coliforms and *E. coli* detection is used as bioindicators of water contamination with feces [5,6]. Although total coliforms and *E. coli* are not considered pathogens, except for *E. coli* 0157:H7, and they normally do not cause illness, their presence is always indicating the coexistence of pathogens from feces.

According to the U.S. Environmental Protection Agency (EPA) report, about "assessment of the Extra-Enteric Behavior of Fecal Indicator Organisms in Ambient Waters", *Bacteroides* have long been suggested as alternative indicators to E. coli and enterococci [7]. In addition, there is a strong correlation between Bacteroides and fecal coliform concentrations [8], while in terms of numbers, Bacteroides are present in 1000-fold higher concentrations than fecal coliform bacteria [7] and hence they could serve as more sensitive bioindicators of coliforms contamination. In fact, in a variety of surface water samples, Bacteroides were more predictive of the presence of bacterial pathogens in water than traditional indicators [9]. It is worth mentioning that Bacteroides are strict anaerobes and are not expected neither to divide nor to survive for extended periods of time under aerobic conditions, which again makes them more accurate bioindicators of fecal coliforms contamination [10,11].

Microbial electrochemical sensors (MESs) are very promising as highly sensitive, label-free, real-time, and selective systems for early detection of microbes [12–15]. MESs attracted a great attention due to their rapid and sensitive response, as well as their simplicity and suitability as portable devices that do not require highly trained personnel [16–19]. Electrochemical impedance spectroscopy (EIS) is a very powerful tool for monitoring the minute changes at the electrode interface. Furthermore, EIS requires a small amplitude perturbation, which makes it a nondestructive technique [20]. The specificity of a biosensor is determined by the biorecognition elements, such as aptamers, peptides, and antibodies [21].

Having that said, development of sensitive and selective electrochemical biosensors for detection of Bacteroides is a necessity. In this work, impedimetric immunosensor was developed for detection of one of the Bacteroides strains, *Bacteroides thetaiotaomicron* (B. theta). The sensor structure is similar to the *M13* phage-EIS system in chapter 3 with replacing M13 with B. theta antibodies. In order to check for the ability of the Anti-B. theta EIS biosensor to detect B. theta cells, a series of concentrations of these bacteria were suspended in PB and the sensor was used to detect them and build the calibration curve. Different control samples were used to eliminate the possibility of false positive readings and to ensure the selectivity of the sensor system.

4.2. Materials and Methods

4.2.1. Materials

Gold chloride hydrate, potassium ferricyanide, 3-mercaptopropanoic acid (MPA), 2-(N-morpholino) ethane sulfonic acid (MES), 1-Ethyl-3-(3-dimethylaminopropyl) carbodiimide (EDC), N-Hydroxysuccinimide (NHS), and Bovine albumin (BSA) were purchased from Sigma-Aldrich (St. Louis, USA). Ethanol amine (EA) was purchased from Acros Organic-Fisher Scientific. Anti-Bacteroides Thetaiotaomicron monoclonal antibody (Anti-B. theta) was purchased from GeneTex (Irvine, USA). Antibody purification, using Sephadex G-25 (PD-10 Desalting Columns) via gravity protocol, was carried out before implementing it into the sensor system. All solutions were prepared with Milli-Q water.

4.2.2. Bacteroides Thetaiotaomicron samples

B. theta stock sample was received from Dr. Joan B. Rose's lab at Michigan State University, as freeze-dried stock samples that when redispersed in 10 mL of PB, the final concentration is 10^8 CFU/mL. Serial dilutions were used to prepare lower concentrations.

4.2.3. Electrodeposition of AuNPs.

AuNPs were electrodeposited on GCE and characterized the same as in the previous chapter 3.

4.2.4. Instruments and measurements

Technical details of instrumentation are explained in detail in chapter 3, section 2.5. Briefly, electrochemical impedance spectroscopy (EIS) was carried out as Faradaic EIS,

and the corresponding charge transfer resistance (Rct) was extracted by simulating the signal with the suitable Randles circuit using CHI's ready-to-use software.

4.2.5. Sensor development

The development process is schematically illustrated in **Fig. 4.1**. GCE with electrodeposited AuNPs was immersed in 0.1 M solution of 3-mercaptopropanoic acid (MPA) in ethanol for 1 h to form a self-assembled monolayer on gold surface, followed by washing with ethanol to remove any physically adsorbed MPA molecules. The carboxyl group of MPA was then activated using EDC/NHS chemistry. Briefly, the Au-MPA electrode was immersed in 0.1 M MES buffer (pH 5.5) containing 0.15 M EDC for 20 min. then removed from EDC solution and immersed in 0.15 M NHS for 20 min. The electrode was washed using MES buffer to remove unreacted EDC/NHS molecules. The modified and activated electrode was incubated with M13 solution (10 μg/mL) at 4 °C for 3 h, followed by rinsing with PB buffer to remove unbound antibodies. Subsequently, the electrode was immersed in 0.1 M ethanolamine solution for 30 min to passivate unreacted -NHS groups, followed by incubation with 0.2 % BSA solution for 30 min to block unfunctionalized Au. The electrode was washed thoroughly with PB solution. In this work, EA+BSA are labeled as "blocker" on graphs and schemes. All the modifications steps

during the electrode fabrication were monitored and characterized using CV and EIS in ferricyanide solution.

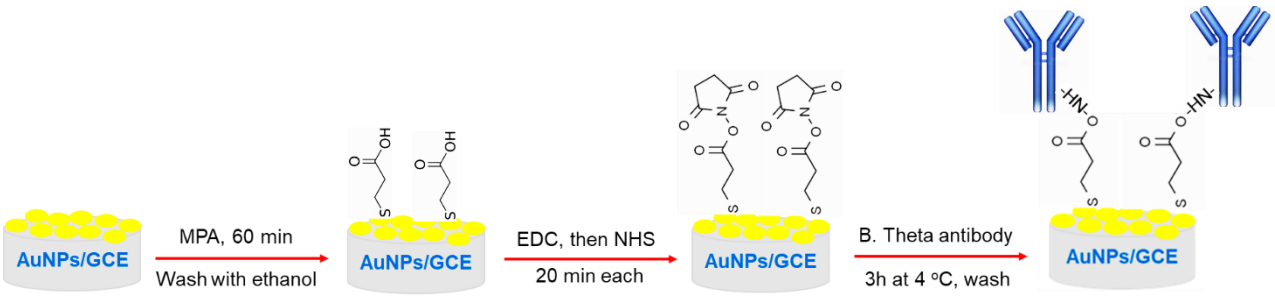

Figure 4.1. Schematic diagram of the Bacteroides immunosensor fabrication process.

4.2.6. SEM imaging

The imaging was conducted on a smooth thin film of gold prepared by e-beam evaporation instead of gold nanoparticles to avoid feature overlap. The thin film's surface was modified the same way as described in the sensor build up section. Then, two sensors were incubated with two concentrations (10^5 and 10^7 CFU/mL) for 20 min, gently washed with PB, and left to dry in the laminar hood for one hour. A thin film of gold was sputtered on the sample to avoid surface charging, as planktonic bacteria, linker, and antibody are non-conductive.

4.3. Results and Discussion

4.3.1. Sensor development

The sensor system's development was monitored using EIS measurements at each modification step, and results are shown in **Fig. 4.2**. The charge transfer resistance (radius of half circle) in EIS increased. This observation is in a good agreement with the expected insulative and charge repulsive effects of the attached negatively charged molecules to the

redox probe of potassium ferricyanide $[Fe(CN)_6]^{3-}$ [22,23]. The resulting electrode was then used as a working electrode in a 3-electrode electrochemical cell for evaluation of analytical figures of merits (sensitivity, limit of detection and selectivity) for anti-B. theta-based EIS biosensor.

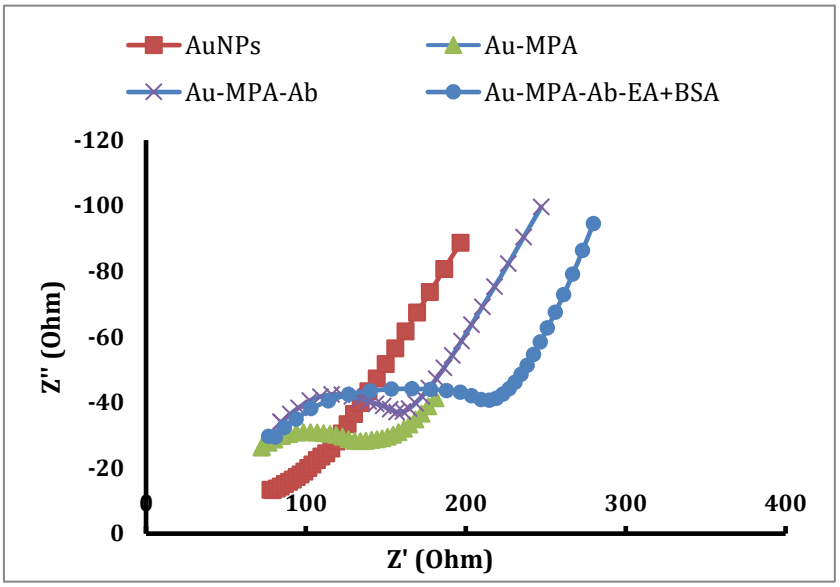

Figure 4.2. Faradaic EIS results of sensor fabrication.

4.3.2. Calibration curve and limit of detection

After verifying the successful fabrication of the impedimetric immunosensor (anti-B. theta-EIS), it was tested for the detection of different concentrations of B. theta spiked in PB. The working electrode was immersed into the solution of b. theta and incubated for 25-30 min, gently washed with PB for three times. Then, the EIS was measured for each concentration and the corresponding Rct value was extracted, and the calibration curve was plotted in terms of change in Rct.

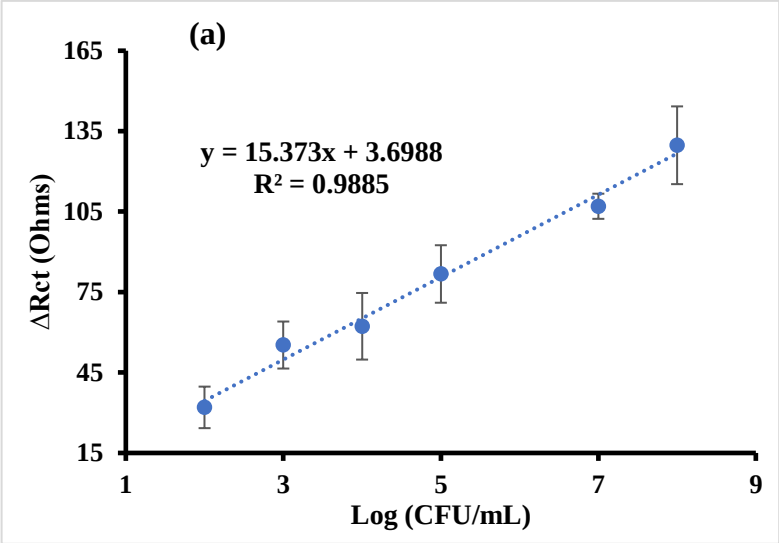

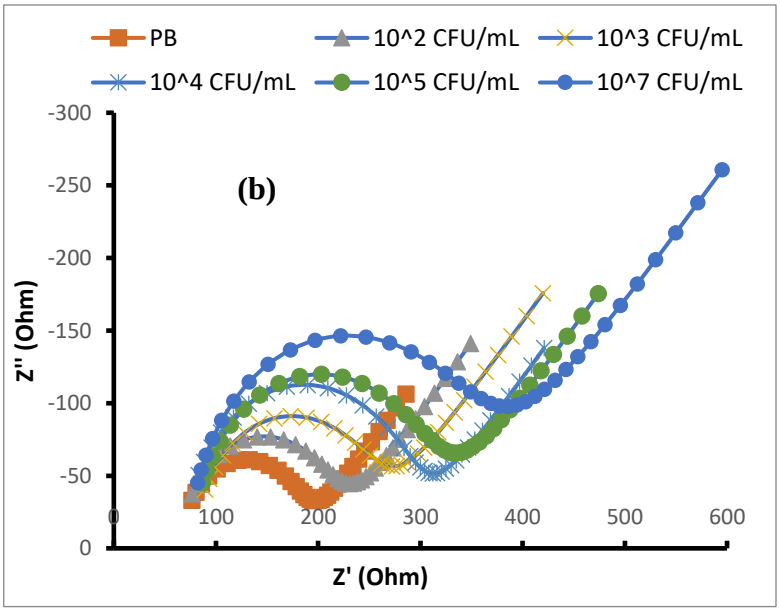

Figure 4.3. (a) Calibration plot of anti-B. theta-based EIS biosensor in buffer Each data point is an average of 4 measurements; 2 electrodes, each measured 2 times. (b) Nyquist plots of one of the electrodes at different concentrations.

Fig. 4.3 summarizes the results. As illustrated in the figure, the new anti-B. theta-EIS shows a wide dynamic range from 10^2 to 10^8 CFU/mL of detecting bacteria with high sensitivity of 15.37 Ohms/Log and an extremely low limit of detection (LOD) of ~10 CFU/mL. The limit of detection was calculated from the equation **LOD = 3*SD/S**, where SD is the standard deviation of blank sample (SD = 4.9 Ohms, n = 4). Results in **Fig. 4.3b** show an increase in the charge transfer resistance with the increased concentration of attached bacteria, which can be attributed to the insulative nature of bacteria and its negative charges that will repel the negatively charged redox probe.

4.3.3. Visualization of detected bacteria using SEM imaging

SEM imaging was used to visualize the detected bacteria and confirm their surface binding after washing with PB. Images in **Fig. 4.4** show nicely distributed B. theta cells captured by the anti-B. theta antibody on gold surface. It is worth mentioning that to keep the 3D structure of bacteria without sophisticated sample preparations, it is important to let it dry in a laminar flow hood for less than an hour, to avoid dehydration and collapsing of the cell membrane. Furthermore, to avoid cells rupture, preserve the cells integrity and eliminate surface charging, gold sputtering is very essential. The density of captured bacteria increased with its concentration from 10^5 to 10^7 CFU/mL in panels (a) and (b), which confirms the positive response of the sensor system.

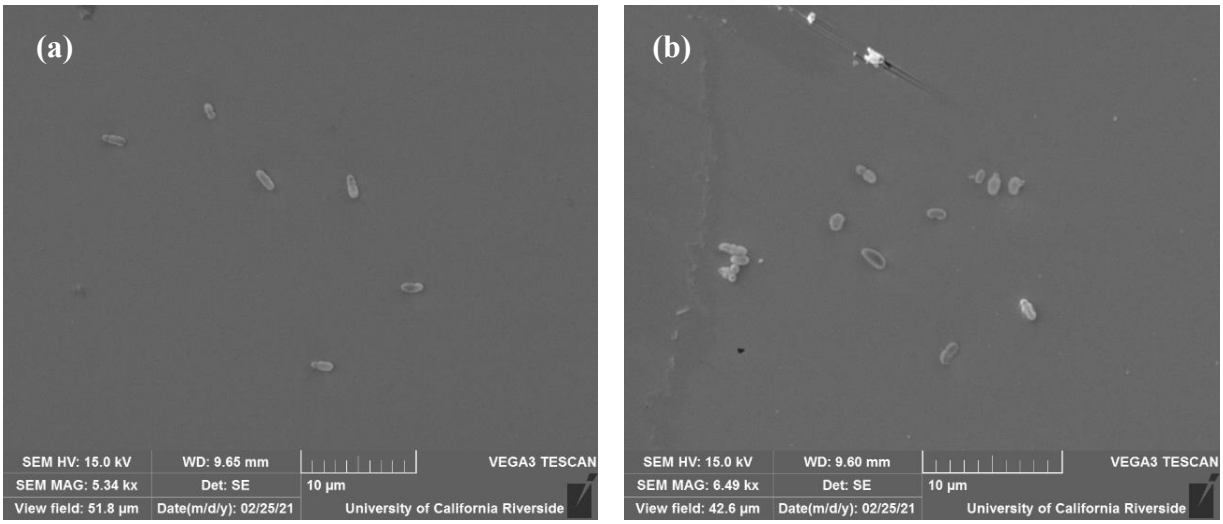

Figure 4.4. SEM imaging of B. theta captured on the sensor surface at two concentrations: 10^5 (a) and 10^7 (b).

4.3.4. Spiked real sample testing

The ability of the sensor to detect B. theta in spiked real river water samples was evaluated. As shown in **Fig. 4.5**, the sensor's response to B. theta in PB and River water is showing almost the same sensitivity (slopes), which is confirming the potential of the real field application of this sensor. However, there is some background shift in the Tap water sample, which can be attributed to the difference in the matrix composition.

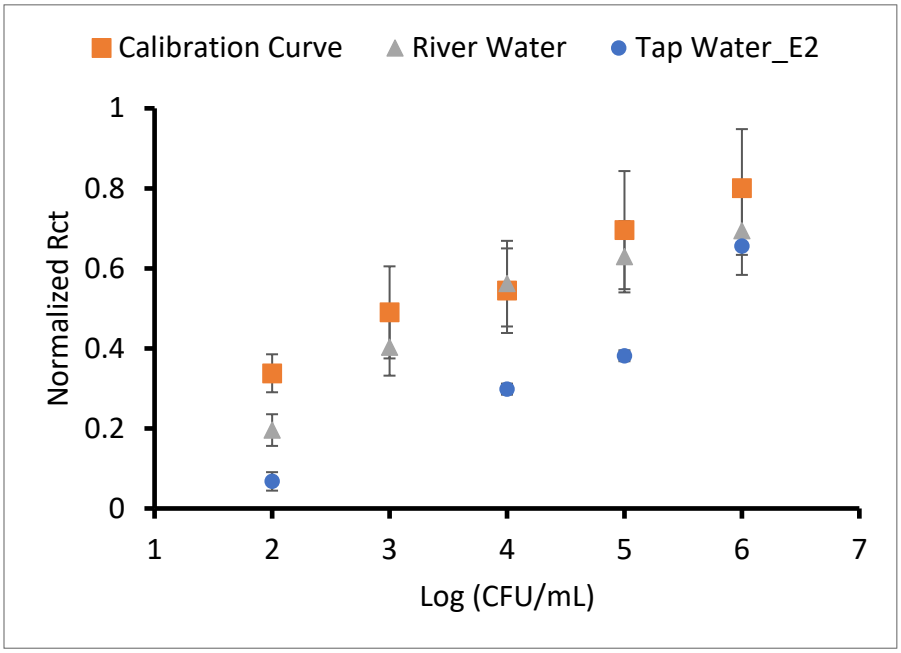

Figure 4.5. Calibration plot of anti-B. theta-based EIS biosensor in PB (calibration curve), river water, and . Each data point is an average of 4 measurements; 2 electrodes, each measured 2 times.

4.3.5. Control experiments

conducted some control experiments to verify that the signal response is coming from the selective binding of the sensor to B. theta cells. First, the sensor functionalized with anti-b theta antibodies was tested for the detection of the non-host cells, E. coli, and there was no significant response detected as shown in **Fig. 4.6** (yellow curve). Second, the anti-B. theta-loaded sensor was tested against a buffer solution that has no bacteria, and there was no detectable response signal (red curve). Lastly, the sensor, containing no antibody, was incubated with the B. theta cells, and there was no remarkable response as well (blue curve). That all confirms that the response signals were coming from the B. theta binding to the sensor in the calibration curve and spiked river water samples.

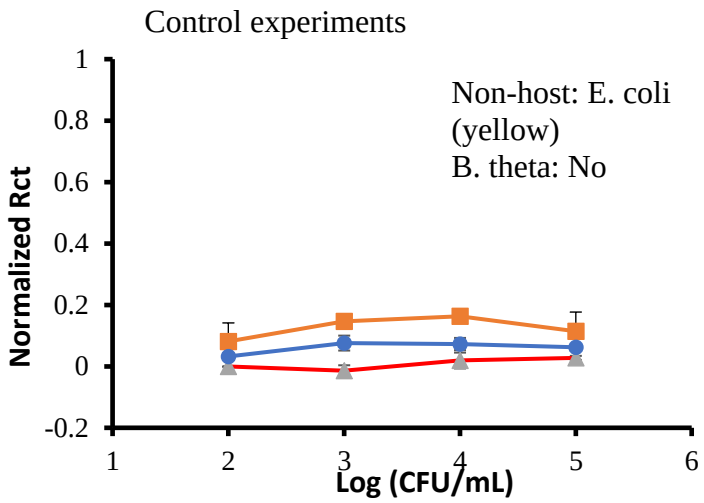

Figure 4.6. Control experiments of anti-B. theta-based EIS sensor.

4.4. Conclusions

In summary, a highly sensitive and selective impedimetric immunosensor was introduced for the first time for the detection of *Bacteroides Thetaiotaomicron* in drinking water. Thanks to the specific biorecognition element, anti-Bacteroides Thetaiotaomicron antibody, the sensor was able to detect the target bacteria only and neglect the non-host cells. Interestingly, the river water matrix did not compromise the performance of the current system. In addition to the specificity of the loaded antibody, blocking the free carboxyl groups from MPA by ethanol amine and blocking the exposed gold with BSA did help in eliminating any possible non-specific bindings. The very low LOD (10 CFU/mL), selectivity, and successful detection in river water, entitles this immunosensor to be used in real field application, as an economic portable sensor system.

4.5. References

[1] R. Bain, R. Cronk, J. Wright, H. Yang, T. Slaymaker, J. Bartram, Fecal contamination of drinking-water in low-and middle-income countries: a systematic review and meta-analysis, PLoS Med. 11 (2014) e1001644.

[2] G.F. White, D.J. Bradley, A.U. White, Drawers of water: domestic water use in East Africa, Bull. World Health Organ. 80 (2002) 63–73.

[3] F. Edition, Guidelines for drinking-water quality, WHO Chron. 38 (2011) 104–108.

[4] R.K. Robinson, Encyclopedia of food microbiology, Academic press, 2014.

[5] E. Li, F. Saleem, T.A. Edge, H.E. Schellhorn, Biological Indicators for Fecal Pollution Detection and Source Tracking: A Review, Processes. 9 (2021) 2058.

[6] N.H. Martin, A. Trmčić, T.-H. Hsieh, K.J. Boor, M. Wiedmann, The evolving role of coliforms as indicators of unhygienic processing conditions in dairy foods, Front. Microbiol. 7 (2016) 1549.

[7] L. Fiksdal, J.S. Maki, S.J. LaCroix, J.T. Staley, Survival and detection of Bacteroides spp., prospective indicator bacteria, Appl. Environ. Microbiol. 49 (1985) 148–150.

[8] L.K. Dick, K.G. Field, Rapid estimation of numbers of fecal Bacteroidetes by use of a quantitative PCR assay for 16S rRNA genes, Appl. Environ. Microbiol. 70 (2004) 5695–5697.

[9] O. Savichtcheva, N. Okayama, S. Okabe, Relationships between Bacteroides 16S rRNA genetic markers and presence of bacterial enteric pathogens and conventional fecal indicators, Water Res. 41 (2007) 3615–3628.

[10] J.A. Ufnar, S.Y. Wang, J.M. Christiansen, H. Yampara-Iquise, C.A. Carson, R.D. Ellender, Detection of the nifH gene of Methanobrevibacter smithii: a potential tool to identify sewage pollution in recreational waters, J. Appl. Microbiol. 101 (2006) 44–52.

[11] B. Hughes, D.J. Beale, P.G. Dennis, S. Cook, W. Ahmed, Cross-comparison of human wastewater-associated molecular markers in relation to fecal indicator bacteria and enteric viruses in recreational beach waters, Appl. Environ. Microbiol. 83 (2017) e00028-17.

[12] H.M.M. Selim, A.M. Kamal, D.M.M. Ali, R.Y.A. Hassan, Bioelectrochemical systems for measuring microbial cellular functions, Electroanalysis. 29 (2017) 1498–1505.

[13] M. Sedki, R.Y.A. Hassan, A. Hefnawy, I.M. El-Sherbiny, Sensing of bacterial cell viability using nanostructured bioelectrochemical system: rGO-hyperbranched chitosan nanocomposite as a novel microbial sensor platform, Sensors Actuators, B Chem. 252 (2017). https://doi.org/10.1016/j.snb.2017.05.163.

[14] D.C. Wallace, W. Fan, V. Procaccio, Mitochondrial energetics and therapeutics, Annu. Rev. Pathol. Mech. Dis. 5 (2010) 297–348.

[15] F.J. Rawson, A.J. Downard, K.H. Baronian, Electrochemical detection of intracellular and cell membrane redox systems in Saccharomyces cerevisiae, Sci. Rep. 4 (2014) 5216.

[16] D. Ivnitski, I. Abdel-Hamid, P. Atanasov, E. Wilkins, S. Stricker, Application of electrochemical biosensors for detection of food pathogenic bacteria, Electroanal. An Int. J. Devoted to Fundam. Pract. Asp. Electroanal. 12 (2000) 317–325.

[17] E.B. Setterington, E.C. Alocilja, Electrochemical biosensor for rapid and sensitive detection of magnetically extracted bacterial pathogens, Biosensors. 2 (2012) 15–31.

[18] C. Bao, L. Chen, T. Wang, C. Lei, F. Tian, D. Cui, Y. Zhou, One step quick detection of cancer cell surface marker by integrated NiFe-based magnetic biosensing cell cultural chip, Nano-Micro Lett. 5 (2013) 213–222.

[19] A. Zhang, W. Guo, H. Ke, X. Zhang, H. Zhang, C. Huang, D. Yang, N. Jia, D. Cui, Sandwich-format ECL immunosensor based on Au star@ BSA-Luminol nanocomposites for determination of human chorionic gonadotropin, Biosens. Bioelectron. 101 (2018) 219–226.

[20] X. Guo, A. Kulkarni, A. Doepke, H.B. Halsall, S. Iyer, W.R. Heineman, Carbohydrate-based label-free detection of Escherichia coli ORN 178 using electrochemical impedance spectroscopy, Anal. Chem. 84 (2011) 241–246.

[21] Y. Zhou, A. Marar, P. Kner, R.P. Ramasamy, Charge-directed immobilization of bacteriophage on nanostructured electrode for whole-cell electrochemical biosensors, Anal. Chem. 89 (2017) 5734–5741.

[22] F. Lisdat, D. Schäfer, The use of electrochemical impedance spectroscopy for biosensing, Anal. Bioanal. Chem. 391 (2008) 1555.

[23] M. Sedki, X. Chen, C. Chen, X. Ge, A. Mulchandani, Non-lytic M13 phage-based highly sensitive impedimetric cytosensor for detection of coliforms, Biosens. Bioelectron. 148 (2020). https://doi.org/10.1016/j.bios.2019.111794.

CHAPTER 5

Synthesis of Pristine Graphene-like Behaving rGO Thin Film: Insights into What Really Matters

Abstract: Despite the huge expansion of GO/rGO market, there is a clear lack of experimental studies on getting high quality, large scale GO and rGO nanosheets/thin sfilms, which is a critical requirement for electronic applications. In this work, a detailed experimental study on the effect of lateral sheet size on properties of GO/rGO, supported by density functional theory (DFT) calculations, is presented for the first time, to help prepare pristine graphene-like rGO. Furthermore, we investigated the effect of thermal reduction at low temperature (200 ^{o}C), under ambient pressure, on the corresponding electronic properties of rGO. Current-voltage (I-V) analysis, optical and electron microscopy, atomic force microscopy, Raman, XPS, and quantitative ^{13}C NMR spectroscopy were used to study and optimize rGO. The optimized rGO-field-effect transistor (rGO-FET) device exhibited the highest charge carrier mobilities, i.e. 2,962 (holes) and 2,183 (electrons) cm^2/V.s. Furthermore, the transconductance characteristics curve of rGO-FET showed the ambipolar behavior of high-quality graphene, with Dirac point around zero. In addition, the optical band gap of rGO nanosheets (~0.4 eV), prepared in this work, is among the smallest reported band gaps for rGO. These findings highlight the significance of our study for synthesizing large-scale graphene-like rGO thin film, for ultra-fast, low-power transistor applications.

5.1. Introduction

Graphene is a two-dimensional (2D) one atom-thick layer of carbon atoms packed in honeycomb hexagonal lattice, with very attractive mechanical, electrical, thermal, and optical properties.[1] It has a high intrinsic mobility of 200,000 cm^2/V.s, high thermal conductivity of ~ 5000 W/m.K, and large specific theoretical surface area of 2630 m^2/g.[1–3] Due to its superior properties, graphene and its derivatives are widely used in a wide range of applications, including batteries [4,5], liquid crystals [6], hydrogen storage [7], field emission cathodes [8], organic photovoltaics[9], transistors [10], reinforcing polymers [11], water membranes [12], etc.

Chemical vapor deposition (CVD) and molecular beam epitaxy (MBE) are getting more attention as versatile bottom up techniques in synthesis of high-quality graphene for electronic applications, compared to liquid phase exfoliation (LPE).[13] Despite being environmentally friend and having a potential for large scale production of graphene, LPE produces low yield (especially for the monolayer sheets), small flake size (<5μm), limited dispersibility, etc.[14] Among many approaches, chemical oxidation of graphite to graphene oxide (GO) and then its reduction to reduced graphene oxide (rGO) is one of the promising mass production routes of graphene.[15],[16] GO solves many of the problems of the CVD-, MBE-, and LPE-prepared graphene, as it is economic and easy to scale up with the desired functionalities, and it achieves high dispersibility of small and large flakes as well as high yields of monolayer sheets [1,15,17]. It can also be used to form stable graphene thin films [18] by means of drop casting, spin coating, or spraying GO suspension to the target surface, and *in situ* reducing it to rGO/graphene thin film at low temperatures.

In addition, the reduction of GO can be controlled to prepare graphene materials with tunable band gaps [19]. Therefore, rGO is an excellent source of graphene.

Nevertheless, GO remains an elusive material [20,21] and there is a huge variation in the properties of the graphene produced by oxidative exfoliation. There are many recent reports on GO/rGO nanosheets and their composites, however, there exists an overwhelming consensus among researchers on the lack of high-quality, electronic-grade graphene on the market [22],[23]. Furthermore, the physicochemical and electrical properties of graphene varies widely due to the lack of fundamental understanding of factors determining the quality of graphene thin films produced from the rGO nanosheets, limiting their usage in the electronic applications, particularly in the field-effect transistor (FET) systems. A recent promising study conducted by Kauling et al. on the LPE graphene from 60 producers demonstrated that there is a huge variation in the quality of produced graphene on market, and they introduced a systematic and reliable protocol to test graphene quality, which should help the market move faster and more efficiently with this method [22].

To the best of our knowledge, there is lack of studies on the main contributing factors in production of high quality rGO thin films that exhibit pristine graphene-like properties. This work also aims at revealing the factors that really matter for producing pristine graphene-like behaving rGO thin film. The number of stacked layers and thickness of drop casted rGO film play a role and hence we kept them uniform through the whole study to understand the effect of other contributing factors. Among many contributing factors, we found that lateral sheet size of GO/rGO, that is defined by the lateral size of the starting

graphite flakes, plays a crucial role in the electronic properties of rGO nanosheets, rGO thin films, and their corresponding FET devices.

In this work, we have studied the effect of lateral sheet size on the electronic properties of the corresponding thin films of rGO. The experimental measurements were supported by density functional theory (DFT) calculations. In addition, we studied the effect of thermal reduction on the chemical composition of the large and small GO nanosheets synthesized by improved Hummers method (IHM) [24] at low temperature (200 ^{o}C), under ambient pressure, which allowed for more insights into the effect of lateral sheet size on the electronic properties of rGO thin films. All electrical measurements were done via rGO-FET, using gold interdigitated electrodes (IDE). The optimized rGO nanosheets showed the smallest optical band gap (0.4 eV) and the highest charge carrier mobilities reported for rGO, to-date. Furthermore, FET characteristic curve of rGO-FET showed the nice ambipolar behavior of high-quality graphene, with Dirac point around zero. These results highlight the importance of this study for both researchers and companies aiming at using rGO for electronic applications.

5.2. Materials and Methods

5.2.1. *Materials*

Graphite powder (0.2 µm), potassium permanganates ($KMnO_4$, 99%), phosphoric acid (H_3PO_4, 85%), sulfuric acid (H_2SO_4, 98%), hydrochloric acid (HCl, 37%) and hydrogen peroxide (H_2O_2, 30%) were procured from Fisher Scientific, USA. Graphite powder (1-2 µm) and (3-Aminopropyl) triethoxysilane (APTES) were purchased from Sigma (St. Louis,

MO, USA). Graphite flakes (7-10 µm) and (40 µm, -325 mesh) were bought from Alfa Aesar (Ward Hill, MA, USA). For the 0.2 µm graphite, it is labeled by the manufacturer as graphite powder. From our characterizations, including AFM imaging, the lateral size was found < 1.0 µm with an average of 0.2 µm. The 40 µm sample is labelled by the manufacturer as graphite flakes -325 mesh.

5.2.2. *Synthesis of GO nanosheets*

GO nanosheets were prepared using the improved Hummers method (IHM) [24], with some changes in reaction temperature and time, as we previously reported [25]. Briefly, 1 g of graphite powder was added to a mixture of 13 mL of phosphoric acid 98% and 120 mL of sulfuric acid 98%, and left under magnetic stirring for half an hour at room temperature. Then, 6 g of potassium permanganate was added portion-wise to the homogenized mixture. The reaction temperature was elevated to 45^{o}C and the reaction mixture was kept stirring for 3 h. The reaction was stopped by slow and cautious pouring of the reaction mixture to a beaker containing a mixture of 150 mL of deionized (D.I.) water and 20 mL of hydrogen peroxide. Excess D.I. water was added to the beaker and the mixture was kept static overnight to settle the prepared graphite oxide (GtO) nanosheets down and make it easy to decant the highly acidic supernatant. The prepared graphite oxide (GtO) sheets were washed several times with hydrochloric acid (5%) and D.I. water by centrifugation, and then with D.I. water to form graphene oxide (GO) nanosheets. Further exfoliation by sonication can be used, however, it is not necessary in this method. The sample was dried at 50^{o}C.

5.2.3. *Fabrication of rGO-FET chips*

Devices (chips) were microfabricated on a highly doped p-type silicon substrate with approximately 300 nm SiO_2 insulating layer deposited on top. Electrodes were patterned on the substrate by photolithography. Next, 5 nm Cr layer was deposited on the substrate, followed by a 50 nm layer of Au, using e-beam evaporation. Each chip had 20 interdigitated gold fingers (10 pairs), the width of each finger was 5 μm and was separated by a gap of 3 μm (**Fig. 5.1a**). Electrodes were then defined using a standard lift-off technique. Chips with patterned electrodes were cut from whole wafer, cleaned, and immersed in ammonia solution, for 1 h, to introduce hydroxyl groups. Next, chips were immersed in 3-aminopropyltriethoxy silane (APTES) for 1 h, to assist GO nanosheets immobilization. Then, 10 μL suspension of GO in D.I. water of different concentrations was drop casted to the five interdigitated electrodes. The GO drop was left to dry and form a thin film at room temperature, and then annealed at 200^{o}C for 120 min.

5.2.4. *Characterizations*

The prepared materials were characterized using scanning electron microscopy (SEM, ThermoFisher Scientific (formerly FEI/Philips) NNS450) and UV-Visible spectrophotometer. Raman spectra were collected by Horiba LabRam using a green laser (λ = 532 nm) for excitation with a power of 10 mW. X-ray photoelectron spectroscopy (XPS) characterization was carried out using a Kratos AXIS ULTRA^{DLD} XPS system equipped with an Al X-ray source and a 165-mm mean radius electron energy hemispherical analyzer. Samples were prepared as thick films (~1 mm) on gold-coated

polyimide substrate. Vacuum pressure was kept below 3×10^{-9} torr during the acquisition. Data were acquired with a step size of 0.2 eV and 0.1 eV for the survey and the high resolution (C1s and O1s) spectra, respectively. Quantitative solid state single pulse ^{13}C magic angle spinning (MAS) NMR spectral analysis was performed using Bruker Avance NEO 600 MHz spectrometer. The samples were ground and packed into a 4 mm rotor. Then, samples were spun at 10 kHz for more than 3000 scans with a relaxation delay of 10 s. 7.2 µs 90-degree pulse excitation was used over a bandwidth of 150 MHz and we used solid adamantane (38.48 ppm) as the reference for ^{13}C spectrum based on the trimethylsilane scale. Electrical measurements were conducted using Keithley 2636 system.

5.3. Results and discussion

GO was synthesized using IHM [24] with some modifications in reaction time and temperature, as we reported [26] in a previous work. Then, GO was thermally reduced at 200 ^{o}C, in open air, for 2 h. All electrical characterizations of rGO reported in this study were conducted via FET system. The configuration and channel dimensions of the gold interdigitated electrodes (IDEs) chip or the FET system are illustrated in **Fig. 5.1a**. Each IDE has 5 µm wide by 200 µm long gold strips/fingers electrodes separated by 3 µm (gaps) with a total working area of 180 x 200 μm^2. Moreover, each chip has a set of 5 IDEs. rGO thin film is covering the whole working area, filling the channel gaps, and bridging the gold strips to close the circuit, as illustrated in the schematic of **Fig. 5.1a**. A simple and efficient preparation method was developed so that a well-connected nice film of rGO was formed on top of the gold IDEs resulting in rGO-FET. Briefly, 10 µL of GO suspension,

with different concentrations, were drop casted to the working area of IDEs, warmed to dry, and then thermally reduced at 200 ^{o}C in oven, under ambient pressure. The effect of concentration of GO, at a fixed volume of 10 µL, on the resistance/transport characteristics was studied. Scanning electron microscopy (SEM) imaging was used to investigate the concentration and quality of the rGO thin film on gold IDEs. SEM images, **Fig 5.1 (c & d)**, show that a thick film with folding/wrinkles was formed at the 10 mg/mL, while a nice transparent and flat thin film of rGO was formed at the concentration of 1.25 mg/mL. Additional SEM images for other concentrations are available in Appendix C, **Fig. C1**. As illustrated in **Fig. 5.1b**, the device's resistance decreased by decreasing GO's concentration from 10 mg/mL to 2.5 mg/mL, stabilized at 1.25 mg/mL and then increased again upon decreasing the concentration below 1.25 mg/mL. Hence, the recommended concentration for use in rGO-FET system preparation is 1.25 mg/mL.

In general, the FET characteristics in the nano-scaled device are determined by the quality of the constituent device elements such as channel, contact and gate. The factors that influence the device characteristics include: 1) properties of channel material, in this case rGO, such as lateral size, and quality of the deposited graphene sheets [27]; and 2) channel length [28] and applied source-drain potential. In our study, we focus on the impact of lateral sheet size on properties of rGO, while keeping other parameters/factors constant. It is worth mentioning that the lateral sheet size of rGO is taken to be the lateral size of starting graphite.

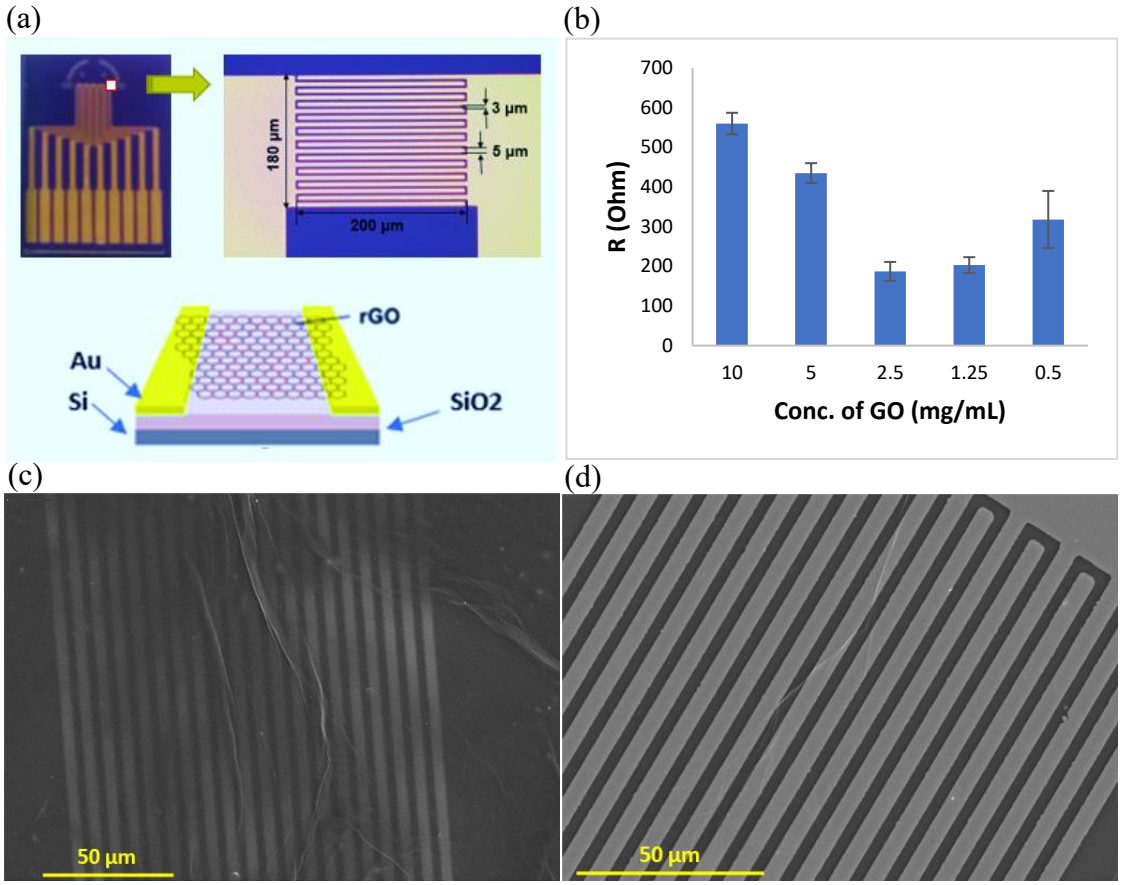

Figure 5.1. (a) camera image of the FET device of 5 IDEs (left), an optical microscopy image of one of the IDEs (right), and a schematic of rGO bridging two gold strips (bottom). (b) Effect of GO's concentration (mg/mL) on the device's resistance (Ohms). (c & d) SEM images of rGO-FET at 10 & 1.25 mg/mL, respectively.

5.3.1. Oxidative exfoliation

The electrical conductivity in graphite is an anisotropic property, and the larger the number of stacked layers, the bigger is the interlayer charge screening and scattering [29]. It is worth mentioning that most of the graphite flakes/powders available in the commercial market have wide range of sheet sizes in the same sample. For example, the 40 µm product had sheets ranging from 5 to 40 µm, with a majority between 15-20 µm; it was the same

for 0.2, 2, and 10 μm sizes. Lateral sizes and thickness distributions of the four GO samples are shown in Appendix C, **Fig. C2**. Hence, we have adapted centrifugation to remove the very small and very large sheets. All the four different size GOs, used in the resistance comparison, were investigated for their level of exfoliation using atomic force microscopy (AFM) imaging. The results in **Fig. 5.2 (a-d)** show that the thickness of the GO nanosheets in 0.2, 2, 10, and 40 μm lateral size samples is uniform at ≈1.2 nm, which corresponds to monolayer GO nanosheets [30,31]. The equal number of layers in the four GO samples confirms that the variation in resistance can be attributed to lateral sheet size effect and not due to the difference in exfoliation. Another important observation was that the sheets larger than 10 μm lateral size tend to fold, **Fig. 5.2 (e & f)**. This correlation between sheet size and folding is reported for the first time. However, the sheet folding problem in general was discussed in a recent report, and it can be explained by the compressive stress on the very flexible GO nanosheets during solution processing and deposition to substrates [32,33]. When the sheet first touches the substrate, it binds to it from one edge and then either to flatten on the surface in a way the other edges bind to substrate or to fold or roll around itself [34]. We believe that is attributed to the mechanical properties of the graphene sheets, especially their bending stress that increases by increasing the lateral size of the sheet, and hence makes it easier to fold and roll.

5.3.2. *Lateral sheet size*

To study the effect of lateral sheet size on device resistance, a potential of 0.1 V was applied between the source and drain of the rGO-FET devices made of thin films of different lateral sizes of rGO and the corresponding resistance was measured (**Table 5.1**). A bimodal linear

correlation between the sheet size and device conductivity is evident from the tabulated data; a clear decrease in resistance with the increase in rGO lateral size from 0.2 to 10 μm and a very minor decrease in larger sizes such as 40 μm. The latter can be ascribed to the folding and rolling of the nanosheets larger than 10 μm, as seen in **Fig. 5.2 (e & f)**. The folding/rolling was quantified using AFM imaging, by measuring the sheet height at the folding/rolling sites and found it 2.1, 2.3, 2.8, and 3.7 nm at four (F_1-F_4) different sites (see **Fig. 5.2 (e & f**), with an average height of 2.73±0.71 nm. This number counts for the thickness of two sheets in addition to the curvature of folding. The thickness of two GO sheets is around 2 nm, and hence the folding/rolling curvature is about 0.73 nm on average. This number is not high due to the high flexibility of GO as well as its large size that increases the compressive pressure and results in flattening of the folded/rolled sheets. Corresponding AFM height profiles of folded/rolled GO nanosheets are shown in **Appendix C, Fig. C3**. For the 40 μm lateral size sample, despite the folding that might increase the surface roughness of a few nanometers, the film continuity is still better, the number of interfaces/grain boundaries is less, and the contribution from edge defects is smaller. A detailed discussion of the effect of lateral size on edge defects is discussed in **section 5.3.2.2**. So, the net result was that the film made from the 40 μm sheets has a slightly lower resistance. To summarize, we attribute the decrease in the resistance with increasing lateral sheet size to the enhanced film continuity, the smaller surface/interface roughness scattering, and lower contribution of non-healable edge defects.

5.3.2.1. Film continuity and interface roughness scattering

Graphene films made from smaller rGO sheets have greater discontinuities, due to the larger number of grain boundaries, and in-turn exhibit more charge screening and interface roughness scattering due to the bridging of randomly distributed small sheets. On the other hand, larger sheets network better to the adjacent sheets and form a well-connected film. The optical microscopy images, **Fig. 5.3a**, show clear discontinuity and random orientation in thin film of small rGO sheets (0.2 μm) on Si/SiO_2 surface. In comparison, large sheets (flakes) of rGO show well-connected thin film with fine wrinkles that are 10-20 μm apart, **Fig. 5.3b**, which secures good electron transfer between the gold electrodes with gaps of 10-20 μm.

It is well known that the increase in surface/interface roughness increases the charge scattering dramatically and reduces the device's carrier mobility [35]. Hence, the surface roughness of thin films of rGO nanosheets of two different sizes (0.2 and 40 μm) were investigated by AFM scanning, **Fig. 5.3 (c-f)**. The AFM image and height profile of 40 μm rGO thin film in **Fig. 5.3 (c & d)** shows some fine wrinkles that are spaced 10 μm apart, as in the optical image in **Fig. 5.3b**. The wrinkles may be due to the difference in the thermal expansion coefficients between rGO and SiO_2/Si substrate, which was reported elsewhere in case of graphene on Cu substrate [36,37]. The surface/interface roughness between wrinkles was 4±3 nm, and when the wrinkles are included, the surface roughness slightly increased to 6±5 nm.

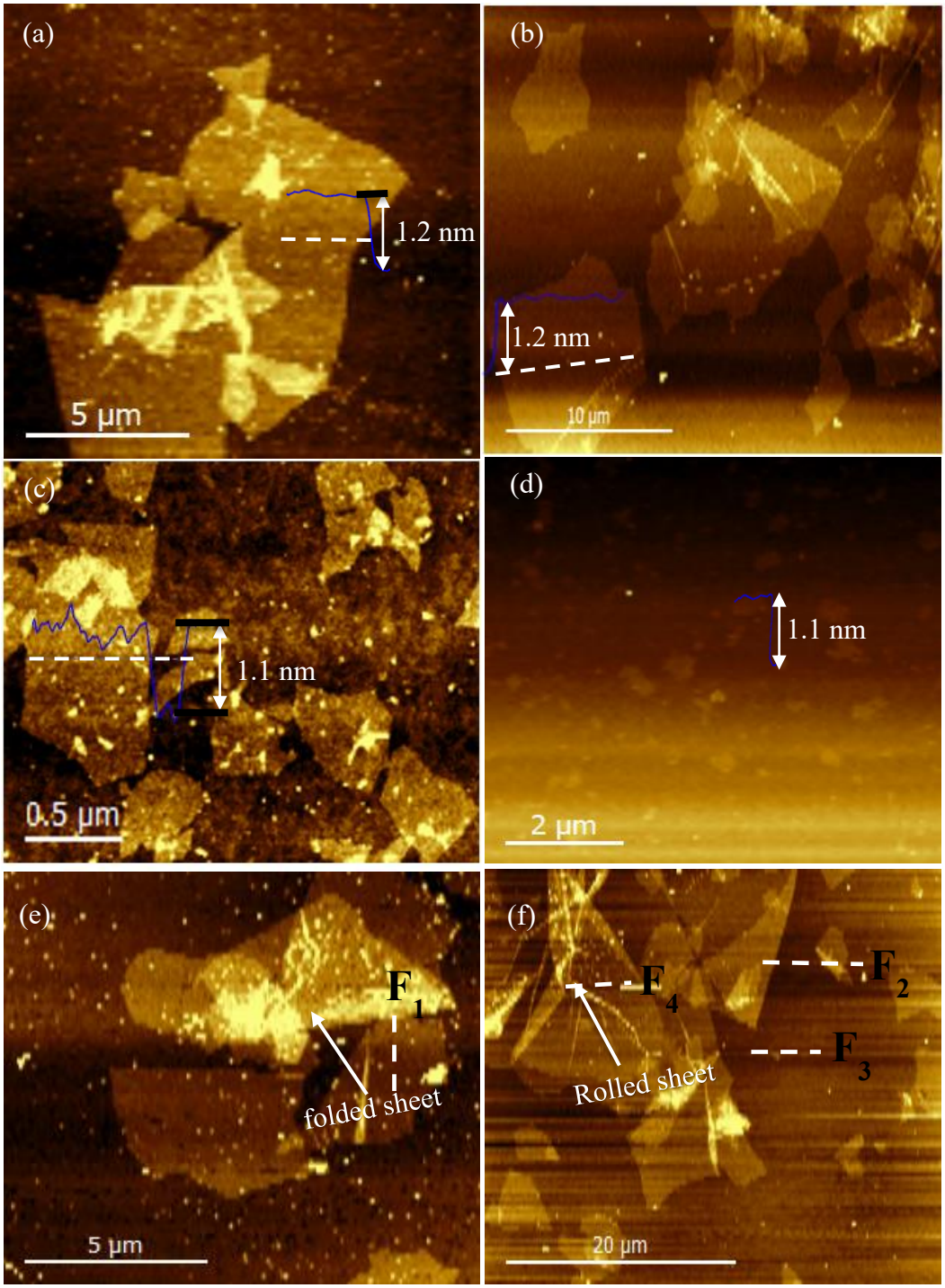

Figure 5.2. AFM images of GO nanosheets with different sizes; (a) 40 µm, (b) 10 µm, (c) 2 µm, and (d) 0.2 µm samples. All samples were dispersed on a clean Si/SiO_2 substrate. Sheets larger than 10 µm tend to fold (e & f) when drop casted from their suspension

Table 5.1. Correlation between lateral sheet size and thin film rGO-FET device's resistance, N = 10, where N is the number of pair electrodes

Lateral sheet size (µm)	Resistance (Ohms)
0.2	700,000±1000
2.0	800±50
10.0	220±18
40.0	200±20

On the other hand, the film surface/interface roughness of the 0.2 µm rGO thin film was 104±50 nm, as shown in **Fig. 5.3 (e & f)**. Therefore, the smaller the sheets, the more random the orientation and the larger the number of grain boundaries resulting in a higher surface roughness and charge scattering of the corresponding thin film. The huge difference in roughness between the two sizes explains part of the variation in the FET device's resistance.

5.3.2.2. Contribution of non-healable edge defects

The oxidation of graphene sheets at the edges results in breaking some of the aromatic rings, and hence formation of non-healable defects in the graphitic domains. Thus, the implementation of the sheets with larger lateral size may reduce the contribution of the edges to the whole sheet and improve the electronic properties of GO and rGO nanosheets. This hypothesis, along with the effect of this low temperature thermal reduction, were studied using Raman spectroscopy, high-resolution X-ray photoelectron spectroscopy (XPS), and quantitative solid-state magic-angle spinning (MAS) ^{13}C NMR. Further investigation was conducted using DFT calculations, see **section 5.3.4**.

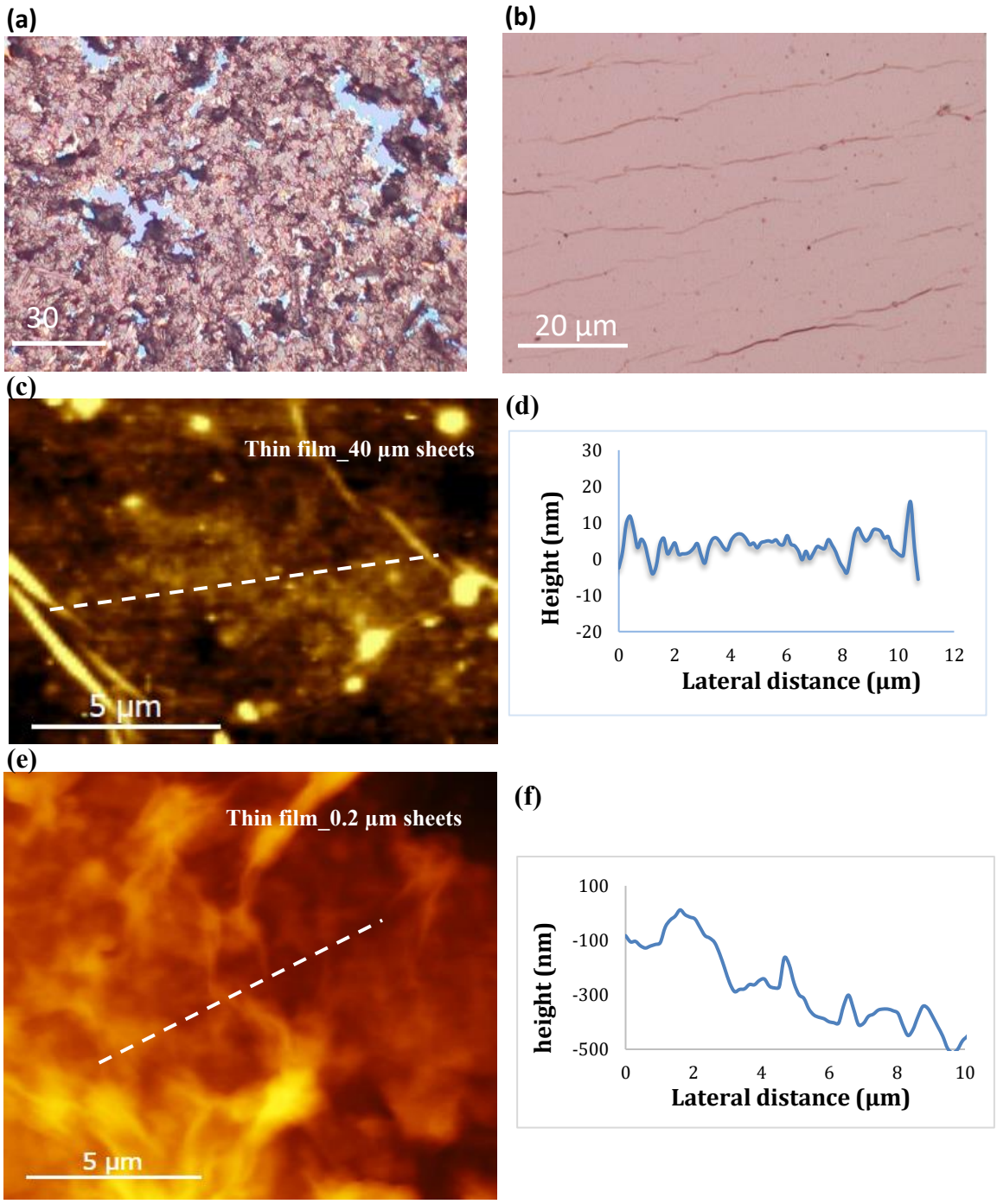

Figure 5. 3. Optical microscope images of thin films of (a) 0.2 µm rGO and (b) 40 µm rGO. AFM imaging (height images) and profiling of (c & d) 40 µm and (e & f) 0.2 µm rGO thin films on Si/SiO_2 substrate.

The other important factor that determines the rGO-FET device performance is the quality of produced rGO nanosheets. The quality here refers to how close rGO is to the pristine graphene and how efficiently the sheets heal from defects. The main parameters that affect the rGO nanosheets quality include graphite oxidation and GO reduction (healing) processes. Please, see the detailed discussion of this part in Appendix C, **section 2**.

Raman spectroscopy is a powerful tool for studying crystal defects. The defects in graphene oxide samples are assessed from the ratio of the intensities (I_d/I_G) [38] of defects-induced D band and C-C bond stretches [39] in the sp^2 domains, and G band that is arising from first order Raman scattering. Raman measurements were conducted to determine the defect changes in GO and rGO thin films for the two different sheet sizes (40 and 0.2 μm), **Fig. 5.4**. Large sheet GO (GO-L) has shown less defects (I_d/I_G = 0.92) compared to small sheets (GO-S) where I_d/I_G was 1.02. After thermal reduction for 120 min at 200 ^oC in air, both samples undergone a sort of self-healing process by restoration of the sp^2 domains and graphitization, which caused a decrease in the I_d/I_G ratios. The decrease in defects over thermal reduction is in a good agreement with literature [38,40–42]. Other studies report an increase in I_d/I_G ratio over thermal or chemical reduction, though [43–46]. As reported by *Paredes et al*., this result of higher defects after reduction is contradicting the anticipated result of restoration of aromaticity and graphitization, and the proposed interpretation by attributing that to a higher number of overall smaller sp^2 domains formation was also argued [47]. The evolution of edge and basal plane defects and vacancies as well as the presence of sp^3 carbons are responsible for the amorphization of GO/rGO and thus the increase in the I_d/I_G ratio. Examples of vacancies are the smaller and larger rings formation

due to the removal of one or more carbons from the adjacent six-membered rings in the oxidation process and the formation of distorted domains of 5-, 7-, or 8-membered rings in the form of the double vacancy (5-8-5 rings) or the common 5-7-7-5 rings disorder known as Stone-Wales defect, in the reduction/healing process [42,48,49]. Hence, the degree of amorphization of graphite in oxidation can reverse the interpretation of D band; in amorphous structures, the increased intensity of D band is associated with a higher level of ordering, and not defects as in graphene/graphite [50]. Thus, the huge variation in synthesis protocols of GO and hence in its quality and proportions of oxygen functionalities in its basal plane, as well as the contribution from edge defects cause variation in quality and interpretation of GO's Raman spectra. In this work, GO was synthesized using IHM (using phosphoric acid) that results in a more intact graphitic basal plane with less defects [24]. Phosphoric acid plays an important role in protection of basal plane, where it reacts with surface hydroxyl groups and prevents further oxidation. Accordingly, the basal plane oxygen groups (e.g. epoxy and hydroxyl) are less damaging when eliminated in reduction and leave less vacancies. Moreover, edge defects are higher in rGO-S (I_d/I_G: 0.91) than in rGO-L (I_d/I_G: 0.84).

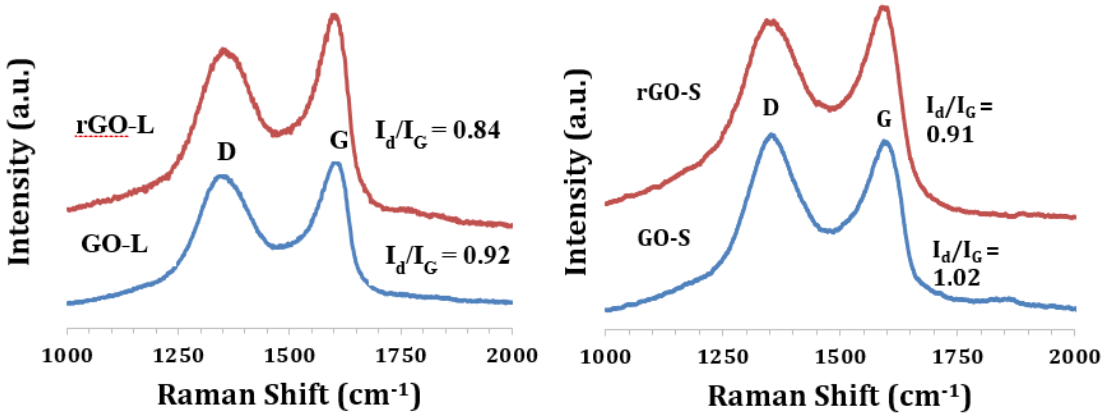

Figure 5.4. Raman spectra of small and large sheets GO and rGO thin films.

Quantitative spectroscopic analyses of the chemical compositions of the large and small (i.e. lateral sheet size) samples of GO and rGO were carried out using XPS and quantitative MAS ^{13}C NMR. High resolution XPS was conducted on thick film samples of GO-S, GO-L, rGO-L, and rGO-S. The survey spectra of GO have shown only two distinct peaks of C1s and O1s, confirming the purity of the samples. After reduction, the survey spectra have shown a gradual decrease in the concentration of O1s peaks with time, Appendix C **Fig. C5.** As shown in **Table 5.2**, the reduction process is clear from the significant increase in C/O ratio of large (L) and small (S) size graphene oxide samples from 2.45 and 2.33 to 4.26 and 4.55, respectively. To better understand the effect of this low temperature reduction on GO, and better explain the superiority of large sheets over small sheets, a detailed deconvolution process of C1s core level spectra was performed. Seven peaks were judiciously fitted, after a Shirley background subtraction, and were assigned to lattice vacancy defects (C-V) [51], sp^2-hybridized carbon atoms from aromatic domains (C=C), sp^3 carbons from aliphatic domains (C-C), hydroxyl and epoxy groups (C-OH and C-O-C), carbonyl (C=O), and carboxyl (COOH) groups, Appendix C **Fig. C6,** and **Fig. 5.5**

[52,53]. All quantitative details of the changes in chemical compositions of the two (L & S) samples are shown in **Table 5.2**. The ratio of C=C/C-C has significantly increased from 5.38 (L) and 5.07 (S) to 19.29 (L) and 18.45 (S), which accounts for a strong restoration of aromatic graphitic domains. In addition, most of the reduction process is due to removal of C-O-C/C-OH groups from the basal plane. On the other hand, the percentage of C=O and COOH groups formed on the edges of GO/rGO has increased by thermal treatment at this low temperature, suggesting that a strong reduction process, by elimination of epoxy/hydroxyl groups, and a mild oxidation process, by forming new C=O/COOH groups, have occurred simultaneously [54]. Interestingly, the large sheets of GO and rGO had shown less carboxyl groups than the small sheets. Quantitatively, %COOH in GO-L was 2.78%, while in GO-S was 3.84%, i.e. GO-S has 15% more COOH groups than rGO-L, i.e. 15% more broken benzene rings at the edges of smaller sheets.

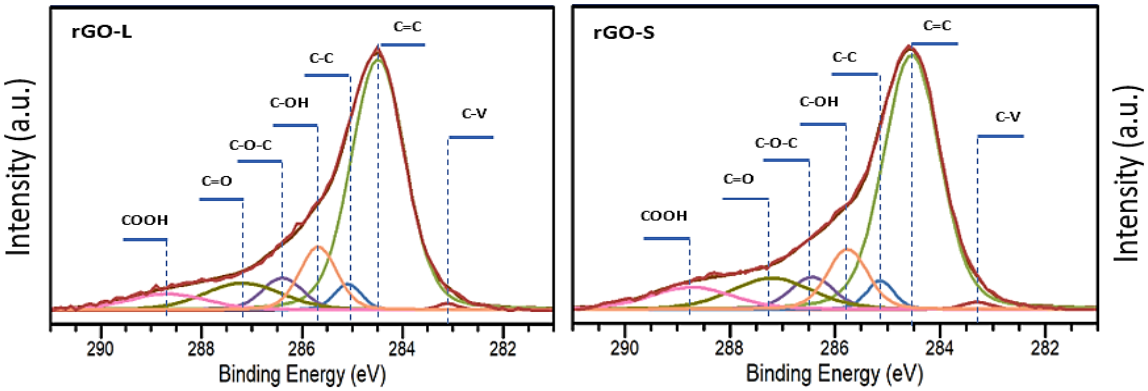

Figure 5.5. High resolution C1s XPS spectra of reduced graphene oxide after 120 min reduction time at 200 ^{o}C in air.

There is a considerable vagueness and subjectiveness in assigning and fitting XPS peaks of GO [53] arising from the huge disparities in literature due to the variation in structural models of GO (e.g. Lerf-Klinowski [55], Dèkàny [56] , and Ajayan [57] models), which allows for different possible theoretical fittings of the XPS data. Hence, pursuing a quantitative MAS ^{13}C NMR [58,59] was very useful in determining the chemical compositions of rGO and supporting the accurate fitting of XPS peaks. The ^{13}C NMR results in **Fig. 5.6 and Table 5.3** are in a good agreement with XPS results and highlight a strong reduction and mild oxidation processes happening concurrently. The epoxy and hydroxyl groups have been ~ 94% and ~ 96% eliminated, and the percentage of conjugated sp^2 carbons (C=C) has increased significantly from ~ 30% to ~ 60%, which explains the highly improved electronic properties of rGO (smaller band gap, lower resistance, and higher carrier mobility). The lower chemical shifts in the ^{13}C NMR spectra are attributed to the restoration of sp^2 conjugation in rGO [60]. The concentrations of COOH groups in GO-S and rGO-S are higher than that in GO-L and rGO-L, as shown in **Table 5.3**, which

is aligning with the results from XPS data. The concentrations of COOH and C=O groups calculated from ^{13}C MAS NMR are slightly higher than those from XPS. This might be assigned to the higher sensitivity of ^{13}C NMR to the periphery groups of GO/rGO than XPS [57,61]. We believe the difference in sensitivity of ^{13}C NMR and XPS to functional groups at edges of GO/rGO nanosheets is due to the difference in the apparatus, where in the XPS measurement the X-ray beam shines on a horizontal spot of the sample that contains more contribution from basal plane than periphery. For ^{13}C NMR, the sample is grinded and stuffed into a rotor where the signal is collected from the whole sample more homogeneously and hence the edges have a better chance to be detected. Due to this higher sensitivity, the difference in %COOH between GO-S and GO-L became more significant; 3.13% for GO-L and 5.99% for GO-S, which means around 30% more broken periphery rings in GO-S.

Table 5. 2. XPS quantitative analyses of the chemical compositions of GO-L, GO-S, rGO-L, and rGO-S.

	%C-V 283.1± 0.2	**%C=C 284.5± 0.2**	**%C-C 285.1± 0.2**	**%C-OH 285.6± 0.2**	**%C-O-C 286.4± 0.2**	**%C=O 287.2± 0.2**	**%COOH 288.6± 0.2**	**C=C /C-C**	**C/O**
GO-L	4.56	34.92	6.48	20.94	24.08	6.24	2.78	5.38	2.45
GO-S	4.87	33.22	6.54	20.43	25.10	6.01	3.84	5.07	2.33
rGO-L	0.62	63.27	3.28	11.07	6.07	9.77	5.92	19.29	4.26
rGO-S	0.83	60.84	3.29	10.29	6.21	10.61	7.94	18.49	4.55

More insights into the thermal reduction and lateral size effects based on Raman, XPS, and quantitative ^{13}C MAS NMR. Most of the oxygen functionalities are epoxy and hydroxyl groups in GO, and carbonyl and carboxyl in thermally reduced GO. Greatest amount of the C=O and COOH remaining in rGO may be distributed on edges and that is why XPS showed them in lower concentrations than ^{13}C NMR did. As per Lerf-Klinowski's [55] and Dèkàny's [56] models of GO, the most acceptable ones, COOH groups form only on edges. That supports our hypothesis of the formation of more non-healing edge defects in the small sheets due to their higher edges-to-core atoms compared to the large sheets, and helps explain one of the causes of the lower electrical conductivity and mobility, and higher Raman defects in rGO-S. The contribution of edge defects and their effects on band gap and electronic properties of rGO is discussed in more details in the computational model and calculations we present in this study.

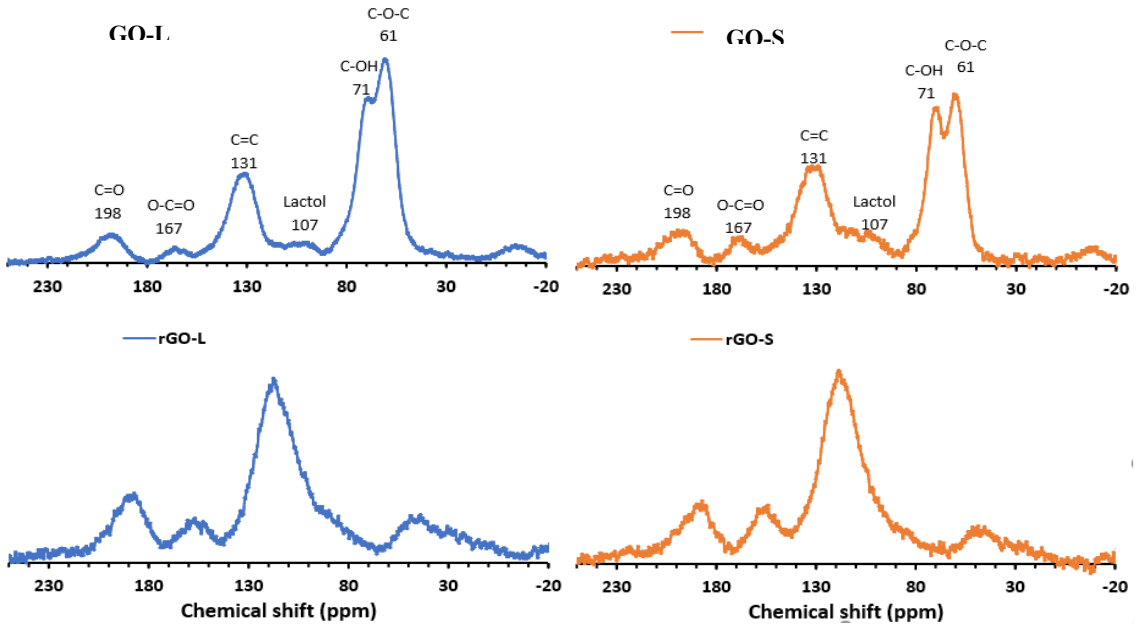

Figure 5.6. Solid state magic-angle spinning ^{13}C NMR spectra of GO and rGO.

The presence of higher C=O/COOH groups in rGO compared to GO, in general, is explained by the different proposed thermal reduction mechanisms [62–66], where the free hydroxyl and hydronium radicals formed from thermal decomposition of adsorbed water molecules attack the oxygen functionalities and convert some of them into C=O and COOH, and react further by removing them in the form of CO, and CO_2, preferentially at edges. As per Lipatov et al.'s work [62], the temperature programmed desorption measurements have revealed that the desorbed gases are mainly H_2O, CO, and CO_2. Part of the released H_2O desorbs at lower temperatures from the physically adsorbed water molecules, while the majority of the release peaks at the same temperature (~150^oC) where CO and CO_2 exhibit their maximum peaks, which confirms that this water has evolved from the removal of same type of groups that evolved as CO and CO_2. Other studies have reported the evolved gases as H_2O, CO_2, CO, H_2, O_2, and H_2O_2 [67–69]. That leaves behind restored sp^2 domains most likely from H_2O, H_2, O_2, and H_2O_2 removal, edge defects and some etch holes from CO and CO_2 elimination. The electrical conductivity and electronic properties improved significantly when the aromatic domains grew enough to allow for percolative electronic transport that bypasses any possible etch holes. That explains the strong electronic properties enhancement after low temperature thermal reduction in air despite the presence of Raman defects. The Raman defects in rGO-S are slightly higher than defects in rGO-L, which can be attributed to the higher contribution from the non-healing edge defects.

Table 5.3. MAS ^{13}C NMR quantitative analyses of the chemical compositions of GO-L, GO-S, rGO-L, and rGO-S.

	%Lactol	%(C=C)	%C-OH	%C-O-C	%C=O	%COOH
GO-L	2.71	28.04	23.52	34.45	8.16	3.13
GO-S	3.97	29.93	20.95	29.46	9.70	5.99
rGO-L	4.92	58.95	6.29	3.60	16.79	8.58
rGO-S	4.48	59.64	5.76	2.48	16.75	10.89

5.3.3. *Optical band gaps*

For a better understanding of the significance of the reduction process in producing high quality GO/rGO nanosheets, changes in the optical band gaps (OBG) of GO/rGO were assessed from UV-Vis absorption spectra using Tauc's plot [70],[71]. As previously reported, the band gap of GO/rGO is related to its carbon-oxygen ratio [72]. In other words, stripping oxygen functionalities from GO by means of reduction lowers its band gap. Furthermore, gradual restoration of graphitic structure and π conjugation by gradual reduction helps tune the band gap in a controlled manner. UV-Vis data and Tauc's plots of the 40 µm GO and rGO samples are presented in Appendix C, **Fig. C7**. Results in **Table C1** of Appendix C show that at 0 min reduction, basically GO, the OBG is 1.8 eV, which is small compared to most of the reported band gaps of GO [73,74]. Hence, GO made by this optimized IHM method is less defected and highly exfoliated to monolayers, which makes it promising for getting high quality rGO nanosheets with a small band gap. In addition, the gradual reduction of GO resulted in a gradual decrease in the corresponding band gaps of rGO nanosheets, which is consistent with our theoretical results (discussed in **section 5.3.4**). Interestingly, after annealing/reduction for 120 min at 200 ^{o}C in air, the band gap of rGO reached 0.4 eV, which, to the best of our knowledge, is the smallest value

reported for rGO [75]. This very small band gap of rGO might be explained in terms of selection of the right sheet size (10-40 μm) that enables lower contribution of the less healable edge defects and the well-optimized oxidation and reduction methods.

5.3.4. *First principle studies of GO and rGO sheets*

To garner the fundamental understanding of the factors influencing the electronic properties of GO and rGO, we performed a set of density functional theory (DFT) calculations. The details on the methods and parameters used are provided in Appendix C.

Among different GOs, epoxy and hydroxyl functionalized structures are known to be thermodynamically more stable, hence are chosen for this study [76]. Each bulk oxygen atom is bonded to its two neighboring carbon atoms to form an epoxy functional group, as illustrated in **Figs. 5.7a** and **5.8a**. The epoxy and hydroxyl groups are added to both sides of the GO sheets to generate a more stable structure compared to their counterpart with functional groups only on one side. Both ends of the sheets are hydrogen (H-) terminated to mimic finite size effect. Hydrogenation is also a common method to convert the sp^2 to sp^3 hybridized carbon bonds and hence form a bandgap in graphene [76,77]. The structures are consistent with previous models of GO discussed elsewhere [77],[78]. Details on the modeling of defected GO and rGO structures are discussed in the subsequent sections.

5.3.4.1. GO's sheet size effect

To investigate the effect of sheet size on GO monolayer's electronic properties, we constructed structures with 4, 6, and 8 carbon layers labeled as Intact-A, Intact-B, and Intact-C, respectively (**Fig. 5.7a)**. Carbon layers refer to the width of nanoribbon parallel to the periodic directions. Though the models representing the experimentally observed sizes are highly desirable, available computational resources limits the modeling of larger flakes. Hence, in this study, we have limited our model to the smaller ones (~1-2 nm). Regardless of the smaller finite sizes, our models exhibit GO behavior, and hence, can be used to predict the stability and electronic properties of larger GOs. **Fig 5.7b** shows the ground-state energy per atom plotted as a function of GO size. The results show that the larger GO sheets are energetically more stable, which can be related to the reduction in the ratio of edge to bulk atoms as the sheet grows. In addition, the larger flakes tend to relax in-plane adsorbate induced strain efficently as compared to smaller flakes, leading to relaively stable configurations. This behavioer is also consistent with the experimental data.

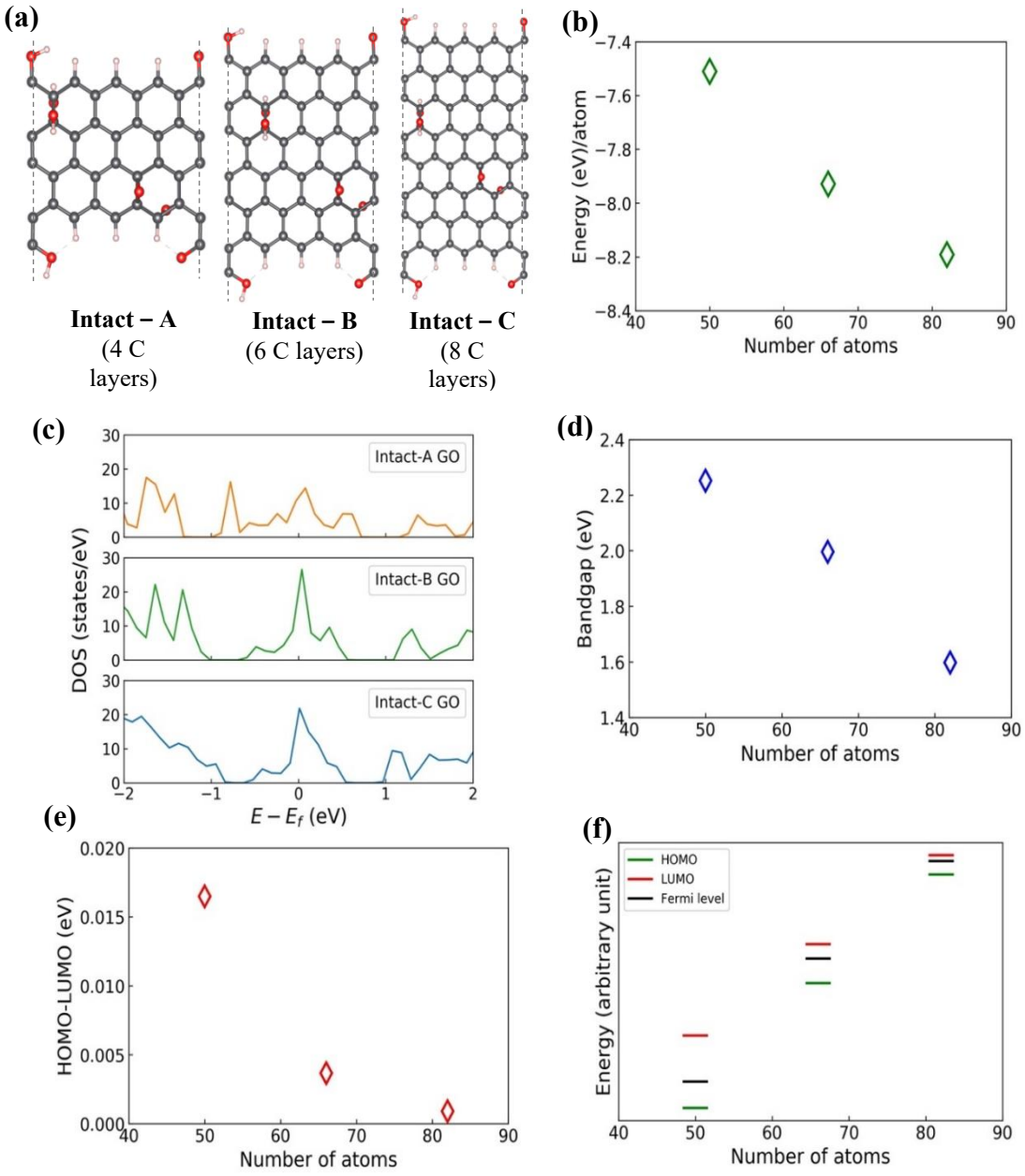

Figure 5.7. (a) GO structures with 4, 6, and 8 carbon layers– intact A, intact B and intact C, respectively (b) Total energy per atom plotted as a function of number of atoms in GO flake. (c) DOS plots of different-sized GO sheets. The sheet size increases from top to bottom. (d) and (e) Bandgap and HOMO-LUMO gaps as a function of GO sheet size, respectively, and (f) schematic evolution of electronic structure (HOMO, LUMO, and fermi level) for the three studied intact GO models, the dashed lines on left and right of plot (a) show the valence band maximum (VBM) and conduction band minimum (CBM), respectively.

Next, we studied the sheet size impact on the electronic properties of GO. **Fig. 5.7c**, depicts the densities of states (DOS) plots for the three GO models. Increasing GO flakes' size reduces the bandgap from 2.25 to 1.6 eV due to the reduction in the quantum confinement effect, as shown in **Fig. 5.7d**. Though the observed size-dependent bandgap trend is unique, it is consistent with the recently reported O/C ratio dependent bandgap [79]. In this study, authors reported variation in the gap from 2 to 1 eV for the O/C ratio of 0.5 to 0.2, respectively. Quantitatively, our intact A, intact B and intact C models possess O/C ratio of 0.16, 0.12 and 0.1 with the energy gap of 2.25, 2.1 and 1.6 eV, respectively. Here, we note that bandgap's absolute value depends on many factors including the ratio of oxygen-to-carbon atoms [76], and the choice of exchange-correlation functionals. PBE functionals are well-known for underestimating the bandgap. Regardless, our goal here is to draw a qualitative comparison with the experimental data, which is evident from the inverse relationship between the bandgap and the sheet size. **Fig. 5.7e** shows the energy gap between the highest occupied molecular orbital (HOMO) and the lowest unoccupied molecular orbital (LUMO), HOMO-LUMO gap, as a function of GO lateral size. As the sheet gets larger, the HOMO-LUMO gap becomes smaller. A schematic comparison of HOMO, LUMO, and fermi level for each model is presented in **Fig. 5.7f,** showing an increase in HOMO, LUMO, and fermi energy values, with the fermi level shifting towards LUMO as the GO sheet gets larger. Since the absolute energy values were small, we plotted these values in arbitrary units for better visualization. The corresponding calculated energy values are provided in Appendix C, **Table C1**. The observed reduction in the electronic bandgap and HOMO-LUMO gap with the increasing GO size can be attributed to the

reduction in the edge-state contribution to the band edges and quantum confinement effect [80] as well as a drop in the ratio of edge to core functional groups. Though the former argument does not hold true for the larger experimental samples, but the latter is valid, making the model developed in this study viable for larger samples. To the knowledge of authors, no previous studies have been reported on DFT calculations of size impact on GO/rGO properties. However, a similar size-dependent trend in electronic properties has been reported for MoS_2 [81] and silicon [82].

5.3.4.2. Defects and reduction

Modeling GO is an involved process. A variety of defected and reduced structures can be generated theoretically [76–78]. In experiments, the position of O and OH groups vary with processing method and conditions [76]. As optimizing defect and oxygen vacancy sites is outside the scope of this study, we limit our discussion to a few of such topologies with zigzag configurations. The purpose of this section is to investigate how defects and oxygen impurities, regardless of their configuration, affect rGO electronic properties. **Fig. 5.8a** depicts the atomic structure of intact and different defected GO flakes. Fully reduced GO models were generated by removing the core epoxy and hydroxyl functional groups.

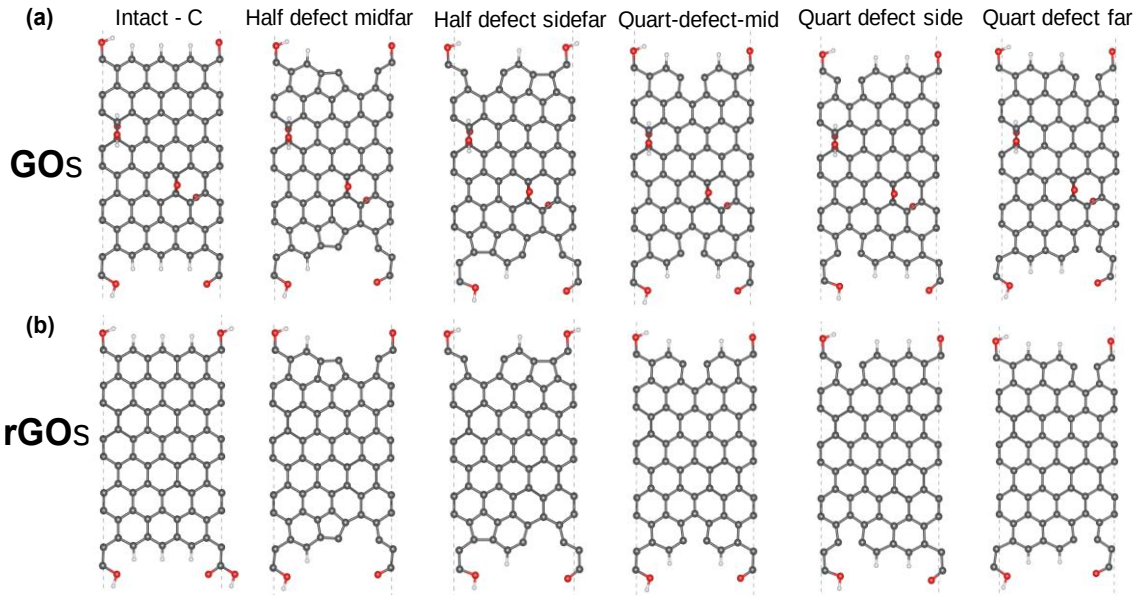

Figure 5.8. Intact and defected atomic models of (a) GO, and (b) rGO models. The structures are labeled based on defect configuration.

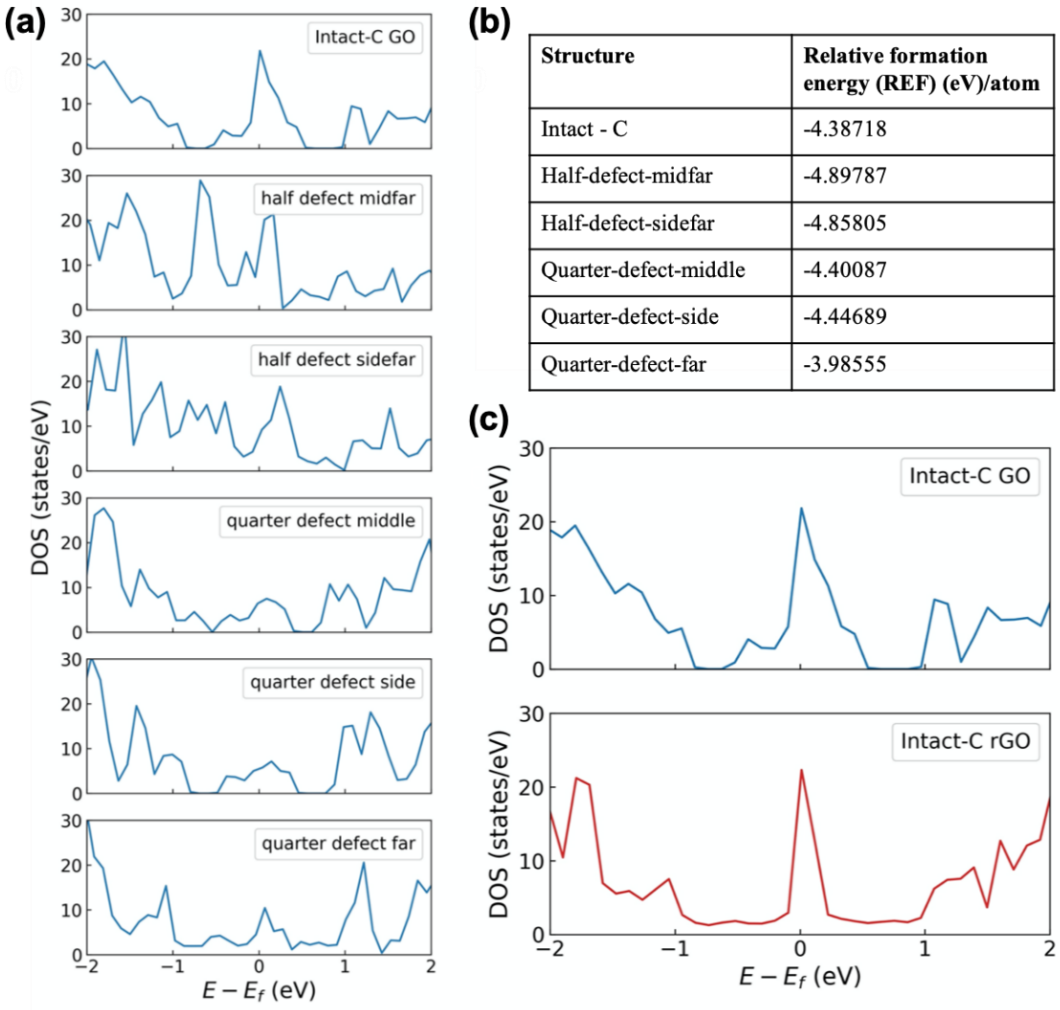

Structure	Relative formation energy (REF) (eV)/atom
Intact - C	-4.38718
Half-defect-midfar	-4.89787
Half-defect-sidefar	-4.85805
Quarter-defect-middle	-4.40087
Quarter-defect-side	-4.44689
Quarter-defect-far	-3.98555

Figure 5.9. (a) Density of states (DOS) plots of intact-C and various defected GO structures (b) Computed relative formation energy (E_{REF}) values for the same structures. (c) The DOS plots for intact-C GO and rGO structures depicted for comparison.

DOS plots for intact and defected GO structures (**Fig. 5.9a**) show a decrease in the bandgap and results in additional localized states appearing in the gap for all defected structures. Introducing edge defects involves breaking some of the sp^3 C–H bonds, increasing the number of unfunctionalized edge carbons with free orbitals, contributing to higher electronic conductivity, and lowering the bandgap. For half defect structures, the bandgap is wholly removed. These are the structures with five-membered rings where the missing

C–C bond increases the ratio of free orbitals, which lowers the energy gap. To compare the stability and tendency of rGO sheets to oxidize, we calculated the relative formation energy (E_{RFE}) defined as the difference between the formation energy of GO and the corresponding rGO structure through **equation 1** [76]:

$$E_{RFE} = (E_{GO} - E_{rGO} - \Delta n_O \mu_O - \Delta n_H \mu_H) \qquad (1)$$

Where E_{GO}, and E_{rGO} are the ground-state energies of GO and rGO, respectively. Δn_O and Δn_H refer to the difference in number of O and H atoms for the original and reduced structures, μ_O and μ_H are the chemical potential of oxygen and hydrogen, respectively. The table of E_{RFE} values is presented in **Fig. 5.9b**. The negative values of E_{RFE} indicate that oxidation makes all structures more stable. The lowest E_{REF} values belong to the half defect structures with five C rings which are expected to have higher reactivity due to their free orbitals.

Following the stability analysis, we performed site-project DOS for the intact-C GO and the corresponding reduced structures. Removal of epoxy groups results in appearance of sp^2 localized states distributing through the whole energy gap of GO. The appearance of these states due to reduction is in line with previous study by Lundie et al [77]. Besides, based on our chemical intuition, since the rGO structures look more similar to pristine graphene compared to their GO opponents, they are expected to show higher electronic conductivity.

5.3.5. *FET characteristics and charge carrier mobility of rGO thin film*

The charge carrier mobility of the rGO nanosheets, after 120 min reduction time, was calculated from **equation 2**, as reported elsewhere [10].

$$\mu = S\frac{L}{W}\frac{1}{\mathrm{Vsd}}\frac{1}{\mathrm{Ci}} \qquad (2)$$

Where S is the slope in the linear part of the I_{sd}-V_g curve, L and W are the length and width of the channel, V_{sd} is the source-drain voltage, and C_i is the gate-channel (interfacial) capacitance. C_i was determined from the electrochemical impedance spectroscopy (EIS) and was found to be 1.48 μF/cm^2, which is in a good agreement with literature [36]·[10]. Details of calculating C_i are in Appendix C, **section 4**.

Fig. 5.10(a-d) shows the FET characteristic curves using electrolyte-gating for rGO of 0.2 μm lateral sheet after 60 min reduction and 40 μm sheet post 30, 60, and 120 min reduction. As shown in **Fig. 5.10d**, the FET curve of optimized rGO exhibit the ambipolar behavior of the pristine graphene. On the other hand, Dirac point of this rGO thin film is at 0.01 V, which indicates that most of the p-type doping defects were removed, and its characteristics resemble pristine graphene like features where the Dirac point is located at the charge neutrality point.

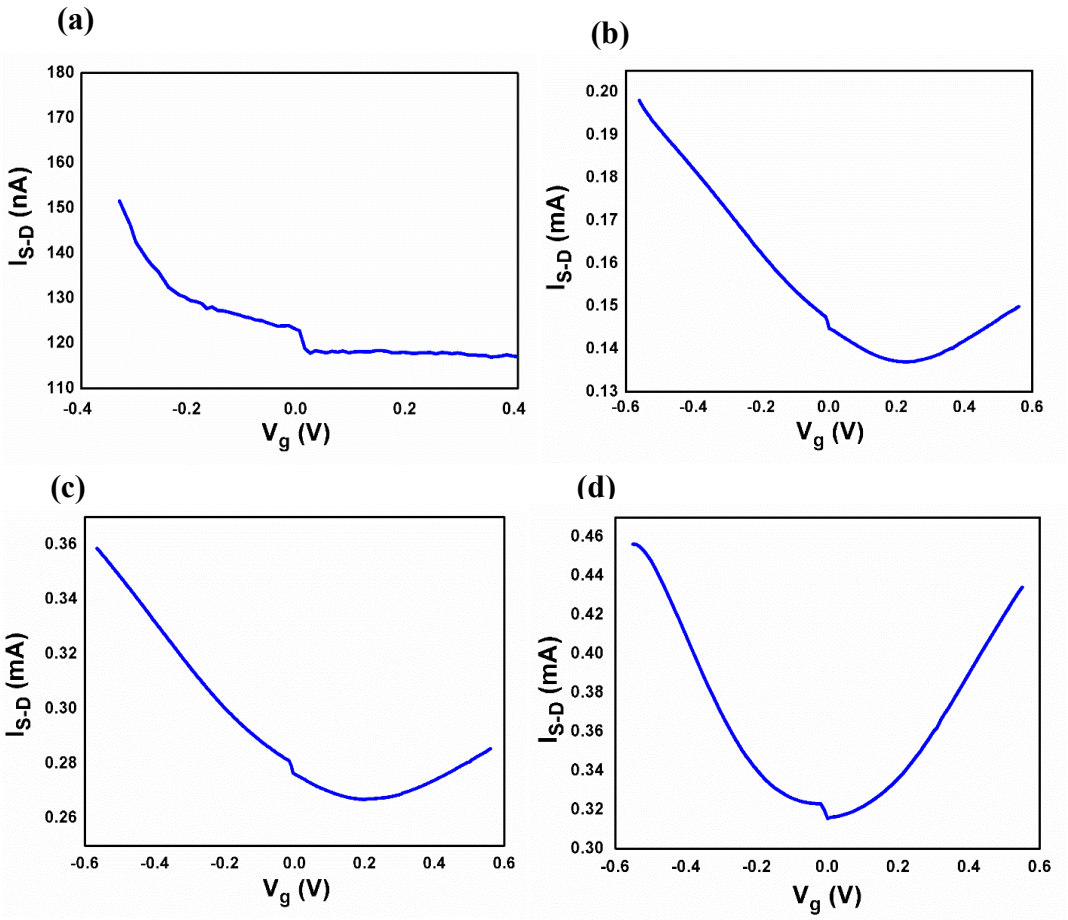

Figure 5.10. The characteristic curves of rGO-FET system of 0.2 µm sheets after 60 min reduction (a) and of 40 µm sheets (a, b, & c) at different reduction times (30, 60, and 120 min) measured at 0.1 V between source and drain. The bias voltage was applied by top-gating with Ag/AgCl electrode and in 10 mM phosphate buffer saline (PBS) electrolyte.

The holes and electrons carrier mobilities of the optimized rGO-FET system were 2,962 and 2,183 $cm^2/V.s$, respectively. These values, to the best of authors knowledge, are the highest reported to-date for rGO-FET, LPE G-FET, and within the highest of the CVD G-FET (**Table 5.4**). It is worth mentioning that the mobility is directly proportional to the slope (dI/dV) of the FET transfer characteristics and hence it is directly proportional to the on-current. Since the on-current in our rGO-FET devices is higher by an order of magnitude as compared to the previously reported state of the art devices (~0.4 mA vis-à-vis 0.001

mA), the mobility is expected to be significantly large compared to literature [48-56, 58]. In summary, we attribute all these interesting pristine graphene-like properties observed in our rGO-FET devices to the high quality of the synthesized rGO nanosheets, the reduced surface roughness and charge scattering and the small contribution of the edge defects due to the right selection of the sheet's lateral size, as well as the good film continuity.

Table 5.4. Charge carrier mobilities of rGO- and CVD graphene (CVD G-) and LPE graphene (LPE G-) FET systems.

FET system	**Mobility (holes) $cm^2/V.s$**	**Mobility (electrons) $cm^2/V.s$**	**Reference**
rGO-FET	16	--	This work (before optimization)
rGO-FET	**2,962**	**2,183**	**This work (after optimization)**
rGO-FET	0.015	--	[83]
rGO-FET	82.5	27.5	[84]
rGO-FET	0.5	--	[85]
rGO-FET	2-200	0.5-30	[86]
rGO-FET	676	496	[87]
CVD G-FET	1,410	--	[88]
CVD G-FET	7.21	--	[37]
CVD G-FET	811	190	[89]
CVD G-FET	900	800	[90]
CVD G-FET	1,800	1,200	[91]
CVD G-FET	7,600	--	[92]
LPE G-FET	18.71	5.04	[93]
LPE G-FET	2.50	0.49	[93]

5.4. Conclusions

This work introduces a detailed experimental study, complemented by DFT modeling, of some of the critical factors affecting the quality of rGO nanosheets and thin films, and proposes a route to achieving pristine graphene-like rGO from the commercially available graphite. We observed that the lateral sheet size, concentration and volume of GO solution, and quality of oxidation and reduction methods are the key factors in realizing a high-quality graphene-like rGO thin film. The optimized large rGO flake exhibits smallest reported optical band gap, lowest FET resistance vis-à-vis highest conductivity, and highest charge carrier mobility. The lateral size of the starting graphite has a significant impact on these properties of the corresponding rGO nanosheets. This observation is consistent with the thickness (lateral size) dependent reduction in the energy gap predicted by the DFT method. The graphite flakes of lateral sizes 10-40 μm are more promising than powder graphite for electronic applications. The larger size better performance was attributed to the better film continuity, smaller roughness and smaller charge scattering, and lower contribution from non-healable edge defects. Raman, XPS and quantitative MAS ^{13}C results gave more insights into the effect of lateral sheet sizes and low temperature thermal reduction on the chemical composition of the film-forming nanosheets and hence the film's electronic properties. The rGO-FET device resistance decreased drastically by increasing lateral sheet size of the thin film rGO sheets from 0.2 to 2.0 and then to 10 μm, but the reduction in resistance plateaued for sizes larger than 10 μm due to the folding of larger sheets that was recorded using AFM imaging. We have also demonstrated that the modified IHM synthesis method is crucial for getting high quality and highly exfoliated GO

nanosheets. During the reduction process, the reduction temperature was optimized to 200 ^{o}C, for 120 min at ambient pressure, which makes it facile method for *in situ* reduction of GO sheets or films on surfaces. In conclusion, a high-quality thin film of rGO sheets with graphene-like ambipolar transfer characteristics, a finite band gap of ~0.4 eV, and high holes (electrons) mobilities of 2,962 (2,183) cm^2/V.s, might be useful in high-frequency, low power device applications, such as TFET, sensors and neuromorphic applications.

5.5. References

[1] Y. Zhu, S. Murali, W. Cai, X. Li, J.W. Suk, J.R. Potts, R.S. Ruoff, Graphene and graphene oxide: synthesis, properties, and applications, Adv. Mater. 22 (2010) 3906–3924.

[2] A.A. Balandin, S. Ghosh, W. Bao, I. Calizo, D. Teweldebrhan, F. Miao, C.N. Lau, Superior thermal conductivity of single-layer graphene, Nano Lett. 8 (2008) 902–907.

[3] S. V Morozov, K.S. Novoselov, M.I. Katsnelson, F. Schedin, D.C. Elias, J.A. Jaszczak, A.K. Geim, Giant intrinsic carrier mobilities in graphene and its bilayer, Phys. Rev. Lett. 100 (2008) 16602.

[4] R. Chen, T. Zhao, T. Tian, S. Cao, P.R. Coxon, K. Xi, D. Fairen-Jimenez, R. Vasant Kumar, A.K. Cheetham, Graphene-wrapped sulfur/metal organic framework-derived microporous carbon composite for lithium sulfur batteries, APL Mater. 2 (2014) 124109.

[5] J. Hassoun, F. Bonaccorso, M. Agostini, M. Angelucci, M.G. Betti, R. Cingolani, M. Gemmi, C. Mariani, S. Panero, V. Pellegrini, An advanced lithium-ion battery based on a graphene anode and a lithium iron phosphate cathode, Nano Lett. 14 (2014) 4901–4906.

[6] M. Hegde, L. Yang, F. Vita, R.J. Fox, R. van de Watering, B. Norder, U. Lafont, O. Francescangeli, L.A. Madsen, S.J. Picken, Strong graphene oxide nanocomposites from aqueous hybrid liquid crystals, Nat. Commun. 11 (2020) 1–7.

[7] V. Tozzini, V. Pellegrini, Prospects for hydrogen storage in graphene, Phys. Chem. Chem. Phys. 15 (2013) 80–89.

[8] G. Viskadouros, D. Konios, E. Kymakis, E. Stratakis, Direct laser writing of flexible graphene field emitters, Appl. Phys. Lett. 105 (2014) 203104.

[9] N. Balis, D. Konios, E. Stratakis, E. Kymakis, Ternary organic solar cells with reduced graphene oxide–Sb2S3 hybrid nanosheets as the cascade material, ChemNanoMat. 1 (2015) 346–352.

[10] C. Reiner-Rozman, M. Larisika, C. Nowak, W. Knoll, Graphene-based liquid-gated field effect transistor for biosensing: Theory and experiments, Biosens. Bioelectron. 70 (2015) 21–27.

[11] G. Mittal, V. Dhand, K.Y. Rhee, S.-J. Park, W.R. Lee, A review on carbon nanotubes and graphene as fillers in reinforced polymer nanocomposites, J. Ind. Eng. Chem. 21 (2015) 11–25.

[12] Q. Yang, Y. Su, C. Chi, C.T. Cherian, K. Huang, V.G. Kravets, F.C. Wang, J.C. Zhang, A. Pratt, A.N. Grigorenko, Ultrathin graphene-based membrane with precise molecular sieving and ultrafast solvent permeation, Nat. Mater. 16 (2017) 1198–1202.

[13] P. Capper, S. Irvine, T. Joyce, Epitaxial crystal growth: Methods and materials, Shep. (2007) 271.

[14] A. Amiri, M. Naraghi, G. Ahmadi, M. Soleymaniha, M. Shanbedi, A review on liquid-phase exfoliation for scalable production of pure graphene, wrinkled, crumpled and

functionalized graphene and challenges, FlatChem. 8 (2018) 40–71.

[15] S. Pei, H.-M. Cheng, The reduction of graphene oxide, Carbon N. Y. 50 (2012) 3210–3228.

[16] H. Feng, R. Cheng, X. Zhao, X. Duan, J. Li, A low-temperature method to produce highly reduced graphene oxide, Nat. Commun. 4 (2013) 1539.

[17] D.W. Boukhvalov, M.I. Katsnelson, Chemical functionalization of graphene, J. Phys. Condens. Matter. 21 (2009) 344205.

[18] M.M. MacInnes, S. Hlynchuk, S. Acharya, N. Lehnert, S. Maldonado, Reduction of Graphene Oxide Thin Films by Cobaltocene and Decamethylcobaltocene, ACS Appl. Mater. Interfaces. 10 (2017) 2004–2015.

[19] M. Acik, Y.J. Chabal, A review on thermal exfoliation of graphene oxide, J. Mater. Sci. Res. 2 (2013) 101.

[20] E. Tegou, G. Pseiropoulos, M.K. Filippidou, S. Chatzandroulis, Low-temperature thermal reduction of graphene oxide films in ambient atmosphere: Infra-red spectroscopic studies and gas sensing applications, Microelectron. Eng. 159 (2016) 146–150.

[21] A.M. Dimiev, T.A. Polson, Contesting the two-component structural model of graphene oxide and reexamining the chemistry of graphene oxide in basic media, Carbon N. Y. 93 (2015) 544–554.

[22] A.P. Kauling, A.T. Seefeldt, D.P. Pisoni, R.C. Pradeep, R. Bentini, R.V.B. Oliveira, K.S. Novoselov, A.H. Castro Neto, The Worldwide graphene flake production, Adv. Mater. 30 (2018) 1803784.

[23] P. Bøggild, The war on fake graphene, (2018) 502–503. https://doi.org/10.1038/d41586-018-06939-4.

[24] D.C. Marcano, D. V Kosynkin, J.M. Berlin, A. Sinitskii, Z. Sun, A. Slesarev, L.B. Alemany, W. Lu, J.M. Tour, Improved synthesis of graphene oxide, ACS Nano. 4 (2010) 4806–4814.

[25] M. Sedki, M.B. Mohamed, M. Fawzy, D.A. Abdelrehim, M.M.S.A. Abdel-Mottaleb, Phytosynthesis of silver-reduced graphene oxide (Ag-RGO) nanocomposite with an enhanced antibacterial effect using Potamogeton pectinatus extract, RSC Adv. 5 (2015) 17358–17365. https://doi.org/10.1039/c4ra13117g.

[26] M. Sedki, R.Y.A. Hassan, A. Hefnawy, I.M. El-Sherbiny, Sensing of bacterial cell viability using nanostructured bioelectrochemical system: rGO-hyperbranched chitosan nanocomposite as a novel microbial sensor platform, Sensors Actuators, B Chem. 252 (2017). https://doi.org/10.1016/j.snb.2017.05.163.

[27] R. Forsyth, A. Devadoss, O.J. Guy, Graphene field effect transistors for biomedical applications: Current status and future prospects, Diagnostics. 7 (2017) 45.

[28] S. Behera, S.R. Pattanaik, G. Dash, Effect of Channel Dimensions on Transfer Characteristics of Graphene FET, in: 2018 IEEE Electron Devices Kolkata Conf., IEEE, 2018: pp. 341–343.

[29] H. Rokni, W. Lu, Layer-by-layer insight into electrostatic charge distribution of few-layer graphene, Sci. Rep. 7 (2017) 42821.

[30] J. Zhang, H. Yang, G. Shen, P. Cheng, J. Zhang, S. Guo, Reduction of graphene oxide via L-ascorbic acid, Chem. Commun. 46 (2010) 1112–1114.

[31] S. Yang, W. Yue, D. Huang, C. Chen, H. Lin, X. Yang, A facile green strategy for rapid reduction of graphene oxide by metallic zinc, Rsc Adv. 2 (2012) 8827–8832.

[32] P. Poulin, R. Jalili, W. Neri, F. Nallet, T. Divoux, A. Colin, S.H. Aboutalebi, G. Wallace, C. Zakri, Superflexibility of graphene oxide, Proc. Natl. Acad. Sci. 113 (2016) 11088–11093.

[33] A.R. Koltonow, C. Luo, J. Luo, J. Huang, Graphene oxide sheets in solvents: To crumple or not to crumple?, ACS Omega. 2 (2017) 8005–8009.

[34] D.K. Pandey, T.F. Chung, G. Prakash, R. Piner, Y.P. Chen, R. Reifenberger, Folding and cracking of graphene oxide sheets upon deposition, Surf. Sci. 605 (2011) 1669–1675.

[35] S. Behura, P. Nguyen, S. Che, R. Debbarma, V. Berry, Large-area, transfer-free, oxide-assisted synthesis of hexagonal boron nitride films and their heterostructures with MoS2 and WS2, J. Am. Chem. Soc. 137 (2015) 13060–13065.

[36] C.T. Thanh, N.H. Binh, N. Van Tu, V.T. Thu, M. Bayle, M. Paillet, J.L. Sauvajol, P.B. Thang, T. Dai Lam, P.N. Minh, An interdigitated ISFET-type sensor based on LPCVD grown graphene for ultrasensitive detection of carbaryl, Sensors Actuators B Chem. 260 (2018) 78–85.

[37] T.T. Cao, H.B. Nguyen, H.T. Bui, T.T. Vu, N.H. Phan, B.T. Phan, L. Hoang, M. Bayle, M. Paillet, J.L. Sauvajol, Fabrication of few-layer graphene film based field effect transistor and its application for trace-detection of herbicide atrazine, Adv. Nat. Sci. Nanosci. Nanotechnol. 7 (2016) 35007.

[38] S. Perumbilavil, P. Sankar, T. Priya Rose, R. Philip, White light Z-scan measurements of ultrafast optical nonlinearity in reduced graphene oxide nanosheets in the 400–700 nm region, Appl. Phys. Lett. 107 (2015) 51104.

[39] K. Krishnamoorthy, M. Veerapandian, R. Mohan, S.-J. Kim, Investigation of Raman and photoluminescence studies of reduced graphene oxide sheets, Appl. Phys. A. 106 (2012) 501–506.

[40] M. Strankowski, D. Włodarczyk, Ł. Piszczyk, J. Strankowska, Polyurethane nanocomposites containing reduced graphene oxide, FTIR, Raman, and XRD studies, J. Spectrosc. 2016 (2016).

[41] C. Fu, G. Zhao, H. Zhang, S. Li, Evaluation and characterization of reduced graphene oxide nanosheets as anode materials for lithium-ion batteries, Int. J. Electrochem. Sci. 8 (2013) 6269–6280.

[42] K.N. Kudin, B. Ozbas, H.C. Schniepp, R.K. Prud'Homme, I.A. Aksay, R. Car, Raman spectra of graphite oxide and functionalized graphene sheets, Nano Lett. 8 (2008)

36–41.

[43] G. Yasin, M. Arif, M. Shakeel, Y. Dun, Y. Zuo, W.Q. Khan, Y. Tang, A. Khan, M. Nadeem, Exploring the Nickel–Graphene Nanocomposite Coatings for Superior Corrosion Resistance: Manipulating the Effect of Deposition Current Density on its Morphology, Mechanical Properties, and Erosion-Corrosion Performance, Adv. Eng. Mater. 20 (2018) 1701166.

[44] A. Dasgupta, J. Sarkar, M. Ghosh, A. Bhattacharya, A. Mukherjee, D. Chattopadhyay, K. Acharya, Green conversion of graphene oxide to graphene nanosheets and its biosafety study, PLoS One. 12 (2017) e0171607.

[45] A. Jabbar, G. Yasin, W.Q. Khan, M.Y. Anwar, R.M. Korai, M.N. Nizam, G. Muhyodin, Electrochemical deposition of nickel graphene composite coatings: effect of deposition temperature on its surface morphology and corrosion resistance, RSC Adv. 7 (2017) 31100–31109.

[46] S. Farah, A. Farkas, J. Madarász, K. László, Comparison of thermally and chemically reduced graphene oxides by thermal analysis and Raman spectroscopy, J. Therm. Anal. Calorim. 142 (2020) 331–337.

[47] J.I. Paredes, S. Villar-Rodil, P. Solís-Fernández, A. Martínez-Alonso, J.M.D. Tascon, Atomic force and scanning tunneling microscopy imaging of graphene nanosheets derived from graphite oxide, Langmuir. 25 (2009) 5957–5968.

[48] J.C. Meyer, C. Kisielowski, R. Erni, M.D. Rossell, M.F. Crommie, A. Zettl, Direct imaging of lattice atoms and topological defects in graphene membranes, Nano Lett. 8 (2008) 3582–3586.

[49] Q.A. Khan, A. Shaur, T.A. Khan, Y.F. Joya, M.S. Awan, Characterization of reduced graphene oxide produced through a modified Hoffman method, Cogent Chem. 3 (2017) 1298980.

[50] A.C. Ferrari, J. Robertson, Interpretation of Raman spectra of disordered and amorphous carbon, Phys. Rev. B. 61 (2000) 14095.

[51] R. Blume, P.R. Kidambi, B.C. Bayer, R.S. Weatherup, Z.-J. Wang, G. Weinberg, M.-G. Willinger, M. Greiner, S. Hofmann, A. Knop-Gericke, The influence of intercalated oxygen on the properties of graphene on polycrystalline Cu under various environmental conditions, Phys. Chem. Chem. Phys. 16 (2014) 25989–26003.

[52] M.K. Rabchinskii, S.A. Ryzhkov, D.A. Kirilenko, N. V Ulin, M. V Baidakova, V. V Shnitov, S.I. Pavlov, R.G. Chumakov, D.Y. Stolyarova, N.A. Besedina, From graphene oxide towards aminated graphene: Facile synthesis, its structure and electronic properties, Sci. Rep. 10 (2020) 1–12.

[53] A. Ganguly, S. Sharma, P. Papakonstantinou, J. Hamilton, Probing the thermal deoxygenation of graphene oxide using high-resolution in situ X-ray-based spectroscopies, J. Phys. Chem. C. 115 (2011) 17009–17019.

[54] J. Jo, S. Lee, J. Gim, J. Song, S. Kim, V. Mathew, M.H. Alfaruqi, S. Kim, J. Lim, J. Kim, Facile synthesis of reduced graphene oxide by modified Hummer’s method as

anode material for Li-, Na-and K-ion secondary batteries, R. Soc. Open Sci. 6 (2019) 181978.

[55] A. Lerf, H. He, M. Forster, J. Klinowski, Structure of graphite oxide revisited, J. Phys. Chem. B. 102 (1998) 4477–4482.

[56] T. Szabó, O. Berkesi, P. Forgó, K. Josepovits, Y. Sanakis, D. Petridis, I. Dékány, Evolution of surface functional groups in a series of progressively oxidized graphite oxides, Chem. Mater. 18 (2006) 2740–2749.

[57] W. Gao, L.B. Alemany, L. Ci, P.M. Ajayan, New insights into the structure and reduction of graphite oxide, Nat. Chem. 1 (2009) 403.

[58] M. Khandelwal, A. Kumar, One-step chemically controlled wet synthesis of graphene nanoribbons from graphene oxide for high performance supercapacitor applications, J. Mater. Chem. A. 3 (2015) 22975–22988.

[59] I.A. Vacchi, C. Spinato, J. Raya, A. Bianco, C. Ménard-Moyon, Chemical reactivity of graphene oxide towards amines elucidated by solid-state NMR, Nanoscale. 8 (2016) 13714–13721.

[60] S. Park, Y. Hu, J.O. Hwang, E.S. Lee, L.B. Casabianca, W. Cai, J.R. Potts, H.W. Ha, S. Chen, J. Oh, Chemical structures of hydrazine-treated graphene oxide and generation of aromatic nitrogen doping. Nat Commun, 3, 638 (2012), (n.d.).

[61] H.W. Kim, H. Park, J.S. Roh, J.E. Shin, T.H. Lee, L. Zhang, Y.H. Cho, H.W. Yoon, V.J. Bukas, J. Guo, Carbon defect characterization of nitrogen-doped reduced graphene oxide electrocatalysts for the two-electron oxygen reduction reaction, Chem. Mater. 31 (2019) 3967–3973.

[62] A. Lipatov, M.J.-F. Guinel, D.S. Muratov, V.O. Vanyushin, P.M. Wilson, A. Kolmakov, A. Sinitskii, Low-temperature thermal reduction of graphene oxide: In situ correlative structural, thermal desorption, and electrical transport measurements, Appl. Phys. Lett. 112 (2018) 53103.

[63] M. Acik, G. Lee, C. Mattevi, A. Pirkle, R.M. Wallace, M. Chhowalla, K. Cho, Y. Chabal, The role of oxygen during thermal reduction of graphene oxide studied by infrared absorption spectroscopy, J. Phys. Chem. C. 115 (2011) 19761–19781.

[64] S. Tian, J. Sun, S. Yang, P. He, S. Ding, G. Ding, X. Xie, Facile thermal annealing of graphite oxide in air for graphene with a higher C/O ratio, RSC Adv. 5 (2015) 69854–69860.

[65] D. Krishnan, F. Kim, J. Luo, R. Cruz-Silva, L.J. Cote, H.D. Jang, J. Huang, Energetic graphene oxide: challenges and opportunities, Nano Today. 7 (2012) 137–152.

[66] L. Klemeyer, H. Park, J. Huang, Geometry-Dependent Thermal Reduction of Graphene Oxide Solid, ACS Mater. Lett. 3 (2021) 511–515.

[67] A. Bagri, R. Grantab, N. V Medhekar, V.B. Shenoy, Stability and formation mechanisms of carbonyl-and hydroxyl-decorated holes in graphene oxide, J. Phys. Chem. C. 114 (2010) 12053–12061.

[68] A. Bagri, C. Mattevi, M. Acik, Y.J. Chabal, M. Chhowalla, V.B. Shenoy, Structural evolution during the reduction of chemically derived graphene oxide, Nat. Chem. 2 (2010) 581–587.

[69] A.F. da Silva, A.M. Christmann, T.M.H. Costa, A.R. Muniz, N.M. Balzaretti, Thermal annealing of graphite oxide under high pressure: An experimental and computational study, Carbon N. Y. 139 (2018) 1035–1047.

[70] M.A. Velasco-Soto, S.A. Pérez-García, J. Alvarez-Quintana, Y. Cao, L. Nyborg, L. Licea-Jiménez, Selective band gap manipulation of graphene oxide by its reduction with mild reagents, Carbon N. Y. 93 (2015) 967–973.

[71] L. Ci, L. Song, C. Jin, D. Jariwala, D. Wu, Y. Li, A. Srivastava, Z.F. Wang, K. Storr, L. Balicas, Atomic layers of hybridized boron nitride and graphene domains, Nat. Mater. 9 (2010) 430–435.

[72] H. Huang, Z. Li, J. She, W. Wang, Oxygen density dependent band gap of reduced graphene oxide, J. Appl. Phys. 111 (2012) 54317.

[73] P. Sehrawat, S.S. Islam, P. Mishra, S. Ahmad, Reduced graphene oxide (rGO) based wideband optical sensor and the role of Temperature, Defect States and Quantum Efficiency, Sci. Rep. 8 (2018) 1–13.

[74] M.T. Hasan, B.J. Senger, C. Ryan, M. Culp, R. Gonzalez-Rodriguez, J.L. Coffer, A. V Naumov, Optical band gap alteration of graphene oxide via ozone treatment, Sci. Rep. 7 (2017) 1–8.

[75] U.A.M. Romero, M.Á.V. Soto, L.L. Jiménez, J.Á. Quintana, S.A.P. García, Graphene Derivatives: Controlled Properties, Nanocomposites, and Energy Harvesting Applications, Graphene Mater. Prop. Modif. (2017).

[76] L. Liu, J. Zhang, H. Gao, L. Wang, X. Jiang, J. Zhao, Tailoring physical properties of graphene: Effects of hydrogenation, oxidation, and grain boundaries by atomistic simulations, Comput. Mater. Sci. 112 (2016) 527–546.

[77] M. Lundie, Ž. Šljivančanin, S. Tomić, Electronic and optical properties of reduced graphene oxide, J. Mater. Chem. C. 3 (2015) 7632–7641.

[78] P. V Kumar, M. Bernardi, J.C. Grossman, The impact of functionalization on the stability, work function, and photoluminescence of reduced graphene oxide, ACS Nano. 7 (2013) 1638–1645.

[79] Y. Jin, Y. Zheng, S.G. Podkolzin, W. Lee, Band gap of reduced graphene oxide tuned by controlling functional groups, J. Mater. Chem. C. 8 (2020) 4885–4894.

[80] R.J. Martín-Palma, J. Martínez-Duart, Nanotechnology for Microelectronics and Photonics, Elsevier, 2017.

[81] M. Javaid, D.W. Drumm, S.P. Russo, A.D. Greentree, A study of size-dependent properties of MoS 2 monolayer nanoflakes using density-functional theory, Sci. Rep. 7 (2017) 1–11.

[82] B. Delley, E.F. Steigmeier, Size dependence of band gaps in silicon nanostructures,

Appl. Phys. Lett. 67 (1995) 2370–2372.

[83] X. Dong, W. Huang, P. Chen, In situ synthesis of reduced graphene oxide and gold nanocomposites for nanoelectronics and biosensing, Nanoscale Res Lett. 6 (2011) 1–6.

[84] J. Yang, J. Kim, H.S. Shin, Facile Method for rGO Field Effect Transistor: Selective Adsorption of rGO on SAM-Treated Gold Electrode by Electrostatic Attraction, Adv. Mater. 24 (2012) 2299–2303.

[85] I.-Y. Sohn, D.-J. Kim, J.-H. Jung, O.J. Yoon, T.N. Thanh, T.T. Quang, N.-E. Lee, pH sensing characteristics and biosensing application of solution-gated reduced graphene oxide field-effect transistors, Biosens. Bioelectron. 45 (2013) 70–76.

[86] C. Gómez-Navarro, R.T. Weitz, A.M. Bittner, M. Scolari, A. Mews, M. Burghard, K. Kern, Electronic transport properties of individual chemically reduced graphene oxide sheets, Nano Lett. 7 (2007) 3499–3503.

[87] S. Tian, J. Sun, S. Yang, P. He, G. Wang, Z. Di, G. Ding, X. Xie, M. Jiang, Controllable edge oxidation and bubbling exfoliation enable the fabrication of high quality water dispersible graphene, Sci. Rep. 6 (2016) 34127.

[88] M.A. Uddin, N. Glavin, A. Singh, R. Naguy, M. Jespersen, A. Voevodin, G. Koley, Mobility enhancement in graphene transistors on low temperature pulsed laser deposited boron nitride, Appl. Phys. Lett. 107 (2015) 203110.

[89] B. Zhang, W.H. Lee, R. Piner, I. Kholmanov, Y. Wu, H. Li, H. Ji, R.S. Ruoff, Low-temperature chemical vapor deposition growth of graphene from toluene on electropolished copper foils, ACS Nano. 6 (2012) 2471–2476.

[90] G. Wang, M. Zhang, Y. Zhu, G. Ding, D. Jiang, Q. Guo, S. Liu, X. Xie, P.K. Chu, Z. Di, Direct growth of graphene film on germanium substrate, Sci. Rep. 3 (2013) 2465.

[91] A. Zak, M.A. Andersson, M. Bauer, J. Matukas, A. Lisauskas, H.G. Roskos, J. Stake, Antenna-integrated 0.6 THz FET direct detectors based on CVD graphene, Nano Lett. 14 (2014) 5834–5838.

[92] D.B. Farmer, H.-Y. Chiu, Y.-M. Lin, K.A. Jenkins, F. Xia, P. Avouris, Utilization of a buffered dielectric to achieve high field-effect carrier mobility in graphene transistors, Nano Lett. 9 (2009) 4474–4478.

[93] S.S. Sukumaran, S. Tripathi, A.N. Resmi, K.G. Gopchandran, K.B. Jinesh, Influence of surfactants on the electronic properties of liquid-phase exfoliated graphene, Mater. Sci. Eng. B. 240 (2019) 62–68.

CHAPTER 6

Label-Free Chemiresistor Biosensor Based on Reduced Graphene Oxide and *M13* Bacteriophage for Detection of Coliforms

Abstract: Coliform bacteria are well known as informative indicators for bacterial pollution in river water. This study presents a novel chemiresistor biosensor using *M13* phage-modified reduced graphene oxide (rGO) for detection of *Escherichia coli* (*E. coli*), as coliform bacteria. *M13* phage, as a biorecognition element, was immobilized on the rGO channel, so that it can bind to negatively charged *E. coli* bacteria, allowing the gating effect on the biosensor and the change in its resistance. The prepared materials and device were characterized using spectroscopic, microscopic, and electrical measurements. FTIR and XRD results proved the successful fabrication of GO and rGO nanosheets. AFM results showed that the prepared nanosheets were monolayer. The SEM micrographs of the *M13*-functionalized devices soaked at two different concentrations of *E. coli*, confirmed the successful capturing of *E. coli* and that the signal change is concentration-dependent. As a result, a linear and specific response towards E. coli was observed and the limit of detection was determined to be 45 CFU/mL. Further, the proposed sensor system showed selectivity towards the tested coliforms. These results suggested this sensing system could be a promising tool for detecting coliforms with an economic, accurate, smaller rapid, and directly applicable process.

6.1.Introduction

Fecal coliforms have received a widespread attention as typical biomarkers for water contamination with bacteria [1]. There are several methods used for detection of coliform.

The first is a basic colony counting method [2]. While simple, the method takes a long time for getting results, usually more than 24 hours. Other methods used in laboratory are based on the principle of ELISA or PCR [3,4]. These methods require specific reagents and instruments for the detection, making the processes expensive and time-consuming, besides the need for trained professionals [5,6]. Biosensors have been developed as economic and more promising tools for identifying coliforms. They offer simple operation and rapid response with accuracy, but still need further optimization and standardization for application. Phages are of a great importance as bioreceptors in biosensors [7,8].

Here, M13 bacteriophage was implemented as a biorecognition element for coliform detection. M13 phage is a non-lytic bacterial virus which infects and grows only in the male strains of *Escherichia coli* (*E. coli*) by recognizing its F-pili [9]. In addition, M13 phage is more stable against the change of pH or temperature, compared to other biorecognition elements such as antibodies [10]. In addition, it is economic and easy to prepare by simple bacterial cultivation methods.

Amongst the different transducers, biosensors based on chemiresistor (CR) are receiving a great deal of attention in recent years for label-free biosensing with a facile procedure [11–15]. CR biosensor is a sensor in which the resistance of the device changes as a result of the changes of its nearby chemical environment. Generally, when biomolecules with electrical charges are near the semiconductor channel, they provide the electrostatic gating effects to the sensing platform, changing the number of charge carriers in the semiconductor channel and thereby the resistance of the CR sensor [16].

Reduced graphene oxide (rGO) is a well-known nanomaterial utilized in a wide range of

applications, including electronic materials and sensors. It has a large surface area, which is available for direct interaction with variety of biomolecules and whole cells [17–19]. Our research group has conducted a detailed study (publication in progress) of the parameters that affect the quality of GO/rGO, which had led to obtaining pristine graphene-like rGO, which improved its charge transport and electronic properties.

This study aims to develop a label-free CR biosensor using M13 bacteriophage and rGO for detecting fecal coliform. We focused on *E. coli* bacteria as biomarker for indicating the presence of infectious pathogen in river water and M13 phage as biorecognition molecule for selective detection of *E. coli*. This sensor has shown good sensitivity and low limit of detection (LOD) of 45 CFU/mL, which is comparable with previous reports. Furthermore, the specificity and applicability of this biosensor are also demonstrated using *Pseudomonas chlororaphis* (*P. chlororaphis*) strain, as non-host bacteria, and simulated river water sample, respectively.

6.2. Materials and methods

6.2.1. Materials

Graphite flakes, phosphoric acid (H_3PO_4, 85%), sulfuric acid (H_2SO_4, 98%), potassium permanganates ($KMnO_4$, 99%), hydrochloric acid (HCl, 37%) and hydrogen peroxide (H_2O_2, 30%) were all purchased from Fisher Scientific, USA. (3-Aminopropyl) triethoxysilane (APTES) was bought from Sigma (St. Louis, MO, USA). 1-pyrene carboxylic acid (PCA), dimethylformamide (DMF), Tween 20 (T20), 1-ethyl-3-(3-dimethylaminopropyl) carbodiimide hydrochloride (EDC), and N-hydroxysuccinimide

(NHS) were all purchased from Sigma- Aldrich (St. Louis, USA). Ethanolamine (EA) was acquired from Acros Organic-Fisher Scientific.

6.2.2. Materials synthesis and characterization

The bacteria solution of *E. coli XL1-blue* and *Pseudomonas chlororaphis* were cultured in LB media by the same way as our previous report. In addition, M13 bacteriophage was prepared same as our previous work [10]. GO nanosheets were prepared as illustrated in our previously published work [20]. The prepared GO and rGO nanosheets were characterized using X-ray diffraction (XRD, PANalytical Empyrean Series 2), Fourier transform infra-red (FTIR, Thermo Nicolet 6700) spectroscopy, atomic force microscopy (AFM, Horiba LabRam/AIST-NT), and scanning electron microscopy (SEM, ThermoFisher Scientific (formerly FEI/Philips) NNS450). All electrical measurements were performed using the Keithley 2636 System Source Meter® (Tektronix, Beaverton, OR, USA).

6.2.3. Fabrication of the biosensor

Fig. 6.1 illustrates a schematic of the rGO-M13 phage biosensor protocol. The interdigitated gold electrodes (chips), shown in **Fig. 6.2a**, were fabricated on a p-type silicon substrate with a 300 nm SiO_2 insulating oxide layer deposited on top. Electrodes were patterned on the Si/SiO_2 substrate by conventional photolithography. Then, Cr (5 nm) and Au (50 nm) layers, were deposited on the substrate using e-beam evaporation.

The devices each have 5 pairs of source and drain electrodes with 5 μm width separated by 3 μm gaps of SiO_2 insulating layer. We used rGO to bridge the gaps of interdigitated gold electrodes.

The interdigitated gold electrodes written on Si/SiO_2 wafers were cleaned sequentially with acetone, isopropanol, methanol and deionized water (DI water) followed by drying with air. The electrodes were first incubated with 30% ammonium hydroxide for 30 min to introduce hydroxyl groups, and then incubated with APTES for 60 min. 15 μL of 1.25 mg/mL GO solution were dropped onto the interdigitated electrodes and dried at 50˚C for 30 min. Subsequently, the interdigitated electrodes were annealed at 200˚C for 120 min in ambient air. The electrodes were further incubated with 100 mM PCA dissolved in DMF for 60 min, washed with DMF, and dried with N_2 gas. After that, the electrodes were incubated with 6.0 mM EDC and 6.0 mM NHS in 100 mM 2-(N-morpholino) ethanesulfonic acid (MES) buffer (pH 5.5), each for 20 min to activate the carboxylic groups, followed by incubation with 25 μL of M13 phage solution at 4˚C for 3 hours. Then the electrodes were incubated with 100 mM EA for 30 min to passivate residual ester groups of NHS and rinsed thoroughly with 10 mM sodium phosphate buffer (PB, pH 7.4), followed by incubation with 1.0% (v/v) T20 for 30 min to block the bare rGO on the electrodes. The chips were washed with the proper buffer after each of the previous modification steps.

The fabrication steps were monitored by measuring the device resistance after each step. The device resistance was determined from the slopes of current-voltage (I-V) curves between V_{SD} of +0.1 V and -0.1 V.

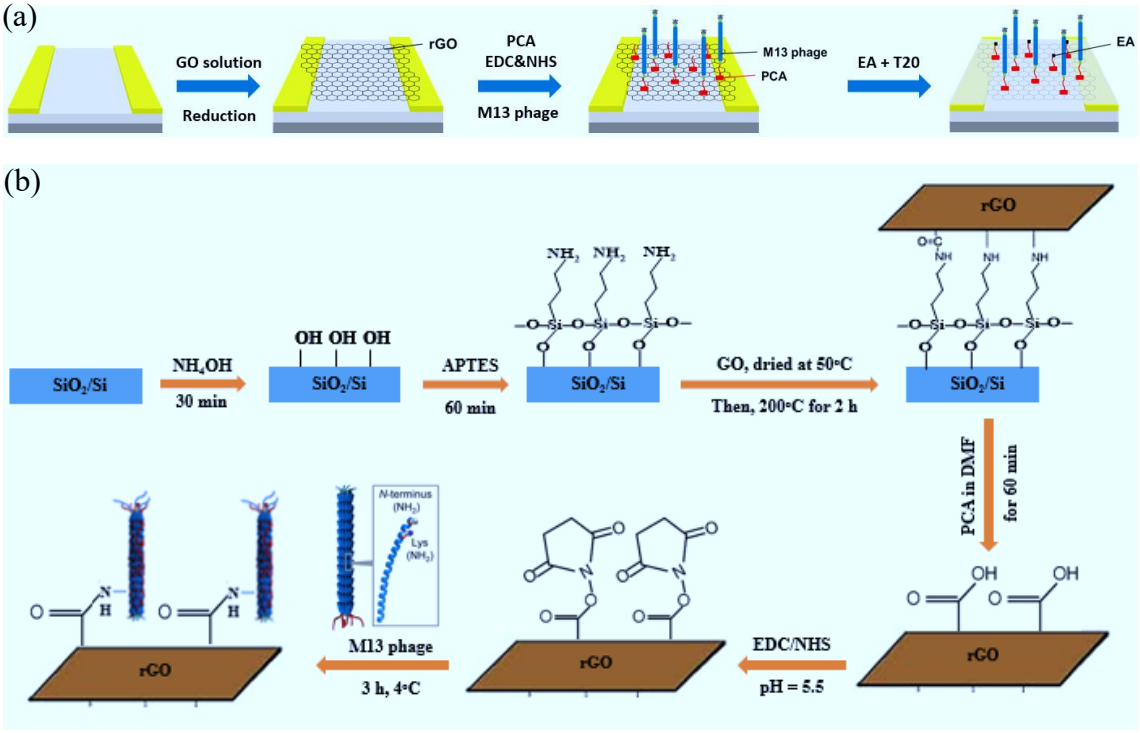

Figure 6.1. (a) A schematic diagram of the preparation procedures of rGO-M13 phage-based biosensor. (b) A more detailed schematic showing the chemistry of sensor fabrication. The red dots on M13 phage represent the amine groups positions.

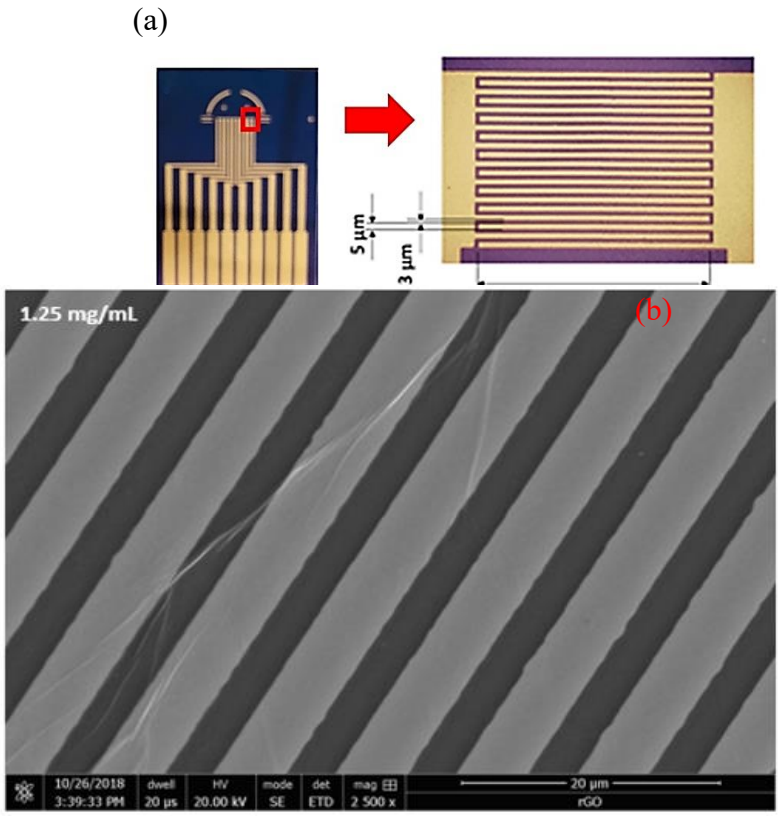

Figure 6.2. The sensor system design. (a) Phone camera image of the gold interdigitated electrodes (device). (b) An SEM image of the device with a thin film of rGO.

6.2.4. *Sample measurement using prepared biosensor*

Sensing procedure consisted of measuring the initial resistance (R_0) of the sensor (determined from the slopes of I−V curves between +0.1 V and −0.1 V) followed by incubation for 30 min with 25 µL of different concentrations of *E. coli XL1-blue* solution, rinsing 3 times with PB and measuring the resistance (R) again. Percentage changes $(R-R_0)/R_0\%$ were plotted as a function of log value of *E. coli* concentration to evaluate the sensor performance characteristics. The same sensors were used for the whole range from 10^2 to 10^7 CFU/mL.

6.3. Results and discussions

6.3.1. Materials characterization

Fig. 6.2b shows the SEM image of the interdigitated gold electrodes with rGO. As shown in the figure, the very thin rGO film totally covered the interdigitated gold electrodes gaps in the sensing area. The strong immobilization of rGO thin film on the substrate is attributed to the chemical bonds' formation between APTES and rGO, **Fig. 6.1b**, which was explained in detail by Ou et al.[21], where epoxy groups from GO encounter ring opening and bind to primary amine groups (-NH_2), which convert into secondary amines (-NH-). On the other hand, amide bond formation between carboxyl groups (-COOH) and -NH_2 are less likely to happen in the absence of coupling agents such as EDC/NHS, at room temperature. However, in this case zwitterionic COO^-NH3^+ linkages are formed, that under the effect of heat (200^{o}C) form -CO-NH- (amide) linkages.

The prepared GO, and rGO nanosheets were characterized by FTIR spectroscopy as shown in **Fig. 6.3a**. In GO sample, the stretching vibrational peaks of hydroxyl groups, carbonyl groups, and C=C double bonds appeared at 3400 cm^{-1}, 1722 cm^{-1}, and 1627 cm^{-1}, respectively [22]. The thermal reduction of GO nanosheets at 200^{o}C and ambient conditions could remove all the hydroxyl and most of the carbonyl groups, and that is clear from the significant decrease in their peak strengths. These results comply with literature [23]. The thermal reduction process can be understood as a degassing process, where most of the oxygen functionalities get removed in the form of CO_2 and water vapor, which in role helps remove the foreign atoms (oxygen) and convert more sp^3 carbons into sp^2 ones

[20,24,25]. Hence, the electrical properties of GO get strongly improved by thermal reduction into rGO.

The XRD patterns, **Fig. 6.3b.**, were recorded using Cu Kα radiation (λ = 1.54 °A) at 45 kV and 40 mA, and in the range of $2\Theta = 9^{o}–44^{o}$. From Bragg's law ($n\lambda = 2d \sin(\Theta)$), graphite has a d-spacing between its graphene sheets of around 0.34 nm ($2\Theta=26^{o}$), corresponding to the (002) planes. Due to the oxide functionalities, GO sheets were pushed further from each other, with a longer d-spacing (d ≈0.84 nm) and a smaller diffraction angle of $2\Theta =10.5^{o}$. By thermal reduction of GO into rGO, the (002) peak shifts to a slightly broader peak at $2\Theta =24^{o}$, corresponding to a smaller d-spacing of ≈0.37 nm. The decrease of d-spacing is attributed to the removal of oxygen functionalities in the reduction process [26]. The thickness, which determines the number of layers, of the prepared GO nanosheets was determined using AFM imaging. The height profile in **Fig. 6.3c** shows that the thickness is 1.2 nm, which corresponds to single layer GO. This thickness is larger than that of single-layer graphene (0.4 nm), as it includes the extra height coming from oxygen functionalities in GO, which pushes the sheet further from the substrate [26–30].

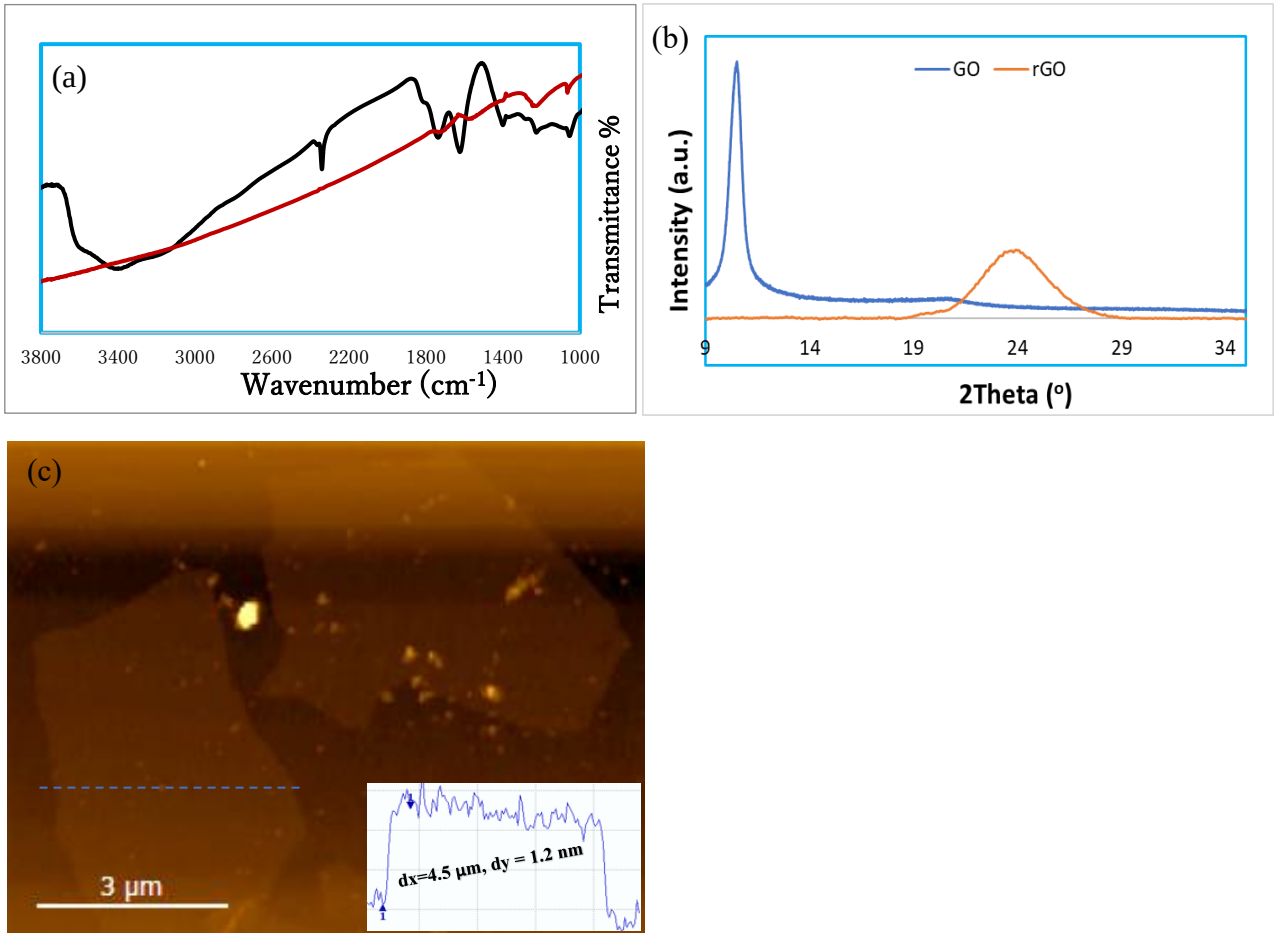

Figure 6.3. The spectroscopic characterizations of GO and rGO nanosheets. (a) FTIR spectra of GO (black) and rGO (red) nanosheets. (b) XRD analysis showing sharp peak of GO at 2theta = 10.4°, and rGO with a diffraction peak centering at 24°. (c) an AFM image of GO with its height profile.

6.3.2. Monitoring of device modifications using I-V measurements

After each modification step, the resistance of the sensor was measured (determined from the slopes of I−V curves between +0.1 V and −0.1 V) for monitoring the modification steps. As shown in **Fig. 6.4**, there were linear I-V curves, indicating Ohmic contact between the Au-electrodes and the overlaying rGO thin film. The resistance of the sensor chip increased after each modification step of PCA, EDC/NHS-M13 phage, EA, and T20, compared to

the interdigitated electrodes with rGO. Especially, the change in resistance of the sensor chip was large after the modification steps of PCA and EDC/NHS-M13 phage. These results suggest that the large molecules modified on the electrodes increased their resistance. On the other hand, small changes in resistance were observed after the modification steps of EA and T20. These results are consistent with literature, confirming that the modification steps of the sensor chip were successful [16].

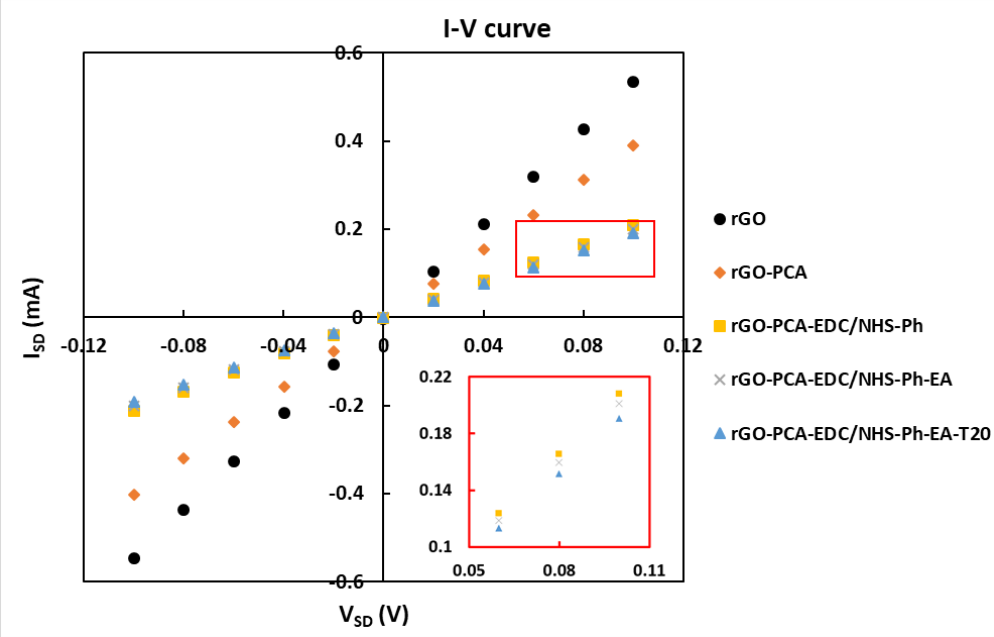

Figure 6.4. The fabrication steps were confirmed by monitoring I-V curves between source and drain, at a V_{SD} of +0.1 V and -0.1 V. The resistance of the sensor system increased after each modification step of PCA, EDC/NHS-M13 phage, EA, and T20, compared to the interdigitated electrodes only with rGO.

6.3.3. Measurement of E. coli bacteria

The biosensors were evaluated for *E. coli* detection by incubating with 10^2 CFU/mL to 10^7 CFU/mL. The sensor response (% resistance change calculated as

$(R-R_0)/R_0*100=\Delta R/R_0*100$, where R_0 is the sensor's resistance before the addition of *E. coli* bacteria, and R is the resistance after the addition and 30 min of incubation of *E. coli* bacteria) was measured after the incubation with 20 μL of *E. coli* bacteria aliquots for 30 min followed by washing with PB (**Fig. 6.5**). As shown in the figure, a linear decrease in the device resistance was observed with the increase of *E. coli* concentration. This can be explained by the electrostatic gating effect induced by negatively charged *E. coli* (**Fig. 6.6**). When M13 phage captured the negatively charged *E. coli*, the density of negative surface changes was increased, which leads to an increase in the amount of hole carriers in the p-type rGO sheets. As shown in **Fig. 6.5**, the biosensor response exhibited an excellent linear correlation to Log_{10}(CFU/mL) over the complete tested concentration range (R^2 =0.9869). The limit of detection (LOD), defined as LOD = 3*Sd/S, where Sd is the standard deviation of the mean of blank measurements, and S is the slope of the calibration curve was estimated as 45 CFU/mL, which is competitive to other reports detecting bacteria by various detection methods (**Table 6.1**). Thakur et al.'s work on detection of *E. coli*, using antibody-Au-Al_2O_3-rGO, had a single cell detection in 1 μL, which is equivalent to 10^3 CFU/mL [18], which is slightly higher than the LOD of this sensor platform (45 CFU/mL). In addition, the introduced sensor implements M13 phage as a bioreceptor, which has a higher stability than the antibody-based biosensors. These results prove the M13 phage rGO-CR biosensor to be a strong candidate system for the detection of coliforms in water.

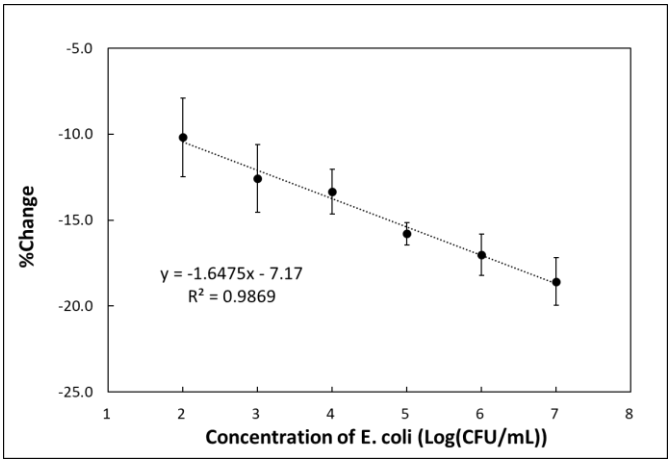

Figure 6.5. Calibration curve plotting % resistance change ($(R-R_0)/R_0$ %) against the concentration of E. coli. R_0 is the resistance of the M13-modified rGO channels after incubation with PB and R is the resistance of the sensor after incubation with different concentrations of E. coli. Each data point is an average of responses from 3 different M13-modified sensors and error bars represent ±1 standard deviation.

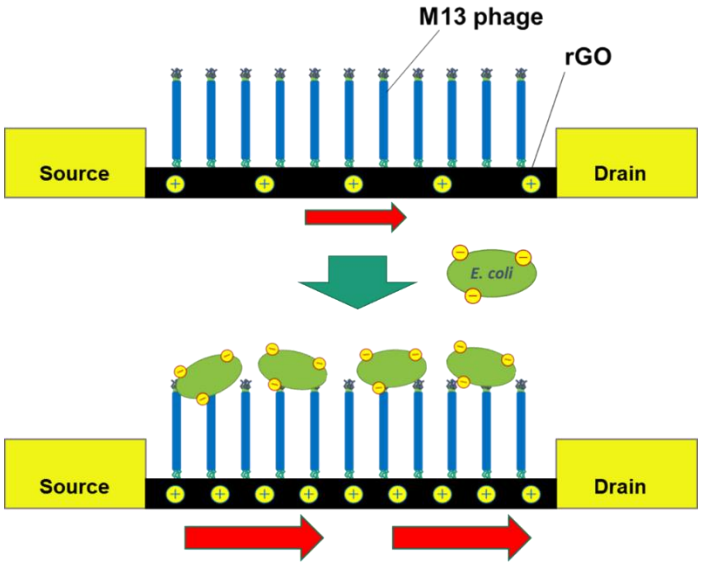

Figure 6.6. The sensing mechanism of the rGO-M13 phage CR-FET biosensor for E. coli detection. Illustration of the change of the charge distribution induced by the binding of the negatively charged E. coli.

Table 6.1. Comparison of the sensing performance for various detection methods.

Method	Detection time	Bacteria	Detection limit	Reference
Flow cytometry	5 min	E. coli and others	10^5 cells/mL	[31]
PCR	4 h	Listeria and others	10^3 CFU/mL	[32]
Fluorescence	20 min	E. coli	50.2 CFU/mL	[33]
Antibody-G-FET	100 s	E. coli	10 CFU/mL	[34]
Aptamer-G-FET	72 s	E. coli	10^2 CFU/mL	[35]
Antibody-G-CR/FET	30 min	E. coli	10 CFU/mL	[19]
Antibody-Au-Al_2O_3-rGO FET	50 s	E. coli	10^3 CFU/mL	[18]
Phage-rGO-CR	30 min	E. coli	45 CFU/mL	This work

6.3.4. SEM imaging of E. coli cells captured by the biosensor

To verify that the increased response of the sensor system was derived from the phage-*E. coli* binding, two different concentrations of *E. coli* (10^3 and 10^6 CFU/mL) were incubated with two sensor chips for 30 min, washed with PB, and then imaged with SEM. The bacteria were captured by M13 phage on the electrodes which were totally covered by a thin film of rGO. The images in **Fig. 6.7** show a clear difference in the number of bacteria between the two concentrations on the two chips. This confirms that the increase in sensor's resistance is attributed to the increase in number of captured bacterial cells.

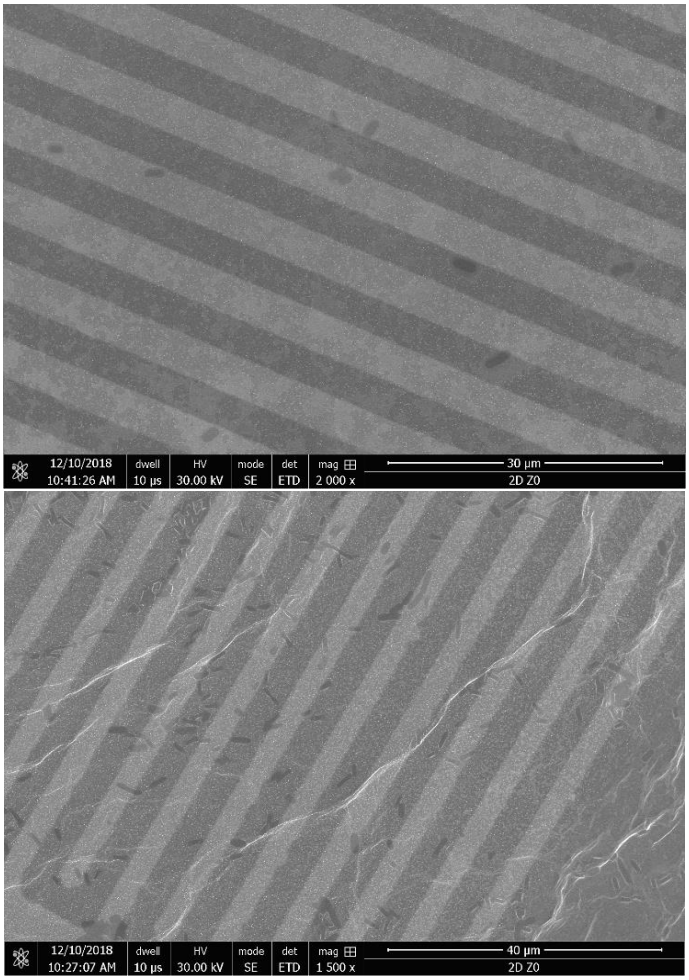

Figure 6.7. SEM micrographs of the fabricated sensor chip incubated with E. coli bacteria at 10^3 CFU/mL (top) and 10^6 CFU/mL (bottom).

6.3.5. *Selectivity and control experiments*

To test the selectivity of the proposed sensor, control experiments were designed (**Fig. 6.8**). Firstly, *P. Chlororaphis* was tested as non-host cells with M13-rGO sensor, and there was no noticeable response. Moreover, as a control experiment, the sensor without M13 phage was tested against *E. coli XL1-blue*. There was also no noticeable response detected. Thus, this sensor system is selective to F-pili of *E. coli* strains such as *XL1-blue*.

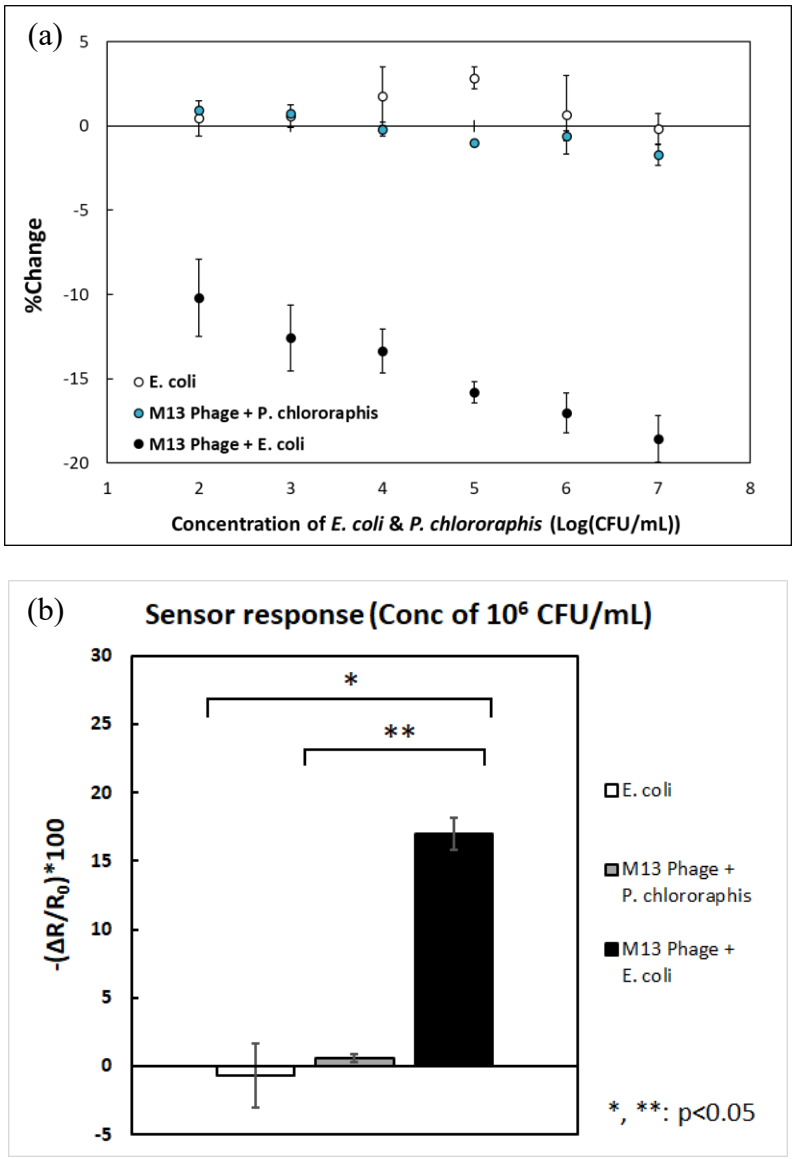

Figure 6.8. Control experiments. (a) Calibration curves plotting % resistance change against the concentration of P. chlororaphis, as non-host bacteria to M13 phage (gray) compared to E. coli (black), as host bacteria. The white column shows the response of the sensor incubated with E. coli in the absence of M13 phage. (b) Responses at the bacteria concentration of 10^6 CFU/mL show no detectable response of the system with P. chlororaphis (in presence of M13 phage), with E. coli in presence and absence of M13 phage. The P value was < 0.05. Each data point is an average of responses from 3 different M13-modified sensors and error bars represent ±1 standard deviation.

6.4. Conclusion

In this study, we reported the rGO-FET M13 phage-based biosensor system for early detection of *E. coli*. The interdigitated gold electrodes were modified with a thin film of rGO as a semiconductor sensing material. For the biorecognition element, M13 phage, a non-lytic and highly stable bacteriophage, was introduced for the selective recognition of F-pili containing *E. coli* strains. The developed sensor showed good sensitivity to detect *E. coli* strain with a LOD of 45 CFU/mL. This value is comparable with other methods which have been previously reported for detecting *E. coli*. Furthermore, this sensor was specific towards target bacteria and not affected by interference with other bacteria. From these observations, we concluded that the introduced sensor has a high sensitivity, and it showed selectivity to *E. coli*. This sensing system could be a promising platform for economic and accurate on-site detection of fecal coliforms with simple operations.

6.5. References

[1] C. Dye, After 2015: infectious diseases in a new era of health and development, Phil. Trans. R. Soc. B. 369 (2014) 20130426.

[2] J.T. Keer, L. Birch, Molecular methods for the assessment of bacterial viability, J. Microbiol. Methods. 53 (2003) 175–183.

[3] F. v. Wintzingerode, U.B. Göbel, E. Stackebrandt, Determination of microbial diversity in environmental samples: pitfalls of PCR-based rRNA analysis, FEMS Microbiol. Rev. 21 (1997) 213–229.

[4] B. Byrne, E. Stack, N. Gilmartin, R. O'Kennedy, Antibody-based sensors: principles, problems and potential for detection of pathogens and associated toxins, Sensors. 9 (2009) 4407–4445.

[5] D. V Lim, J.M. Simpson, E.A. Kearns, M.F. Kramer, Current and developing technologies for monitoring agents of bioterrorism and biowarfare, Clin. Microbiol. Rev. 18 (2005) 583–607.

[6] R.Y.A. Hassan, U. Wollenberger, Mediated bioelectrochemical system for biosensing the cell viability of Staphylococcus aureus, Anal. Bioanal. Chem. 408 (2016) 579–587.

[7] J. Xu, Y. Chau, Y. Lee, Phage-based electrochemical sensors: A review, Micromachines. 10 (2019) 855.

[8] J. Paczesny, Ł. Richter, R. Hołyst, Recent Progress in the Detection of Bacteria Using Bacteriophages: A Review, Viruses. 12 (2020) 845.

[9] J. Rakonjac, M. Russel, S. Khanum, S.J. Brooke, M. Rajič, Filamentous phage: structure and biology, in: Recomb. Antibodies Infect. Dis., Springer, 2017: pp. 1–20.

[10] M. Sedki, X. Chen, C. Chen, X. Ge, A. Mulchandani, Non-lytic M13 phage-based highly sensitive impedimetric cytosensor for detection of coliforms, Biosens. Bioelectron. 148 (2020) 111794.

[11] C. García-Aljaro, L.N. Cella, D.J. Shirale, M. Park, F.J. Muñoz, M. V. Yates, A. Mulchandani, Carbon nanotubes-based chemiresistive biosensors for detection of microorganisms, Biosens. Bioelectron. (2010). https://doi.org/10.1016/j.bios.2010.07.077.

[12] B.K. Das, C. Tlili, S. Badhulika, L.N. Cella, W. Chen, A. Mulchandani, Single-walled carbon nanotubes chemiresistor aptasensors for small molecules: picomolar level detection of adenosine triphosphate, Chem. Commun. 47 (2011) 3793–3795.

[13] M. Park, L.N. Cella, W. Chen, N. V Myung, A. Mulchandani, Carbon nanotubes-based chemiresistive immunosensor for small molecules: Detection of nitroaromatic explosives, Biosens. Bioelectron. 26 (2010) 1297–1301.

[14] C. Tlili, N. V Myung, V. Shetty, A. Mulchandani, Label-free, chemiresistor immunosensor for stress biomarker cortisol in saliva, Biosens. Bioelectron. 26 (2011) 4382–4386.

[15] W. Zhao, Y. Xing, Y. Lin, Y. Gao, M. Wu, J. Xu, Monolayer graphene chemiresistive biosensor for rapid bacteria detection in a microchannel, Sensors and Actuators Reports. 2 (2020) 100004.

[16] M. Hatada, T.-T. Tran, W. Tsugawa, K. Sode, A. Mulchandani, Affinity sensor for haemoglobin A1c based on single-walled carbon nanotube field-effect transistor and fructosyl amino acid binding protein, Biosens. Bioelectron. 129 (2019) 254–259.

[17] L.G. Guex, B. Sacchi, K.F. Peuvot, R.L. Andersson, A.M. Pourrahimi, V. Ström, S. Farris, R.T. Olsson, Experimental review: chemical reduction of graphene oxide (GO) to reduced graphene oxide (rGO) by aqueous chemistry, Nanoscale. 9 (2017) 9562–9571.

[18] B. Thakur, G. Zhou, J. Chang, H. Pu, B. Jin, X. Sui, X. Yuan, C.-H. Yang, M. Magruder, J. Chen, Rapid detection of single E. coli bacteria using a graphene-based field-effect transistor device, Biosens. Bioelectron. 110 (2018) 16–22.

[19] Y. Huang, X. Dong, Y. Liu, L.-J. Li, P. Chen, Graphene-based biosensors for detection of bacteria and their metabolic activities, J. Mater. Chem. 21 (2011) 12358–12362.

[20] M. Sedki, R.Y.A. Hassan, A. Hefnawy, I.M. El-Sherbiny, Sensing of bacterial cell viability using nanostructured bioelectrochemical system: rGO-hyperbranched chitosan nanocomposite as a novel microbial sensor platform, Sensors Actuators, B Chem. 252 (2017). https://doi.org/10.1016/j.snb.2017.05.163.

[21] J. Ou, J. Wang, S. Liu, B. Mu, J. Ren, H. Wang, S. Yang, Tribology study of reduced graphene oxide sheets on silicon substrate synthesized via covalent assembly, Langmuir. 26 (2010) 15830–15836.

[22] M. Sedki, M.B. Mohamed, M. Fawzy, D.A. Abdelrehim, M.M.S.A. Abdel-Mottaleb, Phytosynthesis of silver-reduced graphene oxide (Ag-RGO) nanocomposite with an enhanced antibacterial effect using Potamogeton pectinatus extract, RSC Adv. 5 (2015) 17358–17365. https://doi.org/10.1039/c4ra13117g.

[23] M. Ciszewski, A. Mianowski, P. Szatkowski, G. Nawrat, J. Adamek, Reduced graphene oxide–bismuth oxide composite as electrode material for supercapacitors, Ionics

(Kiel). 21 (2015) 557–563.

[24] D. Krishnan, F. Kim, J. Luo, R. Cruz-Silva, L.J. Cote, H.D. Jang, J. Huang, Energetic graphene oxide: challenges and opportunities, Nano Today. 7 (2012) 137–152.

[25] S. Tian, J. Sun, S. Yang, P. He, S. Ding, G. Ding, X. Xie, Facile thermal annealing of graphite oxide in air for graphene with a higher C/O ratio, RSC Adv. 5 (2015) 69854–69860.

[26] D. Chen, L. Li, L. Guo, An environment-friendly preparation of reduced graphene oxide nanosheets via amino acid, Nanotechnology. 22 (2011) 325601.

[27] D. Li, M.B. Müller, S. Gilje, R.B. Kaner, G.G. Wallace, Processable aqueous dispersions of graphene nanosheets, Nat. Nanotechnol. 3 (2008) 101.

[28] S. Yang, W. Yue, D. Huang, C. Chen, H. Lin, X. Yang, A facile green strategy for rapid reduction of graphene oxide by metallic zinc, Rsc Adv. 2 (2012) 8827–8832.

[29] J.I. Paredes, S. Villar-Rodil, P. Solís-Fernández, A. Martínez-Alonso, J.M.D. Tascon, Atomic force and scanning tunneling microscopy imaging of graphene nanosheets derived from graphite oxide, Langmuir. 25 (2009) 5957–5968.

[30] P. Huang, C. Xu, J. Lin, C. Wang, X. Wang, C. Zhang, X. Zhou, S. Guo, D. Cui, Folic acid-conjugated graphene oxide loaded with photosensitizers for targeting photodynamic therapy, Theranostics. 1 (2011) 240.

[31] H. Mohr, B. Lambrecht, A. Bayer, H. Spengler, S. Nicol, T. Montag, T.H. Müller, Basics of flow cytometry–based sterility testing of platelet concentrates, Transfusion. 46 (2006) 41–49.

[32] M. Schmidt, Comparison of different methods of bacterial detection in blood components, ISBT Sci. Ser. 4 (2009) 80–86.

[33] P. Qi, D. Zhang, Y. Sun, Y. Wan, A selective near-infrared fluorescent probe for hydrogen sulfide and its application in sulfate-reducing bacteria detection, Anal. Methods. 8 (2016) 3339–3344.

[34] J. Chang, S. Mao, Y. Zhang, S. Cui, G. Zhou, X. Wu, C.-H. Yang, J. Chen, Ultrasonic-assisted self-assembly of monolayer graphene oxide for rapid detection of Escherichia coli bacteria, Nanoscale. 5 (2013) 3620–3626.

[35] G. Wu, Z. Dai, X. Tang, Z. Lin, P.K. Lo, M. Meyyappan, K.W.C. Lai, Graphene Field-Effect Transistors for the Sensitive and Selective Detection of Escherichia coli Using Pyrene-Tagged DNA Aptamer, Adv. Healthc. Mater. 6 (2017) 1700736.

CHAPTER 7

CVD synthesis of $MoSe_2$, $MoSe_{2(2-x)}Te_{2x}$ Alloys, and Janus $MoSe_{2(2-y)}Te_{2y}/MoSe_{2(2-x)}Te_{2x}$ Defect-Free Interface Heterostructures for FET Optoelectronics

Abstract: $MoSe_2$ is a semiconductor transition metal dichalcogenide (TMDC), with a relatively low optical band gap (OBG) of 1.52 eV, current switching ratio of 10^4-10^5, and a near-infrared (NIR) photoluminescence (PL). That makes it an excellent material for field-effect transistor (FET) optoelectronic devices. In this work, optimized CVD synthesis of mono- and bi-layer $MoSe_2$ was introduced, and the synthesized material was characterized and implemented into FET device for NO_2 gas sensing. Due to its advantageous NIR optoelectronic activity, $MoSe_2$-FET device showed instantaneous enhancement of device's current output by 40% under illumination with a 780 nm, 10 mW LED. Hence, light-gating was utilized without the need for back-gating in the low-power sensing of NO_2 gas. Much higher sensitivity was acquired with light-gating, and a limit of detection of 40 ppb was achieved, which is lower than the U.S. Environmental Protection Agency regulated limit of 53 ppb. Further, ternary alloys of $MoSe_{2(2-x)}Te_{2x}$ were synthesized using Te doping, characterized, and the corresponding FET device performance was evaluated. Band gap tuning from 1.52 eV to 1.35 eV was successful, and the corresponding FET device performance was greatly enhanced. Janus in-situ prepared $MoSe_{2(2-y)}Te_{2y}/MoSe_{2(2-x)}Te_{2x}$ defect-free interface heterostructures, where $y \neq x$, and $y \geq 0$ were synthesized for the first time. In addition, the Janus heterostructure exhibited antiambipolar FET characteristic, which opens the door for this material for multivalued logic circuits.

7. 1. Introduction

TMDCs are another family of 2D layered materials with the general structure of MX_2 (X-M-X), where M is a transition metal (Ti, Zr, Hf; V, Nb, Ta; Ct, Mo, or W), from groups IV, V, and VI, that is sandwiched between two chalcogen (X) atoms (S, Se, or Te). Analogous to graphene, bulk TMDCs form weak vdW bonding between layers and strong covalent or ionic bonds in the same layer, i.e. between M and X, which makes it easy to exfoliate them. Each transition metal atom is surrounded by six chalcogen atoms in an octahedral, forming *1T* phase, or triangular prism coordination, forming *2H* phase [1]. The type of coordination depends on the nature of bonding between transition metal and chalcogen; group IV transition elements form strong ionic bonds, which result in repulsive Coulomb forces between layers, and hence octahedral coordination is more favored. Contrarily, group VI transition elements form covalent compounds, and stabilize well in trigonal prismatic coordination [2,3]. Due to their moderate ionicity, group V elements can be found in both octahedral and trigonal prismatic coordination [4]. Due to their intriguing optical and electronic properties, TMDCs have garnered a huge attention for the application in FET biosensors. Based on their phase and the number of d-electrons, TMDCs vary between semi-metallic, semiconductors, insulator, or superconductors. As most TMDCs are semiconductor (e.g. MoS_2, $MoSe_2$, WS_2, WSe_2), compared to the semi-metallic graphene, they are more promising as electronic switches in FET sensors [5,6]. MoS_2, owing to is very high on/off current ratio ($\approx 10^8$) [7,8] was the first TMDC to attract attention as a strong material for FET sensors. Semiconductor TMDCs, such as MoS_2 have an indirect band gap in bulk-state, a larger direct band gap and a strong photoluminescence (PL) when they are mono- or few-layers [9]. It is worth mentioning

that the band gap and PL emission of TMDCs are tunable and size- and composition-dependent

Most of the presented TMDCs-FET sensor studies are mainly focused on MoS_2-FETs, while the other semiconducting TMDCs, such as $MoSe_2$, were just not getting their chances yet. $MoSe_2$ has similar electronic properties of carrier mobilities and I_{on}/I_{off} ratio. Moreover, $MoSe_2$ has a smaller band gap of 1.52 eV [10], compared to 1.81 eV of MoS_2 [11], which improves its conductivity. Furthermore, the photoluminescence of $MoSe_2$ is in the near infrared (NIR) region [12,13], compared to the visible light region of MoS_2, which enhances its applicability in optoelectronic devices with less interference with visible light.

On the other hand, alloying in TMDCs is a relatively new approach to tune the optoelectronic properties and improve their sensitivity and current conductivity. However, most of the work has been done on alloying between transition metals, while limited work has been presented on alloying between chalcogenides [14]. Monolayer *2H* $MoTe_2$ has a direct band gap of 1.10 eV, and a relatively high I_{on}/I_{off} ratio [15]. Alloying of Se and Te with Mo, to form ternary $MoSe_{2(2-x)}Te_{2x}$ alloy, has been rarely studied, and the results were very interesting in terms of having a lower band gap of the alloy with increasing the percentage of Te and shifting the PL to longer wavelengths [14]. Building TMDCs heterostructure-FET electronic and optoelectronic devices is another cutting-edge area. There are so many studies were presented on vertical and lateral stacking of 2D material, including TMDCs [16–19], however a humble number was presented for the in-situ/one pot-synthesized Janus TMDC heterostructures. The in-situ prepared Janus TMDC

heterostructures have great advantages of defect-free surfaces, as there is no possibility of transfer-associated interface impurities as in stacked heterostructures, and better device performance as the spacing between the two layers is zero.

Keeping all these interesting properties of $MoSe_2$, we optimized its CVD synthesis to get a large area of mono/bi-layers, fabricated $MoSe_2$-FET optoelectronic devices, and applying them to gas sensing. In addition, Ternary alloys of $MoSe_{2(2-x)}Te_{2x}$ were synthesized, characterized, and the corresponding FET device performance was evaluated. Band gap tuning was successful, and the corresponding FET device performance was greatly enhanced. Janus in-situ prepared $MoSe_{2(2-y)}Te_{2y}/MoSe_{2(2-x)}Te_{2x}$ defect-free interface heterostructures, where $y \neq x$, and $y \geq 0$ were synthesized and characterized. Raman mapping and XPS spectroscopy were used to give more insights into the uniformity of the structure and the corresponding elemental ratio for each band gap.

7.2. Materials and methods

In this objective, $MoSe_2$, and $MoSe_{2(2-x)}Te_{2x}$ alloys were synthesized using chemical vapor deposition (CVD), with a gradient variation in (x) to tune the band gap and carrier mobility of the corresponding alloy for optoelectronic devices.

7.2.1. CVD synthesis of monolayer $MoSe_2$

MoO_3 and Se powders were used as precursors, and under inert gas purging (Ar) mixed with reducing gas (H_2) in a 100:5 sccm rate. 5 mg of MoO_3 and 40 mg of Se were placed in two different ceramic boats and loaded to the furnace tube. The growth substrate

(SiO_2/Si) was placed on the MoO_3 boat and kept upside down. The two boats were separated by around 25 cm, and each one had its own heating zone, without having any cold region in between. Ar/H_2 gas mixture was purged for 15 min at room temperature to remove air oxygen. Then, Se's heating zone was set to 250 ^oC and kept running for 5 min before turning MoO_3's heating zone on at 750 ^oC. It took 10 min for to reach the reaction temperature (750 ^oC), and the reaction time was 5 min. MoO_3's heating zone was turned off first, and after 5 min, the Se'e heating was turned off as well. The CVD furnace door was opened for about 3 cm until the temperature reached 400 ^oC, and then was opened completely. After cooling down to < 100 ^oC, the growth substrate was taken out of the furnace for characterization.

7.2.2. CVD synthesis of monolayer $MoSe_{2(2-x)}Te_{2x}$

The optimized protocol is the same as above with some changes: x (1, 2, or 3) mg of Te powder was placed in in a third boat and positioned with a third heat jacket between Se and MoO_3 boats. The Te's heater was started 3 min after Se and 2 min before MoO_3. Reaction time was also 3 min. The heating zone of Te was turned off at the same time with Se.

7.2.3. *CVD synthesis of monolayer $MoSe_{2(2-y)}Te_{2y}/MoSe_{2(2-x)}Te_{2x}$*

The purpose here is to grow a second layer with less Te, so the reaction time was set for 5 min and the Te's heater was turned off 5 min ahead of Se, i.e. at the same time with MoO_3.

7.2.4. Materials Characterization

Raman spectra were collected by Horiba LabRam using a green laser (λ = 532 nm) for excitation with a power of 10 mW. AFM imaging was carried out using Horiba

microscope. TEM imaging was performed using imaged using JEOL JEM-2800 TEM at 200 kV. X-ray photoelectron spectroscopy (XPS) characterization was carried out using Kratos AXIS-Supra XPS with a dual anode Al/Ag monochromatic X-ray source. Electrical measurements were conducted using Keithley 2636 system.

7.2.5. Sample preparation for TEM imaging

PMMA thin film was spin-coated at 2000 rpm for 45 s on the as-grown $MoSe_{2(2-x)}Te_{2x}$ on SiO_2/Si substrate, then baked at 180 ^oC for 2 min. The substrate with PMMA was immersed in 1M KOH for 1 h to dissolve the SiO_2 layer and have the material with PMMA floating. A small piece was then phished and suspended in D.I. water for removal of traces KOH. Then, a small piece was transferred to the TEM carbon grid by phishing. The grid with loaded material was transferred to acetone very gently to dissolve the PMMA polymer. The grid with $MoSe_{2(2-x)}Te_{2x}$ was suspended in D.I. water, dried, and annealed at 100 ^oC for several hours.

7.2.6. Devices fabrication

Different devices were prepared using conventional photolithography techniques with different hard masks for different electrode configurations, followed by e-beam evaporation of 5 nm Cr and 50 nm Au. A lift-off step was conducted in acetone. For back-gating, all devices were wet etched from the back with buffered HF solution for 5 min, and then Cr/Au (5/50 nm) layer was deposited to the back.

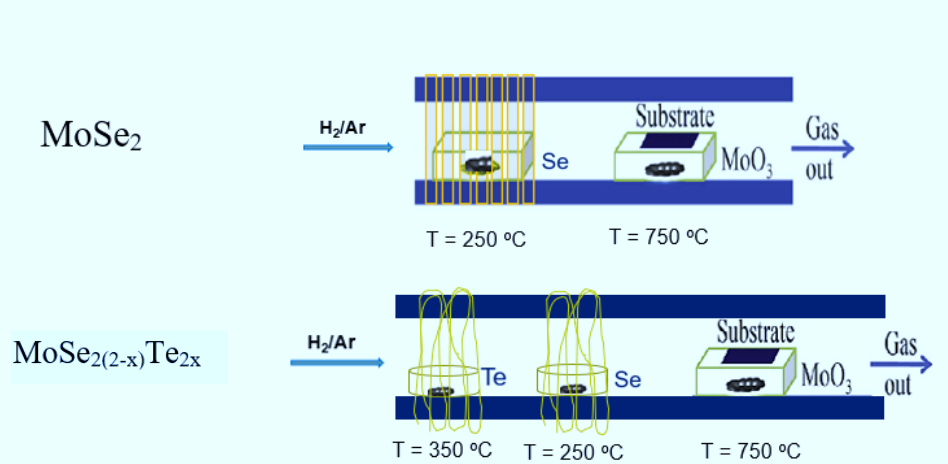

Figure 7.1. schematic diagrams of the CVD system for synthesis of $MoSe_2$, $MoSe_{2(2-x)}Te_{2x}$ and $MoSe_{2(2-y)}Te_{2y}/MoSe_{2(2-x)}Te_{2x}$.

7.3. Results and discussions

Results and discussions of MoSe2 and its gas sensing performance will be presented first, followed by results of $MoSe_{2(2-y)}Te_{2y}$ alloy, and in-situ prepared $MoSe_{2(2-y)}Te_{2y}/MoSe_{2(2-x)}Te_{2x}$ defect-free interface Janus heterostructures, where $y \neq x$, and $y \geq 0$.

7.3.1. Microscopic characterization of $MoSe_2$

The CVD grown $MoSe_2$ nanosheets were imaged using optical microscopy, as shown in **Fig. 7.2 (a-c)**. Panel (a) shows the edge of the grown thin film where triangles can be distinguished and moving to the core of the film in panel (b), a continuous film of what is believed to be monolayer $MoSe_2$ is observed. Nucleation of a second layer can be seen, which is normal. Another spot at the edge of the film was imaged, panel (c), where the large triangular domains are shown. Atomic force microscopy, panel (d), was implemented to study the surface topology of the prepared $MoSe_2$ and measure its thickness. The sample

looks smooth and clean, with 0.8 nm thickness, which corresponds to a monolayer structure [20,21].

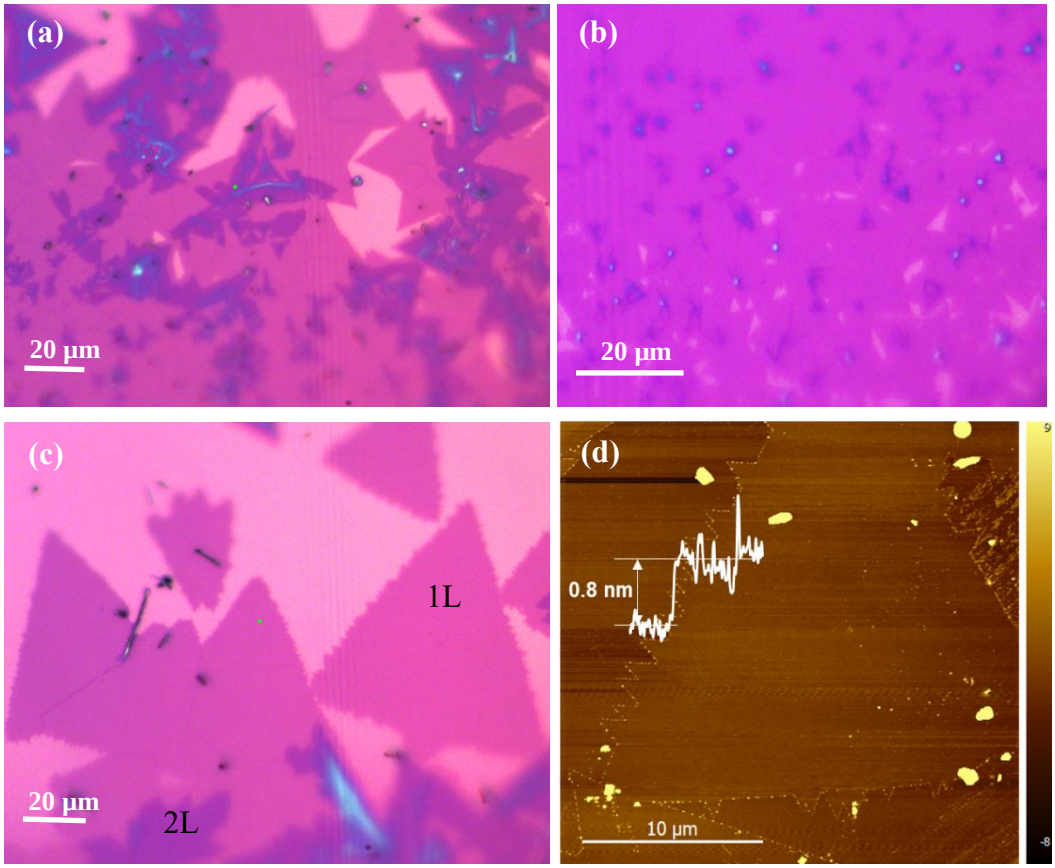

Figure 7.2. (a-c) optical microscopy images of CVD grown $MoSe_2$ thin film. (d) AFM image and height profile of $MoSe_2$.

7.3.2. Raman, photoluminescence, and band gap

Raman is a very powerful tool for characterizing TMDCs, where the vibrational peak positions carry information about the sheet thickness and purity. For $MoSe_2$, there are two main vibrational peaks; out-of-plane mode (A_{1g}), and in-plane mode (E'_{2g}), which exhibit thickness-dependent shift of its Raman peaks. Raman spectroscopic results in **Fig. 7.3b** show the two main characteristic peaks of $MoSe_2$. The A_{1g} peak position at 239.5 cm^{-1} is

characteristic for monolayer sheets, while the second peak position at 240.5 cm^{-1} is characteristic for bilayer sheets, or nucleation of a second layer [22,23]. In addition, using the same laser beam (532 nm), photoluminescence (PL) and optical band gap (OBG) can be obtained. As shown in **Fig. 7.3 (c&d)**, the prepared $MoSe_2$ monolayer sheets have strong PL peak at 815 nm, and an OBG at 1.52 eV, which are characteristic for $MoSe_2$ nanosheets [12,13].

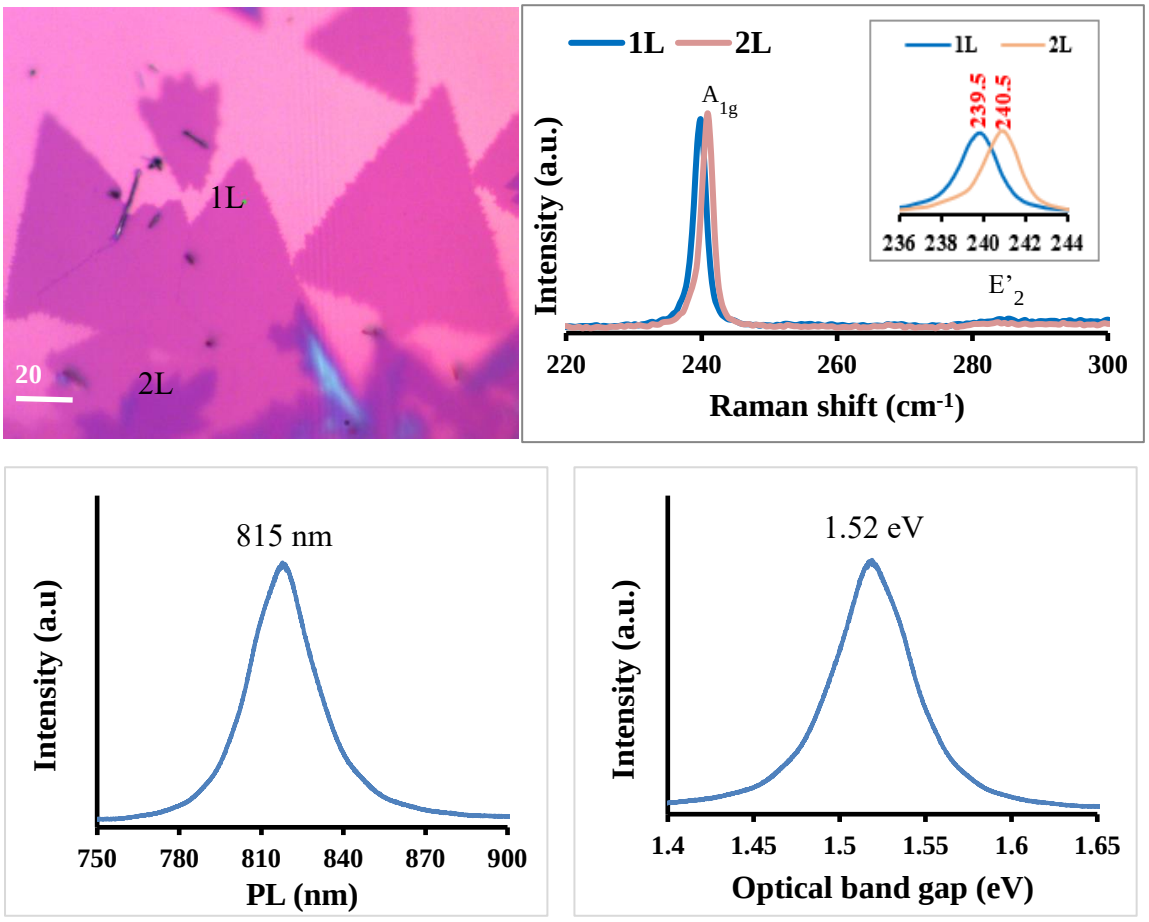

Figure 7.3. (a) optical microscopy image of MoSe2 grown on SiO2/Si substrate. (b) Raman spectra of a monolayer and bilayer $MoSe_2$. (c) photoluminescence (PL) and (d) optical band gap of $MoSe_2$. These measurements were conducted using a 532 nm laser with 15 mW power and 0.1% filter.

7.3.3. FET characteristic curve and carrier mobility

In order to study the electronic properties of the grown thin films, a device microfabrication was pursued for building a back-gated FET transistor as shown in **Fig. 7.4**. We use two different electrode configurations: interdigitated (panel b) and single gap (panel c) electrodes. A source-drain voltage (V_{SD}) was applied to the device, where the synthesized material was bridging the two electrodes. Back-gate potential was also swept through the back of the device to create an electric field that modulates the material properties based on its nature (n-, p-, or ambipolar-type). The current-voltage (I_{SD}-V_{SD}) measurements show curved line (S-shape), **Fig. 7.4c**, which illustrates a difference in work-function between $MoSe_2$ and Au, creating Schottky barrier [24]. A few previous studies have reported n-type behavior of MoSe2 [25,26]. The FET characteristic curve, **Fig. 7.4d**, shows that the material has an ambipolar behavior with a predominant n-type characteristic, which can be attributed to Se vacancies and/or oxygen impurities, which is in a good agreement with literature [27–30]. We believe that the material transfer step, using PMMA, KOH, and open air heating, plays the main role in the p-type contribution due to the formation of carbon residues from PMMA, and defects from the harsh chemical (KOH) that enhances the p-type characteristic [31]. Some devices have shown more p-type predominant behavior, especially when annealing with H_2/Ar was not conducted, as shown in **Fig. 7.4f**. The p-type behavior of $MoSe_2$ due to adsorbed oxygen was reported by another group [32].

The current switch ($I_{on/off}$) ratio was found ~ 10^4, which indicates a high sensitivity and wide dynamic range of the corresponding gas sensor. The electron carrier mobility was calculated from the following equation, $\mu = [dI_{SD}/dV_g] * [L/(W*Ci*V_{SD})]$ [33,34], where

L (10 µm) and W (10 µm) are the length and width of the single gap channel, V_{SD} is the applied source-drain voltage (5 V), and Ci is the oxide gate capacitance per unit area (Ci = $\varepsilon \times \varepsilon r$ /d; $\varepsilon = 8.85 \times 10^{-12}$ $F \cdot m^{-1}$, $\varepsilon r = 3.9$; d = 300 nm), which is 0.115 x 10^{-3} F/m^2. The electron carrier mobility was found ~5 $cm^2/V.s$.

7.3.4. Optoelectronic response of $MoSe_2$-FET device

The fabricated device was illuminated with a near-infrared (NIR, 780 nm) LED with a power of 10 mW, as show in the camera picture of the actual system in **Fig. 7.5a**. The corresponding FET curves and time-dependent responses were recorded. A clear enhancement of the current on both sides of the FET curve, **Fig. 7.5b**, illustrating a higher conductivity because of light that excited more charge carrier to the conduction band. For the time-dependent current response, a fixed V_{SD} of 1 V was applied, and without any gate potential.

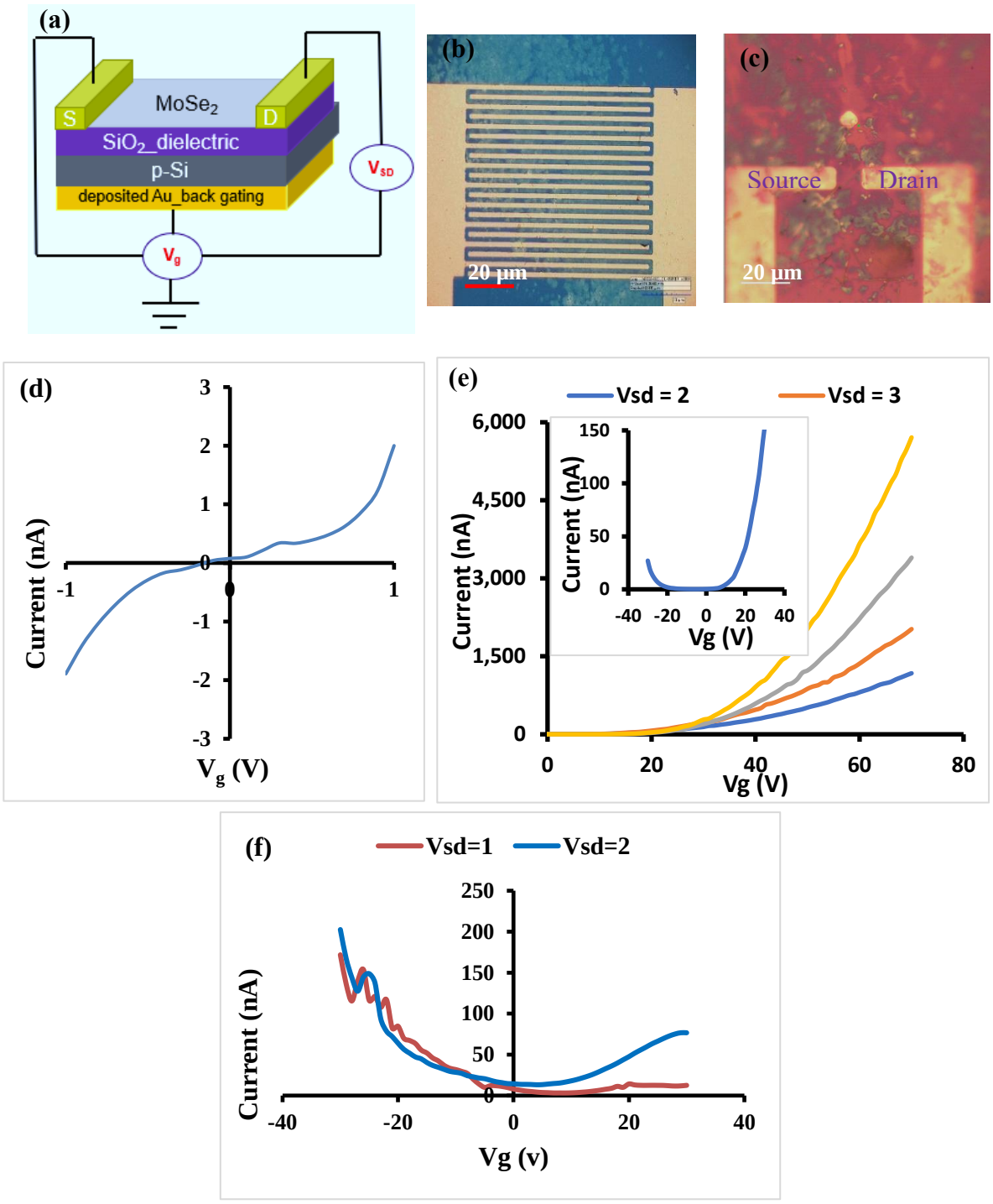

Figure 7.4. (a) a schematic representation the fabricated back-gated $MoSe_2$-FET. (b) interdigitated, and (c) single gap electrodes configuration. (d) I_{SD}-V_{SD} characterization. (e&f) FET characteristic curves of the fabricated device.

The device's current recorded an immediate increase by 40% when the LED was turned on, followed by current stability, and an immediate relaxation to the original current once the LED was switched off. This huge jump in device's current under illumination with NIR LED, without the need for back-gating, opens the door for low power NIR-optoelectronic applications of this device with light-gating, which avoids interference with visible light and expands the applicability of this device.

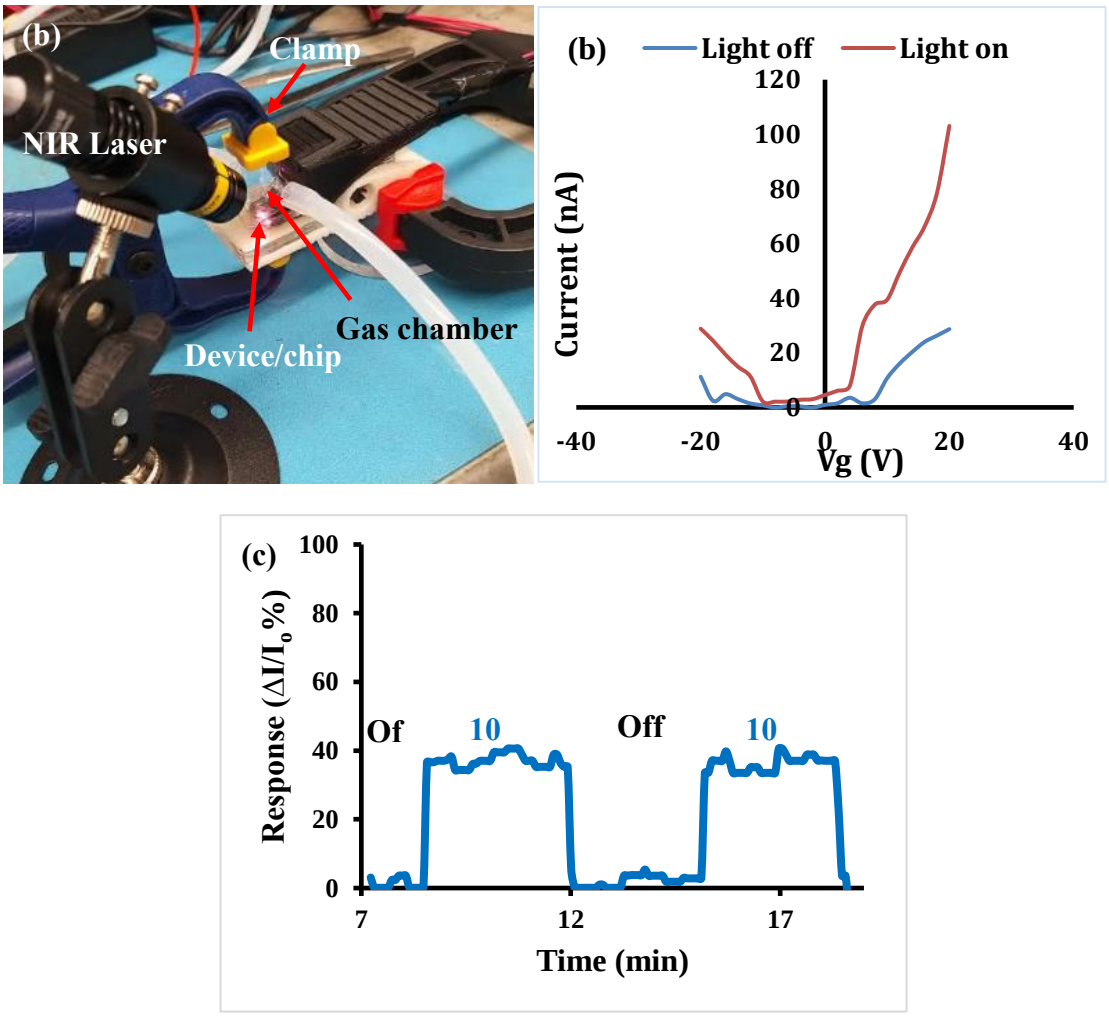

Figure 7.5. (a) camera picture of the actual device setup. (b) FET characteristic curves with and without LED illumination at V_{SD} of 1V. (c) time-dependent current response at a fixed V_{SD} potential of 1 V.

7.3.5. Light-gated NO_2 gas sensing

Gas sensing of the prepared device was tested using NO_2 gas without applying any back-gating. First, N_2 gas was purged at a rate of 400 Sccm for two min until the device's current stabilized. Then, different concentrations of NO_2 were purged by dilution with N_2 gas, so that the NO_2 sensing time is 8 min, followed by another 8 min washing by purging N_2 gas. The sensor response was tested before and after light-gating with 10 mW NIR (780 nm) LED. The gas sensing experiment was designed as a time-dependent current response at a fixed V_{SD} of 1 V. The non-gated device showed increase in current by increasing the detected gas concentration. At the same gas concentrations, **Fig. 7.6 (a & b),** the device showed a significantly higher sensitivity, from to 4.53 nA/ppm, which is attributed to the light-gating effect. The light-gated device was tested for lower gas concentrations (10-320 ppb) and shorter sensing and washing times of 5 min each, **Fig. 7.6 (c & d)**. The experimental limit of detection was 30 ppb, which is the lowest recorded for $MoSe_2$-FET, and it is below the United States Environmental Protection Agency (U.S. EPA) regulation of a limit of detection of 53 ppb [35]. As NO_2 gas is an electron withdrawing molecule and the device's current increased with detected gas concentration, then that means the device behaved as a p-type transistor [32]. The original device response was ambipolar, but right after exposure to NO_2 gas, its behavior changed into a true p-type as shown in **Fig. 7.6e.**

7.3.6. Microscopic characterization of $MoSe_{2(2-x)}Te_{2x}$ ternary alloy

A controllable amount of Te doping was achieved by controlling the ratios between Se and Te, their temperatures, and the timing for starting and stopping the heating process of each of them. For obtaining $MoSe_{2(2-x)}Te_{2x}$ ternary alloy, the amount of Se powder was kept constant (40 mg), while the amount of Te powder was varied from 1 mg to 3 mg, and the corresponding grown alloys were imaged and characterized. As shown in **Fig. 7.7a**, when only 1 mg of Te was used, the domain shape was distorted triangles. By increasing the amount of Te to 2 mg, the domain shape changed to to distorted hexagons, and finally into hexagons at 3 mg of Te, panel (c). These observations are in a good agreement with the previous work of *Apte et al*. [14], although the protocol of synthesis is very different.

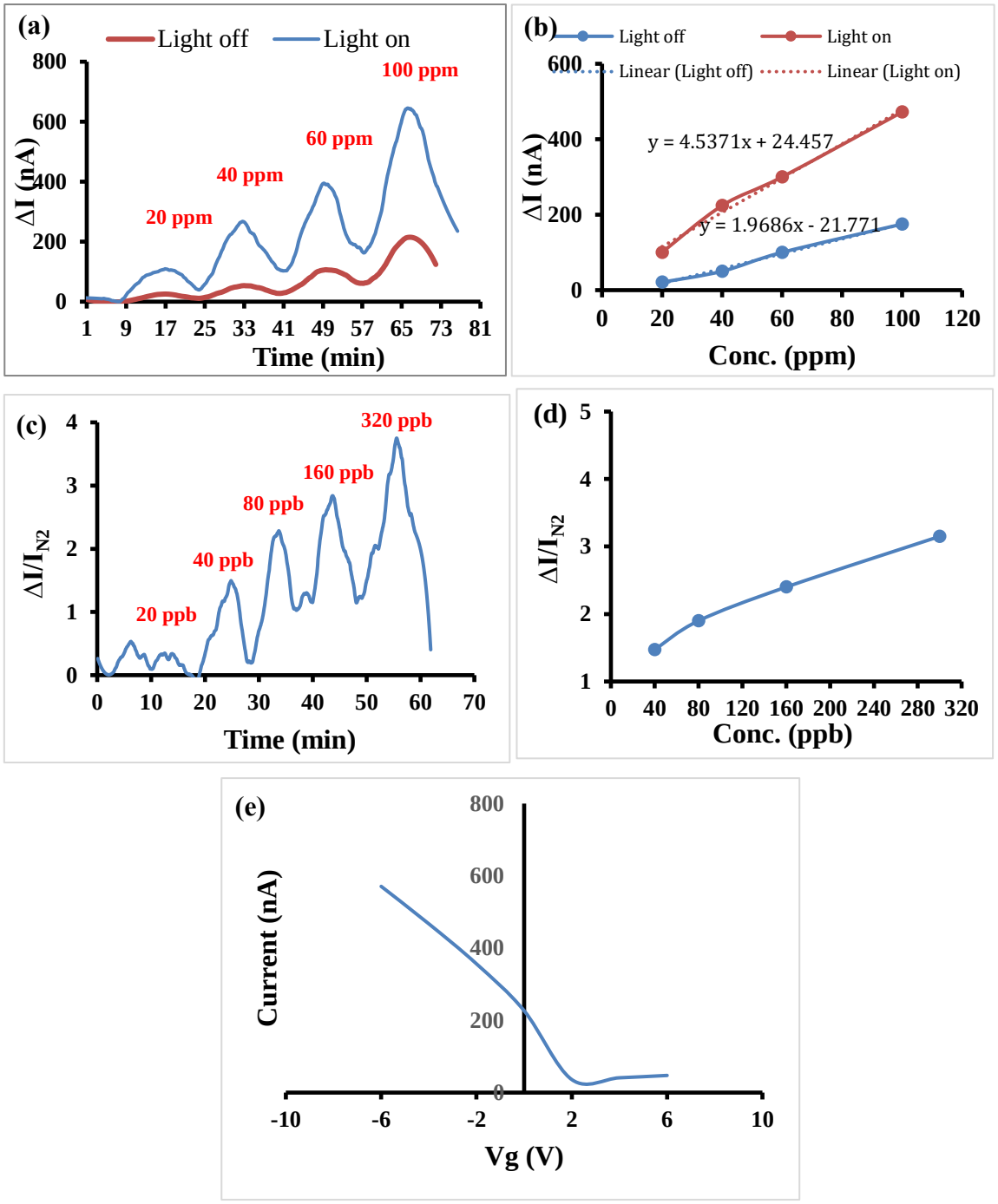

Figure 7.6. (a & b) NO_2 gas sensing at ppm levels with and without light-gating, with consecutive sensing and washing times of 8 min each. (c & d) NO_2 gas sensing ppb levels, with sensing and washing times of 5 min each. (e) FET characteristic curve after exposure to NO_2 gas.

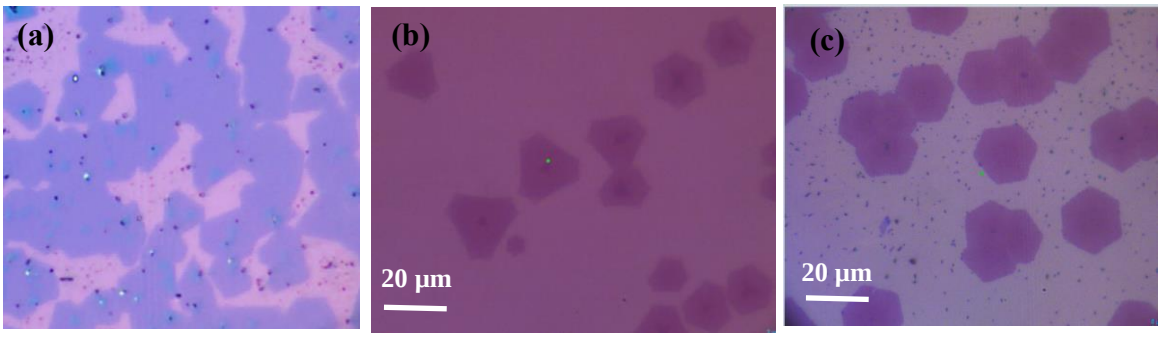

Figure 7.7. Optical microscopy images of $MoSe_{2(2-x)}Te_{2x}$ ternary alloys at different ratios of Te.

7.3.7. Raman, photoluminescence, and band gap

As discussed in the introduction, adding more Te to the $MoSe_2$ crystal is expected to tune its band gap into lower numbers, and shift its PL to a higher wavelength, as shown in **Fig. 7.8.**

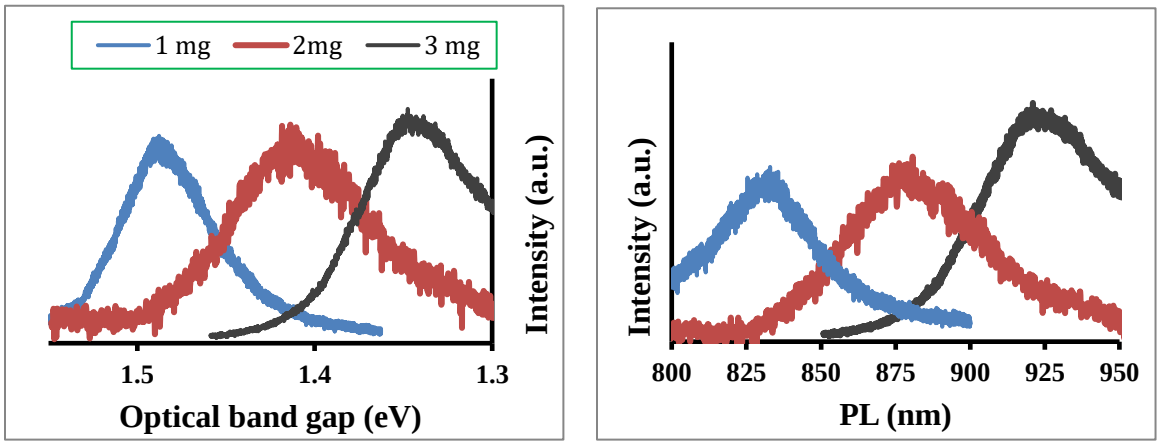

Figure 7.8. PL and optical band gap data of $MoSe_{2(2-x)}Te_{2x}$ ternary alloys at different ratios of Te.

Raman mapping data of the sample where Te was 3 mg, **Fig. 7.9**, show that the structure is homogenous and it all is having the same A_{1g} peak position, except for the very center

that has a new small nucleation of $MoSe_2$. The A1g peak is centered at 235 cm^{-1}, with a band gap of 1.35 eV, and PL at 925 nm at the infrared region. All these results confirm the successful synthesis of Te-rich alloy that is expected to have a strong current output compared to $MoSe_2$, due to its lower band gap.

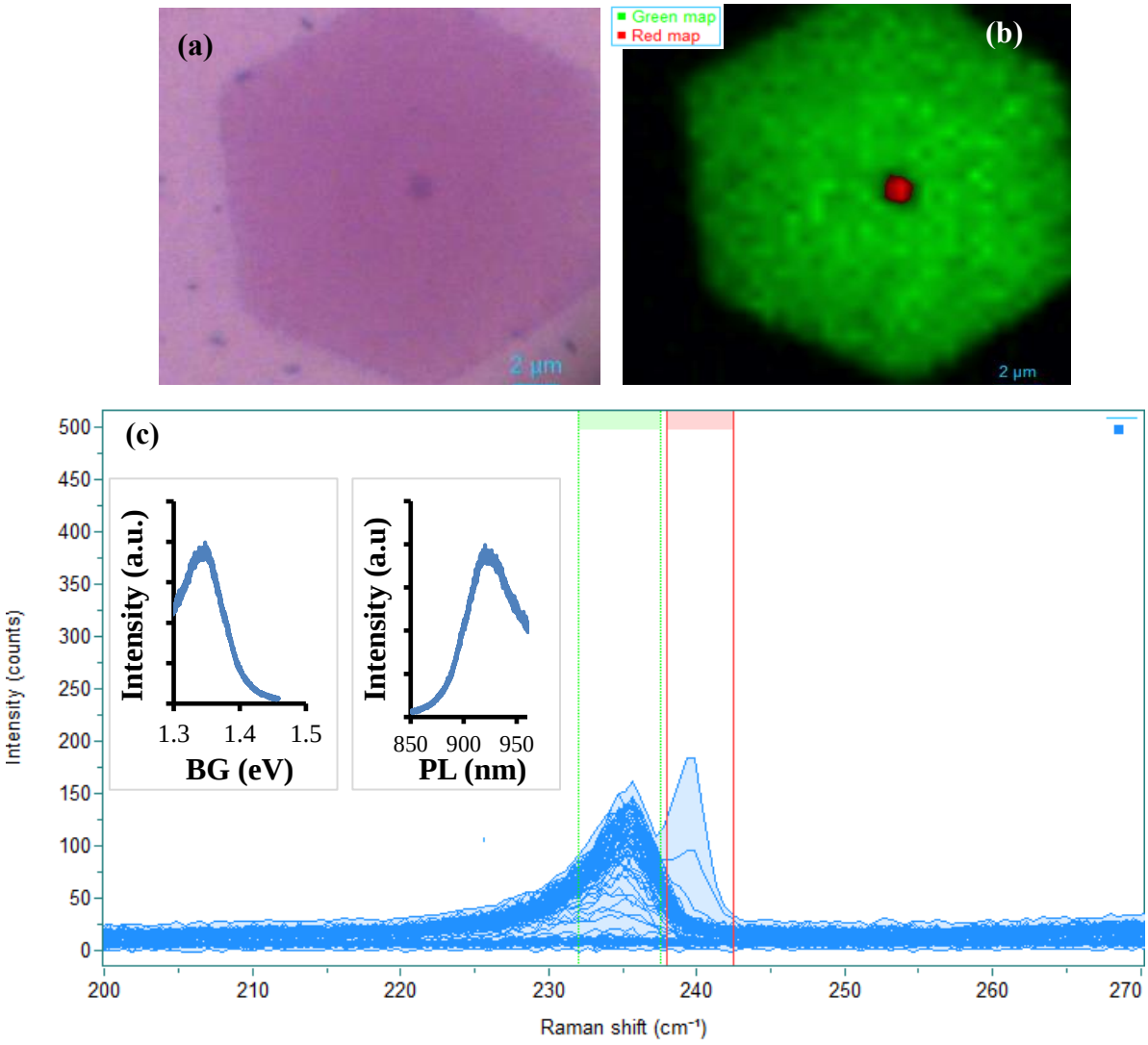

Figure 7.9. Raman mapping of one of the ternary alloy sample (3 mg Te), with band gap and PL data.

7.3.8. XPS analysis and quantification of Te

X-ray photoelectron spectroscopy (XPS) was implemented to quantify the amount of Te in each sample (namely 1 mg, 2 mg, and 3 mg), as well as to give insights into the susceptibility to oxygen at different ratios of Te. Three $MoSe_{2(2-x)}Te_{2x}$ alloys with different initial Te precursor amounts (1, 2, and 3 mg) were synthesized, kept in low vacuum (0.6 MPa), and XPS spectra were collected after 30 days. It is worth mentioning that the samples were taken out of vacuum and exposed to air a few times, where Raman, photoluminescence and band gap characterizations were performed, as well as travelling to another city for XPS. As shown in **Fig. 7.10a**, Mo $3d_{5/2}$ and $3d_{3/2}$ peaks (1 mg sample) appeared at binding energies 229.4 and 232.6 eV suggesting a Mo^{4+} valence for 2H phase. For Se, the $3d_{5/2}$ and $3d_{3/2}$ peaks appeared at 55.4 and 56 eV, confirming the Se^{2-} valence. The corresponding $3d_{5/2}$ and $3d_{3/2}$ peaks of Te^{2-} occurred at 573.5 and 583.8 eV, respectively. These results are in a good agreement with previous work [37]. In addition, there were very small oxide peaks of MoOx and TeOx in the 1 mg sample, which is attributed to a mild oxidation process due to acquired air oxygen over 30 days. By increasing the amount of Te precursor to 2 mg, a lower binding energy shift was observed with Mo and Te, which is expected due to the lower electronegativity of Te compared to Se. Further, the intensity of TeOx and MoOx peaks increased with increasing Te in the crystal. When 3 mg of Te precursor were used, a significant oxide peaks were observed with the three elements (Mo, Se, and Te), which indicates that the higher the amount of Te in the crystal, the higher oxygen susceptibility. The relatively oxygen susceptibility of $MoTe_2$ was revealed by other literature [38,39]. The MoOx and TeOx peak positions match

the previously published work [38,40]. Furthermore, the lower crystal stability against oxygen is expected from the lower binding energy shift, as the lower the binding energy, the less stable the crystal is.

The 3 mg sample (Te is 62%) was etched in two gradual steps (2 and 4 s) using a cluster of 1000 Ar (Ar1000+) at 10 kV and ion beam current of ~0.2uA. The first etching process did remove part of the surface and edges of the sample and the results in **Fig. 7.10(e-f**) show that the oxygen was completely removed from Se, and significantly removed from Mo and Te. However, it was not completely removed from Mo and Te, which illustrates that it is not only at the edges or surface, but also to the core of the structure. Hence, a protection/passivation layer is recommended when such high amount of Te is used in the alloy.

To correlate the electronic properties of the different $MoSe_{2(2-x)}Te_{2x}$ alloys, the actual amount of Te was determined by calculating the area under the peak of the 3d orbitals and dividing it by the corresponding relative sensitivity factors (RSF) for each element. The 1, 2, and 3 mg samples were equivalent to 29, 36, and 62% of Te, respectively, calculated using the following equation [Te/(Se+Te)]x100, as shown in **Fig. 7.10j.**

To better understand whether the acquired oxygen was from the CVD growth step or air oxygen acquired over time, fresh samples ($MoSe_2$, and $MoSe_{2(2-x)}Te_{2x}$ with 36% Te) were prepared one day ahead of the XPS measurement and kept under low vacuum. XPS results in **Fig. 7.10(g-i)** show that $MoSe_2$ did not show any considerable oxide peak. In addition, the 36% Te alloy did not show any considerable Mo or Se oxide peaks, but it did show very small oxide peaks of TeOx. Comparing the fresh (1 day) to the old (30 days) samples

of 36% Te alloy, we can conclude that the oxidation process is mainly post synthesis, and it is significant only at the high Te percentages of ~ >36%. For long term stability, either 36% Te or less is recommended or surface passivation is necessary to maintain the interesting properties of the alloys in higher Te percentages. A recent work encapsulated $MoTe_2$ in SiO_2 thin films and showed air stability [2].

7.3.9. TEM imaging and EDX mapping

The sample was imaged using JEOL JEM-2800 TEM at 200 kV. The low magnification low-magnification annular dark-field (ADF) image in **Fig. 7.11** shows a piece of the alloy covered with part of the carbon grid as confirmed by the EDX mapping, panel (b). Se and Te are homogenously distributed around Mo, which verifies that the $MoSe_{2(2-x)}Te_{2x}$ crystal grows as a homogenous alloy. Further, the fast Fourier transform (FFT) diffraction pattern in panel (f) confirms the high crystallinity of the grown alloy.

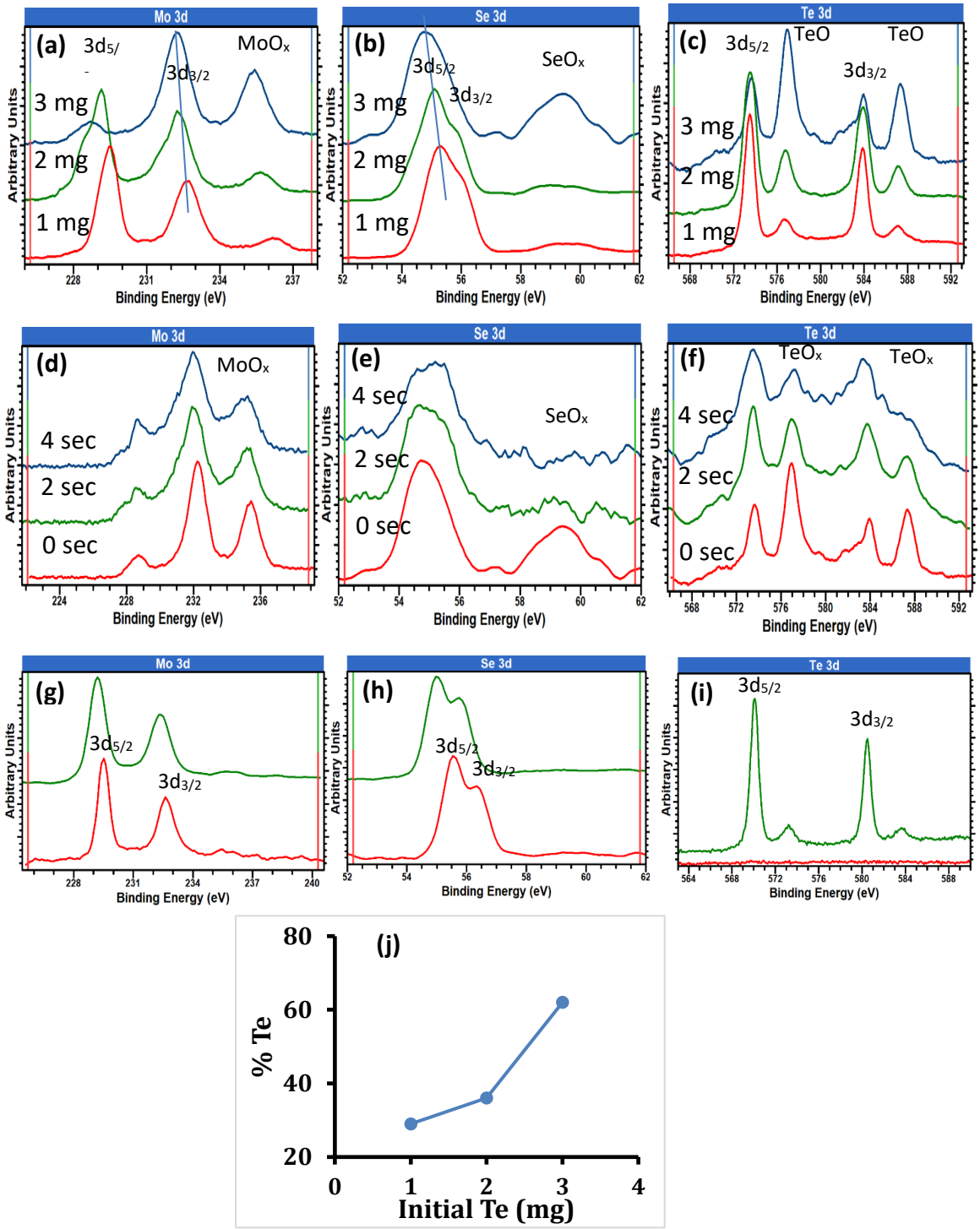

Figure 7. 10. (a-c) XPS analysis of 30 days old samples (1, 2, and 3 mg). (d-f) XPS results of etching of sample 3 mg. (g-i) XPS of fresh MoSe2 and 1 mg $MoSe_{2(2-x)}Te_{2x}$. (j) quantification results of the percentage of Te in the three alloys.

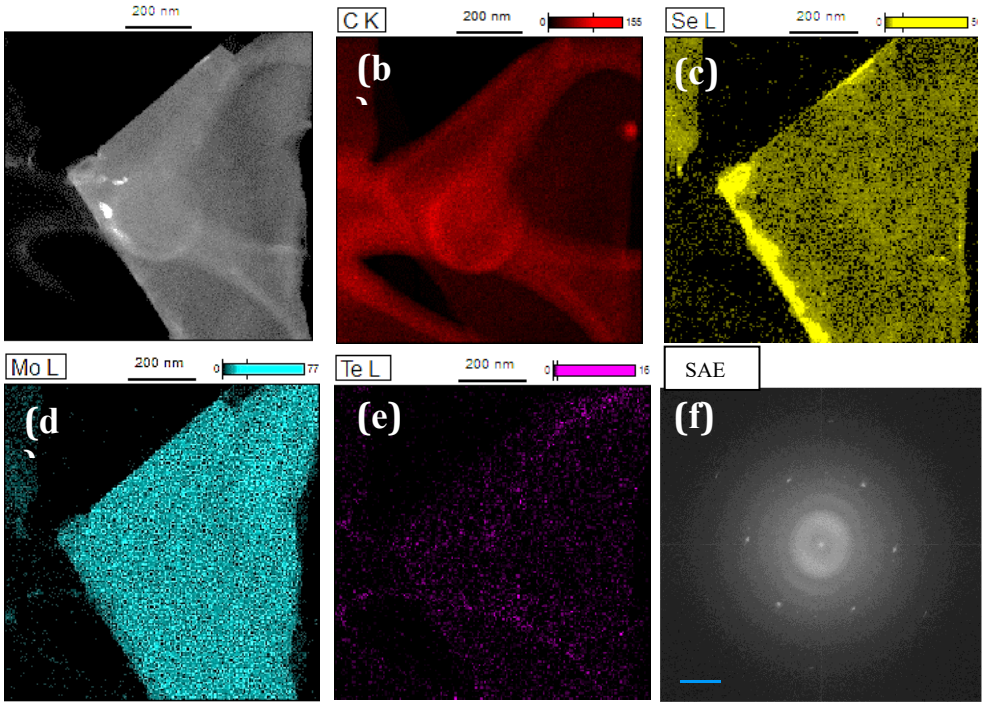

Figure 7. 11. (a) Low-magnification ADF TEM image of a piece of the alloy. (b-e) TEM EDX mapping of C, Se, Mo, and Te, respectively. (e) FFT diffraction pattern.

7.3.10. FET characteristic curve and optoelectronic response

FET characteristic curves in **Fig. 7.12** show around three orders of magnitude enhancement in the device output (current) to reach microampere readings, at zero gate potential, instead of nanoampere without doping, which increases the applicability as a low power device. The device's optoelectronic response is shown in panel (b), and it is confirming the current improvement with NIR LED illumination. However, the optoelectronic response is a bit weaker than in $MoSe_2$-FET device, which might be because in the case of the Te-highly doped alloy more electrons are already in the conduction band.

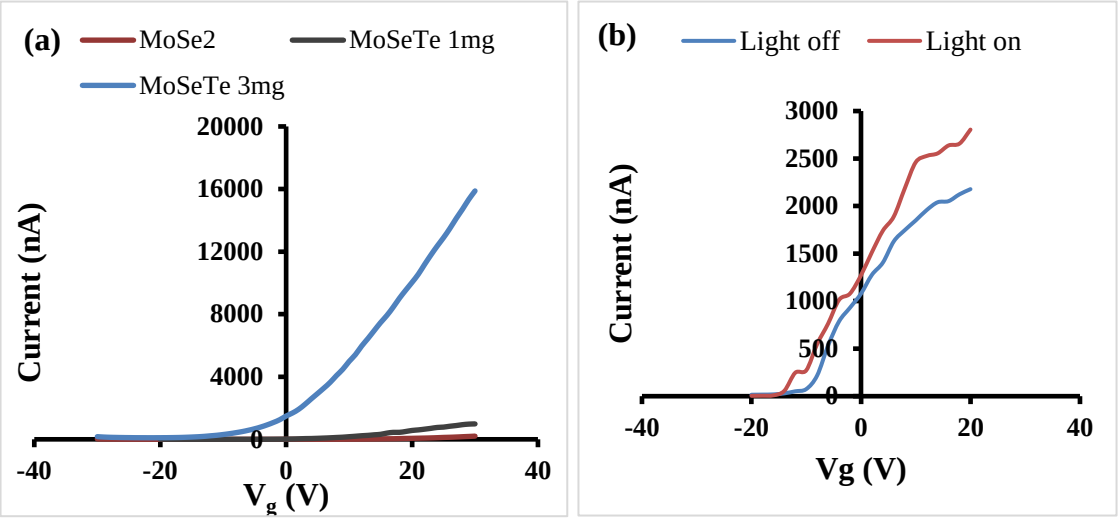

Figure 7. 12. (a) FET characteristic curves of the ternary alloy at different initial amounts of Te (0, 2, and 3 mg), and (b) the optoelectronic response of the ternary alloy at 3 mg of Te.

7.3.11. In-situ preparation of Janus $MoSe_{2(2-y)}Te_{2y}/MoSe_{2(2-x)}Te_{2x}$

In this section, the in-situ preparation results of $MoSe_{2(2-y)}Te_{2y}/MoSe_{2(2-x)}Te_{2x}$ defect-free interface Janus heterostructures, where $y \neq x$, and $y \geq 0$. To minimize the number of possible resulting structures, the initial amounts of Se, Te, and MoO_3 powders were kept constant at 40, 3, and 5 mg. To achieve this goal, the epitaxial growth reaction is run for five min, and then the furnace (heating zone of MoO_3) is stopped and the temperature at the heating zone of Te is reduced from 350 to 250 ^oC, while the heating zone of Se is kept at 250 ^oC for five more minutes after reducing Te's temperature. Even after stopping the furnace heating, MoO_3 heating zone is still hot enough (<750 ^oC and >690 ^oC) to grow a second layer that is richer in Se. Controlling the chemical composition of the top and bottom layer and having it different, results in Janus heterostructure with no interface defects. It also opens the door for unlimited number of applications, such as building unidirectional current

flow devices between smaller (bottom) and larger (top) band gap layered structure. Building antiambipolar transistors is another promising and novel application of this material as well.

7.3.12. Optical microscopy and Raman mapping

The optical microscopy images in **Fig. 7.13** illustrate the Janus heterostructure between the top layer that has a higher band gap (triangle) and the bottom layer that has a lower band gap (hexagon). The top layer is having a band gap of ~1.5 eV, while the bottom one is 1.35 eV, as shown in **Fig. 7.14.** Raman mapping shows the difference in Raman signal that is coming from the difference top and bottom layer compositions and hence their electronic properties.

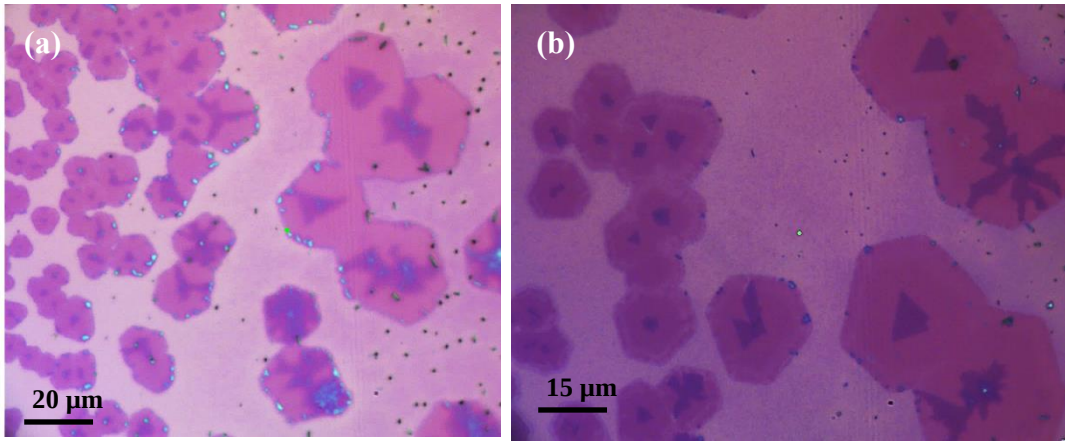

Figure 7. 13. Optical microscopy imaging of the prepared Janus $MoSe_{2(2-y)}Te_{2y}/MoSe_{2(2-x)}Te_{2x}$ heterostructures, where $y \neq x$, and $y \geq 0$.

7.3.13. FET characteristic curve

The grown Janus heterostructures were patterned using photolithography and then etched using O_2 plasma (100 W, 5 min), and then the corresponding devices were patterned using a solid mask. Au/Cr electrodes were deposited by e-beam evaporator, followed by lift-off in acetone. The patterning process is schematically shown in **Fig. 7.15a**. Au/Cr were deposited to the back of the device, after wet etching using buffered HF, for back-gating. The actual device is shown in panel (b). The device was then heated in air at 80 ^{o}C for 2 h to introduce oxygen dopants to the heterostructure. As shown from the XPS data and literature [36], the bottom layer that is richer in Te has a higher affinity to oxygen and converts into a p-type material, while Se-richer top layer will stay ambipolar. Combining the p-type characteristic of the Te-richer layer with the ambipolar characteristic of the Se-richer, resulted in the formation of antiambipolar FET transistor, **Fig. 7.15c**, of the Janus heterostructure. The device was then annealed at 200 ^{o}C under Ar/H_2 (100/5 sccm) for 2 h When the device was annealed at inert conditions, the driving voltage (V_{peak}) shifted from -10 V to 5 V, which can be attributed to the reduced p-type characteristics. The peak-to-valley ratio (PVR = I_{peak}/I_{valley}) was ~ 10^4. The antiambipolar FET transistor became recently a hot topic for multivalued logic circuits, and many stacked heterostructure materials were tried for this application [41], however the concept of in-situ prepared Janus heterostructures for antiambipolar FET, with defect-free interface, is very new.

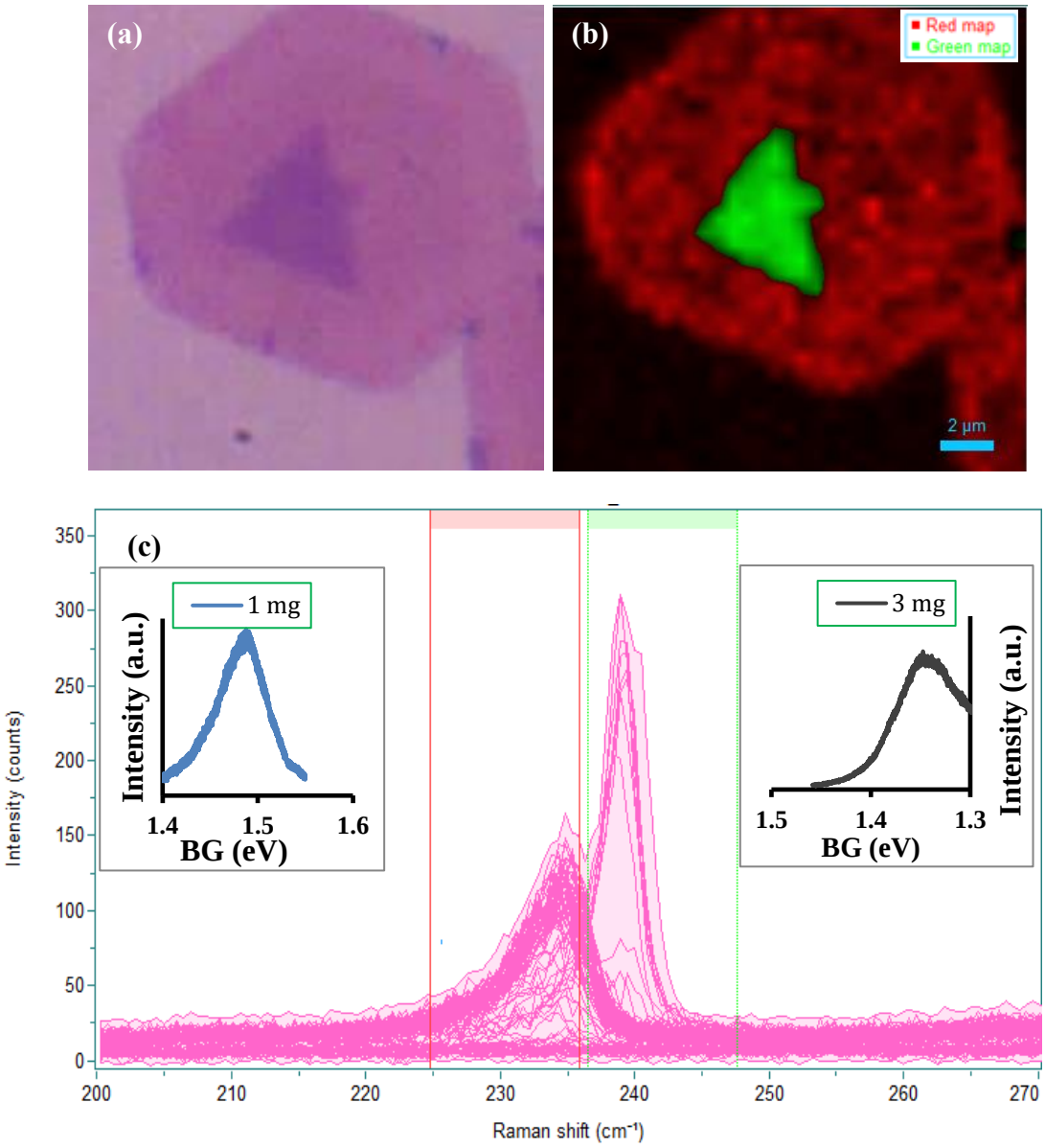

Figure 7.14. Raman mapping of the of the prepared Janus $MoSe_{2(2-y)}Te_{2y}/MoSe_{2(2-x)}Te_{2x}$ heterostructures, where $y \neq x$, and $y \geq 0$

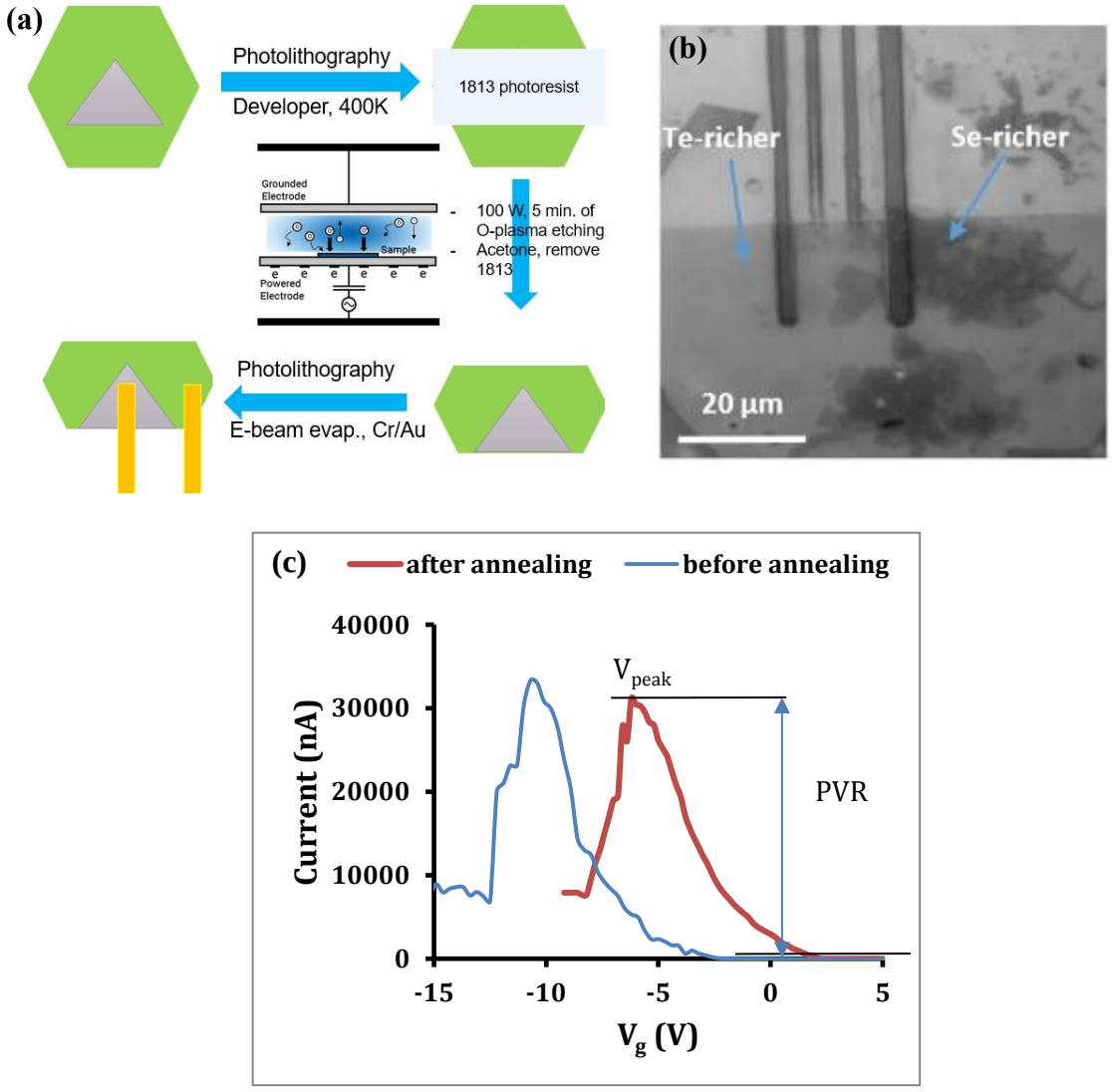

Figure 7.15. (a) a schematic of the fabrication process of the device. (b) optical microscopy image of the actual device. (c) The FET characteristic curve of the corresponding antiambipolar transistor behavior.

7.4. Conclusions

A large area and high quality $MoSe_2$ nanosheets were synthesized using chemical vapor deposition, characterized, and implemented for the first time as a near-infrared (NIR) optoelectronic device for the detection of NO_2 gas. A strong enhancement in the device's response was observed under NIR LED illumination due to exciting more electrons to the conduction band. A low limit of detection of NO_2 gas of 40 ppb was achieved, which is below the allowed limit of this toxic gas. Further, doping of $MoSe_2$ crystal with Te, to form ternary $MoSe_{2(2-x)}Te_{2x}$ alloys was successful and a strong band gap reduction from 1.52 eV to 1.35 eV was recorded. The ternary alloy with 3 mg of initially added Te has shown a three orders of magnitude enhancement in the device output. In addition, Janus in-situ prepared $MoSe_{2(2-y)}Te_{2y}/MoSe_{2(2-x)}Te_{2x}$ defect-free interface heterostructures, where $y \neq x$, and $y \geq 0$, were synthesized, and characterized. The Janus heterostructure showed antiambipolar behavior which is promising for multivalued logic circuits.

7.5. References

[1] R. Lv, J.A. Robinson, R.E. Schaak, D. Sun, Y. Sun, T.E. Mallouk, M. Terrones, Transition metal dichalcogenides and beyond: synthesis, properties, and applications of single-and few-layer nanosheets, Acc. Chem. Res. 48 (2015) 56–64.

[2] X. Zong, H. Yan, G. Wu, G. Ma, F. Wen, L. Wang, C. Li, Enhancement of photocatalytic H2 evolution on CdS by loading MoS2 as cocatalyst under visible light irradiation, J. Am. Chem. Soc. 130 (2008) 7176–7177.

[3] J.A. Wilson, A.D. Yoffe, The transition metal dichalcogenides discussion and interpretation of the observed optical, electrical and structural properties, Adv. Phys. 18 (1969) 193–335.

[4] Y.J. Zhang, M. Yoshida, R. Suzuki, Y. Iwasa, 2D crystals of transition metal dichalcogenide and their iontronic functionalities, 2D Mater. 2 (2015) 44004.

[5] A. Kutana, E.S. Penev, B.I. Yakobson, Engineering electronic properties of layered transition-metal dichalcogenide compounds through alloying, Nanoscale. 6 (2014) 5820–5825.

[6] Z. Meng, R.M. Stolz, L. Mendecki, K.A. Mirica, Electrically-transduced chemical sensors based on two-dimensional nanomaterials, Chem. Rev. 119 (2019) 478–598.

[7] W. Wu, D. De, S.-C. Chang, Y. Wang, H. Peng, J. Bao, S.-S. Pei, High mobility and high on/off ratio field-effect transistors based on chemical vapor deposited single-crystal MoS2 grains, Appl. Phys. Lett. 102 (2013) 142106.

[8] A. Islam, J. Lee, P.X.-L. Feng, All-dry transferred single-and few-layer MoS2 field effect transistor with enhanced performance by thermal annealing, J. Appl. Phys. 123 (2018) 25701.

[9] Z. Li, G. Ezhilarasu, I. Chatzakis, R. Dhall, C.-C. Chen, S.B. Cronin, Indirect band gap emission by hot electron injection in metal/MoS2 and metal/WSe2 heterojunctions, Nano Lett. 15 (2015) 3977–3982.

[10] Y.-H. Chang, W. Zhang, Y. Zhu, Y. Han, J. Pu, J.-K. Chang, W.-T. Hsu, J.-K. Huang, C.-L. Hsu, M.-H. Chiu, Monolayer MoSe2 grown by chemical vapor deposition for fast photodetection, ACS Nano. 8 (2014) 8582–8590.

[11] J. Ryou, Y.-S. Kim, S. Kc, K. Cho, Monolayer MoS2 bandgap modulation by dielectric environments and tunable bandgap transistors, Sci. Rep. 6 (2016) 1–8.

[12] B. Zheng, Y. Chen, Controllable growth of monolayer MoS2 and MoSe2 crystals using three-temperature-zone furnace, in: Proc. IOP Conf. Ser., Mater. Sci. Eng., 2017: p. 12085.

[13] S. Tongay, J. Suh, C. Ataca, W. Fan, A. Luce, J.S. Kang, J. Liu, C. Ko, R. Raghunathanan, J. Zhou, Defects activated photoluminescence in two-dimensional

semiconductors: interplay between bound, charged and free excitons, Sci. Rep. 3 (2013) 1–5.

[14] A. Apte, A. Krishnamoorthy, J.A. Hachtel, S. Susarla, J.C. Idrobo, A. Nakano, R.K. Kalia, P. Vashishta, C.S. Tiwary, P.M. Ajayan, Telluride-based atomically thin layers of ternary two-dimensional transition metal dichalcogenide alloys, Chem. Mater. 30 (2018) 7262–7268.

[15] B. Sirota, N. Glavin, S. Krylyuk, A. V Davydov, A.A. Voevodin, Hexagonal MoTe 2 with amorphous BN passivation layer for improved oxidation resistance and endurance of 2D field effect transistors, Sci. Rep. 8 (2018) 1–8.

[16] Y. Xi, J. Zhuang, W. Hao, Y. Du, Recent Progress on Two-Dimensional Heterostructures for Catalytic, Optoelectronic, and Energy Applications, ChemElectroChem. 6 (2019) 2841–2851.

[17] Y. Liu, S. Zhang, J. He, Z.M. Wang, Z. Liu, Recent progress in the fabrication, properties, and devices of heterostructures based on 2D materials, Nano-Micro Lett. 11 (2019) 1–24.

[18] J.Y. Lee, J.-H. Shin, G.-H. Lee, C.-H. Lee, Two-dimensional semiconductor optoelectronics based on van der Waals heterostructures, Nanomaterials. 6 (2016) 193.

[19] J. Cheng, C. Wang, X. Zou, L. Liao, Recent advances in optoelectronic devices based on 2D materials and their heterostructures, Adv. Opt. Mater. 7 (2019) 1800441.

[20] J. Quereda, T.S. Ghiasi, J.-S. You, J. van den Brink, B.J. van Wees, C.H. van der Wal, Symmetry regimes for circular photocurrents in monolayer MoSe2, Nat. Commun. 9 (2018) 1–8.

[21] Z. Chen, H. Liu, X. Chen, G. Chu, S. Chu, H. Zhang, Wafer-size and single-crystal MoSe2 atomically thin films grown on GaN substrate for light emission and harvesting, ACS Appl. Mater. Interfaces. 8 (2016) 20267–20273.

[22] Y. Zhao, H. Lee, W. Choi, W. Fei, C.J. Lee, Large-area synthesis of monolayer MoSe 2 films on SiO 2/Si substrates by atmospheric pressure chemical vapor deposition, RSC Adv. 7 (2017) 27969–27973.

[23] P. Tonndorf, R. Schmidt, P. Böttger, X. Zhang, J. Börner, A. Liebig, M. Albrecht, C. Kloc, O. Gordan, D.R.T. Zahn, Photoluminescence emission and Raman response of monolayer MoS 2, MoSe 2, and WSe 2, Opt. Express. 21 (2013) 4908–4916.

[24] W. Xu, A. Chin, L. Ye, C.-Z. Ning, H. Yu, Electrical and optical characterization of individual GaSb nanowires, in: Quantum Dots, Part. Nanoclusters VI, SPIE, 2009: pp. 84–90.

[25] S. Larentis, B. Fallahazad, E. Tutuc, Field-effect transistors and intrinsic mobility in ultra-thin MoSe2 layers, Appl. Phys. Lett. 101 (2012) 223104.

[26] X. Wang, Y. Gong, G. Shi, W.L. Chow, K. Keyshar, G. Ye, R. Vajtai, J. Lou, Z. Liu, E. Ringe, Chemical vapor deposition growth of crystalline monolayer MoSe2, ACS Nano. 8 (2014) 5125–5131.

[27] C. Jung, S.M. Kim, H. Moon, G. Han, J. Kwon, Y.K. Hong, I. Omkaram, Y. Yoon, S. Kim, J. Park, Highly crystalline CVD-grown multilayer MoSe2 thin film transistor for fast photodetector, Sci. Rep. 5 (2015) 1–9.

[28] N.R. Pradhan, D. Rhodes, Y. Xin, S. Memaran, L. Bhaskaran, M. Siddiq, S. Hill, P.M. Ajayan, L. Balicas, Ambipolar molybdenum diselenide field-effect transistors: field-effect and hall mobilities, ACS Nano. 8 (2014) 7923–7929.

[29] M.-W. Chen, D. Ovchinnikov, S. Lazar, M. Pizzochero, M.B. Whitwick, A. Surrente, M. Baranowski, O.L. Sanchez, P. Gillet, P. Plochocka, Highly oriented atomically thin ambipolar MoSe2 grown by molecular beam epitaxy, ACS Nano. 11 (2017) 6355–6361.

[30] H. Lee, J. Ahn, S. Im, J. Kim, W. Choi, High-responsivity multilayer MoSe2 phototransistors with fast response time, Sci. Rep. 8 (2018) 1–7.

[31] A.J. Watson, W. Lu, M. Guimaraes, M. Stöhr, Transfer of large-scale two-dimensional semiconductors: Challenges and developments, 2D Mater. (2021).

[32] S.Y. Choi, Y. Kim, H.-S. Chung, A.R. Kim, J.-D. Kwon, J. Park, Y.L. Kim, S.-H. Kwon, M.G. Hahm, B. Cho, Effect of Nb doping on chemical sensing performance of two-dimensional layered MoSe2, ACS Appl. Mater. Interfaces. 9 (2017) 3817–3823.

[33] R.N. Jenjeti, R. Kumar, M.P. Austeria, S. Sampath, Field effect transistor based on layered NiPS 3, Sci. Rep. 8 (2018) 1–9.

[34] K. Lee, H. Kim, M. Lotya, J.N. Coleman, G. Kim, G.S. Duesberg, Electrical characteristics of molybdenum disulfide flakes produced by liquid exfoliation, Adv. Mater. 23 (2011) 4178–4182.

[35] U.S. Environmental Protection Agency, Nitrogen dioxide (NO2) primary standards, n.d. https://www3.epa.gov/ttn/naaqs/standards/nox/s_nox_history.html#4.

[36] G. Mirabelli, C. McGeough, M. Schmidt, E.K. McCarthy, S. Monaghan, I.M. Povey, M. McCarthy, F. Gity, R. Nagle, G. Hughes, Air sensitivity of MoS2, MoSe2, MoTe2, HfS2, and HfSe2, J. Appl. Phys. 120 (2016) 125102.

[37] A. Apte, A. Krishnamoorthy, J.A. Hachtel, S. Susarla, J.C. Idrobo, A. Nakano, R.K. Kalia, P. Vashishta, C.S. Tiwary, P.M. Ajayan, Telluride-based atomically thin layers of ternary two-dimensional transition metal dichalcogenide alloys, Chemistry of Materials. 30 (2018) 7262–7268.

[38] J.H. Huang, H.H. Hsu, D. Wang, W.T. Lin, C.C. Cheng, Y.J. Lee, T.H. Hou, Polymorphism Control of Layered MoTe2 through Two-Dimensional Solid-Phase Crystallization, Scientific Reports. 9 (2019). https://doi.org/10.1038/s41598-019-45142-x.

[39] G. Mirabelli, C. McGeough, M. Schmidt, E.K. McCarthy, S. Monaghan, I.M. Povey, M. McCarthy, F. Gity, R. Nagle, G. Hughes, Air sensitivity of MoS2, MoSe2, MoTe2, HfS2, and HfSe2, Journal of Applied Physics. 120 (2016) 125102.

[40] X. Zheng, Y. Wei, C. Deng, H. Huang, Y. Yu, G. Wang, G. Peng, Z. Zhu, Y. Zhang, T. Jiang, S. Qin, R. Zhang, X. Zhang, Controlled Layer-by-Layer Oxidation of MoTe2 via O3 Exposure, ACS Applied Materials and Interfaces. 10 (2018). https://doi.org/10.1021/acsami.8b11003.

[41] Y. Wakayama, R. Hayakawa, Antiambipolar transistor: A newcomer for future flexible electronics, Adv. Funct. Mater. 30 (2020) 1903724.

CHAPTER 8

Conclusions

8.1 Summary

Chemical and biological sensors play crucial roles in our daily lives, where they help mitigate the cost, time, and availability of specialized units for urgent analyses, such as body vitals, screening for microbial infections (e.g. COVID-19) to reduce transmissions, water quality monitoring, environmental contaminants monitoring (e.g. toxic gas exhaust) in manufacturing plants, etc. Hence, the development of highly sensitive and selective new sensors at acceptable costs is a real need. In this research, the work was focused on materials interface improvements, which determine the sensitivity and stability of any sensor system.

The in-situ prepared Fe_3O_4-Au nanocomposite achieved a high sensitivity in the electrochemical detection of As(III) at a trace level. That can be attributed to the newly introduced synthesis protocol, because: 1) it produced very tiny (≈10 nm) Fe_3O_4NPs that enhanced the surface area for As(III) adsorption, 2) it did not use a linker between gold and magnetite, which enhanced their combined electrocatalytic effects. In addition, mixing the prepared nanocomposite with ionic liquid (IL) enhanced the mechanical stability of the material at the electrode surface and increased its electron transfer.

The M13 bacteriophage-based impedimetric cytosensor showed a high sensitivity towards detection of E. coli, which is one of the main bioindicators for water contamination with fecal coliforms. The high sensitivity is a hybrid effect between the high sensitivity of the

selected transducer, EIS, and the no-lytic nature of M13 nanofibers that kept the signal stable and prevented interruptive signals from possible bacterial cell rupture. This was the first time to introduce M13 as recognition element for electrochemical detection of bacteria, where a super low limit of detection was achieved. Furthermore, the thermal and chemical stability of the introduced system, entitles it for real field applications. In addition, the same impedimetric sensor was utilized for detection of Bacteroides Thetaiotaomicron, but in this case antibody was used as a biorecognition element.

Lateral sheet size effect on the properties of rGO thin films was experimentally and theoretically studied for the first time. The role of low-temperature thermal reduction in the enhancement of rGO's electronic properties was also revealed. The strong revealed insights into the role of lateral sheet size and low temperature reduction enabled for the synthesis of pristine graphene-like behaving rGO thin, with the lowest band gap and highest carrier mobility reported for this material.

$MoSe_2$ nanosheets were synthesized using chemical vapor deposition and applied as novel near-infrared (NIR) optoelectronic devices for light-gated, low-power FET gas sensor. A low limit of detection of NO_2 gas of 40 ppb was achieved. Further, ternary $MoSe_{2(2-x)}Te_{2x}$ alloys were synthesized in a controllable band gap approach. The ternary alloy exhibited three orders of magnitude enhancement in the device output. In addition, Janus in-situ prepared $MoSe_{2(2-y)}Te_{2y}/MoSe_{2(2-x)}Te_{2x}$ defect-free interface heterostructures, where $y \neq x$, and $y \geq 0$, were synthesized, and characterized. The Janus heterostructure showed antiambipolar behavior which is promising for multivalued logic circuits.

8.2. Future work

The prepared pristine graphene-like rGO is a promising material for many electronic applications, including its feasibility for screen printed electrodes and conductive ink printing. So further work in this area might be of interest.

M13 phage can be engineered to selectively detect as bacterial strains, and hence this can be investigated, and the corresponding electrical and electrochemical sensors can be built the same way we introduced in this work, but for a wider range of applications.

The ternary alloys of Mo/Se/Te can be further studied for different applications, including gas sensing. Also, high resolution STEM mapping of the structure for revealing more details about the nature of alloying is important.

Janus in-situ prepared $MoSe_{2(2-y)}Te_{2y}/MoSe_{2(2-x)}Te_{2x}$ defect-free interface heterostructures are very new materials and a huge work is still available on both materials and devices level. This new synthesis approach can be implemented in other Janus heterostructure, as well. The antiambipolar behavior is an open research area for further work, as the results here are very preliminary, and the improvement in maximum current is important.

APPENDIX A

Linker-free magnetite-decorated gold nanoparticles (Fe_3O_4-Au): Synthesis, characterization, and application for electrochemical detection of Arsenic (III)

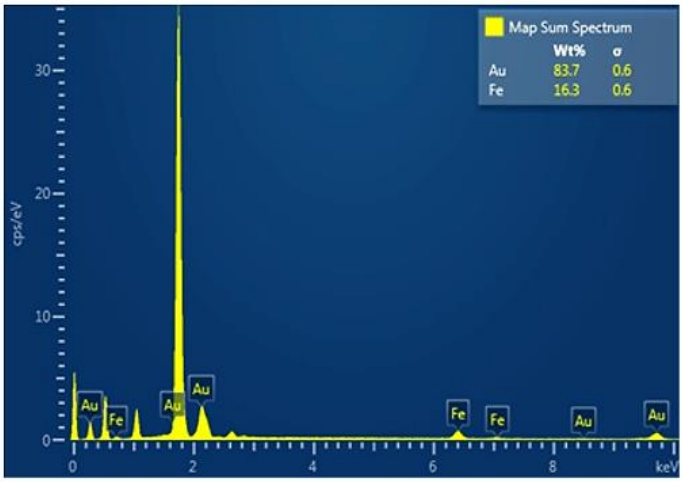

Figure A1. EDX spectrum of the Fe_3O_4-Au nanocomposite on a piece of Pd/Pt-sputtered silicon wafer with the weight percentage.

Table A1. The composition of synthetic raw wastewater

Compounds	***Amount* (mg) *added to 500 mL***
CH_3COONa	128.20
CH_3COONH_4	120.44
KH_2PO_4	21.97
$NaHCO_3$	62.50
$FeCl_2$	0.188
$MnSO_4$	0.02
$ZnSO_4$	0.18
NaCl	292.50
Humic acid sodium	25.00
$MgSO_4$	12.50
$CaCl_2$	5.00

Table A2. Comparison of different electrodes for the detection of As(III).

Electrodes	Technique	Linear range (µg/L)	LOD (µg/L)	Reference
AuNP/BDD electrode	SWASV	100-1500	20	[1]
Au-Pd/GCE	ASV	1-25	0.5	[2]
nano-Au/PANI/GCE	SWV	610-3050	0.4	[3]
AuNPs-PCWEs	CS	2-50	2.2	[4]
rGO/Fe_3O_4/SPCE	SWASV	2-20	0.3	[5]
AuNPs/GCE	SWASV	0-15	0.25	[6]
NanoPt-Fe(III)/MWCNT/GCE	ASV	1.35-14.5	0.75	[7]
Fe_3O_4-Au-IL/GCE	SWASV	0-100	0.22	This work

AuNP/BDD: gold nanoparticles on a boron-doped diamond; nano-Au/PANI/GCE: nanogold-particle/polyaniline-modified Glassy Carbon Electrode; SWV: Square Wave Voltammetric; AuNPs-PCWEs: gold-modified paper-based carbon working electrodes; CS: Chronoamperometric Stripping; rGO: reduced graphene oxide; SPCE: screen-printed carbon electrode; platinum-iron(III) nanoparticles modified multi-walled carbon nanotube on glassy carbon electrode: nanoPt-Fe(III)/MWCNT/GCE; GCE: glassy carbon electrode

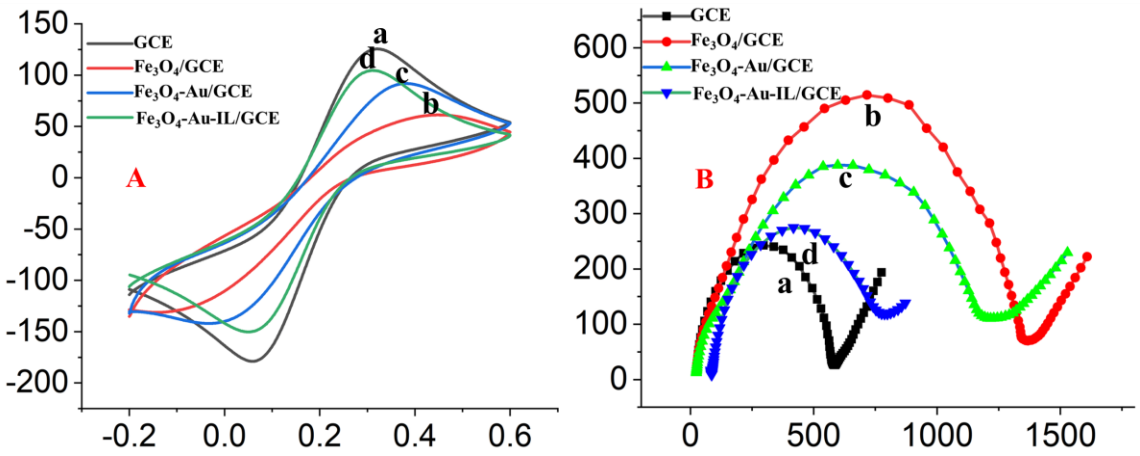

Fig. A2. (A) Cyclic voltammograms and (B) Nyquist plot of electrochemical impedance spectra of 5mM $[Fe(CN)_6]^{3-/4-}$ in 0.1 M KCl: (a) bare GCE, (b) Fe_3O_4/GCE, (c) Fe_3O_4-Au/GCE and (d) Fe_3O_4-Au-IL/GCE.

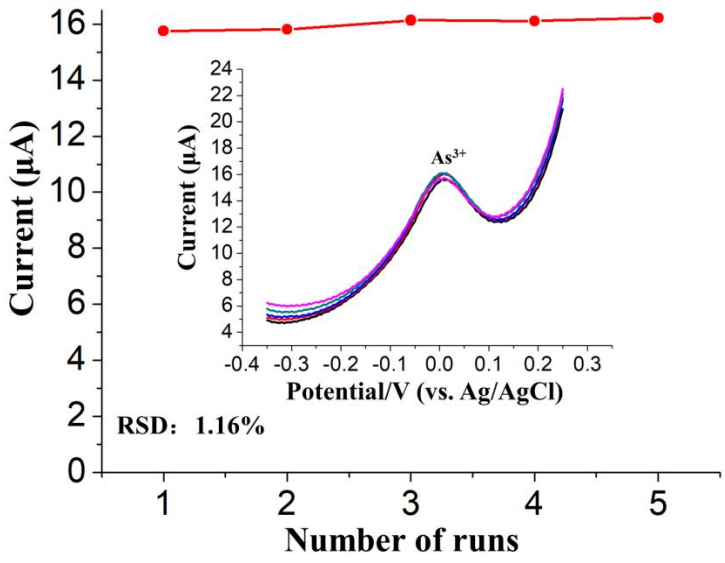

Fig. A3. Five repetitive stripping current measurements of 60 μg/L As(III) using the Fe_3O_4-Au-IL/GCE in 0.2 M acetate buffer (pH 5.0). The insets are the data collected from every SWASV response for five runs.

Reference

1. Pungjunun, K.; Chaiyo, S.; Jantrahong, I.; Nantaphol, S.; Siangproh, W.; Chailapakul, O. Anodic stripping voltammetric determination of total arsenic using a gold nanoparticle-modified boron-doped diamond electrode on a paper-based device. *Microchim. Acta* **2018**, *185*, 324.

2. Lan, Y.; Luo, H.; Ren, X.; Wang, Y.; Liu, Y. Anodic stripping voltammetric determination of arsenic (III) using a glassy carbon electrode modified with gold-palladium bimetallic nanoparticles. *Microchim. Acta* **2012**, *178*, 153–161.

3. Chowdhury, A.; Ferdousi, S.; Islam, M.M.; Okajima, T.; Ohsaka, T. Arsenic detection by nanogold/conducting-polymer-modified glassy carbon electrodes. *J. Appl. Polym. Sci.* **2007**, *104*, 1306–1311.

4. Nunez-Bajo, E.; Blanco-López, M.C.; Costa-García, A.; Fernández-Abedul, M.T. Electrogeneration of Gold Nanoparticles on Porous-Carbon Paper-Based Electrodes and Application to Inorganic Arsenic Analysis in White Wines by Chronoamperometric Stripping. *Anal. Chem.* **2017**, *89*, 6415–6423.

5. Xie, Z.; Xu, J.; Xie, F.; Xiong, S. Electrochemical Detection of As (III) by a rGO/Fe3O4-modified Screen-Printed Carbon Electrode. *Anal. Sci.* **2016**, *32*, 1053–1058.

6. Majid, E.; Hrapovic, S.; Liu, Y.; Male, K.B.; Luong, J.H.T. Electrochemical determination of arsenite using a gold nanoparticle modified glassy carbon electrode and flow analysis. *Anal. Chem.* **2006**, *78*, 762–769.

7. Shin, S.-H.; Hong, H.-G. Anodic stripping voltammetric detection of arsenic (III) at platinum-iron (III) nanoparticle modified carbon nanotube on glassy carbon electrode. *Bull. Korean Chem. Soc.* **2010**, *31*, 3077–3083.

APPENDIX B

Non-lytic M13 phage-based highly sensitive impedimetric cytosensor for detection of coliforms

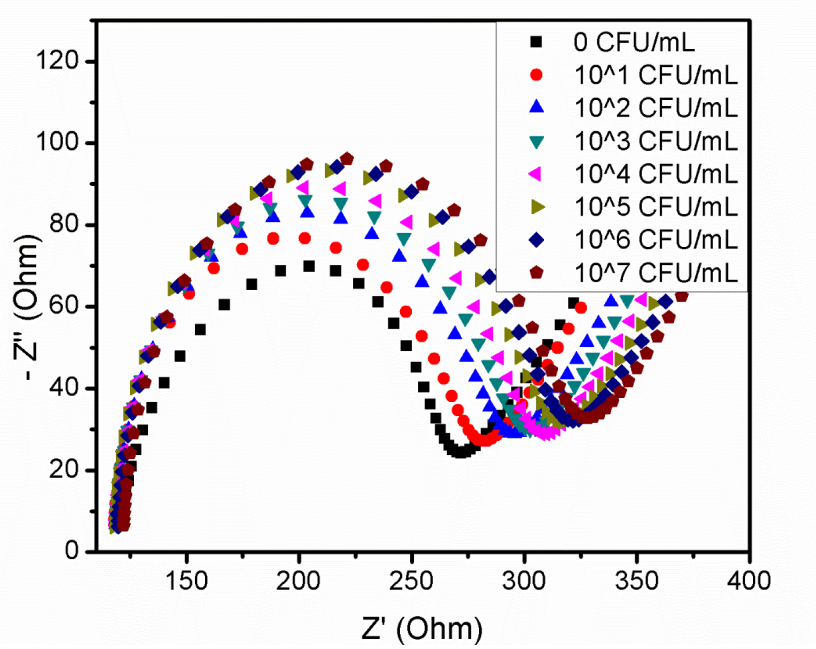

Figure B1. Nyquist plot of the sensor's response to different concentrations of E. Coli XL1-Blue in PB solution.

Table B1. Relative standard deviation (RSD) of the sensors' responses at each concentration of *E. coli XL1-Blue.*

Log (CFU/mL)	Mean (Ohms)	SD (Ohms)	RSD (%)
1	13.30	1.12	8.47
2	25.63	1.46	5.70
3	33.30	2.33	7.02
4	38.13	2.00	5.25
5	45.96	2.05	4.46
6	48.66	2.38	4.90
7	51.90	2.57	4.95

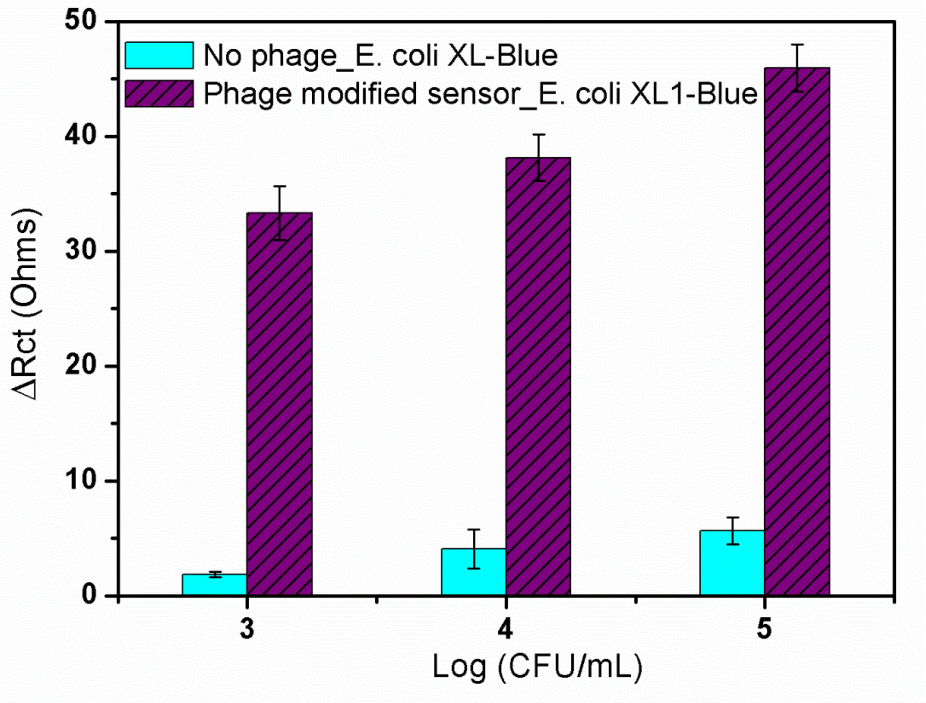

Figure B2. Comparison of responses of electrodes with and without M13 bioreceptor to *E. coli XL1-Blue*

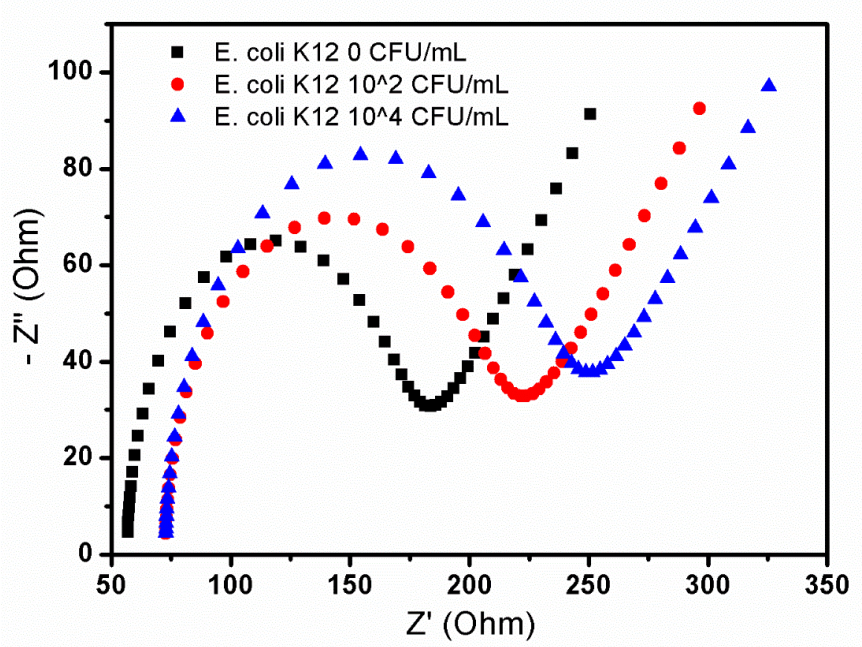

Figure B3. Nyquist plots of the EIS responses of M13-modified electrodes to *E. coli* K12.

Table B2. Stability of the cytosensor when stored at 22°C (room temperature) and 45°C.

22 °C Stability		**45 °C Stability**	
Incubation (days)	**%(ΔR/Ro)**	**Incubation (days)**	**%(ΔR/Ro)**
0	55.2±2.2	**0**	55.2±2.2
2	53.4±5.3	**1**	62.4±3.1
9	58.1±10	**2**	50.6±15.7
16	60.2±2.3	**16**	49.3±7.8

Each data point is an average of responses from 1 electrode, measured 3 times and error bars represent ± 1 standard deviation.

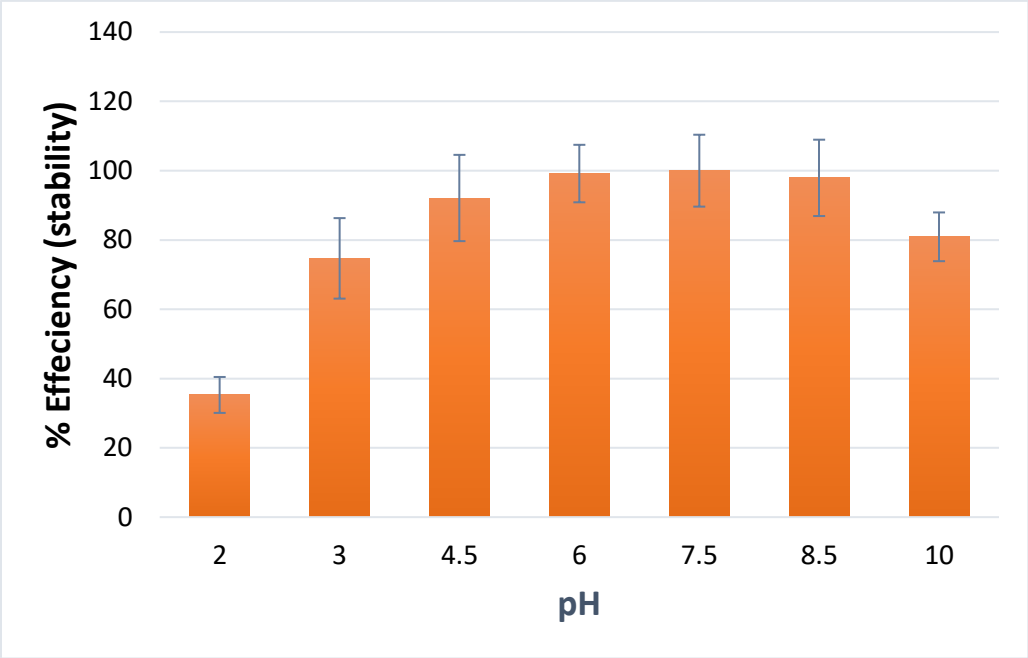

Figure B4. Effect of incubating cytosensor in varying pH buffers for an hour on sensor response. Each data point is an average of responses from 1 electrode, measured 3 times and error bars represent ± 1 standard deviation.

APPENDIX C

Synthesis of Pristine Graphene-like Behaving rGO Thin Film: Insights into What Really Matters

1. Optimization of GO's concentration for rGO-FET devices

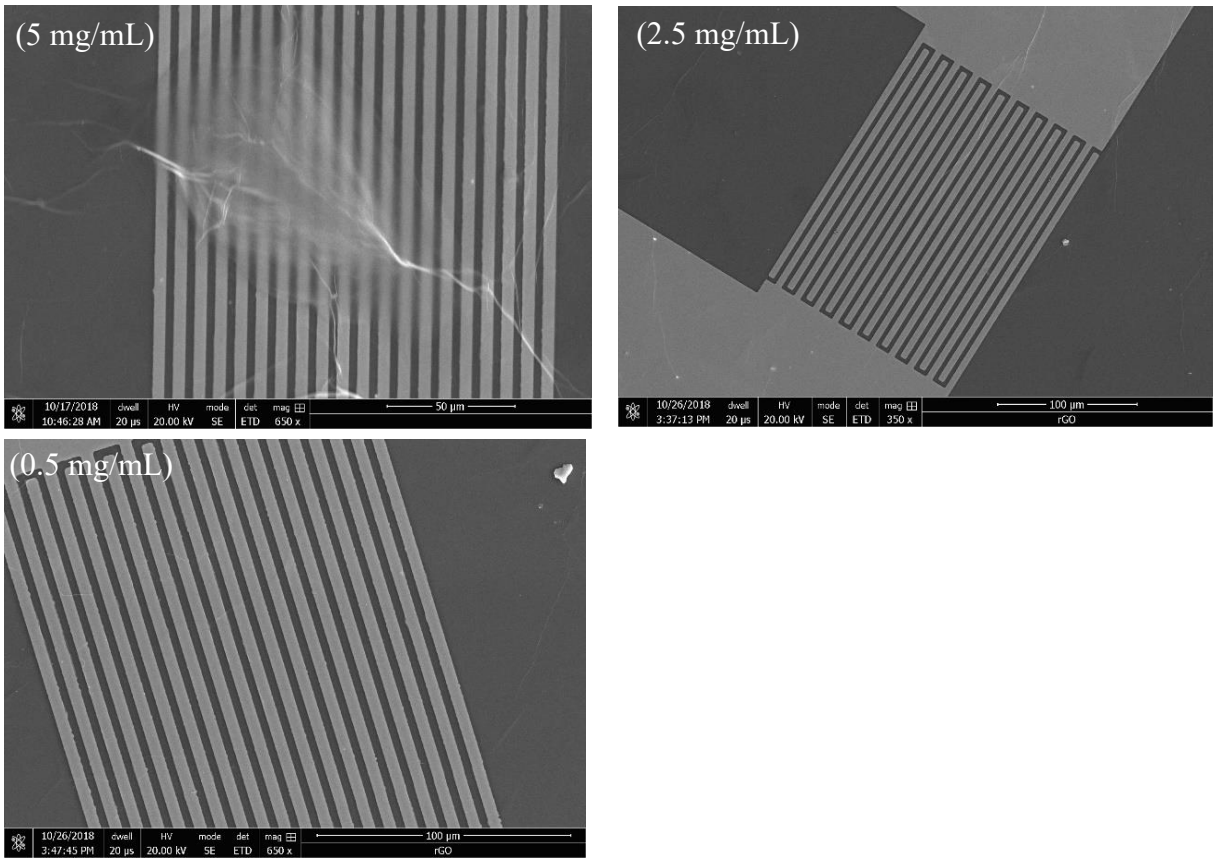

Fig. C1. More SEM images of rGO thin films on gold interdigitated electrodes, prepared by drop casting of 10 µL of GO with different concentrations, followed by drying and thermal reduction**.**

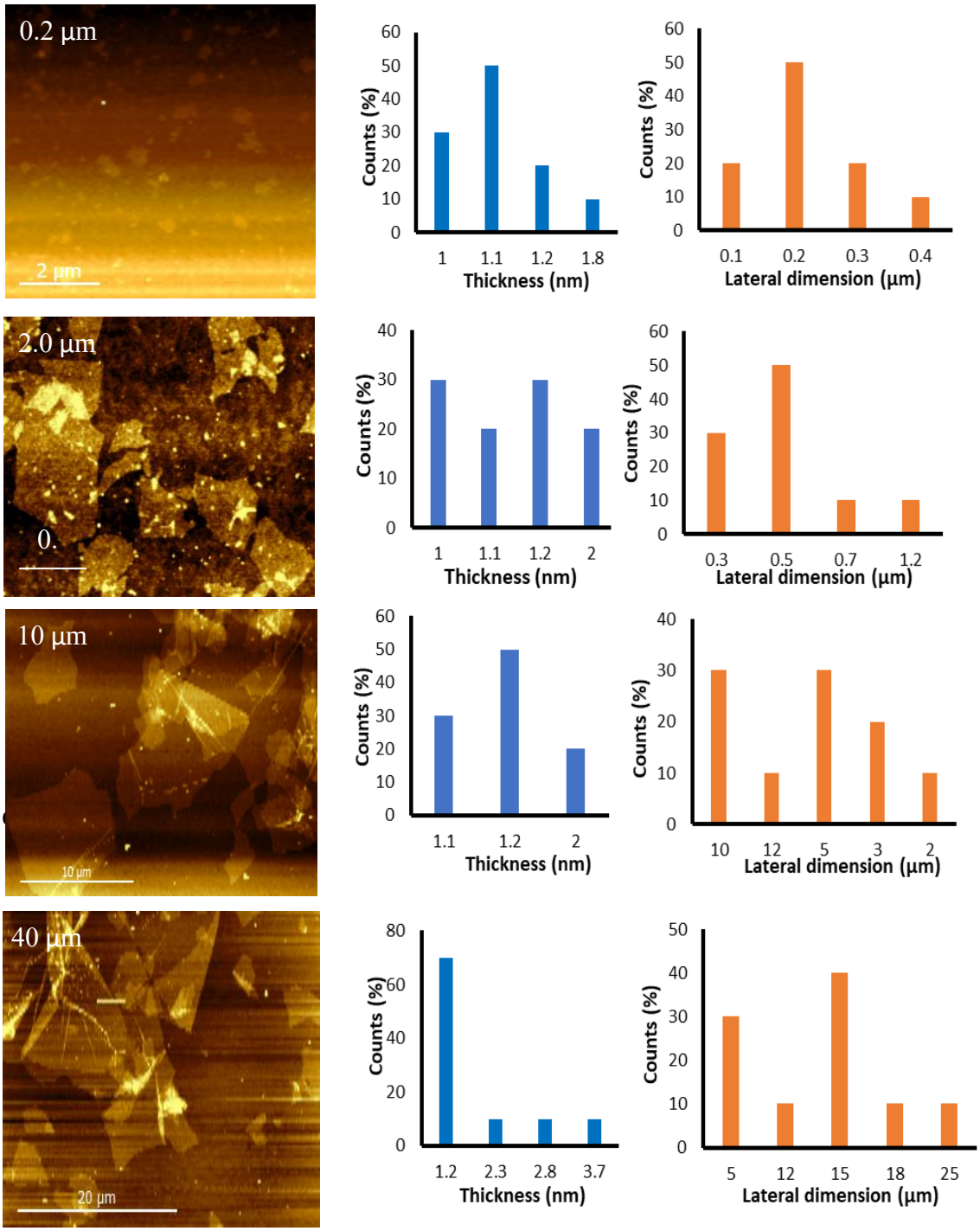

Fig. C2. Thickness and lateral size distribution of 0.2, 2.0, 10, and 40 µm GO nanosheets.

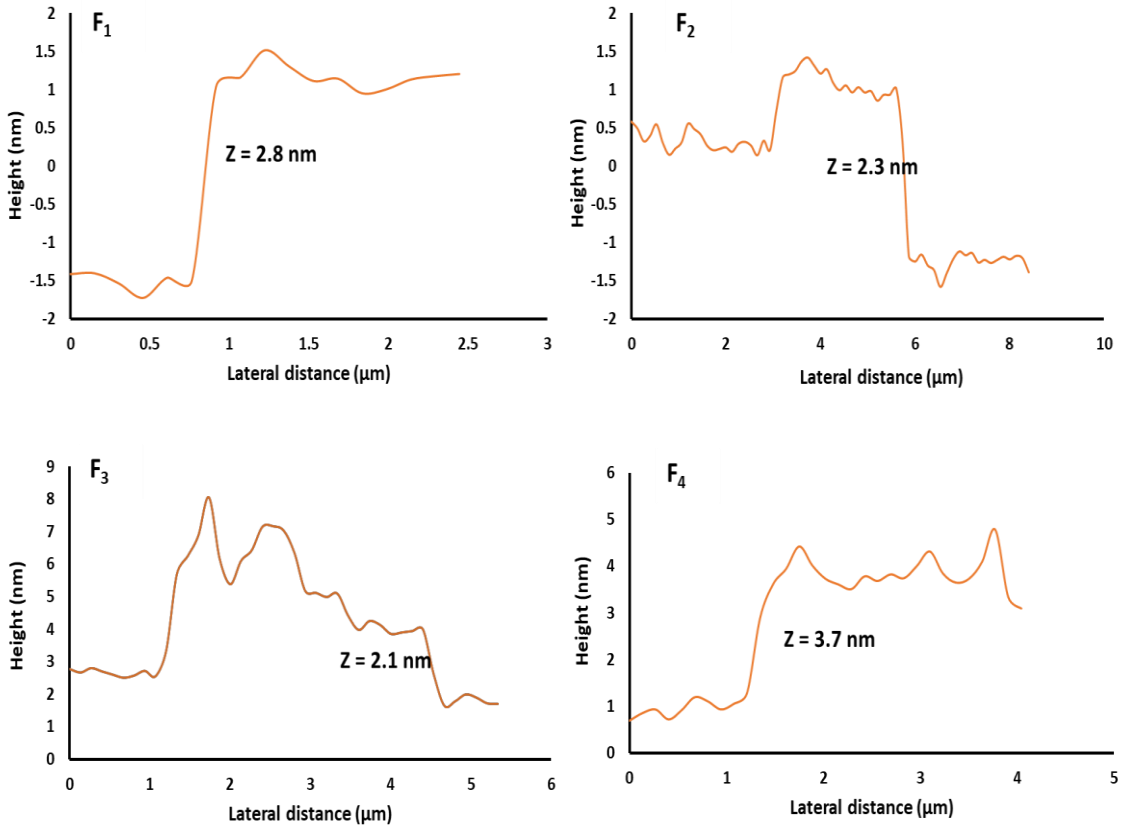

Fig. C3. AFM height profiles of folded/rolled GO nanosheets. Corresponding labels (F_1-F_4) are on images e&f of Fig. 2.

2. Effect of oxidation/reduction process on sheets properties

The oxidation method plays a crucial role in the exfoliation of graphite into GO nanosheets, and the degree and type of defects introduced. As reported by **Marcano et al.**, in comparison to Hummers method (HM), improved Hummers method (IHM) produces higher quality GO; more hydroxyl and epoxy groups and hence less number of stacked layers and fewer carboxyl groups because of the use of phosphoric acid instead of sodium nitrate [1]. It is worth mentioning that the hydroxyl and epoxy groups are considered

healable defects, while carboxyl groups are considered less/non-healable as they result from breaking aromatic rings in the graphene sheets. Phosphoric acid helps protect the basal plane of GO nanosheets and reduces the number of carbonyl/carboxyl groups [2,3]. Consequently, IHM was used in the synthesis of all GO samples in this work [4].

Reduction of GO to rGO is basically a healing process in which the sp^2 hybridized honeycomb structure is restored and the oxygen-containing groups are removed [5]. The chemical reduction approaches most commonly employed in GO reduction [6], however, employ toxic chemicals, and result in chemical doping of the produced rGO nanosheets and thereby tuning of band gap, which is not always desirable. On the other hand, thermal annealing (reduction) is a clean process in which oxygen-containing groups are removed as CO, CO_2, and water vapor and the rGO product can be considered as graphene. Further, this reduction method is suitable for the bulk production of graphene [7].

To understand the contribution of the reduction time to the electronic properties of corresponding devices made of rGO thin films, a set of rGO-FET devices were fabricated using 0, 10, 30, 60, and 120 min reduced GO thin films. The resistance of the devices was measured as a factor of reduction time, as illustrated in **Fig. C4**. The results of 0- and 10-min reduction time are not shown as these devices were very unstable. The results show a decrease in resistance by increasing reduction time, which can be attributed to the healing reduction process. In addition, the standard deviation of results becomes very small at 120 min, as all the rGO nanosheets are evenly reduced. So, thermal reduction of GO at 200^{o}C for 120 min in open air is recommended for producing stable rGO-FET devices.

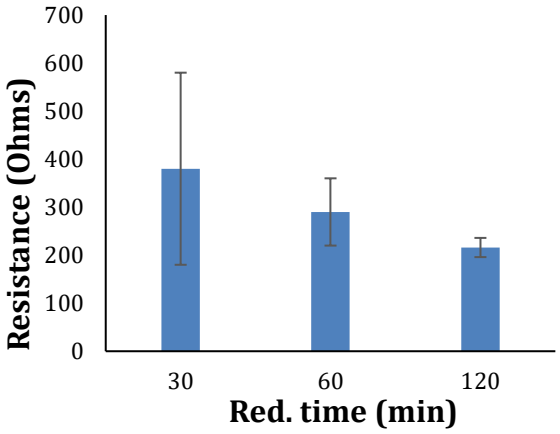

Figure C4. Correlation between reduction (healing) time and rGO-FET device's initial resistance.

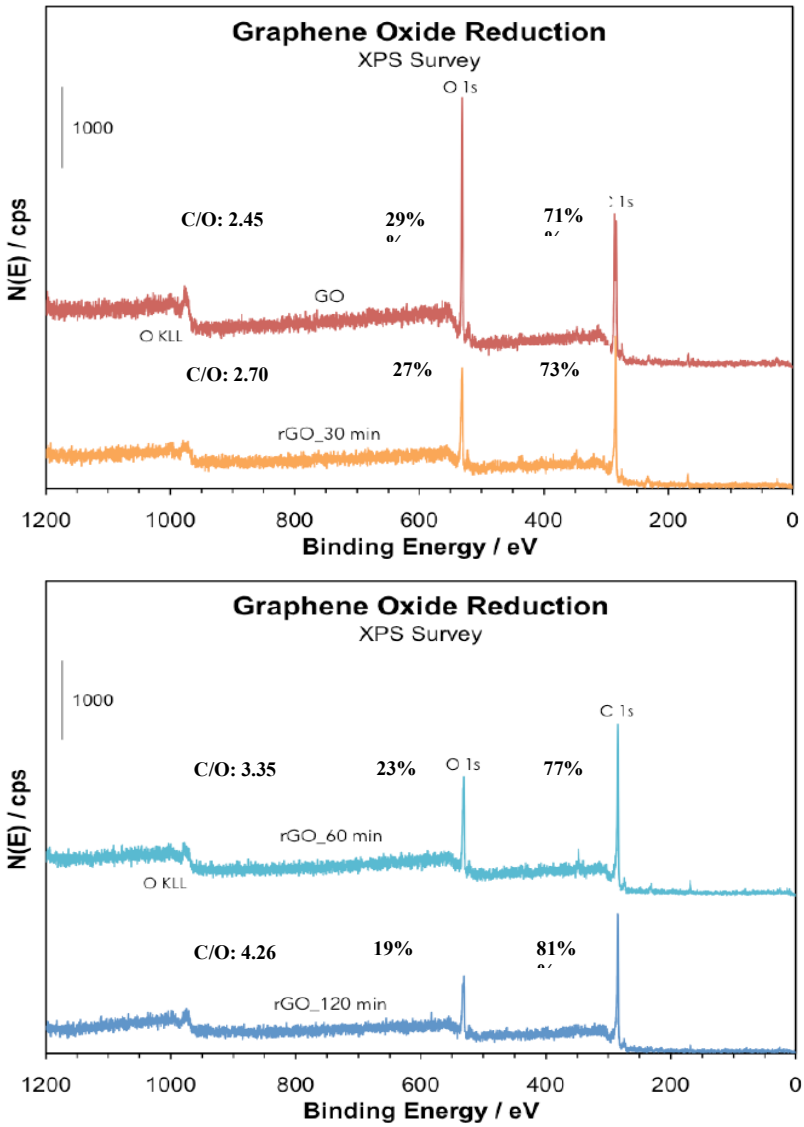

Fig. C5. Survey spectra of GO showing the C/O ratio at different reduction times.

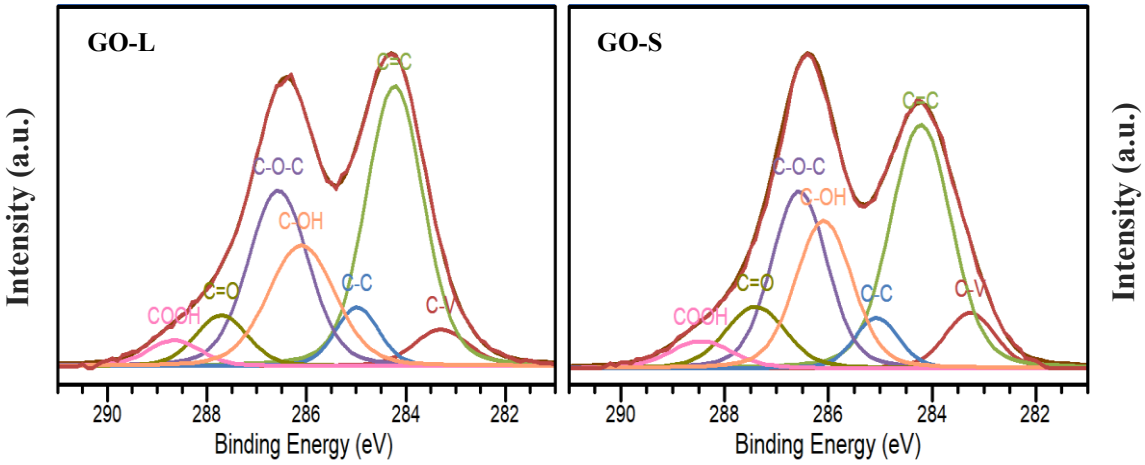

Fig. C6. Deconvoluted C1s spectra of GO-L and GO-S samples.

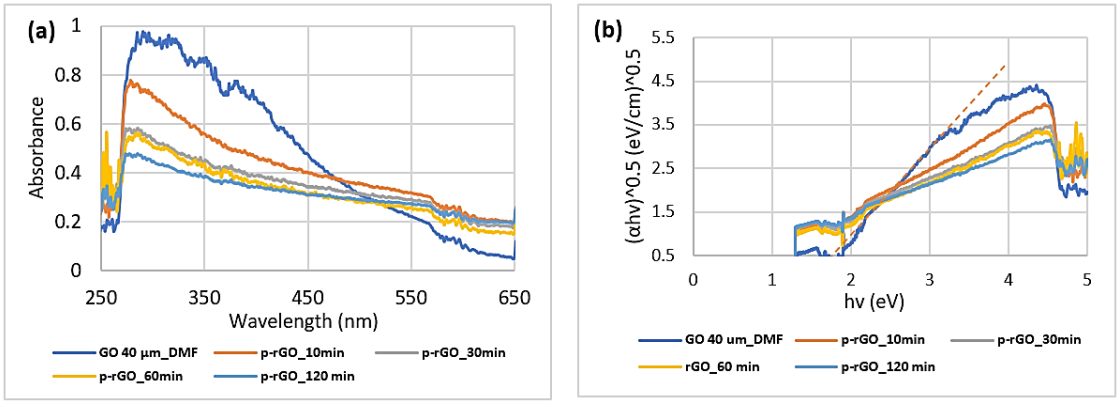

Figure. C7. UV-Vis spectra (a) and Tauc's plots (b) of GO/rGO nanosheets.

Table C1. Optical band gaps of large sheets GO at different reduction times.

Reduction time (min)	Optical band gap (eV)
0.0	1.8
10.0	0.9-1.35
30.0	0.7-0.93
60.0	0.7
120.0	0.4

3. Density functional theory (DFT) calculations

3.1. Method

The structure optimizations were performed using the Vienna ab-initio Simulation Package (VASP) and adopting the Perdew-Berke-Ernzerhof (PBE) general gradient approximation (GGA) as the exchange correlation functionals [8,9]. A cutoff energy of 520 eV was used, and the Brillouin Zone was sampled using a 8×1×18 gamma-centered k-point mesh for the larger flakes, and the smaller ones were adjusted accordingly. These values were chosen carefully to ensure the convergence of forces on ions to better than 0.001 eV.

All GO and rGO samples were modeled with periodic boundary only in one lattice direction, with a spacing of 20 Å and 15 Å in the other two directions (*x*-axis and *y*-axis, respectively) to avoid coulombic interactions between the adjacent sheets.

3.2. GO sheet size effect

The computed energy values for the highest occupied molecular orbital (HOMO), lowest occupied molecular orbital (LUMO), HOMO-LUMO gap, valence band maximum (VBM), conduction band minimum (CBM), bandgap, and Fermi level are shown in **Table C2.**

Table C2. energy values of HOMO, LUMO, HOMO-LUMO gap, valence band maximum (VBM), conduction band minimum (CBM), Bandgap, and the Fermi level for intact graphene oxide structures with four (A), six (B), and eight (C) carbon layers

Structure	HOMO (eV)	LUMO (eV)	HOMO-LUMO gap (eV)	VBM (eV)	CBM (eV)	Bandgap (eV)	Fermi level (eV)
Intact – A	-3.984405	-3.967918	0.016487	-2.937	5.189	2.252	-3.98224662
Intact – B	-3.781092	-3.777442	0.003650	-2.793	4.789	1.996	-3.77894928
Intact – C	-3.607161	-3.606264	0.000897	-2.743	4.340	1.597	-3.60629952

3. Determination of C_i of rGO thin film using EIS

Interfacial capacitance (C_i) of rGO thin film was determined using EIS measurements, as reported elsewhere [10,11]. Briefly, 10 μL of a 1.25 mg/mL solution of GO was drop casted, dried and thermally reduced on gold electrodes. Ag/AgCl was used as a reference electrode and a Pt mesh was used as an auxiliary electrode. The measurements were performed in 10 mM PBS (pH 7.2), at different potentials (-0.6 to 0.6 V). The EIS data

were collected using CHI6005E in a frequency range of 1-1000 Hz. The C_i was calculated using the CHI6005E simulation software at each potential point. Results in **Fig. S8**, show that rGO thin film's interfacial capacitance varies from 2.6 to 0.9 $\mu F/cm^2$, with an average of 1.48 $\mu F/cm^2$.

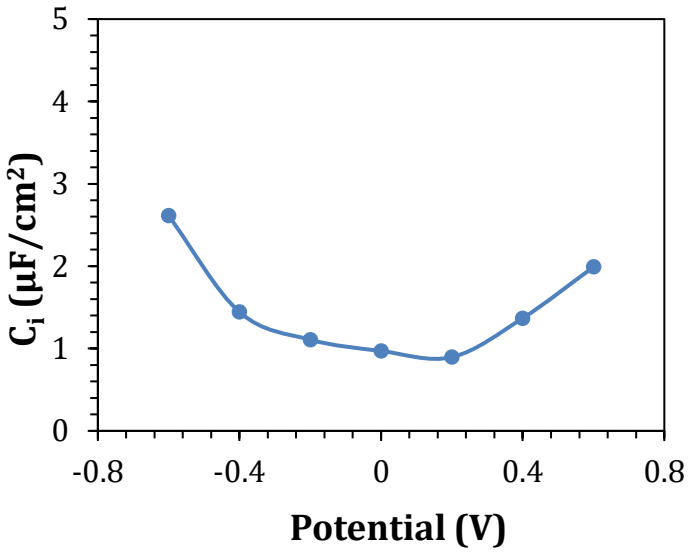

Figure C8. C_i of rGO thin film at a potential range of -0.6 to 0.6 V.

References

[1] D.C. Marcano, D. V Kosynkin, J.M. Berlin, A. Sinitskii, Z. Sun, A. Slesarev, L.B. Alemany, W. Lu, J.M. Tour, Improved synthesis of graphene oxide, ACS Nano. 4 (2010) 4806–4814.

[2] A.L. Higginbotham, D. V Kosynkin, A. Sinitskii, Z. Sun, J.M. Tour, Lower-defect graphene oxide nanoribbons from multiwalled carbon nanotubes, ACS Nano. 4 (2010) 2059–2069.

[3] H.-C. Hsu, I. Shown, H.-Y. Wei, Y.-C. Chang, H.-Y. Du, Y.-G. Lin, C.-A. Tseng, C.-H. Wang, L.-C. Chen, Y.-C. Lin, Graphene oxide as a promising photocatalyst for CO 2 to methanol conversion, Nanoscale. 5 (2013) 262–268.

[4] M. Sedki, M.B. Mohamed, M. Fawzy, D.A. Abdelrehim, M.M.S.A. Abdel-Mottaleb, Phytosynthesis of silver-reduced graphene oxide (Ag-RGO) nanocomposite with an enhanced antibacterial effect using Potamogeton pectinatus extract, RSC Adv. 5 (2015) 17358–17365. https://doi.org/10.1039/c4ra13117g.

[5] H. Feng, R. Cheng, X. Zhao, X. Duan, J. Li, A low-temperature method to produce highly reduced graphene oxide, Nat. Commun. 4 (2013) 1539.

[6] S. Park, R.S. Ruoff, Chemical methods for the production of graphenes, Nat. Nanotechnol. 4 (2009) 217.

[7] I. Sengupta, S. Chakraborty, M. Talukdar, S.K. Pal, S. Chakraborty, Thermal reduction of graphene oxide: How temperature influences purity, J. Mater. Res. 33 (2018) 4113–4122.

[8] G. Kresse, J. Furthmüller, Efficiency of ab-initio total energy calculations for metals and semiconductors using a plane-wave basis set, Comput. Mater. Sci. 6 (1996) 15–50.

[9] J.P. Perdew, K. Burke, M. Ernzerhof, Generalized gradient approximation made simple, Phys. Rev. Lett. 77 (1996) 3865.

[10] M.D. Stoller, C.W. Magnuson, Y. Zhu, S. Murali, J.W. Suk, R. Piner, R.S. Ruoff, Interfacial capacitance of single layer graphene, Energy Environ. Sci. 4 (2011) 4685–4689.

[11] J. Xia, F. Chen, J. Li, N. Tao, Measurement of the quantum capacitance of graphene, Nat. Nanotechnol. 4 (2009) 505.